Ph.D. Thesis

Magnetic excitations from first principles

Thorbjørn Skovhus

Kongens Lyngby, 2021

Magnetic excitations from first principles

Ph.D. Thesis
October 31st, 2021

By
Thorbjørn Skovhus

Preface

This thesis is submitted in candidacy for a Ph.D. degree in Physics from the Technical University of Denmark (DTU). The Ph.D project was carried out at the Center for Atomic-scale Materials Design (CAMD) at the DTU Department of Physics between September 2018 and October 2021. The project was supervised by Main Supervisor Associate Professor Thomas Olsen and Supervisor Senior Scientist Niels Bech Christensen, while funded by an internal stipend from DTU.

The thesis also includes work conducted at an external stay hosted by Associate Professor Henrik M. Rønnow at the Laboratory for Quantum Magnetism under the Institute of Physics at the École Polytechnique Fédérale de Lausanne during the months of March, June and July 2020. In addition, the thesis also includes work carried out in contribution to joint projects of the CAMD section, supervised by Professor Kristian S. Thygesen.

<div align="right">

Thorbjørn Skovhus

Kongens Lyngby, October 31st, 2021

</div>

Abstract

Quantum magnetism in condensed matter is an intriguing field of research, with promising applications for future technology. However, the progress towards a disruption of data center computing with spintronics or a large-scale employment of high-temperature superconductors in modern energy infrastructure has been slow at best. One of several reasons for the slow progress is the profound theoretical difficulty associated with the treatment of magnetic quantum effects in real materials, both from a modelling perspective and within a first principles approach. Beyond the contemporary theoretical barriers, there is a vast realm of uncharted territory, where one may drive forward the technological applications of tomorrow, but also discover new physics.

In this thesis, the theoretical background of linear response time-dependent density functional theory is presented in order to illustrate how the fundamental magnetic excitations of real materials can be computationally characterized in terms of the transverse magnetic susceptibility. A concrete computer implementation of the first principles methodology is developed, relying on the projector augmented-wave method to compute plane wave susceptibilities. Using an appropriate gap error correction scheme, the implementation is proven to be both accurate and effective, yielding converged magnon dispersion relations even for the challenging class of itinerant ferromagnets.

Studies of the transverse magnetic excitations in itinerant ferromagnets Fe, Ni, Co and MnBi are presented along with a study of the antiferromagnets Cr and Cr_2O_3. Using the adiabatic local density approximation for the exchange-correlation kernel, a parabolic magnon dispersion is obtained for the investigated ferromagnets and a linear dispersion is obtained for the antiferromagnets. For Fe, Co and MnBi, the studies reveal a satisfactory match to experiment, although for MnBi only when applying a Hubbard correction to the local density approximation. For Ni and Cr_2O_3, the magnon stiffness/velocity is overestimated by roughly a factor of two, whereas sufficient experimental data is lacking in order to benchmark Cr. The thesis also presents a discussion of the itinerant electron effects in the magnon spectra of Fe, Ni, Co and Cr, including the observation of a new optical collective mode in Cr, which seems to be unaffected by Landau damping. Also the magnetic frustration in MnBi is discussed in detail and it is proposed that a magnetic phase transition to helical order can be realized in Cr alloys, potentially in combination with externally applied strain.

Furthermore, the thesis presents a newly developed class of nonlocal exchange-correlation functionals designed to improve short-range correlations based on the correlation hole of the homogeneous electron gas. The functionals use an effective density in the functional form for the local density approximation, which is shown to consistently improve the functional performance, also in the atomic limit. Finally, the thesis covers a recent computational development towards streamlining material simulation recipes.

Resumé

Kvantemagnetiske materialer er et fascinerende forskningsområde med lovende teknologiske anvendelsesmuligheder. Desværre har udviklingen frem mod fx en anvendelse af spintroniske komponenter i moderne computerteknologi eller en udrulning af højtemperatursuperledere i vores energiinfrastruktur været særdeles træg. En af årsagerne er, at de kvantemagnetiske materialer er svære at håndtere teoretisk, med modeller såvel som startende fra de kvantemekaniske grundprincipper. Hvis de nuværende teoretiske forhindringer overkommes, vil der være rig mulighed for at bidrage til fremtidig teknologi, mens der også vil være mulighed for, at nye fysiske fænomener træder frem.

For at illustrere hvorledes et materiales anslåede tilstande kan karakteriseres ved hjælp af computersimuleringer, gennemgår denne afhandling den underliggende teori for beregninger af det lineære systemrespons vha. tidsafhængig tæthedsfunktionalteori. Derudover præsenteres en ny computerimplementering af teorien til beregning af det tværgående magnetiske respons, hvorigennem man kan studere et materiales magnoner. Responsfunktionen er repræsenteret i en planbølgebasis og er udregnet ved hjælp af PAW-metoden til lokalt at forstærke bølgerne gennem lineær afbildning. Gennem en række grundige test viser metoden sig velegnet til præcist at udregne magnondispersionen i den ellers svært tilgængelige materialeklasse af ferromagnetiske metaller.

I afhandlingen bruges den nyudviklede metode til at studere magnonspektrene i de ferromagnetiske metaller Fe, Ni, Co og MnBi, samt i antiferromagneterne Cr of Cr_2O_3. Ved anvendelse af den adiabatiske lokale tæthedsapproksimation beregnes magnondispersionen til at være kvadratisk for ferromagneter og lineær for antiferromagneter, i overensstemmelse med eksperimenter. For Fe, Co og MnBi opnår vi i det hele taget en god eksperimentel overensstemmelse, omend vi er nødt til at tilføje en Hubbardkorrektion for MnBi's vedkommende. Det samme kan desværre ikke siges for Ni og Cr_2O_3, hvor krumningen/hældning på magnondispersionen er estimeret til omkring det dobbelte af de eksperimentelt observerede værdier. I afhandlingen diskuteres også indflydelsen fra de metalliske elektroner på magnonspektrene i Fe, Ni, Co og Cr, hvilket bl.a. leder til observationen af en ny slags kollektiv resonans i Cr, der lader til at være upåvirket af Landau spredning. Ydermere diskuteres også den magnetiske frustration i MnBi og det foreslås at en magnetisk faseovergang til en helisk magnetisk orden kan være mulig i Cr-legeringer af materialet.

Afslutningsvis præsenteres også en ny række ikke-lokale tilnærmelser til korrelationsenergifunktionalet i tæthedsfunktionalteori. Tilnærmelserne er designet til at forbedre de kortrækkende korrelationer i den homogene elektrongas. Funktionalerne viser sig dog også at forbedre overensstemmelsen med eksperimenter i den atomare grænse sammenlignet med en lokal tilnærmelse. Afslutningsvis præsenteres også et nyt kodebibliotek udviklet til at strømline atomart baserede materialesimuleringer.

Acknowledgements

Finally there are no one, whom I am more indebted to than my friends and family. Without your love and support, I could not have come this far. This Ph.D. candidacy has required a lot of sacrifices from my side and the unconditional support from my parents, sister and close friends means the world to me. And to Ida: We made it! I feel blessed with your presence in my life and together we have fought our way through some incredibly hard times locked up in the home office.

List of Publications

[A] T. Skovhus and T. Olsen,
"Dynamic transverse magnetic susceptibility in the projector augmented-wave method: Application to Fe, Ni, and Co," Physical Review B **103**, 245110 (2021).

Printed in copy from page 37.

[B] T. Skovhus, T. Olsen, and H. M. Rønnow,
"Interplay between static and dynamic correlation in itinerant magnets - a first principles study of magnons in MnBi," *submitted*, arXiv:2110.07282.

Printed in copy from page 70.

[C] T. Skovhus and T. Olsen,
"Magnons in antiferromagnetic bcc-Cr and Cr_2O_3 from time-dependent density functional theory," *in preparation*.

Printed in copy from page 87.

[D] M. Gjerding, T. Skovhus, A. Rasmussen, F. Bertoldo, A. H. Larsen, J. J. Mortensen, and K. S. Thygesen,
"Atomic Simulation Recipes – A Python framework and library for automated workflows," Computational Materials Science **199**, 110731 (2021).

Printed in copy from page 144.

Contents

Introduction

To fully understand and exploit the unique properties of magnetic materials, it is necessary to go beyond the magnetic ground state and investigate also the magnetic excitations. Not only do the excited states govern intrinsic material properties related to the fundamental fluctuations of the underlying quantum system, they also govern how a material can react to changes in its external environment. As a result, one may characterize both the fluctuations and the material response towards external perturbations in terms a single quantity, the dynamic susceptibility. In particular, the transverse magnetic susceptibility determines the change in the transverse magnetization induced by a dynamic transverse magnetic field, to linear order. As a linear response function, it is comprised of poles at the available eigenstate transitions at thermal equilibrium, transitions which in the case of the transverse magnetic susceptibility imply that the spin angular momentum has been either raised or lowered by a single unit.

The spin-raising and spin-lowering excitations in a magnetic material are typically divided into two categories. The Stoner pair excitations are the electron hole pairs which include a flip of the electronic spin. In a single-particle band picture, such an excitation is generated by promoting an electron from an occupied single-particle state to an unoccupied state with some added energy $\hbar\omega$, some additional crystal momentum $\hbar\mathbf{q}$ and of the opposite spin. Due to the continuous electronic bands, the Stoner pair excitations form a continuum, the Stoner continuum, and in the fully interacting many-body system, the continuum is renormalized according to the attractive interaction of the Stoner pairs. The second type of excitation, residing below the Stoner continuum, corresponds to the collective resonance of the entire Stoner spectrum and is referred to as a magnon excitation. Like the Stoner pair excitations, also the magnon excitations are characterized by the change in energy, crystal momentum and spin angular momentum which they imply. Thus, one may think of magnons as effective quasi-particles with exactly these properties, and a magnon excitation as the process in which such a quasi-particle is added to the material at thermal equilibrium.

In a typical magnetic ground state, bands of similar orbital character, but opposite spin, are split due to exchange. Therefore, the Stoner continuum is gaped at the Γ point according to the exchange splitting Δ_x. However, in the nonrelativistic limit there is no energy associated with a rigid rotation of all electronic spins, why there must exist a gapless acoustic magnon mode, the so-called Goldstone mode, according to the Goldstone theorem. The acoustic magnon mode is essential for the understanding properties relating to the low frequency transverse magnetic excitations, and it is also characteristic of the given magnetic order, attaining a parabolic dispersion in ferromagnets and a linear dispersion for antiferromagnets.

The magnetic excitations and the intrinsic fluctuations that they drive are important for many different material properties. The magnetic excitations directly give rise to (zero-point) fluctuations of the local magnetic moments [1, 2] and relate also to thermodynamic properties such as the heat capacity [3]. In particular, an understanding of the magnon excitations is crucial in order to predict the Curie/Néel temperature of a material, that is, the temperature at which the long-range magnetic order is lost. Furthermore, the magnons themselves have been proposed as an effective medium for computer chip communication [4] and the associated fluctuations to play an important role in the unconventional high-temperature superconductivity [5, 6] found in specific classes of magnetic quantum materials such as the transition metal pnictides [7–9].

In a traditional theoretical treatment of magnetic excitations, the material is modelled in terms of a localized spin Hamiltonian. The localized spin picture is physically well motivated for insulating magnetic materials, in which case the collective magnon excitations are well described at the Heisenberg model level, with magnons constituting linear spin wave excitations to the magnetically ordered ground state [10, 11]. In a first principles approach, one may compute the Heisenberg model parameters in density functional theory based on an energy mapping analysis of various local spin configurations [12–14] or using the magnetic force theorem [15–17]. However, this does not overcome the inherent inability to describe itinerant electron effects in a traditional localized spin model. In particular, one needs to include a lot of long-range exchange parameters in order to obtain an accurate Heisenberg model for metals, which in turn makes the fitting process to experimental magnon dispersions a dubious affair. Even when long-range interactions are accounted for theoretically, the Heisenberg model does not fully capture the influence of the Stoner continuum on the magnon spectrum, including effects such as line broadening due to Landau damping, renormalization of the magnon dispersion and stripe-like features in the spectrum [18, 19].

Experimentally, the spectrum of transverse magnetic excitations can be directly inferred from the energy dissipation of external probes that exchange energy and angular momentum with a given magnetic material. This includes spectroscopic techniques such as inelastic neutron scattering [20] and spin-polarized electron energy loss spectroscopy [21, 22]. In a theoretical first principles approach, one may try to mimic the strategy of experimental spectroscopy. If one can compute the dynamic transverse magnetic susceptibility without having to explicitly treat the many-body ground and excited states, the transverse magnetic excitations can be characterized directly in terms of the dissipative part of the susceptibility. Not only does the dissipative part of the susceptibility directly provide a spectral function for the transverse magnetic excitations, it also facilitates a direct interpretation of the corresponding experimental techniques, including in principle the capability of computing absolute spectral intensities and form factors for the various techniques.

Generally, there exists two different branches of theoretical magnon spectroscopy: Many-body perturbation theory [19, 23–27] and time-dependent density functional theory [18, 28–34]. In the work leading to this thesis, we have explored the linear response formulation of the latter, where the full many-body susceptibility is obtained from the corresponding single-particle susceptibility via a Dyson equation [35, 36]. We have implemented a transverse magnetic susceptibility module into the GPAW open-

source code [37, 38], relying on the projector augmented-wave method [39] to accurately compute the susceptibility in a plane wave basis without any formal loss of generality. We have used the developed code along with the adiabatic local density approximation to study the transverse magnetic excitations in ferromagnetic Fe, Ni, Co and MnBi as well as antiferromagnetic Cr and Cr_2O_3.

In this thesis, our studies of theoretical magnon spectroscopy will be presented along with an in-depth theoretical background, including a review of relevant topics in the Kubo theory of linear response. Furthermore, the thesis will present a new class of non-local exchange-correlation functionals that we have developed specifically to improve the description of dynamic short-range correlations in the homogeneous electron gas, which the local density approximation is known not to capture appropriately [40]. It is our hope, that such functionals in the future can improve the accuracy of theoretical magnon spectroscopy, but also be of use for a wealth of additional material properties. Lastly, an effort to standardize and improve existing and future computational recipes for material simulations is presented.

Thesis overview

The thesis is structured as follows. In the first three chapters of the thesis, the background theory for theoretical magnon spectroscopy is presented. In **Chapter 1**, the Kubo theory of linear response is reviewed, specifically targeting quasi-particle spectroscopy in periodic crystals. In **Chapter 2**, the ground state density functional theory is introduced and in **Chapter 3** it is shown how the transverse magnetic susceptibility may be calculated within the framework of linear response time-dependent density functional theory.

After the first three chapters, the thesis changes pace. In **Chapter 4**, the developed projector augmented-wave implementation for computing plane wave susceptibilities is presented, but only on an overview level, as the details of the method are described in Publication [A]. Similarly, **Chapters 5 and 6** rely on Publications [A], [B] and [C] to present the majority of the results regarding the magnon dispersion in the itinerant ferromagnets Fe, Ni, Co and MnBi as well as the antiferromagnetic phases of bulk Cr and Cr_2O_3 respectively. In the main body of the thesis text, the individual results will instead be discussed in a broader perspective.

After having presented the theoretical magnon spectroscopy results of the thesis, there will be another change of gears. First, the development of the new class of nonlocal exchange-correlation functionals will be presented. In **Chapter 7**, the theoretical background for exchange-correlation functionals is elaborated, before the functional development itself is presented in **Chapter 8**. Secondly, the development of a new common platform for Python material simulations is presented in **Chapter 9**, namely the "Atomic Simulation Recipes" framework. Also in this case, the details will be presented in the form of a journal article, that is, Publication [D].

Finally, the thesis will conclude with a **Summary** and an **Outlook**.

Theory: Generalized susceptibility and quasi-particle excitations

In this thesis, only the fundamental excitations, which can be induced to linear order by a perturbative field coupling to a single system coordinate, are considered. The reason why such fundamental excitations are decisive for a wide range of material properties, falls back to their linearity. Not only do they give the available transitions for a simple external perturbation to linear order, they compose a compact region of the Hilbert space enclosing the ground state itself. For this reason, they are in many regards the physically most relevant excited states, especially for the system properties at thermal equilibrium.

Formally, the fundamental system excitations are unified in the Kubo theory of linear response, where the system response is characterized by its generalized susceptibility. In this chapter, key results of the theory relevant to the characterization of magnon excitations are presented. In addition, a thorough topical review on the Kubo theory is given in the appendices of Publications [A] and [C]. Hyperlinks to these appendices are provided towards the end of the chapter.

1.1 Linear response theory

In the theory of linear response, a weak time-dependent external perturbation is considered, characterized by the external classical coordinate $f(t)$, coupling to the system $\hat{H}_0$ through the system coordinate $\hat{A}$:

$$\hat{H}(t) = \hat{H}_0 + \hat{H}_{\mathrm{ext}}(t), \quad \hat{H}_{\mathrm{ext}}(t) = \hat{A}f(t). \tag{1.1}$$

The induced change in some system coordinate $\hat{B}$ to linear order in the perturbation is then given by the retarded susceptibility $\chi_{BA}(t - t')$,

$$\langle \delta\hat{B}(t) \rangle = \langle \hat{B}(t) \rangle - \langle \hat{B} \rangle_0 = \int_{-\infty}^{\infty} dt' \, \chi_{BA}(t - t')f(t'), \tag{1.2}$$

where $\langle \cdot \rangle_0$ refers to the expectation value with respect to the unperturbed system. Thus, the retarded susceptibility comprises the central object of interest for the theory,

which fundamentally relies on the fact that $\chi_{BA}(t - t')$ can be written in the closed form known as the *Kubo formula* [41]:

$$\chi_{BA}(t - t') = -\frac{i}{\hbar}\theta(t - t')\langle\,[\hat{B}_0(t - t'), \hat{A}]\,\rangle_0. \tag{1.3}$$

Here, $\theta(t - t')$ is the unit step function and the operator $\hat{B}$ carries the time-dependence in the interaction picture:

$$\hat{B}_0(t) = e^{i\hat{H}_0 t/\hbar}\,\hat{B}\,e^{-i\hat{H}_0 t/\hbar}. \tag{1.4}$$

In the Kubo formalism, the linear order spectral properties of the system are governed by the Fourier-Laplace transform of the retarded susceptibility (1.3), which is analytic in the upper half of the complex frequency plane (for definitions of the Fourier transform, see [A]). From the Kubo formula (1.3), the dynamic susceptibility, or generalized susceptibility, can be written in terms the energy eigenstates to the system Hamiltonian, $\hat{H}_0|\alpha\rangle = E_\alpha|\alpha\rangle$,

$$\chi_{BA}(z = \omega + i\eta) = \sum_{\alpha,\alpha'}\frac{\langle\alpha|\hat{B}|\alpha'\rangle\langle\alpha'|\hat{A}|\alpha\rangle}{\hbar\omega - (E_{\alpha'} - E_\alpha) + i\hbar\eta}(n_\alpha - n_{\alpha'}), \tag{1.5}$$

where z denotes the complex frequency composed of the real and imaginary frequencies ω and η, with $\eta > 0$. In this way, the Lehmann representation (1.5) decomposes the generalized susceptibility of any system $\hat{H}_0$, into the available eigenstate transitions, each weighted by the transition amplitudes and difference in population factors, $(n_\alpha - n_{\alpha'})$, of the given states at thermal equilibrium.

1.2   Energy dissipation and the quasi-particle spectrum

It is generally instructive to further decompose the Lehmann representation (1.5) into the reactive and dissipative parts of the susceptibility [42],

$$\chi_{BA}(z) = \chi'_{BA}(z) + i\chi''_{BA}(z), \tag{1.6a}$$

$$\chi'_{BA}(z) = \chi'_{AB}(-z^*) = \frac{1}{2}\left[\chi_{BA}(z) + \chi_{AB}(-z^*)\right], \tag{1.6b}$$

$$\chi''_{BA}(z) = -\chi''_{AB}(-z^*) = \frac{1}{2i}\left[\chi_{BA}(z) - \chi_{AB}(-z^*)\right], \tag{1.6c}$$

where the reactive and dissipative parts each yield the real and imaginary parts of the frequency dependence:

$$\chi'_{BA}(\omega + i\eta) = \sum_{\alpha,\alpha'}\langle\alpha|\hat{B}|\alpha'\rangle\langle\alpha'|\hat{A}|\alpha\rangle(n_\alpha - n_{\alpha'})\,\mathrm{Re}\left[\frac{1}{\hbar\omega - (E_{\alpha'} - E_\alpha) + i\hbar\eta}\right], \tag{1.7a}$$

$$\chi''_{BA}(\omega + i\eta) = \sum_{\alpha,\alpha'}\langle\alpha|\hat{B}|\alpha'\rangle\langle\alpha'|\hat{A}|\alpha\rangle(n_\alpha - n_{\alpha'})\,\mathrm{Im}\left[\frac{1}{\hbar\omega - (E_{\alpha'} - E_\alpha) + i\hbar\eta}\right]. \tag{1.7b}$$

Through this decomposition, it is easy to see that the dissipative part of the susceptibility directly constitutes a spectral function for the induced transitions of the system, representing each transition by a Lorentzian peak of width $2\hbar\eta$ and amplitude $-\pi$.

As the name suggests, the dissipative part of the susceptibility is responsible for the net dissipation of energy into the system, resulting from the external perturbation. Considering a harmonic perturbation on the form $f(t) = f_0 \cos(\omega_0 t)$, the mean rate of energy absorption $\bar{Q}$ is given by

$$\bar{Q} = -\frac{1}{2} f_0^2 \omega_0 \chi''_{AA}(\omega_0), \tag{1.8}$$

where functions of the real frequency ω refer to the complex frequency limit $\eta \to 0^+$, such that $\chi_{BA}(\omega) = \chi_{BA}(\omega + i0^+)$. It should be noted that the dissipative part of the generalized susceptibility $\chi_{BA}(\omega)$ is equal to the imaginary part along the diagonal, which enters Equation (1.8). For additional details, see [A]. Thanks to Fermi's golden rule, it comes as no surprise that the energy dissipation is proportional to the spectrum of induced transitions characterized by the dissipative part (1.7b). In fact, one may in the zero temperature limit express this spectrum,

$$S_{BA}(\omega) = -\frac{\chi''_{BA}(\omega)}{\pi} = A_{BA}(\omega) - A_{AB}(-\omega), \tag{1.9}$$

in terms of the excited states spectral functions:

$$A_{BA}(\omega) = \sum_{\alpha \neq \alpha_0} \langle \alpha_0 | \hat{B} | \alpha \rangle \langle \alpha | \hat{A} | \alpha_0 \rangle \, \delta\big(\hbar\omega - (E_\alpha - E_0)\big). \tag{1.10}$$

Here, it is assumed that the system resides in the ground state $|\alpha_0\rangle$ with energy E_0 prior to the application of the perturbation, and $\delta(\hbar\omega - \Delta E)$ denotes the Dirac δ-function. In the quasi-particle picture, linear excitations to the ground state are thought of as effective quasi-particles added to an effective vacuum state, the ground state. Thanks to Equations (1.8), (1.9) and (1.10), one may thus extract the quasi-particle energies, $\hbar\omega = E_\alpha - E_0$, directly from the dissipative part of any susceptibility which characterizes the response to a perturbation with the ability to excite that given quasi-particle. In this way, quasi-particles spectra can be probed by tracking the energy dissipation in a material.

1.3   Fluctuation-dissipation theorem

Not only does the generalized susceptibility govern the energy dissipation of a system to linear order, it also characterizes the fundamental system fluctuations. To illustrate this relation, the retarded susceptibility, as defined by the Kubo formula (1.3), is written in terms of the noncausal response function [42]

$$K_{BA}(t) = -\frac{i}{\hbar} \langle \, [\hat{B}_0(t), \hat{A}] \, \rangle_0, \tag{1.11}$$

with $\chi_{BA}(t - t') = \theta(t - t')K_{BA}(t - t')$. The noncausal response function can itself be decomposed into correlation functions,

$$K_{BA}(t) = -\frac{i}{\hbar}\left(C_{BA}(t) - C_{AB}(-t)\right), \tag{1.12}$$

with $C_{BA}(t) = \langle \hat{B}_0(t)\hat{A}\rangle_0 - \langle \hat{B}\rangle_0\langle \hat{A}\rangle_0$. Because the noncausal response function can be finite both for positive and negative time arguments t, its Fourier-Laplace transform is defined accordingly in order to make sure that $K_{BA}(z)$ is analytic in the upper half of the complex frequency plane:

$$K_{BA}(z = \omega + i\eta) = \int_{-\infty}^{\infty} dt\, K_{BA}(t)e^{i(\omega t + i\eta|t|)}. \tag{1.13}$$

Inserting a factor $(\theta(t) + \theta(-t))$ and using the symmetry relation $K_{BA}(t) = -K_{AB}(-t)$ (see Equation (1.12)), it is straight-forward to show that the spectral components of the noncausal response function are given by the dissipative part of the generalized susceptibility:

$$K_{BA}(z) = \chi_{BA}(z) - \chi_{AB}(-z^*) = 2i\chi''_{BA}(z). \tag{1.14}$$

On the other hand, inserting Equation (1.12) into the Fourier-Laplace transform (1.13) gives

$$K_{BA}(z) = -\frac{i}{\hbar}\left(C_{BA}(z) - C_{AB}(-z^*)\right), \tag{1.15}$$

which in combination with Equation (1.14) yields a generalized *fluctuation-dissipation theorem* [43–45]:

$$\chi''_{BA}(z) = -\frac{1}{2\hbar}\left(C_{BA}(z) - C_{AB}(-z^*)\right). \tag{1.16}$$

In essence, the theorem illustrates the fundamental physical fact that both a system's inherent fluctuations and its ability to dissipate energy of an external source are proportional to the spectrum of available eigenstate transitions around thermal equilibrium.

At zero temperature, this relation is especially obvious. Assuming that the system resides in the ground state $|\alpha_0\rangle$, one can rewrite the correlation function in terms of the system eigenstates:

$$C_{BA}(t) = \sum_{\alpha \neq \alpha_0} \langle\alpha_0|\hat{B}|\alpha\rangle\langle\alpha|\hat{A}|\alpha_0\rangle e^{-i(E_\alpha - E_0)t/\hbar}. \tag{1.17}$$

Applying the Fourier-Laplace transform (1.13) then gives:

$$C_{BA}(z = \omega + i\eta) = -2\hbar \sum_{\alpha \neq \alpha_0} \langle\alpha_0|\hat{B}|\alpha\rangle\langle\alpha|\hat{A}|\alpha_0\rangle \text{Im}\left[\frac{1}{\hbar\omega - (E_\alpha - E_0) + i\hbar\eta}\right]. \tag{1.18}$$

Thus, the spectral components of the correlation function are simply proportional to the quasi-particle spectrum (1.10), with $C_{BA}(\omega) = 2\hbar\pi A_{BA}(\omega)$. In turn, the quasi-particle spectrum makes up the dissipative part of the generalized susceptibility as

shown in Equation (1.9), and the fluctuation-dissipation theorem (1.16) simply gives the direct relation between the two system properties.

At finite temperatures, the functional forms for the correlation function and generalized susceptibility are less simple, but it is actually possible to simplify the relation between the two. Using the cyclic property of the trace, the correlation functions can be shown to fulfill the relations $C_{BA}(t) = C_{AB}(-t-i\beta\hbar)$ and $C_{BA}(\omega) = e^{\beta\hbar\omega}C_{AB}(-\omega)$, where $\beta = 1/(k_\mathrm{B}T)$ [42]. Inserting the latter relation into Equation (1.16) then gives the classic fluctuation-dissipation theorem:

$$C_{BA}(\omega) = -\frac{2\hbar}{1 - e^{-\beta\hbar\omega}}\chi''_{BA}(\omega). \tag{1.19}$$

1.4 Onsager relations

So far when the zero temperature limit has been taken, the system has simply been assumed to reside in a given ground state $|\alpha_0\rangle$. However, what happens, if some symmetry is spontaneously broken, meaning that multiple ground states exist? In the context of this thesis, this is an especially relevant question since time-reversal symmetry is broken in a magnetically ordered ground state. One may generalize this question even further: How are the symmetries of the system Hamiltonian $\hat{H}_0$ reflected in the generalized susceptibility $\chi_{BA}(\omega)$, and what role does spontaneously broken symmetries play in this regard? It turns out, that the answer to such questions is a simple set of relations inspired by statistical mechanics.

First of all, the generalized susceptibility is a property of the system at thermal equilibrium. Therefore, an assumption that the system resides in the ground state $|\alpha_0\rangle$ really is an assumption that the system is in thermal equilibrium in $|\alpha_0\rangle$. That is, that the probability of observing any other ground state due to thermal fluctuations vanishes in the zero temperature limit. In this case, the retarded susceptibility may be given with respect to $|\alpha_0\rangle$, even though multiple ground states may exist:

$$\chi_{BA}(\alpha_0, t - t') = -\frac{i}{\hbar}\theta(t - t')\langle\alpha_0|[\hat{B}_0(t - t'), \hat{A}]|\alpha_0\rangle. \tag{1.20}$$

In particular, if the system is subject to some symmetry generated by the unitary or anti-unitary operator $\hat{U}$, with the inverse $\hat{U}^{-1}$, the commutation relation $[\hat{H}_0, \hat{U}] = 0$ implies that:

$$\hat{H}_0\hat{U}|\alpha_0\rangle = \hat{U}\hat{H}_0|\alpha_0\rangle = E_0\hat{U}|\alpha_0\rangle. \tag{1.21}$$

If the ground state $|\alpha_0\rangle$ is invariant under the symmetry operation $\hat{U}$, this equation is trivial. However, if $\hat{U}$ maps the ground state $|\alpha_0\rangle$ into a *different* state $|\hat{U}\alpha_0\rangle$, the symmetry generated by $\hat{U}$ is said to be spontaneously broken and $|\hat{U}\alpha_0\rangle$ forms a *new* degenerate ground state with its own generalized susceptibility $\chi_{BA}(\hat{U}\alpha_0, \omega)$.

Now, regardless of whether a given symmetry of the system is spontaneously broken or not, it gives rise to the following symmetry relation for the generalized susceptibility, known as the *Onsager relation* [C],

$$\chi_{BA}(\alpha_0, \omega) = \chi_{B^U A^U}(\hat{U}\alpha_0, \omega), \quad \text{if } \hat{U} \text{ is unitary}, \tag{1.22a}$$

$$\chi_{B^\dagger A^\dagger}(\alpha_0, \omega) = \chi_{A^U B^U}(\hat{U}\alpha_0, \omega), \quad \text{if } \hat{U} \text{ is anti-unitary,} \qquad (1.22b)$$

where $\hat{A}^U = \hat{U}\hat{A}\hat{U}^{-1}$. The relation derives its name from the analogous statement in classical statistical mechanics, relating the correlation function of forward motion in a magnetic field B to the reversed motion in the reversed magnetic field $-B$ [46–48]. In a similar fashion, the quantum mechanical Onsager relation (1.22) may be used to relate the the susceptibility of a magnetic system with magnetization $\mathbf{m}(\mathbf{r})$ to the same system with magnetization $-\mathbf{m}(\mathbf{r})$. In the absence of external magnetic fields, the system respects time-reversal symmetry, $[\hat{H}_0, \hat{T}] = 0$, and the Onsager relation (1.22b) yields the classic statement [41, 49, 50]

$$\chi_{BA}(\alpha_0, \omega) = \varepsilon_A^T \varepsilon_B^T \chi_{AB}(\hat{T}\alpha_0, \omega), \qquad (1.23)$$

where $\hat{B}$ and $\hat{A}$ are assumed to be observables of the system translating either as even or odd variables under time-reversal, $\hat{T}\hat{A}\hat{T}^{-1} = \varepsilon_A^T \hat{A}$ with $\varepsilon_A^T = \pm 1$. Furthermore, in the case where time-reversal symmetry is preserved by ground state $|\alpha_0\rangle$, the Onsager relation (1.23) implies that the dynamic susceptibility is either reciprocal or anti-reciprocal.

1.5   Linear response in periodic crystals

For real life materials treated in terms of their electronic degrees of freedom (employing the Born-Oppenheimer approximation), one may in the linear response formalism consider a general external perturbation entering the problem as a classical time-dependent field $f(\mathbf{r}, t)$,

$$\hat{H}_{\text{ext}}(t) = \int d\mathbf{r} \, \hat{A}(\mathbf{r}) f(\mathbf{r}, t), \qquad (1.24)$$

where $\hat{A}(\mathbf{r}) = \hat{A}^\dagger(\mathbf{r})$ is some one-body electronic operator. The corresponding response relation (1.2) then relates a one-body observable $B(\mathbf{r})$ at time t to the external field at position $\mathbf{r}'$ and time t':

$$\langle \delta \hat{B}(\mathbf{r}, t) \rangle = \int_{-\infty}^{\infty} dt' \int d\mathbf{r}' \, \chi_{BA}(\mathbf{r}, \mathbf{r}', t - t') f(\mathbf{r}', t'). \qquad (1.25)$$

It is important to stress that there is no novelty here and the full machinery of the Kubo theory presented in the previous sections can be directly reused. In particular, one may reuse the Lehmann representation (1.5) for the dynamic susceptibility $\chi_{BA}(\mathbf{r}, \mathbf{r}', z)$, with the only difference that the transition matrix elements now carry a spatial dependence:

$$A_{\alpha'\alpha}(\mathbf{r}) = \langle \alpha' | \hat{A}(\mathbf{r}) | \alpha \rangle. \qquad (1.26)$$

For periodic crystals, where the system is invariant under lattice translations, $[\hat{H}_0, \hat{T}_{\mathbf{R}}] = 0$, the transition matrix elements transform as Bloch waves [A]:

$$A_{\alpha'\alpha}(\mathbf{r}) = \frac{\Omega_{\text{cell}}}{\Omega} e^{-i\mathbf{q}_{\alpha'\alpha} \cdot \mathbf{r}} a_{\alpha'\alpha}(\mathbf{r}). \qquad (1.27)$$

Here, $a_{\alpha'\alpha}(\mathbf{r}+\mathbf{R}) = a_{\alpha'\alpha}(\mathbf{r})$ denotes the periodic part of the transition matrix element, which is normalized to the unit cell by extracting the cell and crystal volumes Ω_{cell} and Ω. Furthermore, the Bloch wave vector $\mathbf{q}_{\alpha'\alpha}$ is determined from the difference in eigenstate crystal momentum $\hbar(\mathbf{k}_{\alpha'} - \mathbf{k}_{\alpha})$, such that it lies within the first Brillouin zone. The Bloch wave properties of the transition matrix elements have a range of consequences. It directly implies that also the dynamic susceptibility is invariant under lattice translations, $\chi_{BA}(\mathbf{r} + \mathbf{R}, \mathbf{r}' + \mathbf{R}, z) = \chi_{BA}(\mathbf{r}, \mathbf{r}', z)$, which in turn implies that the response is diagonal in the reduced wave vector $\mathbf{q}$. This is important not only for the physical interpretation of the response, but also for the representation of the susceptibility, which will be illustrated in the following sections. Before proceeding, it is worth noting that the periodicity of the generalized susceptibility is valid at any temperature T. In the zero temperature limit however, it may be viewed simply as a consequence of the Onsager relation (1.22a).

1.5.1 Bloch susceptibility

For periodic crystals, the response may be characterized in terms the lattice Fourier transform of the susceptibility [18]:

$$\chi_{BA}(\mathbf{r}, \mathbf{r}', \mathbf{q}, z) = \sum_{\mathbf{R}'} e^{i\mathbf{q}\cdot\mathbf{R}'} \chi_{BA}(\mathbf{r}, \mathbf{r}' + \mathbf{R}', z). \tag{1.28}$$

This is advantageous because the periodicity of the dynamic susceptibility implies that $\chi_{BA}(\mathbf{r}, \mathbf{r}', \mathbf{q}, z)$ transforms as a Bloch wave:

$$\chi_{BA}(\mathbf{r} + \mathbf{R}, \mathbf{r}', \mathbf{q}, z) = e^{i\mathbf{q}\cdot\mathbf{R}} \chi_{BA}(\mathbf{r}, \mathbf{r}', \mathbf{q}, z), \tag{1.29a}$$

$$\chi_{BA}(\mathbf{r}, \mathbf{r}' + \mathbf{R}, \mathbf{q}, z) = e^{-i\mathbf{q}\cdot\mathbf{R}} \chi_{BA}(\mathbf{r}, \mathbf{r}', \mathbf{q}, z). \tag{1.29b}$$

As a result, the lattice Fourier transform may be represented by its periodic part $\bar{\chi}_{BA}(\mathbf{r}, \mathbf{r}', \mathbf{q}, z)$, which is periodic in both the $\mathbf{r}$ and $\mathbf{r}'$ entries independently:

$$\chi_{BA}(\mathbf{r}, \mathbf{r}', \mathbf{q}, z) = e^{i\mathbf{q}\cdot(\mathbf{r}-\mathbf{r}')} \bar{\chi}_{BA}(\mathbf{r}, \mathbf{r}', \mathbf{q}, z). \tag{1.30}$$

In this way, the overall basis representation needed to represent the linear response of a periodic crystal is limited to the unit cell, not the entire crystal. However, $\bar{\chi}_{BA}(\mathbf{r}, \mathbf{r}', \mathbf{q}, z)$ is not just an efficient representation of the response, it also directly characterizes the response to harmonic perturbations on the form

$$\hat{H}_{\text{ext}}(t) = \int d\mathbf{r} \, \hat{A}(\mathbf{r}) \frac{f(\mathbf{r})}{2} \left[e^{i(\mathbf{q}_0\cdot\mathbf{r} - \omega_0 t)} + \text{c.c.} \right], \tag{1.31}$$

where $f(\mathbf{r}+\mathbf{R}) = f(\mathbf{r})$ is a periodic function. Insertion into the linear response relation (1.25) and application of the convolution theorem then yields:

$$\langle \delta\hat{B}(\mathbf{r}, t) \rangle = \int_{\Omega_{\text{cell}}} d\mathbf{r}' \frac{f(\mathbf{r}')}{2} \Big[\bar{\chi}_{BA}(\mathbf{r}, \mathbf{r}', \mathbf{q}_0, \omega_0) e^{i(\mathbf{q}_0\cdot\mathbf{r} - \omega_0 t)}$$
$$+ \bar{\chi}_{BA}(\mathbf{r}, \mathbf{r}', -\mathbf{q}_0, -\omega_0) e^{-i(\mathbf{q}_0\cdot\mathbf{r} - \omega_0 t)} \Big]. \tag{1.32}$$

In this way, $\bar{\chi}_{BA}(\mathbf{r}, \mathbf{r}', \mathbf{q}, \omega)$ may be viewed simply as the generalized susceptibility towards perturbations on the Bloch wave form. For this reason, it will henceforward be referred to as the Bloch susceptibility.

In order to make a connection with the quasi-particle picture, the lattice Fourier transformed susceptibility is written in the Lehmann representation (1.5). Doing so, Equation (1.27) implies that only transitions $\alpha \to \alpha'$ with a difference in crystal momentum $\hbar\mathbf{q}$ contribute to the Bloch susceptibility:

$$\chi_{BA}(\mathbf{r}, \mathbf{r}', \mathbf{q}, \omega + i\eta) = e^{i\mathbf{q}\cdot(\mathbf{r}-\mathbf{r}')}\frac{\Omega_{\text{cell}}}{\Omega}\sum_{\alpha,\alpha'}\frac{b_{\alpha\alpha'}(\mathbf{r})a_{\alpha'\alpha}(\mathbf{r}')}{\hbar\omega - (E_{\alpha'} - E_\alpha) + i\hbar\eta}(n_\alpha - n_{\alpha'})\delta_{\mathbf{q},\mathbf{q}_{\alpha'\alpha}}.$$

(1.33)

Thus, the Bloch susceptibility not only characterizes quasi-particles of energy $E_{\alpha'} - E_\alpha = \hbar\omega$, but specifically of crystal momentum $\hbar\mathbf{q}_{\alpha'\alpha} = \hbar\mathbf{q}$.

1.5.2 Plane wave susceptibility

In order to compute the Bloch susceptibility, one needs to make a choice of real-space representation. One such basis, is the plane wave basis

$$\chi_{BA}^{\mathbf{G}\mathbf{G}'}(\mathbf{q}, z) = \iint \frac{d\mathbf{r}d\mathbf{r}'}{\Omega}e^{-i(\mathbf{G}+\mathbf{q})\cdot\mathbf{r}}\chi_{BA}(\mathbf{r}, \mathbf{r}', z)e^{i(\mathbf{G}'+\mathbf{q})\cdot\mathbf{r}'},$$

(1.34)

$$= \iint_{\Omega_{\text{cell}}} \frac{d\mathbf{r}d\mathbf{r}'}{\Omega_{\text{cell}}}e^{-i\mathbf{G}\cdot\mathbf{r}}\bar{\chi}_{BA}(\mathbf{r}, \mathbf{r}', \mathbf{q}, z)e^{i\mathbf{G}'\cdot\mathbf{r}'},$$

(1.35)

where $\mathbf{G}$ and $\mathbf{G}'$ are reciprocal lattice vectors. Once more, it is possible to assign an actual physical interpretation to $\chi_{BA}^{\mathbf{G}\mathbf{G}'}(\mathbf{q}, z)$ as the generalized susceptibility towards plane wave perturbations on the form:

$$\hat{H}_{\text{ext}}(t) = \int d\mathbf{r}\, \hat{A}(\mathbf{r})\frac{f_0}{2}\left[e^{i([\mathbf{G}_0+\mathbf{q}_0]\cdot\mathbf{r}-\omega_0 t)} + \text{c.c.}\right].$$

(1.36)

Analogously to the response relation (1.32), $\chi_{BA}^{\mathbf{G}\mathbf{G}'}(\mathbf{q}, z)$ then gives the plane wave coefficients of the response [A],

$$\langle\delta\hat{B}(\mathbf{r}, t)\rangle = \frac{f_0}{2}\sum_{\mathbf{G}}\left[\chi_{BA}^{\mathbf{G}\mathbf{G}_0}(\mathbf{q}_0, \omega_0)e^{i([\mathbf{G}+\mathbf{q}_0]\cdot\mathbf{r}-\omega_0 t)}\right.$$

$$\left. + \chi_{BA}^{-\mathbf{G}-\mathbf{G}_0}(-\mathbf{q}_0, -\omega_0)e^{-i([\mathbf{G}+\mathbf{q}_0]\cdot\mathbf{r}-\omega_0 t)}\right],$$

(1.37)

why one may simply refer to $\chi_{BA}^{\mathbf{G}\mathbf{G}'}(\mathbf{q}, z)$ as the plane wave susceptibility.

Now, one of the great advantages of the plane wave susceptibility is that it can be defined in terms of the Kubo formula (1.3) by casting the field operators in the Fourier basis [A],

$$\hat{A}(\mathbf{Q}) = \int d\mathbf{r}\, e^{-i\mathbf{Q}\cdot\mathbf{r}}\hat{A}(\mathbf{r}),$$

(1.38)

such that:

$$\chi_{BA}^{\mathbf{G}\mathbf{G}'}(\mathbf{q}, z) = \frac{1}{\Omega}\,\chi_{\beta\alpha}(z), \tag{1.39a}$$

$$\hat{\beta} = \hat{B}(\mathbf{G} + \mathbf{q}), \quad \hat{\alpha} = \hat{A}(-\mathbf{G}' - \mathbf{q}). \tag{1.39b}$$

This means that all the relations derived from the Kubo formula (1.3) also hold for the plane wave susceptibility, including the separation into reactive and dissipative parts (1.7) and the Onsager relations (1.22). In particular, one may introduce the plane wave spectrum of induced transitions in terms of the dissipative part of the plane wave susceptibility

$$S_{BA}^{\mathbf{G}\mathbf{G}'}(\mathbf{q}, \omega) = -\frac{1}{\Omega}\frac{\chi_{\beta\alpha}''(\omega)}{\pi} = -\frac{1}{2\pi i}\left[\chi_{BA}^{\mathbf{G}\mathbf{G}'}(\mathbf{q}, \omega) - \chi_{AB}^{-\mathbf{G}'-\mathbf{G}}(-\mathbf{q}, -\omega)\right], \tag{1.40}$$

$$= \frac{1}{\Omega}\sum_{\alpha,\alpha'} b_{\alpha\alpha'}(\mathbf{G})a_{\alpha'\alpha}(-\mathbf{G}')(n_\alpha - n_{\alpha'})\delta_{\mathbf{q},\mathbf{q}_{\alpha'\alpha}}\delta\big(\hbar\omega - (E_{\alpha'} - E_\alpha)\big), \tag{1.41}$$

where Equations (1.33) and (1.35) were used in the last equality and:

$$a_{\alpha'\alpha}(\mathbf{G}) = \int_{\Omega_{\text{cell}}} d\mathbf{r}\, e^{-i\mathbf{G}\cdot\mathbf{r}}a_{\alpha'\alpha}(\mathbf{r}). \tag{1.42}$$

In the zero temperature limit, the plane wave spectrum then decomposes into excited states spectral functions,

$$S_{BA}^{\mathbf{G}\mathbf{G}'}(\mathbf{q}, \omega) = A_{BA}^{\mathbf{G}\mathbf{G}'}(\mathbf{q}, \omega) - A_{AB}^{-\mathbf{G}'-\mathbf{G}'}(-\mathbf{q}, -\omega). \tag{1.43}$$

such that $S_{BA}^{\mathbf{G}\mathbf{G}'}(\mathbf{q}, \omega)$ directly yields the spectrum of quasi-particle excitations of energy $\hbar\omega$ and crystal momentum $\hbar\mathbf{q}$, weighted by the transition matrix elements (1.42):

$$A_{BA}^{\mathbf{G}\mathbf{G}'}(\mathbf{q}, \omega) = \frac{1}{\Omega}\sum_{\alpha\neq\alpha_0} b_{0\alpha}(\mathbf{G})a_{\alpha 0}(-\mathbf{G}')\delta_{\mathbf{q},\mathbf{q}_{\alpha 0}}\delta\big(\hbar\omega - (E_\alpha - E_0)\big). \tag{1.44}$$

1.6 Further reading

As mentioned in the introduction to this chapter, Publications [A] and [C] include a more detailed presentation of the Kubo theory relevant for theoretical magnon spectroscopy. In particular, it might benefit the reader already at this point to skip ahead to Appendix A of Publication [A], starting on page 58 of this thesis, where the core Kubo theory and the connection to quasi-particles are described in detail. Similarly, the curious reader may consult Appendix A of Publication [C], starting on page 98, for a proof of the quantum mechanical Onsager relation.

Theory: Density functional theory for magnetic materials

For many magnetic properties, including the magnon spectrum, one may to a good approximation consider the atomic positions of the material in question as static and consider only the electronic degrees of freedom, in what is known as the Born-Oppenheimer approximation. However, to make any progress from Kubo's formal treatment of excited states spectroscopy towards an actual calculation of a magnon spectrum in a real magnetic material, a feasible scheme is needed in order to treat the many-body electronic structure problem. Such a scheme is provided by the framework of density functional theory (DFT), in which ground state properties are viewed as exact functionals of the density $n(\mathbf{r})$ (and magnetization $\mathbf{m}(\mathbf{r})$). In this chapter, the basics of DFT are presented in order to provide the basis for the corresponding time-dependent theory, in which dynamic susceptibilities of real materials may be evaluated.

2.1 The Hohenberg-Kohn theorems

In the Born-Oppenheimer approximation, the material itself is characterized by its number of electrons and its atomic arrangement, which manifests itself as an electrostatic potential, $V_{\text{nuc}}(\mathbf{r})$. The electronic system Hamiltonian is given by

$$\hat{H}_0 = \hat{T} + \hat{V} + \hat{U}, \tag{2.1}$$

where $\hat{T}$, $\hat{V}$ and $\hat{U}$ are the kinetic energy, electrostatic potential and electron-electron Coulomb interaction operators. DFT then relies on a simple observation: The only system-dependent term in the Hamiltonian is the electrostatic potential. For two systems of potential V and V', differing by more than a constant, this means that also the ground states $|\psi_0\rangle$ and $|\psi_0'\rangle$ (assumed to be nondegenerate) will be different, and that

$$E = \langle\psi|\hat{T} + \hat{U}|\psi\rangle + \langle\psi|\hat{V}|\psi\rangle \quad \text{will be minimal using } |\psi\rangle = |\psi_0\rangle, \text{ not } |\psi_0'\rangle, \tag{2.2a}$$

$$E' = \langle\psi|\hat{T} + \hat{U}|\psi\rangle + \langle\psi|\hat{V}'|\psi\rangle \quad \text{will be minimal using } |\psi\rangle = |\psi_0'\rangle, \text{ not } |\psi_0\rangle. \tag{2.2b}$$

Whereas the kinetic energy and the electron-electron interaction operate on the individual electronic degrees of freedom, the electrostatic potential operates only on the

electron density as a whole. In the absence of external electromagnetic fields,

$$\langle\psi|\hat{V}|\psi\rangle = \int d\mathbf{r}\, \langle\psi|\hat{n}(\mathbf{r})|\psi\rangle V_{\mathrm{nuc}}(\mathbf{r}) = -e \int d\mathbf{r}\, n(\mathbf{r})\phi_{\mathrm{nuc}}(\mathbf{r}), \qquad (2.3)$$

where $\hat{n}(\mathbf{r})$ is the electron density operator, $-e$ is the electron charge and $\phi_{\mathrm{nuc}}(\mathbf{r})$ is the scalar potential of the nuclei. As a result, both of the statements (2.2) cannot be true, unless also the ground state densities are different among the two systems, $n(\mathbf{r}) \neq n'(\mathbf{r})$. Thus, for electronic system Hamiltonians on the form (2.1), there is a one-to-one correspondence between the nuclear potential and the ground state electron density [51]:

$$n(\mathbf{r}) \leftrightarrow V_{\mathrm{nuc}}(\mathbf{r}) \quad \text{(up to a constant)}. \qquad (2.4)$$

As a consequence, one can regard the nuclear potential as a functional of the ground state density: $V_{\mathrm{nuc}} = V_{\mathrm{nuc}}[n]$. Because the potential in turn defines the electronic structure problem itself, all relevant quantities can in principle be written as functionals of the ground state density, that is, without reference to the individual electronic degrees of freedom. In particular, the many-body ground state, $|\psi_0\rangle$, is a functional of the ground state density, and so is the energy:

$$E[n] = \langle\psi_0|\hat{T} + \hat{U}|\psi_0\rangle + \int d\mathbf{r}\, n(\mathbf{r})V_{\mathrm{nuc}}(\mathbf{r}). \qquad (2.5)$$

For densities n, which correspond to ground state densities of Hamiltonians on the form (2.1) (said to be V-representable), the energy functional (2.5) attains its minimum (the ground state energy) at the correct ground state density, when minimized under the constraint of a fixed number of electrons [51]. Thus, in DFT, the electronic structure problem can be reformulated as a minimization of the energy functional (2.5).

2.2   The Kohn-Sham system

Although it is formally exact to write all observable quantities as a functional of the ground state density, acquiring an exact form for a given functional is as overwhelming a task as solving the many-body problem (2.1) for all meaningful electrostatic potentials at once. In particular, it would be an obvious advantage to compute the energy as a functional of the ground state density, but not if this implies determining the many-body ground state for every density n, as is indicated formally in Equation (2.5). Instead, one may assume the existence of an auxiliary system of noninteracting electrons with the same ground state density as in the many-body problem [52]:

$$\hat{H}_{\mathrm{KS}} = \hat{T} + \hat{V}_{\mathrm{s}}. \qquad (2.6)$$

In the so-called Kohn-Sham system, the ground state is a Slater determinant of the single-particle eigenstates given from the time-independent Schrödinger equation

$$\left(-\frac{\hbar^2\nabla^2}{2m} + V_{\mathrm{s}}(\mathbf{r})\right)\psi_i(\mathbf{r}) = \epsilon_i\psi_i(\mathbf{r}). \qquad (2.7)$$

As a result, one can regard the kinetic energy of the noninteracting system as a *known* functional of the ground state density, $T_s[n]$, where the density is calculated as a simple sum over the single-particle eigenstates weighted by their occupation numbers f_i:

$$n(\mathbf{r}) = \sum_i f_i |\psi_i(\mathbf{r})|^2. \tag{2.8}$$

In addition to the single-particle contribution to the kinetic energy, also the classical Coulomb energy contribution is a well-known functional of the electron density. The so-called Hartree energy functional is given by

$$E_H[n] = \frac{1}{2} \iint d\mathbf{r}d\mathbf{r}'\, n(\mathbf{r})v_c(\mathbf{r} - \mathbf{r}')n(\mathbf{r}'), \tag{2.9}$$

where v_c is the electronic Coulomb potential, $v_c(\mathbf{r} - \mathbf{r}') = e^2/(4\pi\epsilon_0|\mathbf{r} - \mathbf{r}'|)$. With this, the energy functional (2.5) can be written:

$$E[n] = T_s[n] + E_H[n] + E_{xc}[n] + \int d\mathbf{r}\, n(\mathbf{r})V_{nuc}(\mathbf{r}), \tag{2.10}$$

where the so-called exchange-correlation (xc) functional $E_{xc}[n]$ accounts for the difference between the kinetic energy of the many-body and noninteracting systems as well as the difference between the full Coulomb interaction and the classical counterpart. Minimizing (2.10) under the constraint of a fixed number of electrons, $\int d\mathbf{r}\, n(\mathbf{r}) = N$, is then equivalent to solving the single-particle Schrödinger equation (2.7) with [52]

$$V_s(\mathbf{r}) = V_s[n](\mathbf{r}) = V_{nuc}(\mathbf{r}) + V_H[n](\mathbf{r}) + V_{xc}[n](\mathbf{r}), \tag{2.11}$$

where

$$V_H[n](\mathbf{r}) = \frac{\delta E_H[n]}{\delta n(\mathbf{r})} = \int d\mathbf{r}' v_c(\mathbf{r} - \mathbf{r}')n(\mathbf{r}'), \tag{2.12}$$

and

$$V_{xc}[n](\mathbf{r}) = \frac{\delta E_{xc}[n]}{\delta n(\mathbf{r})}. \tag{2.13}$$

The usefulness of the theory then relies on obtaining an accurate approximation for the exchange-correlation functional $E_{xc}[n]$. With an approximation in hand, the ground state density can be determined by solving the equations (2.7), (2.8) and (2.11) self-consistently, upon which the ground state energy can be computed.

2.3   Spin-density functional theory

The electronic system Hamiltonian (2.1) does not formally differentiate between magnetic and nonmagnetic materials and the preceding theory is equally valid in both cases. However, it is nontrivial to approximate the exchange-correlation functional, $E_{xc}[n]$, in a way that is sensitive to the magnetic degrees of freedom, when it is a functional only of the total electron density. To circumvent this issue, the magnetic order parameter can be included explicitly in the formalism, resulting in what is known as spin-density functional theory. As this variant constitutes the standard practice for magnetic materials, the distinction from regular DFT is often left implicit and both variants simply referred to as "DFT". This practice is adopted throughout most of this thesis.

2.3.1 The four-component density operator

In spin-density functional theory, the electrostatic potential in Equation (2.1) is substituted by a static electromagnetic potential, which couples to the electronic system through the four-component electron density operator:

$$\hat{n}^{\mu}(\mathbf{r}) = \sum_{s,s'} \sigma^{\mu}_{ss'} \, \hat{\psi}^{\dagger}_{s}(\mathbf{r})\hat{\psi}_{s'}(\mathbf{r}). \tag{2.14}$$

The μ-index indicates the component, $\mu \in \{0, x, y, z\}$, s indexes the spin, $s \in \{\uparrow, \downarrow\}$, and $\sigma^{\mu}_{ss'}$ equals the 2×2 identity matrix for $\mu = 0$ and the corresponding Pauli matrix for $\mu \in \{x, y, z\}$. The system Hamiltonian is then written

$$\hat{H}_0 = \hat{T} + \hat{W} + \hat{U}, \tag{2.15}$$

where

$$\hat{W} = \sum_{\mu} \int d\mathbf{r} \, \hat{n}^{\mu}(\mathbf{r})W^{\mu}(\mathbf{r}). \tag{2.16}$$

Neglecting contributions from the orbital current density, this corresponds to a material placed in an external electromagnetic field,

$$\begin{aligned}
\big(W^{\mu}(\mathbf{r})\big) &= \big(V_{\text{nuc}}(\mathbf{r}) + V_{\text{ext}}(\mathbf{r}), \mathbf{W}_{\text{ext}}(\mathbf{r})\big) \\
&= \big(-e\,[\phi_{\text{nuc}}(\mathbf{r}) + \phi_{\text{ext}}(\mathbf{r})]\,, \mu_{\text{B}}\mathbf{B}_{\text{ext}}(\mathbf{r})\big),
\end{aligned} \tag{2.17}$$

where μ_{B} is the Bohr magneton, $\phi_{\text{ext}}(\mathbf{r})$ is the external scalar potential and the $\mathbf{B}_{\text{ext}}(\mathbf{r})$ is the external magnetic field. In Equation (2.16), the magnetic field interaction enters as a Zeeman term, which is apparent when recasting the operator $\hat{W}$ in terms of the magnetization, $\hat{\mathbf{m}}(\mathbf{r}) = -\mu_{\text{B}}\,(\hat{n}^{x}(\mathbf{r}), \hat{n}^{y}(\mathbf{r}), \hat{n}^{z}(\mathbf{r}))$:

$$\hat{W} = \int d\mathbf{r} \left[\hat{n}(\mathbf{r})\big(V_{\text{nuc}}(\mathbf{r}) + V_{\text{ext}}(\mathbf{r})\big) - \hat{\mathbf{m}}(\mathbf{r}) \cdot \mathbf{B}_{\text{ext}}(\mathbf{r})\right]. \tag{2.18}$$

2.3.2 Hohenberg-Kohn-Sham theory

It is straight-forward to extend the Hohenberg-Kohn theorems to hold also for Hamiltonians of the form (2.15) [53]. For two electromagnetic potentials W and W' yielding different nondegenerate ground states $|\psi_0\rangle$ and $|\psi_0'\rangle$:

$$E = \langle\psi|\hat{T} + \hat{U}|\psi\rangle + \langle\psi|\hat{W}|\psi\rangle \quad \text{will be minimal using } |\psi\rangle = |\psi_0\rangle, \text{ not } |\psi_0'\rangle, \tag{2.19a}$$

$$E' = \langle\psi|\hat{T} + \hat{U}|\psi\rangle + \langle\psi|\hat{W}'|\psi\rangle \quad \text{will be minimal using } |\psi\rangle = |\psi_0'\rangle, \text{ not } |\psi_0\rangle. \tag{2.19b}$$

This can only be true if also the four-component density of the ground state is different among the two systems, $\big(n(\mathbf{r}), \mathbf{m}(\mathbf{r})\big) \neq \big(n'(\mathbf{r}), \mathbf{m}'(\mathbf{r})\big)$. Thus, there is a one-to-one correspondence between the ground state four-component density, $n^{\mu}(\mathbf{r})$, and the many-body ground state itself. As a result, the ground state can be written formally as a functional of n^{μ} and found by minimizing the energy functional $E[n^{\mu}]$ in complete analogy with Equation (2.5). However, on the contrary to the regular DFT case, the full

electronic system is *not* a functional of the ground state four-component density [54, 55]. Take e.g. a system which yields a fully spin-polarized ground state $\mathbf{m}(\mathbf{r}) = -\mu_{\text{B}} n(\mathbf{r}) \mathbf{e}_z$. In this case, adding a constant magnetic field $-B\mathbf{e}_z$ to the Hamiltonian (2.15) will not change the ground state, but it will (at least) change the energy of some excited states.

To minimize $E[n^\mu]$ in practise, it is assumed that an auxiliary Kohn-Sham system of noninteracting electrons exists, yielding the same ground state four-component density as in the many-body system. Minimizing the energy functional,

$$E[n^\mu] = T_{\text{s}}[n^\mu] + E_{\text{H}}[n] + E_{\text{xc}}[n^\mu] + \sum_\mu \int d\mathbf{r}\, n^\mu(\mathbf{r}) W^\mu(\mathbf{r}), \qquad (2.20)$$

under the constraint of a fixed number of electrons then yields a spinorial single-particle Schrödinger equation for the Kohn-Sham system [53, 56]:

$$\left(-\frac{\hbar^2 \nabla^2}{2m} + V_{\text{s}}(\mathbf{r}) + \bar{\boldsymbol{\sigma}} \cdot \mathbf{W}_{\text{s}}(\mathbf{r}) \right) \psi_i(\mathbf{r}) = \epsilon_i \psi_i(\mathbf{r}). \qquad (2.21)$$

Here $\bar{\boldsymbol{\sigma}}$ is the Pauli matrix vector, with the bar accent indicating that the equation is spinorial and that the Kohn-Sham eigenstates that enter are spinors, $\psi_i(\mathbf{r}) = (\psi_{i\uparrow}(\mathbf{r}), \psi_{i\downarrow}(\mathbf{r}))$. The effective electromagnetic potential is given by

$$\left(W_{\text{s}}^\mu(\mathbf{r}) \right) = \left(V_{\text{s}}(\mathbf{r}), \mathbf{W}_{\text{s}}(\mathbf{r}) \right), \qquad (2.22)$$

with

$$W_{\text{s}}^\mu(\mathbf{r}) = W_{\text{s}}^\mu[n^\nu](\mathbf{r}) = W^\mu(\mathbf{r}) + \delta_{\mu,0} V_{\text{H}}[n](\mathbf{r}) + W_{\text{xc}}^\mu[n^\nu](\mathbf{r}), \qquad (2.23)$$

where $\delta_{\mu,0}$ denotes the Kroenecker-δ and

$$W_{\text{xc}}^\mu[n^\nu](\mathbf{r}) = \frac{\delta E_{\text{xc}}[n^\nu]}{\delta n^\mu(\mathbf{r})}. \qquad (2.24)$$

Ground state properties can then be determined by solving the Kohn-Sham system (2.21) self-consistently with the effective potential (2.23) calculated from the ground state four-component electron density of the Kohn-Sham system itself:

$$n^\mu(\mathbf{r}) = \sum_i f_i \sum_{s,s'} \sigma_{ss'}^\mu \psi_{is}^*(\mathbf{r}) \psi_{is'}(\mathbf{r}). \qquad (2.25)$$

By including the magnetic degrees of freedom into the formalism, the Kohn-Sham system (2.21) now includes an effective Zeeman term and produces a ground state magnetization, $\mathbf{m}(\mathbf{r}) = -\mu_{\text{B}} \left(n^x(\mathbf{r}), n^y(\mathbf{r}), n^z(\mathbf{r}) \right)$, which is equal to the ground state magnetization of the many-body system. Neglecting contributions from the orbital current density, see Equation (2.17), and expressing quantities as functionals of the electron density and magnetization, the Zeeman interaction can be associated with an effective electromagnetic field,

$$\left(-\frac{\hbar \nabla^2}{2m} + V_{\text{s}}(\mathbf{r}) + \mu_{\text{B}} \bar{\boldsymbol{\sigma}} \cdot \mathbf{B}_{\text{s}}(\mathbf{r}) \right) \psi_i(\mathbf{r}) = \epsilon_i \psi_i(\mathbf{r}), \qquad (2.26)$$

where

$$V_{\mathrm{s}}(\mathbf{r}) = V_{\mathrm{s}}[n, \mathbf{m}](\mathbf{r}) = V_{\mathrm{nuc}}(\mathbf{r}) + V_{\mathrm{ext}}(\mathbf{r}) + V_{\mathrm{H}}[n](\mathbf{r}) + V_{\mathrm{xc}}[n, \mathbf{m}](\mathbf{r}), \quad (2.27)$$

$$\mathbf{B}_{\mathrm{s}}(\mathbf{r}) = \mathbf{B}_{\mathrm{s}}[n, \mathbf{m}](\mathbf{r}) = \mathbf{B}_{\mathrm{ext}}(\mathbf{r}) + \mathbf{B}_{\mathrm{xc}}[n, \mathbf{m}](\mathbf{r}), \quad (2.28)$$

and

$$\mathbf{B}_{\mathrm{xc}}[n, \mathbf{m}](\mathbf{r}) = -\frac{\delta E_{\mathrm{xc}}[n, \mathbf{m}]}{\delta \mathbf{m}(\mathbf{r})}. \quad (2.29)$$

For a bare material in the absence of external magnetic fields, the electronic system Hamiltonian (2.15) reduces to the regular DFT Hamiltonian (2.1) and both theories will, without approximations, yield the same ground state properties. However, in spin-density functional theory, it is much more obvious when a material is magnetic, namely when it is energetically favorable for the Kohn-Sham system to produce a spontaneous spin-polarization according to a finite exchange-correlation magnetic field, $\mathbf{B}_{\mathrm{xc}}$. Of course, the usefulness of the framework still relies on the ability to approximate $E_{\mathrm{xc}}[n, \mathbf{m}]$, but as will be shown in this thesis, one can come quite far in terms of predictability of magnetic material properties even with simple approximations to the exchange-correlation functional.

2.4   Local exchange-correlation functionals

The simplest approximation to the exchange-correlation functional is of course a local one. However, for magnon spectroscopy it is actually one of the only approximations available, for which reason it has been used extensively for the work leading to this thesis. In the present section, the local density approximation (LDA) is introduced and Hubbard corrections to the approximation discussed. Furthermore, in Chapters 7 and 8 approximations beyond the LDA are discussed in detail, in concurrence with the presentation of a newly developed class of nonlocal functionals.

2.4.1   Local density approximation

In the LDA, the exchange-correlation functional is approximated based on the homogeneous electron gas (HEG). The electron density at every point in space, $n(\mathbf{r})$, contributes locally to the exchange-correlation energy as if the corresponding volume element was part of an HEG of density n,

$$E_{\mathrm{xc}}^{\mathrm{LDA}}[n] = \int d\mathbf{r} \, \epsilon_{\mathrm{xc}}\big(n(\mathbf{r})\big) n(\mathbf{r}), \quad (2.30)$$

where $\epsilon_{\mathrm{xc}}(n)$ is the exchange-correlation energy per electron of an HEG. In the HEG limit, LDA is exact and thus it is expected to perform well for systems of slowly varying density. For localized electrons however, LDA suffers from the self-interaction error, meaning that individual electrons feel a net repulsive effective interaction from themselves. This leads to a delocalization of the electron density and ultimately a tendency to overestimate binding energies of molecules and underestimate lattice constants of

solids, see e.g. [57]. However, the LDA remains a surprisingly good approximation for many systems and properties, all the while providing the foundation for most higher-order approximations. The exchange-correlation potential in the LDA is given by:

$$V_{\text{xc}}^{\text{LDA}}[n](\mathbf{r}) = \left.\frac{\partial \left[\epsilon_{\text{xc}}(n)n\right]}{\partial n}\right|_{n=n(\mathbf{r})} = \left.\frac{\partial \epsilon_{\text{xc}}(n)}{\partial n}\right|_{n=n(\mathbf{r})} n(\mathbf{r}) + \epsilon_{\text{xc}}\big(n(\mathbf{r})\big) = V_{\text{xc}}^{\text{LDA}}\big(n(\mathbf{r})\big)$$

(2.31)

2.4.2 Local spin-density approximation

The local spin-density approximation (LSDA) is the natural extension of LDA for spin-density functional theory, in which the electrons contribute locally with an exchange-correlation energy per electron corresponding to a HEG of density n and magnetization $\mathbf{m}$, $\epsilon_{\text{xc}}(n) \to \epsilon_{\text{xc}}(n, |\mathbf{m}|)$:

$$E_{\text{xc}}^{\text{LSDA}}[n, \mathbf{m}] = \int d\mathbf{r}\, \epsilon_{\text{xc}}\big(n(\mathbf{r}), |\mathbf{m}(\mathbf{r})|\big)n(\mathbf{r}).$$

(2.32)

LSDA is sometimes referred to simply as LDA, when used for magnetic systems. This is also the case for the present thesis. The electrostatic xc potential is calculated in full analogy with Equation (2.31), and the exchange-correlation magnetic field is obtained using

$$\frac{\partial}{\partial \mathbf{m}} = \frac{\mathbf{m}}{m}\frac{\partial}{\partial m},$$

(2.33)

where $m = |\mathbf{m}|$, yielding

$$\begin{aligned}\mathbf{B}_{\text{xc}}^{\text{LSDA}}[n, \mathbf{m}](\mathbf{r}) &= -\left.\frac{\mathbf{m}}{m}\frac{\partial \left[\epsilon_{\text{xc}}(n, m)n\right]}{\partial m}\right|_{n=n(\mathbf{r}),\mathbf{m}=\mathbf{m}(\mathbf{r})} \\ &= \frac{\mathbf{m}(\mathbf{r})}{|\mathbf{m}(\mathbf{r})|}B_{\text{xc}}^{\text{LSDA}}\big(n(\mathbf{r}), |\mathbf{m}(\mathbf{r})|\big) = \mathbf{B}_{\text{xc}}^{\text{LSDA}}\big(n(\mathbf{r}), \mathbf{m}(\mathbf{r})\big)\end{aligned}$$

(2.34)

where:

$$B_{\text{xc}}^{\text{LSDA}}\big(n, m\big) = -\frac{\partial \epsilon_{\text{xc}}(n, m)}{\partial m}n.$$

(2.35)

It is worth noting, that since $\mathbf{m}$ points in the opposite direction of the spin-polarization, $B_{\text{xc}}^{\text{LSDA}}\big(n, |\mathbf{m}|\big)$ needs to be a positive quantity in order for the effective Zeeman term in (2.26) to locally lower the energy.

For collinear systems, where S^z can be chosen as a good quantum number and the ground state magnetization aligned to the z-axis, $\mathbf{m}(\mathbf{r}) = -\mu_{\text{B}}n^z(\mathbf{r})\mathbf{e}_z$, the transverse components of the exchange-correlation magnetic field (2.34) vanish and the spinorial components in the Kohn-Sham system (2.26) cease to mix. In this case, the spinorial components may be separated completely and the spin included in the state index $i \to (is)$, yielding two scalar Schrödinger equations for the Kohn-Sham system,

$$\left(-\frac{\hbar \nabla^2}{2m} + V_{\text{s}}(\mathbf{r}) + W_{\text{xc}}^z(\mathbf{r})\right)\psi_{i\uparrow}(\mathbf{r}) = \epsilon_{i\uparrow}\psi_{i\uparrow}(\mathbf{r}),$$

(2.36a)

$$\left(-\frac{\hbar \nabla^2}{2m} + V_{\mathrm{s}}(\mathbf{r}) - W_{\mathrm{xc}}^z(\mathbf{r}) \right) \psi_{i\downarrow}(\mathbf{r}) = \epsilon_{i\downarrow} \psi_{i\downarrow}(\mathbf{r}), \tag{2.36b}$$

where the external magnetic field has been set to zero, and:

$$W_{\mathrm{xc}}^z(\mathbf{r}) = W_{\mathrm{xc}}^{z,\mathrm{LSDA}}[n, n^z](\mathbf{r}) = \left. \frac{\partial \epsilon_{\mathrm{xc}}(n, n^z)}{\partial n^z} \right|_{n=n(\mathbf{r}), n^z = n^z(\mathbf{r})} n(\mathbf{r}). \tag{2.37}$$

Thus, in the collinear LSDA case, one has to solve two scalar Schrödinger equations self-consistently with spin-dependent effective potentials, $V_{\mathrm{s}}^\uparrow(\mathbf{r}) = V_{\mathrm{s}}(\mathbf{r}) + W_{\mathrm{xc}}^z(\mathbf{r})$ and $V_{\mathrm{s}}^\downarrow(\mathbf{r}) = V_{\mathrm{s}}(\mathbf{r}) - W_{\mathrm{xc}}^z(\mathbf{r})$, producing the ground state density and spin-polarization:

$$n(\mathbf{r}) = \sum_{is} f_{is} |\psi_{is}(\mathbf{r})|^2, \quad n^z(\mathbf{r}) = \sum_{is} f_{is} \sigma_{ss}^z |\psi_{is}(\mathbf{r})|^2. \tag{2.38}$$

2.4.3   Hubbard correction

Because of the delocalization error in LDA, the approximation fails most drastically in localized electron systems subject to strong correlation effects, typically involving localized d and f electrons. For such materials, the delocalization of electrons in the LDA leads to an over-stabilization of metallic ground states, ultimately leading to a tendency to misclassify Mott insulators as metals [58].

A popular strategy for including localized electronic correlation effects on top of the LDA is to use a Hubbard correction. Here, the strategy is to consider a Hubbard Hamiltonian in the mean field approximation and include the correlation effects that are missing in a phenomenological sense from the LDA [59–61].

2.4.3.1   Hubbard model

For the purpose of this thesis, a Hubbard model for the valence d-electrons of a given material is considered. If the electrons are sufficiently localized in the d-atomic orbitals (characterized by Wannier functions of quantum number m, localized at site j), one may to a good approximation consider only the onsite Coulomb repulsion, such that

$$\hat{H}_0 = \hat{H}_{\mathrm{nonint.}} + \hat{U}_{\mathrm{intra}}, \tag{2.39}$$

where $\hat{H}_{\mathrm{nonint.}}$ is a noninteracting (tight-binding) Hamiltonian for the system. The onsite Coulomb repulsion is then given by the Coulomb and exchange energy integrals $U_{jmm'}$ and $J_{jmm'}$ respectively [3]:

$$\hat{U}_{\mathrm{intra}} = \frac{1}{2} \sum_j \sum_s \left(\sum_{m,m'} U_{jmm'} \hat{n}_{jms} \hat{n}_{jm'\bar{s}} + \sum_{m \neq m'} \left[(U_{jmm'} - J_{jmm'}) \hat{n}_{jms} \hat{n}_{jm's} \right. \right.$$
$$\left. \left. - J_{jmm'} \hat{c}_{jms}^\dagger \hat{c}_{jm\bar{s}} \hat{c}_{jm'\bar{s}}^\dagger \hat{c}_{jm's} \right] \right). \tag{2.40}$$

Here s denotes the spin, with opposite spin $\bar{s}$, while $\hat{c}_{jms}^\dagger$ and $\hat{c}_{jms}$ are the creation/annihilation operators for the m'th d-orbital of site j, with $\hat{n}_{jms} = \hat{c}_{jms}^\dagger \hat{c}_{jms}$.

2.4.3.2 LDA+U in the Dudarev scheme

Usually, one does not differentiate between the individual d-electron orbitals on the same atom j, when it comes to the Coulomb and exchange integrals. Instead, $U_{jmm'}$ and $J_{jmm'}$ are substituted by their averages $\bar{U}_j$ and $\bar{J}_j$. Furthermore, the exchange integral integral is typically smaller than the corresponding Coulomb integral for strongly correlated systems. For this reason, the spin-flip exchange of Equation (2.40) will be neglected in the following, such that the onsite Coulomb repulsion at a given site j may be approximated as simply as

$$\hat{U}_j = \frac{\bar{U}}{2} \sum_s \sum_{m,m'} \hat{n}_{ms}\,\hat{n}_{m'\bar{s}} + \frac{\bar{U}-\bar{J}}{2} \sum_s \sum_{m \neq m'} \hat{n}_{ms}\,\hat{n}_{m's}, \tag{2.41}$$

where the j index is left implicit on the right-hand side.

In a proper mean-field treatment of the onsite Coulomb repulsion (2.41), second order fluctuations in the individual orbital occupancies are neglected,

$$\hat{n}_{ms}\hat{n}_{m's'} = (\langle\hat{n}_{ms}\rangle + \delta\hat{n}_{ms})\,(\langle\hat{n}_{m's'}\rangle + \delta\hat{n}_{m's'})$$
$$\simeq \hat{n}_{ms}n_{m's'} + n_{ms}\hat{n}_{m's'} - n_{ms}n_{m's'}, \tag{2.42}$$

where n_{ms} is the expected occupancy of orbital m with an electron of spin s. Thus, in the mean-field approximation, the onsite Coulomb energy is given by:

$$\langle\hat{U}_j^{\mathrm{MF}}\rangle = \frac{\bar{U}}{2} \sum_s \sum_{m,m'} n_{ms}\,n_{m'\bar{s}} + \frac{\bar{U}-\bar{J}}{2} \sum_s \sum_{m \neq m'} n_{ms}\,n_{m's} \tag{2.43}$$

Now, in order to formulate a correction to the LDA functional based on the Hubbard model, a conjecture is needed for the phenomenological significance of the LDA in the context of mean-field approximations to the Coulomb repulsion. A natural conjecture to make is, that the LSDA only accounts for fluctuations in *total* site occupancy $\hat{N}_s$, not the individual orbital occupancies. This conjecture aligns well with the fact that the LDA bears no reference to the individual orbitals, only the local total density of electrons, $n(\mathbf{r})$. In order to see the significance of this conjecture, the onsite Coulomb repulsion (2.41) is rewritten

$$
\begin{aligned}
\hat{U}_j =& \frac{\bar{U}}{2} \sum_s \left(\sum_m \hat{n}_{ms}\right)\left(\sum_{m'} \hat{n}_{m'\bar{s}}\right) \\
&+ \frac{\bar{U}-\bar{J}}{2} \sum_s \left(\sum_m \hat{n}_{ms}\right)\left(\sum_{m'} \hat{n}_{m's}\right) - \frac{\bar{U}-\bar{J}}{2} \sum_s \sum_m \hat{n}_{ms}^2 \\
=& \frac{\bar{U}}{2} \sum_s \hat{N}_s \hat{N}_{\bar{s}} + \frac{\bar{U}-\bar{J}}{2} \sum_s \hat{N}_s \hat{N}_s - \frac{\bar{U}-\bar{J}}{2} \sum_s \hat{N}_s,
\end{aligned} \tag{2.44}
$$

where, to reach the last equality, it is used that fermionic counting operators fulfill the identity $\hat{n}_{ms}^2 = \hat{n}_{ms}$. Applying now a mean-field approximation to the total site occupancy,

$$\hat{N}_s\hat{N}_{s'} \simeq N_s\hat{N}_{s'} + \hat{N}_s N_{s'} - N_s N_{s'}, \tag{2.45}$$

the LDA mean-field onsite Coulomb energy is, by conjecture, given by:

$$\langle \hat{U}_j^{\text{LDA}} \rangle = \frac{\bar{U}}{2} \sum_s N_s N_{\bar{s}} + \frac{\bar{U} - \bar{J}}{2} \sum_s N_s^2 - \frac{\bar{U} - \bar{J}}{2} \sum_s N_s. \tag{2.46}$$

Comparison with the proper mean-field treatment of the onsite Coulomb repulsion (2.43) then yields the Dudarev Hubbard correction [61]:

$$E_{\text{xc}}^{\text{LDA+U}}[n, \mathbf{m}] = E_{\text{xc}}^{\text{LSDA}}[n, \mathbf{m}] + \sum_j \left(\langle \hat{U}_j^{\text{MF}} \rangle - \langle \hat{U}_j^{\text{LDA}} \rangle \right)$$

$$= E_{\text{xc}}^{\text{LSDA}}[n, \mathbf{m}] + \frac{1}{2} \sum_j U_{\text{eff}}^j \sum_{ms} \left(n_{jms} - n_{jms}^2 \right), \tag{2.47}$$

where $U_{\text{eff}}^j = \bar{U}_j - \bar{J}_j$ is the effective onsite Coulomb repulsion of the valence d-electrons of site j. In this way, the Hubbard correction punishes fractional occupation of the d-electron orbitals, favoring gaped d-bands over metallic ones, in a scheme that is relatively simple to implement in a DFT code.

Theory: LR-TDDFT and magnons

From the previous chapters, a road map for the characterization of excited states begins to materialize. Combining the formally exact electronic structure framework of DFT with the Kubo theory of linear response, quasi-particle excitations such as magnons may be characterized by the means of an associated material susceptibility. However, to compute dynamic susceptibilities within the framework of DFT, one needs to go beyond the static limit in order to treat (at least formally) time-dependent external perturbations.

In this chapter, the missing link (time-dependent DFT) is introduced, along with the four-component susceptibility tensor, which characterizes the susceptibility of the electronic system in terms of its core variable, the four-component electron density. From the four-component susceptibility tensor, the connection to fundamental magnetic excitations is illustrated, such that the spectrum of magnon quasi-particles may be extracted. To this end, it is shown how the transverse magnetic susceptibility can be calculated based on a given DFT ground state.

Many of the topics of this chapter are described in further detail in Publication [A] of this thesis. A hyperlink to the appropriate section of the paper is provided towards the end of the chapter.

3.1 Time-dependent density functional theory

In the relevant spin-dependent version of time-dependent density functional theory (TDDFT), the following problem is considered: Given that an electronic system is prepared in the state $|\psi(0)\rangle$ at time $t = 0$, how does the system evolve under the influence of a classical external time-dependent electromagnetic field,

$$\hat{H}(t) = \hat{H}_0 + \hat{H}_{\text{ext}}(t), \tag{3.1}$$

with the magnetic field interaction accounted for in terms of a Zeeman term:

$$\hat{H}_{\text{ext}}(t) = \sum_{\mu} \int d\mathbf{r} \, \hat{n}^{\mu}(\mathbf{r}) W_{\text{ext}}^{\mu}(\mathbf{r}, t), \tag{3.2a}$$

$$\left(W_{\text{ext}}^{\mu}(\mathbf{r}, t) \right) = \left(V_{\text{ext}}^{\mu}(\mathbf{r}, t), \mathbf{W}_{\text{ext}}^{\mu}(\mathbf{r}, t) \right) = \left(-e\phi_{\text{ext}}(\mathbf{r}, t), \, \mu_{\text{B}} \mathbf{B}_{\text{ext}}(\mathbf{r}, t) \right). \tag{3.2b}$$

Using the usual spin-dependent system Hamiltonian (2.15), with the static external fields set to zero, this composes a time-dependent generalization of the electronic structure problem of spin-density functional theory. According to the Runge-Gross theorem [35], there is then, in full analogy with static DFT, a one-to-one correspondence between the time-dependent four-component electron density and the many-body wave function:

$$\left(n^\mu(\mathbf{r}, t)\right) \leftrightarrow |\psi(t)\rangle, \quad \text{given } |\psi(0)\rangle. \tag{3.3}$$

Furthermore, one can avoid treating the many-body problem directly by considering the corresponding auxiliary Kohn-Sham system of noninteracting electrons,

$$i\frac{\partial \psi_i(\mathbf{r}, t)}{\partial t} = \left(-\frac{\hbar^2 \nabla^2}{2m} + V_\mathrm{s}(\mathbf{r}, t) + \bar{\boldsymbol{\sigma}} \cdot \mathbf{W}_\mathrm{s}(\mathbf{r}, t)\right) \psi_i(\mathbf{r}, t), \tag{3.4}$$

which, by construction, yields the same time-dependent four-component electron density as the many-body system. In this way, the problem is reduced to the solution of the time-dependent Schrödinger equation with time-dependent effective fields

$$W_\mathrm{s}^\mu(\mathbf{r}, t) = W_\mathrm{s}^\mu[n^\nu](\mathbf{r}, t) = \delta_{\mu,0} V_\mathrm{nuc}(\mathbf{r}) + W_\mathrm{ext}^\mu(\mathbf{r}, t) + \delta_{\mu,0} V_\mathrm{H}[n(t)](\mathbf{r}) + W_\mathrm{xc}^\mu[n^\nu](\mathbf{r}, t), \tag{3.5}$$

where $V_\mathrm{H}[n(t)](\mathbf{r})$ denotes the instantaneous Hartree potential (2.12), evaluated using $n(\mathbf{r}, t)$. As usual however, the formal difficulty of the scheme lies in finding suitable approximations to the time-dependent exchange-correlation potential, which now formally depends on the four-component density $n^\mu(\mathbf{r}, t')$ at all previous times $t' \leq t$. For the remainder of this chapter, the focus will be to use the framework of TDDFT to compute susceptibilities of materials. For an in-depth treatment of TDDFT and related topics, the reader is referred to relevant literature such as [62].

3.2   Four-component susceptibility tensor

If the external electromagnetic field (3.2a) is weak, the response to the perturbation will be linear and may be characterized in terms of the four-component susceptibility tensor. That is, the induced change in four-component electron density will, to linear order, be given by the response relation (1.25),

$$\delta n^\mu(\mathbf{r}, t) = \sum_\nu \int_{-\infty}^{\infty} dt' \int d\mathbf{r}' \, \chi^{\mu\nu}(\mathbf{r}, \mathbf{r}', t - t') W_\mathrm{ext}^\nu(\mathbf{r}', t'), \tag{3.6}$$

where $\chi^{\mu\nu}(\mathbf{r}, \mathbf{r}', t - t')$ is the retarded susceptibility in the four-component electron density coordinates of the system, as defined by the Kubo formula (1.3):

$$\chi^{\mu\nu}(\mathbf{r}, \mathbf{r}', t - t') = -\frac{i}{\hbar}\theta(t - t')\langle\,[\hat{n}_0^\mu(\mathbf{r}, t - t'), \hat{n}^\nu(\mathbf{r}')]\,\rangle_0. \tag{3.7}$$

Likewise, one may from the Kubo theory directly write up the spectrum of induced eigenstate transitions from the dissipative part of the susceptibility (1.7b),

$$S^{\mu\nu}(\mathbf{r}, \mathbf{r}', \omega) = -\frac{1}{2\pi i} \left[\chi^{\mu\nu}(\mathbf{r}, \mathbf{r}', \omega) - \chi^{\nu\mu}(\mathbf{r}', \mathbf{r}, -\omega) \right] \tag{3.8}$$

$$= \sum_{\alpha,\alpha'} n^{\mu}_{\alpha\alpha'}(\mathbf{r}) n^{\nu}_{\alpha'\alpha}(\mathbf{r}')(n_\alpha - n_{\alpha'}) \delta\big(\hbar\omega - (E_{\alpha'} - E_\alpha)\big). \tag{3.9}$$

In this way, the four-component susceptibility tensor comprises the central object of interest for studying the (linear) spectral properties of any electronic system. The transition matrix elements weighting the spectrum are the four-component pair densities, $n^{\mu}_{\alpha\alpha'}(\mathbf{r}) = \langle \alpha | \hat{n}^{\mu}(\mathbf{r}) | \alpha' \rangle$, and each element of the tensor represents the transitions that can be induced by specific components of the external field. In particular, the mean rate of energy absorption from a harmonic perturbation $W^{\mu}_{\text{ext}}(\mathbf{r}, t) = W^{\mu}_{\text{ext}}(\mathbf{r}) \cos(\omega_0 t)$, is given by [A]

$$\bar{Q} = \frac{\pi\omega_0}{2} \sum_{\mu,\nu} \iint d\mathbf{r} d\mathbf{r}' \, W^{\mu}_{\text{ext}}(\mathbf{r}) S^{\mu\nu}(\mathbf{r}, \mathbf{r}', \omega_0) W^{\nu}_{\text{ext}}(\mathbf{r}'), \tag{3.10}$$

thus providing a formal theoretical background for spectroscopic techniques such as inelastic neutron scattering [20].

3.2.1 Four-component plane wave susceptibility

For periodic crystals, where the response is diagonal in the reduced wave vector $\mathbf{q}$, one may represent the susceptibility tensor in the plane wave basis, that is, in terms of the four-component plane wave susceptibility:

$$\chi^{\mu\nu}_{\mathbf{GG}'}(\mathbf{q}, \omega) = \iint \frac{d\mathbf{r} d\mathbf{r}'}{\Omega} e^{-i(\mathbf{G}+\mathbf{q})\cdot\mathbf{r}} \chi^{\mu\nu}(\mathbf{r}, \mathbf{r}', \omega) e^{i(\mathbf{G}'+\mathbf{q})\cdot\mathbf{r}'}. \tag{3.11}$$

In the Lehmann representation, see Equations (1.5) and (1.39), $\chi^{\mu\nu}_{\mathbf{GG}'}(\mathbf{q}, \omega)$ stands out as a clear spin-dependent generalization of the dielectric function, first derived by Adler [63] and Wiser [64]:

$$\chi^{\mu\nu}_{\mathbf{GG}'}(\mathbf{q}, \omega) = \lim_{\eta\to 0^+} \frac{1}{\Omega} \sum_{\alpha,\alpha'} \frac{n^{\mu}_{\alpha\alpha'}(\mathbf{G}+\mathbf{q}) n^{\nu}_{\alpha'\alpha}(-\mathbf{G}'-\mathbf{q})}{\hbar\omega - (E_{\alpha'} - E_\alpha) + i\hbar\eta}(n_\alpha - n_{\alpha'}). \tag{3.12}$$

Similar to the dielectric function, the four-component plane wave susceptibility only includes transitions with a difference in crystal momentum $\hbar\mathbf{q}_{\alpha'\alpha} = \hbar\mathbf{q}$. Otherwise, the reciprocal space pair densities,

$$n^{\mu}_{\alpha\alpha'}(\mathbf{G}+\mathbf{q}) = \int d\mathbf{r} \, e^{-i(\mathbf{G}+\mathbf{q})\cdot\mathbf{r}} n^{\mu}_{\alpha\alpha'}(\mathbf{r}), \tag{3.13}$$

vanish. Thus, the four-component plane wave susceptibility specifically characterizes quasi-particle excitations of crystal momentum $\hbar\mathbf{q}$.

To illustrate the direct physical significance of the four-component plane wave susceptibility, the response to a general Bloch wave perturbation (1.31) is considered,

$$\hat{H}_{\text{ext}}(t) = \sum_{\nu} \sum_{\mathbf{G}'} \int d\mathbf{r}\, \hat{n}^{\nu}(\mathbf{r}) \frac{1}{2} \left[W^{\nu}_{\text{ext},\mathbf{G}'}\, e^{i([\mathbf{G}'+\mathbf{q}_0]\cdot\mathbf{r}-\omega_0 t)} + \text{c.c.} \right], \tag{3.14}$$

$$= \sum_{\nu} \sum_{\mathbf{G}'} \int d\mathbf{r}\, \hat{n}^{\nu}(\mathbf{r}) \Big[\text{Re}\left\{ W^{\nu}_{\text{ext},\mathbf{G}'} \right\} \cos([\mathbf{G}'+\mathbf{q}_0]\cdot\mathbf{r}-\omega_0 t)$$

$$- \text{Im}\left\{ W^{\nu}_{\text{ext},\mathbf{G}'} \right\} \sin([\mathbf{G}'+\mathbf{q}_0]\cdot\mathbf{r}-\omega_0 t) \Big], \tag{3.15}$$

where the plane wave coefficient $W^{\nu}_{\text{ext},\mathbf{G}'}$ are allowed to be complex in order to include the possible mixing of even and uneven frequency components. Using the response (1.37) to a single plane wave perturbation (1.36), the induced change in the four-component electron density can then be written up directly,

$$\delta n^{\mu}(\mathbf{r},t) = \sum_{\nu} \sum_{\mathbf{G},\mathbf{G}'} \frac{1}{2} \Big[\chi^{\mu\nu}_{\mathbf{G}\mathbf{G}'}(\mathbf{q}_0,\omega_0) W^{\nu}_{\text{ext},\mathbf{G}'}\, e^{i([\mathbf{G}+\mathbf{q}_0]\cdot\mathbf{r}-\omega_0 t)}$$

$$+ \chi^{\mu\nu}_{-\mathbf{G}-\mathbf{G}'}(-\mathbf{q}_0,-\omega_0) W^{\nu*}_{\text{ext},\mathbf{G}'}\, e^{-i([\mathbf{G}+\mathbf{q}_0]\cdot\mathbf{r}-\omega_0 t)} \Big], \tag{3.16}$$

illustrating once again the literal interpretation of $\chi^{\mu\nu}_{\mathbf{G}\mathbf{G}'}(\mathbf{q},\omega)$ as a plane wave susceptibility. Using this result, the mean rate of energy absorbed by the system can be calculated [42]:

$$\bar{Q} = \frac{\omega_0}{2\pi} \int_0^{2\pi/\omega_0} dt \sum_{\mu} \int d\mathbf{r}\, \frac{dW^{\mu}_{\text{ext}}(\mathbf{r},t)}{dt} \delta n^{\mu}(\mathbf{r},t). \tag{3.17}$$

The procedure goes as follows. First, the time average is carried out. This retains only the terms, where the perturbation and the response are out-of-phase, see Equations (3.14) and (3.16). Secondly, the plane wave components are matched by the spatial integration. Lastly, indices on half of the terms are exchanged to rewrite the absorption in terms of the spectrum of induced transitions (1.40):

$$\bar{Q} = -\frac{\omega_0}{2} \sum_{\mu,\nu} \sum_{\mathbf{G},\mathbf{G}',\mathbf{G}''} \int d\mathbf{r}\, \frac{1}{2i} \Big[W^{\mu*}_{\text{ext},\mathbf{G}}\, e^{-i\mathbf{G}\cdot\mathbf{r}}\, \chi^{\mu\nu}_{\mathbf{G}'\mathbf{G}''}(\mathbf{q}_0,\omega_0) W^{\nu}_{\text{ext},\mathbf{G}''}\, e^{i\mathbf{G}'\cdot\mathbf{r}}$$

$$- W^{\mu}_{\text{ext},\mathbf{G}}\, e^{i\mathbf{G}\cdot\mathbf{r}}\, \chi^{\mu\nu}_{-\mathbf{G}'-\mathbf{G}''}(-\mathbf{q}_0,-\omega_0) W^{\nu*}_{\text{ext},\mathbf{G}''}\, e^{-i\mathbf{G}'\cdot\mathbf{r}} \Big],$$

$$= -\frac{\omega_0}{2}\Omega \sum_{\mu,\nu} \sum_{\mathbf{G},\mathbf{G}'} \frac{1}{2i} \Big[W^{\mu*}_{\text{ext},\mathbf{G}}\, \chi^{\mu\nu}_{\mathbf{G}\mathbf{G}'}(\mathbf{q}_0,\omega_0) W^{\nu}_{\text{ext},\mathbf{G}'}$$

$$- W^{\mu}_{\text{ext},\mathbf{G}}\, \chi^{\mu\nu}_{-\mathbf{G}-\mathbf{G}'}(-\mathbf{q}_0,-\omega_0) W^{\nu*}_{\text{ext},\mathbf{G}'} \Big],$$

$$= \frac{\pi\omega_0}{2}\Omega \sum_{\mu,\nu} \sum_{\mathbf{G},\mathbf{G}'} W^{\mu*}_{\text{ext},\mathbf{G}}\, S^{\mu\nu}_{\mathbf{G}\mathbf{G}'}(\mathbf{q}_0,\omega_0) W^{\nu}_{\text{ext},\mathbf{G}'}. \tag{3.18}$$

In this way, the analogy to the real-space representation of (3.10) is complete. The mean rate of energy absorption is of course a real quantity, even though it is not so

clear from Equation (3.18). However, as the four-component density is an Hermitian operator, $S^{\mu\nu}_{\mathbf{GG}'}(\mathbf{q},\omega) = S^{\nu\mu*}_{\mathbf{G}'\mathbf{G}}(\mathbf{q},\omega)$[1]. Using this identity, it is straight-forward to show that the imaginary terms in Equation (3.18) cancel out identically, so that:

$$\bar{Q} = \frac{\pi\omega_0}{2}\Omega \sum_{\mu,\nu} \sum_{\mathbf{G},\mathbf{G}'} \mathrm{Re}\left[W^{\mu*}_{\mathrm{ext},\mathbf{G}}\, S^{\mu\nu}_{\mathbf{GG}'}(\mathbf{q}_0,\omega_0) W^{\nu}_{\mathrm{ext},\mathbf{G}'} \right]. \qquad (3.19)$$

Looking at Equation (3.15), one can thus conclude that the real part of $S^{\mu\nu}_{\mathbf{GG}'}(\mathbf{q},\omega)$ is responsible for the energy dissipation from external electromagnetic field components that oscillate in-phase, whereas the imaginary part of $S^{\mu\nu}_{\mathbf{GG}'}(\mathbf{q},\omega)$ gives the energy dissipation resulting from the out-of-phase field components.

3.2.2 Transverse magnetic susceptibility

In order to study quasi-particle excitations which change the spin angular momentum of the system, the relevant component of the susceptibility tensor is the transverse magnetic susceptibility,

$$\chi^{+-}(\mathbf{r},\mathbf{r}',t-t') = -\frac{i}{\hbar}\theta(t-t')\langle\, [\hat{n}^+_0(\mathbf{r},t-t'),\hat{n}^-(\mathbf{r}')]\,\rangle_0, \qquad (3.20)$$

where $\hat{n}^+(\mathbf{r})$ and $\hat{n}^-(\mathbf{r})$ are the spin-raising and spin-lowering electron density operators respectively:

$$\hat{n}^+(\mathbf{r}) = \frac{1}{2}\Big(\hat{n}^x(\mathbf{r}) + i\hat{n}^y(\mathbf{r})\Big) = \hat{\psi}^\dagger_\uparrow(\mathbf{r})\hat{\psi}_\downarrow(\mathbf{r}), \qquad (3.21)$$

$$\hat{n}^-(\mathbf{r}) = \frac{1}{2}\Big(\hat{n}^x(\mathbf{r}) - i\hat{n}^y(\mathbf{r})\Big) = \hat{\psi}^\dagger_\downarrow(\mathbf{r})\hat{\psi}_\uparrow(\mathbf{r}). \qquad (3.22)$$

Similarly, one may also interchange the $+$ and $-$ indices in Equation (3.20) to define χ^{-+}, but as $\hat{n}^+(\mathbf{r})$ and $\hat{n}^-(\mathbf{r})$ are each others Hermitian conjugates, $\chi^{+-}(\mathbf{r},\mathbf{r}',\omega) = \chi^{-+*}(\mathbf{r},\mathbf{r}',-\omega)$ [A], and it is sufficient to study only one of them.

The transverse magnetic susceptibility directly characterizes the response towards perturbations in the circular magnetic field components $W^\pm_{\mathrm{ext}}(\mathbf{r},t) = W^x_{\mathrm{ext}}(\mathbf{r},t) \pm i\,W^y_{\mathrm{ext}}(\mathbf{r},t)$. Rewriting the linear response relation (3.6) in circular coordinates $j \in \{0,+,-,z\}$ [A]:

$$\delta n^j(\mathbf{r},t) = \sum_k \int_{-\infty}^{\infty} dt' \int d\mathbf{r}'\, \chi^{jk}(\mathbf{r},\mathbf{r}',t-t')\breve{W}^k_{\mathrm{ext}}(\mathbf{r}',t'). \qquad (3.23)$$

Here, χ^{jk} is the four-component susceptibility in circular coordinates, defined from the Kubo formula (3.7), and the breve accent on the external field is responsible for matching $+$ and $-$ components, $\big(\breve{W}^j\big) = \big(V, W^-, W^+, W^z\big)$. Thus, in the nonrelativistic limit, where the total spin projection along the z-axis, S^z, is taken as a good quantum

---

[1]Actually, it directly implies that $\chi^{\mu\nu}_{\mathbf{GG}'}(\mathbf{q},\omega) = \chi^{\mu\nu*}_{-\mathbf{G}-\mathbf{G}'}(-\mathbf{q},-\omega)$ [A]. However, from this identity: $S^{\mu\nu}_{\mathbf{GG}'}(\mathbf{q},\omega) = [\chi^{\mu\nu}_{\mathbf{GG}'}(\mathbf{q},\omega) - \chi^{\nu\mu}_{-\mathbf{G}'-\mathbf{G}}(-\mathbf{q},-\omega)]/(2i) = [\chi^{\mu\nu*}_{-\mathbf{G}-\mathbf{G}'}(-\mathbf{q},-\omega) - \chi^{\nu\mu*}_{\mathbf{G}'\mathbf{G}}(\mathbf{q},\omega)]/(2i) = S^{\nu\mu*}_{\mathbf{G}'\mathbf{G}}(\mathbf{q},\omega)$.

number, one may probe the spin-raising and spin-lowering eigenstate transitions of a material, by using perturbative methods that couple to the system like a transverse magnetic field. In particular, by tracking the energy dissipation (3.19), one may directly probe the spectrum of transverse magnetic transitions $S_{\mathbf{GG'}}^{+-}(\mathbf{q}, \omega)$, see Equation (1.40). In the zero temperature limit, see Equations (1.43) and (1.44), the spectrum directly yields the spectral functions for spin-raising and spin-lowering excitations to the ground state $|\alpha_0\rangle$, at negative and positive frequencies respectively:

$$S_{\mathbf{GG'}}^{+-}(\mathbf{q}, \omega) = A_{\mathbf{GG'}}^{+-}(\mathbf{q}, \omega) - A_{-\mathbf{G'}-\mathbf{G}}^{-+}(-\mathbf{q}, -\omega), \tag{3.24}$$

$$A_{\mathbf{GG'}}^{+-}(\mathbf{q}, \omega) = \frac{1}{\Omega} \sum_{\alpha \neq \alpha_0} n_{0\alpha}^{+}(\mathbf{G} + \mathbf{q}) n_{\alpha 0}^{-}(-\mathbf{G'} - \mathbf{q}) \delta\big(\hbar\omega - (E_\alpha - E_0)\big). \tag{3.25}$$

In this way, one can directly study transverse magnetic quasi-particles of energy $\hbar\omega = E_\alpha - E_0$, crystal momentum $\hbar\mathbf{q}$ and spin projection $\pm\hbar$. In particular, one may extract the magnon dispersion relation and probe the many-body Stoner continuum of spin-flipped electron hole pairs.

3.3   Linear response TDDFT

The general aim of theoretical spectroscopy is similar to that of the analogous experimental techniques, that is, to compute excited states spectra like $S_{\mathbf{GG'}}^{+-}(\mathbf{q}, \omega)$ directly, without explicitly having to deal with the many-body wave function of the ground and excited states. Within the framework of linear response TDDFT (LR-TDDFT), this aim is achieved by utilizing that it is, in principle, straight-forward to calculate the susceptibility of the noninteracting Kohn-Sham system at zero temperature. In particular, the Kohn-Sham four-component susceptibility tensor is given by the Lehmann representation [A]

$$\chi_{\text{KS}}^{\mu\nu}(\mathbf{r}, \mathbf{r}', \omega) = \lim_{\eta \to 0^+} \frac{1}{N_k^2} \sum_{n\mathbf{k}} \sum_{m\mathbf{k}'} (f_{n\mathbf{k}} - f_{m\mathbf{k}'}) \frac{n_{n\mathbf{k}, m\mathbf{k}'}^{\mu}(\mathbf{r}) \, n_{m\mathbf{k}', n\mathbf{k}}^{\nu}(\mathbf{r}')}{\hbar\omega - (\epsilon_{m\mathbf{k}'} - \epsilon_{n\mathbf{k}}) + i\hbar\eta}, \tag{3.26}$$

where $n_{n\mathbf{k}, m\mathbf{k}'}^{\mu}(\mathbf{r})$ are the Kohn-Sham four-component pair densities of the Kohn-Sham Bloch wave spinors of band indices n, m and wave vectors $\mathbf{k}$, $\mathbf{k}'$, with single-particle energies $\epsilon_{n\mathbf{k}}$, $\epsilon_{m\mathbf{k}'}$ and occupation numbers $f_{n\mathbf{k}}$, $f_{m\mathbf{k}'}$:

$$n_{n\mathbf{k}, m\mathbf{k}'}^{\mu}(\mathbf{r}) = \sum_{s, s'} \sigma_{ss'}^{\mu} \psi_{n\mathbf{k}s}^{*}(\mathbf{r}) \psi_{m\mathbf{k}'s'}(\mathbf{r}). \tag{3.27}$$

Comparing Equation (3.26) to the generalized Lehmann representation (1.5), factors of $N_k = \Omega/\Omega_{\text{cell}}$ have been extracted from the Kohn-Sham spinors in order to normalize the pair densities to the unit cell. Now, whereas the Kohn-Sham susceptibility may be used to study noninteracting electron-hole pair excitations in the Kohn-Sham band structure, it is not in general a good approximation for the many-body susceptibility. However, assuming that the induced change in the xc potential with respect to

the ground state ($\delta W_{\mathrm{xc}}^{\mu}(\mathbf{r}, t)$) depends linearly on the external electromagnetic fields $W_{\mathrm{ext}}^{\mu}(\mathbf{r}, t)$ in the limit where the perturbation is weak, the change of effective fields in the Kohn-Sham system, $\delta W_{\mathrm{s}}^{\mu}(\mathbf{r}, t)$, is itself a perturbative quantity. In this case, the Kohn-Sham susceptibility can be related directly to the many-body susceptibility of the system through a Dyson equation [36]:

$$
\begin{aligned}
\chi^{\mu\nu}(\mathbf{r}, \mathbf{r}', \omega) = &\chi_{\mathrm{KS}}^{\mu\nu}(\mathbf{r}, \mathbf{r}', \omega) \\
&+ \sum_{\tau_1, \tau_2} \iint d\mathbf{r}_1 d\mathbf{r}_2 \, \chi_{\mathrm{KS}}^{\mu\tau_1}(\mathbf{r}, \mathbf{r}_1, \omega) K_{\mathrm{Hxc}}^{\tau_1\tau_2}(\mathbf{r}_1, \mathbf{r}_2, \omega) \chi^{\tau_2\nu}(\mathbf{r}_2, \mathbf{r}', \omega).
\end{aligned}
\tag{3.28}
$$

The only ingredient needed from TDDFT is the Hartree-exchange-correlation kernel,

$$
K_{\mathrm{Hxc}}^{\tau_1\tau_2}(\mathbf{r}_1, \mathbf{r}_2, t_1 - t_2) = \frac{\delta W_{\mathrm{Hxc}}^{\tau_1}(\mathbf{r}_1, t_1)}{\delta n^{\tau_2}(\mathbf{r}_2, t_2)},
\tag{3.29}
$$

which itself is evaluated at the ground state four-component density $n^{\mu}(\mathbf{r})$. In this way, one can compute the Kohn-Sham susceptibility and Hxc kernel based on a given DFT ground state and retrieve the full many-body susceptibility by inversion of the Dyson equation (3.28). However, $\delta W_{\mathrm{s}}^{\mu}(\mathbf{r}, t)$ can only be treated as a perturbative quantity, if the approximation to the exchange-correlation kernel is consistent with the xc potential of the ground state. Otherwise, the Dyson equation (3.28) breaks down and one is not guaranteed to obtain a meaningful approximation for $\chi^{\mu\nu}(\mathbf{r}, \mathbf{r}', \omega)$.

3.4 Adiabatic local density approximation

The simplest, and most widely used, class of approximations to the exchange-correlation kernel are the adiabatic kernels. In this section, the adiabatic LDA kernel is introduced, first in the context of the spin-paired theory, generalizing to spin-density functional theory afterwards.

3.4.1 ALDA for spin-paired DFT

The philosophy of the adiabatic kernel is to neglect the memory of the xc potential, that is, let the potential depend only on the instantaneous electron density [65],

$$
V_{\mathrm{xc}}^{\mathrm{adia}}[n](\mathbf{r}, t) = V_{\mathrm{xc}}^{\mathrm{gs}}[n(t)](\mathbf{r}),
\tag{3.30}
$$

using some approximation for the ground state xc potential $V_{\mathrm{xc}}^{\mathrm{gs}}[n](\mathbf{r})$. In the adiabatic limit, where the time-scale of the external potential is much longer than any time-scale of the electronic system, the system will always be in its instantaneous ground state, making the adiabatic form (3.30) exact [65]. However, as the work of the present thesis also illustrates, the adiabatic approximation can also be an appropriate one beyond the $\omega \to 0$ limit. In the adiabatic approximation, the time-dependent kernel is written in terms of the static kernel $f_{\mathrm{xc}}(\mathbf{r}, \mathbf{r}')$,

$$
K_{\mathrm{xc}}^{\mathrm{adia}}[n](\mathbf{r}, \mathbf{r}', t - t') = \frac{\delta V_{\mathrm{xc}}^{\mathrm{gs}}[n](\mathbf{r})}{\delta n(\mathbf{r}')}\Bigg|_{n=n(\mathbf{r})} \delta(t - t') = f_{\mathrm{xc}}[n](\mathbf{r}, \mathbf{r}') \, \delta(t - t'),
\tag{3.31}
$$

where $n(\mathbf{r})$ is the ground state density in absence of the external perturbation and

$$f_{\mathrm{xc}}[n](\mathbf{r}, \mathbf{r}') = \frac{\delta^2 E_{\mathrm{xc}}[n]}{\delta n(\mathbf{r}) \delta n(\mathbf{r}')}, \tag{3.32}$$

using some approximation for the (ground state) exchange-correlation functional $E_{\mathrm{xc}}[n]$.

Applying the adiabatic approximation to the LDA exchange-correlation functional (2.30), the so-called adiabatic local density approximation (ALDA) is obtained. In the LDA,

$$f_{\mathrm{xc}}^{\mathrm{LDA}}[n](\mathbf{r}, \mathbf{r}') = \left[\left. \frac{\partial^2 \epsilon_{\mathrm{xc}}}{\partial n^2} \right|_{n=n(\mathbf{r})} n(\mathbf{r}) + 2 \left. \frac{\partial \epsilon_{\mathrm{xc}}}{\partial n} \right|_{n=n(\mathbf{r})} \right] \delta(\mathbf{r} - \mathbf{r}') = f_{\mathrm{xc}}^{\mathrm{LDA}}\big(n(\mathbf{r})\big)\delta(\mathbf{r} - \mathbf{r}'),$$

$$\tag{3.33}$$

meaning that the static kernel is completely local and depends only on the local electron density $n(\mathbf{r})$. By design, the ALDA kernel is exact in the static long wavelength limit of the homogeneous electron gas, see [66] and the references therein. For the HEG, where $n(\mathbf{r}) = n$, the static LDA kernel becomes a simple function of n and $\mathbf{r} - \mathbf{r}'$,

$$f_{\mathrm{xc}}^{\mathrm{LDA}}(n, \mathbf{r} - \mathbf{r}') = \left[\frac{\partial^2 \epsilon_{\mathrm{xc}}}{\partial n^2} n + 2 \frac{\partial \epsilon_{\mathrm{xc}}}{\partial n} \right] \delta(\mathbf{r} - \mathbf{r}') = f_{\mathrm{xc}}^{\mathrm{LDA}}(n)\delta(\mathbf{r} - \mathbf{r}'), \tag{3.34}$$

yielding a constant kernel in reciprocal space $f_{\mathrm{xc}}^{\mathrm{LDA}}(n, q) = f_{\mathrm{xc}}^{\mathrm{LDA}}(n) = f_{\mathrm{xc}}^{\mathrm{HEG}}(q \to 0, \omega = 0)$. It is important to note, that the ALDA is not exact for the HEG beyond the long wavelength limit. This is discussed in much more detail in Section 7.5 and essentially provides the starting point for the development of a new class of nonlocal exchange-correlation functionals presented in Chapter 8.

3.4.2   ALDA for spin-density functional theory

Also the spin-dependent ALDA kernel is local in space and time, in this case depending locally on the ground state electron density $n(\mathbf{r})$ and the magnetization $\mathbf{m}(\mathbf{r})$. Based on the LSDA functional (2.32),

$$K_{\mathrm{ALDA}}^{\tau_1 \tau_2}(\mathbf{r}_1, \mathbf{r}_2, t_1 - t_2) = f_{\mathrm{LSDA}}^{\tau_1 \tau_2}\big(n(\mathbf{r}_1), \mathbf{m}(\mathbf{r}_1)\big)\delta(\mathbf{r}_1 - \mathbf{r}_2)\,\delta(t_1 - t_2), \tag{3.35}$$

where the static LSDA kernel is straight-forward to evaluate from the xc energy per electron of the homogeneous electron gas:

$$f_{\mathrm{LSDA}}^{\tau_1 \tau_2}\big(n(\mathbf{r}), \mathbf{m}(\mathbf{r})\big) = \left. \frac{\partial^2 \big[\epsilon_{\mathrm{xc}}(n, |\mathbf{m}|)n\big]}{\partial n^{\tau_1} \partial n^{\tau_2}} \right|_{n=n(\mathbf{r}), \mathbf{m}=\mathbf{m}(\mathbf{r})}. \tag{3.36}$$

In particular, if the there is no transverse magnetization in the ground state, $n^x(\mathbf{r}) = n^y(\mathbf{r}) = 0$, the transverse LSDA kernel may be evaluated directly from the effective spin-polarizing field:

$$f_{\mathrm{LSDA}}^{-+}\big(n(\mathbf{r}), n^z(\mathbf{r})\big) = \frac{2W_{\mathrm{xc,LSDA}}^z\big(n(\mathbf{r}), n^z(\mathbf{r})\big)}{n^z(\mathbf{r})}. \tag{3.37}$$

3.5 Transverse magnetic susceptibility with LR-TDDFT

For the work leading to this thesis, the transverse magnetic susceptibility is computed in a collinear approximation only. In the nonrelativistic limit, the four-component susceptibility tensor becomes block diagonal,

$$\chi^{[0,+,-,z]} = \begin{pmatrix} \chi^{00} & 0 & 0 & \chi^{0z} \\ 0 & 0 & \chi^{+-} & 0 \\ 0 & \chi^{-+} & 0 & 0 \\ \chi^{z0} & 0 & 0 & \chi^{zz} \end{pmatrix}, \tag{3.38}$$

and for collinear ground states, the transverse magnetic susceptibility decouples from the remaining components of the Dyson equation (3.28), see e.g. [A]. Using the transverse LSDA kernel (3.37), one is thus left with a single Dyson equation to invert:

$$\chi^{+-}(\mathbf{r},\mathbf{r}',\omega) = \chi_{\mathrm{KS}}^{+-}(\mathbf{r},\mathbf{r}',\omega) + \int d\mathbf{r}_1\, \chi_{\mathrm{KS}}^{+-}(\mathbf{r},\mathbf{r}_1,\omega) f_{\mathrm{LSDA}}^{-+}(\mathbf{r}_1) \chi^{+-}(\mathbf{r}_1,\mathbf{r}',\omega). \tag{3.39}$$

In the computer implementation developed for this thesis, the Dyson equation is inverted as a simple matrix equation in the plane wave basis:

$$\chi_{[\mathbf{G}]}^{+-}(\mathbf{q},\omega) = \left(1 - \chi_{\mathrm{KS}}^{+-}(\mathbf{q},\omega) f_{\mathrm{LSDA}}^{-+}\right)_{[\mathbf{G}]}^{-1} \chi_{\mathrm{KS},[\mathbf{G}]}^{+-}(\mathbf{q},\omega). \tag{3.40}$$

The computationally most expensive step is therefore to compute the Kohn-Sham plane wave susceptibility, which for a collinear ground state is given by [A]

$$\chi_{\mathrm{KS},\mathbf{GG}'}^{+-}(\mathbf{q},\omega) = \lim_{\eta \to 0^+} \frac{1}{\Omega} \sum_{\mathbf{k}} \sum_{n,m} (f_{n\mathbf{k}\uparrow} - f_{m\mathbf{k}+\mathbf{q}\downarrow})$$
$$\times \frac{n_{n\mathbf{k}\uparrow,m\mathbf{k}+\mathbf{q}\downarrow}(\mathbf{G}+\mathbf{q})\, n_{m\mathbf{k}+\mathbf{q}\downarrow,n\mathbf{k}\uparrow}(-\mathbf{G}'-\mathbf{q})}{\hbar\omega - (\epsilon_{m\mathbf{k}+\mathbf{q}\downarrow} - \epsilon_{n\mathbf{k}\uparrow}) + i\hbar\eta}, \tag{3.41}$$

where spin now is included in the state index, see Equation (2.36). The collinear Kohn-Sham reciprocal space pair densities are readily calculated from the unit cell normalized Kohn-Sham orbitals,

$$n_{n\mathbf{k}s,m\mathbf{k}+\mathbf{q}s'}(\mathbf{G}+\mathbf{q}) = \int_{\Omega_{\mathrm{cell}}} d\mathbf{r}\, e^{-i(\mathbf{G}+\mathbf{q})\cdot\mathbf{r}} \psi_{n\mathbf{k}s}^*(\mathbf{r}) \psi_{m\mathbf{k}+\mathbf{q}s'}(\mathbf{r}), \tag{3.42}$$

such that the dynamic transverse magnetic susceptibility can be computed based on properties of the time-independent Kohn-Sham system alone.

3.6 Further reading

This chapter concludes the theoretical background for the main project of this thesis: Computing transverse magnetic excitation spectra from first principles. In Publication [A], an extensive theoretical treatment of the four-component susceptibility tensor can be found, focusing particularly on the calculation of the transverse magnetic susceptibility within LR-TDDFT. Therefore, it might benefit the reader at this point to consult Section II of the paper, named "Theoretical magnon spectroscopy". The section starts at page 38 of this thesis.

Methodology: Transverse magnetic susceptibility in the PAW method

To enable the computation of magnon spectra from first principles, we have developed a transverse magnetic susceptibility module for the linear response implementation [67] in the open-source GPAW electronic structure code [37, 38]. In this module, $\chi^{+-}_{\mathbf{GG'}}(\mathbf{q}, \omega)$ can be calculated within the projector augmented-wave (PAW) method [39] using the ALDA xc kernel. The details of the implementation are thoroughly described in Publication [A], which also documents the magnon dispersion convergence for the itinerant ferromagnets Fe, Ni and Co with respect to the key computational parameters.

The major achievement of the implementation is, that we are able to demonstrate strict convergence of the magnon dispersion relation. Because the PAW method is formally exact and that the plane wave basis in the limit of an infinite plane wave cutoff is complete, our results are without loss in generality up to the limitations of the actual PAW setups. For this reason, we consider our methodology to be ideal for benchmarking the performance of ALDA LR-TDDFT for theoretical magnon spectroscopy.

Instead of reiterating the computational details and convergence study of our method paper, we will instead use the present chapter to highlight the essential novelties of the method development, without which absolute convergence could not have been achieved. In this way, the reader is provided with a look "under the hood" and hopefully also some benefit of hindsight. For the remainder of the chapter, we will therefore assume that the reader is familiar with the content of Section III of Publication [A], named "Computational implementation". The section starts on page 43 of this thesis.

4.1   Plane wave expansion of the ALDA kernel

The major numerical difficulty associated with computing plane wave susceptibilities within the LR-TDDFT framework is, perhaps to some surprise, performing spatial Fourier transforms. In the PAW method such steps are separated into two: (1) Fourier transforming the smooth contribution to a quantity due to the pseudowaves and (2) Fourier transforming the PAW correction. The first is easy enough. Smooth quantities such as the smooth pair densities $\tilde{n}_{n\mathbf{k}s,m\mathbf{k}+\mathbf{q}s'}(\mathbf{r})$ and the smooth LSDA kernel

$f_{\text{LSDA}}^{-+}\big(\tilde{n}(\mathbf{r}), \tilde{n}^z(\mathbf{r})\big)$ can be represented effectively on a regular real space grid and fast-fourier-transformed to reciprocal space. However, this is not the case for the PAW corrections, which need fine-grained evaluation inside the augmentation spheres of each atom in the unit cell.

In the original response implementation [67], the PAW correction for the reciprocal space kernel was evaluated by point integrating the Fourier transform inside the augmentation sphere of each atom a:

$$\Delta f_{\text{LSDA}}^{a,-+}(\mathbf{K}) = e^{-i\mathbf{K}\cdot\mathbf{R}_a} \int_0^{R_c^a} r^2 dr \int d\hat{\mathbf{r}}\, e^{-i\mathbf{K}\cdot r\hat{\mathbf{r}}} \Delta f_{\text{LSDA}}^{a,-+}(r\hat{\mathbf{r}}). \qquad (4.1)$$

For the radial part of the integration, a dense nonlinear grid was used, and for the angular degrees of freedom, a Lebedev quadrature of degree 11. On such a quadrature, angular integrals can be evaluated exactly for polynomials up to order 11. This is of course very impressive, but the problem is, that the plane wave components $e^{-i\mathbf{K}\cdot r\hat{\mathbf{r}}}$ rapidly breaks the polynomial order, and already for plane wave components at a cutoff of 225 eV, the integration becomes imprecise for $r > a_0$.

Of course, one could then use a progressively more dense angular grid with increasing locality of the plane wave components. However, to obtain a scalable implementation, we instead take advantage of the fact that the kernel correction itself, $\Delta f_{\text{LSDA}}^{a,-+}(r\hat{\mathbf{r}})$, does not break the polynomial order. Thus, it is straight-forward to represent the kernel in terms of real spherical harmonics, which can be Fourier transformed analytically. Furthermore, this strategy is also consistent with the original implementation of the the pair density PAW corrections [67].

4.2 Convergence of the Kohn-Sham Stoner continuum

When we compute the Kohn-Sham susceptibility (3.41), the summation over k-points is performed by means of point integration using a finite broadening parameter η. However, as we show in great detail in Publication [A], this makes it a significant challenge to obtain a strict convergence of the low frequency Stoner continuum, and thus the magnon dispersion of itinerant magnets in turn.

The main difficulty arises, because the k-point grid density and broadening parameter η cannot be chosen independently. Essentially, the broadening parameter η defines a minimal k-point density needed to converge the Stoner continuum, while η should also be chosen small enough as not to influence the magnon dispersion. In fact, we find that a choice of $\eta \leq 50$ meV is needed for a reliable benchmark of the magnon dispersion in Fe, Ni and Co. However, overcoming this difficulty was worth the effort: It was only once we had a firm grasp on the Stoner continuum convergence, that we actually were able to demonstrate convergence of the magnon dispersion with a finite plane wave basis cutoff.

To evaluate the convergence of the Stoner continuum, we compare the spectrum of differently aligned k-point grids with the same k-point density. To be as transparent as possible, we introduce a quantitative heuristic for the convergence of the low

frequency Stoner continuum, namely the average frequency displacement $\langle \Delta \omega \rangle$. The low frequency spectrum is then considered fully converged, if $\langle \Delta \omega \rangle \leq 5$ meV for a given k-point density and broadening η. In general, we believe that it is healthy to have a quantitative measure of Kohn-Sham spectrum convergence for the purpose of benchmark studies. However, for more general studies, where the convergence criteria can be relaxed a bit, it would in most cases be sufficient simply to conduct a visual comparison of the Kohn-Sham spectra at different grid alignments.

At this point, it is important to stress, that a strict convergence of the Kohn-Sham spectra using the presented methodology is a costly affair. We end up using k-point grid densities of 23-29 Å, which makes the evaluation of magnon spectra a computationally very demanding task, even for mono-atomic systems. Going forward, one should therefore strongly consider to implement more advanced methodology in order to lower the k-point density demand for obtaining converged spectra at a given broadening η. In this regard, both the techniques of analytic continuation and linear tetrahedron interpolation have previously been proved effective [18, 19].

4.3   Gap error corrections

Whereas the spin rotational symmetry in the nonrelativistic limit physically implies the existence of a gapless acoustic magnon mode, this is well-known not to be guaranteed within the numerical approximations of an actual LR-TDDFT implementation [18, 28, 30]. Indeed, it seems from our results, that one would need an infinite plane wave basis in order to converge the gap error ω_Γ. Our strategy to circumvent this issue is a simple one. We simply apply a rigid shift to the magnon dispersion, such that $\omega_{\mathbf{q=0}} = 0$ independently of the numerical parameters. This is trivially an exact procedure in the limit of vanishing numerical approximations, and we can take the converged magnon dispersion calculated this way as numerically accurate. For this reason, it is not a trivial result, that we find the magnon dispersion to converge with a finite number of bands and a finite plane wave cutoff. Rather, it means that a gap error correction scheme *can* be accurate, even though the gap error itself is finite.

CHAPTER 5

Results: Magnons in itinerant ferromagnets

Using the implemented methodology, we have studied the transverse magnetic excitations in the itinerant ferromagnets Fe, Ni, Co (fcc/hcp) and MnBi, with results documented in Publications [A] and [B]. Whereas, the ferromagnets Fe, Ni and Co have been thoroughly studied in previous literature and serve more as a benchmark for our computational implementation, the permanent magnet candidate MnBi has not previously been studied by the means of theoretical magnon spectroscopy. Scientifically, MnBi is furthermore an interesting system to study due to its pronounced correlation effects, despite being a metal.

In this chapter and the next, we will rely heavily on the publications of the thesis to present the results and conclusions from our studies. In the main body of the text, we will instead briefly summarize major results and add a bit of discussion in regards to the overall scope of the project.

5.1 Publication A: Dynamic transverse magnetic susceptibility in the projector augmented-wave method: Application to Fe, Ni, and Co

In Publication [A], we manage to reproduce the conclusions from previous theoretical accounts [18, 25, 27, 30, 31, 33] of the general agreement between theoretical ALDA results and the experimentally observed magnon dispersion of basic itinerant ferromagnets. For Fe and hcp-Co, the comparison to experiment is good, for fcc-Co it is excellent, but for fcc-Ni, ALDA fails to reproduce the experimental dispersion. The shortcoming in the case of Ni is, at least in part, due to the exchange splitting being overestimated by a factor of two in LDA [25]. Therefore, in order to theoretically reproduce experimental dispersion relations consistently, or just to match the fcc-Ni dispersion in particular, approximations beyond the ALDA are needed. However, it is neither sufficient to apply a Hubbard correction to the ground state functional nor to add a gradient correction in the adiabatic approximation [25, 31]. On the contrary, both extensions to the LDA actually increase the magnon bandwidth, opposite of the desired trend. Instead, it has been proposed to look towards nonlocal effects in the xc kernel [68]. This gives reason to hope that the new class of nonlocal xc functionals and

kernels which is presented in Chapter 8 could possibly improve the correspondence
with experiment. However, the development is still at a very early stage, far from
actual testing for the use within theoretical magnon spectroscopy.

In Publication [A], we also discuss similarities and differences between the (A)LDA
magnon dispersions resulting from different implementations. In general, all implemen-
tations, including ours, yield similar dispersion relations in the long wavelength $\mathbf{q} \rightarrow \mathbf{0}$
limit, where the magnons are undamped. However, there is only a qualitative agree-
ment of results for Landau damped magnon branches inside the Stoner continuum. We
believe that the main source of discrepancies in this regard are derived from the un-
derlying DFT ground states, maybe with some influence from the gap error correction
schemes as well. Despite the quantitative discrepancies inside the Stoner continuum,
there is a good qualitative agreement between the methods, when it comes to the
itinerant magnon effects observed in the spectra. Especially in Fe and Ni there are
pronounced effects of itinerancy, such as stripe-like Stoner pair features, coexistence of
multiple magnon modes and disappearance of the collective magnon mode. Especially
in the case of Fe, it would be of fundamental interest to experimentally investigate
the short wavelength magnon excitations in more detail, to see if the itinerant electron
effects predicted with the ALDA can be directly observed in actual experiments.

On the next pages, Publication [A] is printed in copy. If the reader has followed
the chronology of the thesis, taking the given suggestions for individual paper passages
to read, the reader will already be familiar with Sections II and III, as well as the
appendix of the paper. Upon reading the introduction of the paper, the reader might
therefore want to jump directly to Section IV, named "Results". This section starts at
page 53 of the thesis.

Dynamic transverse magnetic susceptibility in the projector augmented-wave method: Application to Fe, Ni, and Co

Thorbjørn Skovhus ® and Thomas Olsen ®*

CAMD, Department of Physics, Technical University of Denmark, 2800 Kgs. Lyngby, Denmark

We present a first principles implementation of the dynamic transverse magnetic susceptibility in the framework of linear response time-dependent density functional theory. The dynamic susceptibility allows one to obtain the magnon dispersion as well as magnon lifetimes for a particular material, which strongly facilitates the interpretation of inelastic neutron scattering experiments as well as other spectroscopic techniques. We apply the method to Fe, Ni, and Co and perform a thorough convergence analysis with respect to the basis set size, k-point sampling, spectral smearing, and unoccupied bands. In particular, it is shown that while the gap error (acoustic magnon energy at $\mathbf{q} = \mathbf{0}$) is highly challenging to converge, the spin-wave stiffness and the dispersion relation itself are much less sensitive to convergence parameters. Our final results agree well with experimentally extracted magnon dispersion relations except for Ni, where it is well known that the exchange splitting energy is poorly represented in the local density approximation. We also find good agreement with previous first principles calculations and explain how differences in the calculated dispersion relations can arise from subtle differences in computational approaches.

I. INTRODUCTION

The dynamic transverse magnetic susceptibility is a central object of interest in the study of magnetic excitations. It is a fundamental material property giving the induced transverse magnetization in response to external perturbations such as transverse magnetic fields. In particular, the susceptibility has poles at frequencies corresponding to the magnon quasiparticle excitations of the material. Magnons are relevant for both theoretical development and technological applications. They have been proposed to play a role in the pairing mechanism of certain classes of high-temperature superconductors [1,2] and may possibly be used as a medium for data communication and processing in future magnonics-based information technology devices [3]. Moreover, a wide range of thermodynamical properties, such as the heat capacity and Curie/Néel temperature, are directly related to the temperature dependence of the susceptibility [4].

Experimentally, the transverse magnetic susceptibility can be directly probed by, or at least inferred from, a wide range of different spectroscopic techniques including inelastic neutron scattering (INS) [5,6], spin-polarized electron energy loss spectroscopy (SPEELS) [7,8], inelastic scanning tunneling spectroscopy (ISTS) [9–11], and resonant inelastic x-ray spectroscopy (RIXS) [12]. From the measured magnon dispersion, it is possible to extract valuable information about the underlying quantum system. The interpretation and analysis needed to accomplish this often rely on theoretical calculations—based on either models or a first principles treatment.

From a computational point of view, calculating the magnon dispersion poses a major challenge due to the many-

body nature of collective magnetic excitations. For first principles calculations there essentially exist two different approaches for obtaining the linear dynamic susceptibility: (1) many-body perturbation theory where the susceptibility is obtained by solving a Bethe-Salpeter equation [13–18] and (2) time-dependent density functional theory (TDDFT) [19–21], which (although exact in principle) is limited by approximations for the applied exchange-correlation kernel. Both of these methods are restricted to $T = 0$ and thermodynamical properties are currently inaccessible by direct *ab initio* methods. Nevertheless, the $T = 0$ limit of the susceptibility provides fundamental insight into the magnetic properties of a given material and one can directly extract the magnon spectrum from it. In this paper, we present an implementation of the transverse magnetic susceptibility within linear response time-dependent density functional theory (LR-TDDFT) [19–22] in the projected augmented wave method (PAW) [23]. Applying the adiabatic local density approximation (ALDA) for the exchange-correlation kernel, we study the magnon spectrum of itinerant ferromagnets iron, nickel, and cobalt. The extracted magnon dispersions agree well with experimental results, except for the case of fcc-Ni, where LDA is known to overestimate the exchange splitting energy by a factor of two [15].

Through a rigorous convergence analysis, we address some of the general computational challenges in performing theoretical magnon spectroscopy on itinerant ferromagnets. We neglect spin-obit effects in our calculations, which implies the existence of a gapless acoustic magnon mode with $\omega_{\mathbf{q}=\mathbf{0}} = 0$. The gapless mode is fundamentally protected by symmetry, but in a numerical treatment the vanishing gap is not protected against numerical inconsistencies or general numerical limitations such as truncation of basis sets or electronic bands. Through a systematic convergence analysis, we pinpoint

*tolsen@fysik.dtu.dk

contributions to the gap error from different computational parameters and show that the problem can be effectively overcome by applying a gap error correction procedure. This conclusion validates the common practice in the literature [24–27]. Furthermore, we discuss the convergence of magnon modes inside the Stoner continuum, the transverse magnetic continuum of single-particle excitations. Overlap with the Stoner continuum gives rise to Landau damping of the collective magnon modes, which manifests itself as a broadening in the magnon line shape. From a numerical perspective, the treatment of Landau damped magnons is particularly challenging as they require a good continuum description of the low-frequency Stoner excitations. In this regard, we present an empirical convergence parameter, which directly allows one to extract the minimal spectral broadening required to smoothen out the low-frequency Stoner excitations of a given k-point sampling.

The paper is organized as follows. In Sec. II the dynamic transverse magnetic susceptibility is formally introduced and its relation to quasiparticle excitations discussed. The LR-TDDFT methodology is presented, and it is shown how one can compute the dynamic transverse magnetic susceptibility within the ALDA. In Secs. III A–III C the technical details of the implementation within the PAW method are given, and in Secs. III D–III G the convergence analysis of the implementation is provided. The converged transverse magnetic excitation spectra of bcc-Fe, fcc-Ni, fcc-Co, and hcp-Co are presented and discussed in Sec. IV. Finally, a summary and outlook are given in Sec. V. The general theoretical framework applied throughout the paper is complemented by Appendix A, which provides a self-contained presentation of the *Kubo theory* for spectroscopy in periodic crystals.

II. THEORETICAL MAGNON SPECTROSCOPY

In this section, the fundamentals of theoretical magnon spectroscopy are presented. The transverse magnetic plane wave susceptibility is introduced as the central macroscopic quantity of interest, its connection with magnon quasiparticles is discussed, and it is shown how to compute it within LR-TDDFT. Finally, the Goldstone theorem and sum rules are discussed.

Throughout the main body of the paper, the Born-Oppenheimer approximation is employed, and only the linear response in electronic coordinates is considered. Furthermore, zero temperature is assumed, and contributions from the orbital magnetization are neglected.

A. The four-component susceptibility tensor

For an electronic Hamiltonian, $\hat{H}_0$, the magnetic response (neglecting contributions from orbital magnetization) may be described in terms of the four-component electron density operator

$$\hat{n}^{\mu}(\mathbf{r}) = \sum_{s,s'} \sigma^{\mu}_{ss'} \hat{\psi}^{\dagger}_{s}(\mathbf{r}) \hat{\psi}_{s'}(\mathbf{r}), \tag{1}$$

with $\mu \in \{0, x, y, z\}$. The index s indicates the spin projection, $\uparrow$ or $\downarrow$, and $\sigma^{\mu} = (\sigma^0, \sigma^x, \sigma^y, \sigma^z)$ is composed of the Pauli matrices augmented by the 2×2 identity matrix σ^0. The

electron density degrees of freedom are perturbed by an external (classical) electromagnetic field:

$$\hat{H}_{\text{ext}}(t) = \sum_{\mu} \int d\mathbf{r} \, \hat{n}^{\mu}(\mathbf{r}) W^{\mu}_{\text{ext}}(\mathbf{r}, t), \tag{2a}$$

$$\begin{aligned}
\left(W^{\mu}_{\text{ext}}(\mathbf{r}, t) \right) &= \left(V^{\mu}_{\text{ext}}(\mathbf{r}, t), \mathbf{W}^{\mu}_{\text{ext}}(\mathbf{r}, t) \right) \\
&= \left(-e\phi_{\text{ext}}(\mathbf{r}, t), \, \mu_{\text{B}} \mathbf{B}_{\text{ext}}(\mathbf{r}, t) \right),
\end{aligned} \tag{2b}$$

where $-e$ is the electron charge, μ_{B} is the Bohr magneton, while $\phi_{\text{ext}}(\mathbf{r}, t)$ and $\mathbf{B}_{\text{ext}}(\mathbf{r}, t)$ are the external scalar potential and magnetic field, respectively. The response to the perturbation (2) may be quantified in terms of the change in four-component density, $\delta n^{\mu}(\mathbf{r}, t) = \langle \hat{n}^{\mu}(\mathbf{r}, t) \rangle - \langle \hat{n}^{\mu}(\mathbf{r}) \rangle_0$, where $\langle \cdot \rangle_0$ denotes the expectation value with respect to the unperturbed ground state [see also Eqs. (A1) and (A2)]. To linear order in the perturbing field, the induced density can be written formally as

$$\delta n^{\mu}(\mathbf{r}, t) = \sum_{\nu} \int_{-\infty}^{\infty} dt' \int d\mathbf{r}' \, \chi^{\mu\nu}(\mathbf{r}, \mathbf{r}', t - t') W^{\nu}_{\text{ext}}(\mathbf{r}', t'). \tag{3}$$

This equation defines the retarded four-component susceptibility tensor $\chi^{\mu\nu}$, which fully characterizes the linear response of the system.

The susceptibility may be calculated from the *Kubo formula* [Eq. (A3)]:

$$\chi^{\mu\nu}(\mathbf{r}, \mathbf{r}', t - t') = -\frac{i}{\hbar} \theta(t - t') \left\langle \left[\hat{n}^{\mu}_0(\mathbf{r}, t), \hat{n}^{\nu}_0(\mathbf{r}', t') \right] \right\rangle_0, \tag{4}$$

in which the four-component density operators carry the time-dependence of the interaction picture, $\hat{n}^{\mu}_0(\mathbf{r}, t) \equiv e^{i\hat{H}_0 t/\hbar} \hat{n}^{\mu}(\mathbf{r}) e^{-i\hat{H}_0 t/\hbar}$. In the frequency domain, one may express the susceptibility in terms of the system eigenstates, $\hat{H}_0 |\alpha\rangle = E_{\alpha} |\alpha\rangle$, that is, within the Lehmann representation [see Eqs. (A4) and (A7)]

$$\begin{aligned}
\chi^{\mu\nu}(\mathbf{r}, \mathbf{r}', \omega) = \lim_{\eta \to 0^+} \sum_{\alpha \neq \alpha_0} \Bigg[& \frac{n^{\mu}_{0\alpha}(\mathbf{r}) n^{\nu}_{\alpha 0}(\mathbf{r}')}{\hbar\omega - (E_{\alpha} - E_0) + i\hbar\eta} \\
& - \frac{n^{\nu}_{0\alpha}(\mathbf{r}') n^{\mu}_{\alpha 0}(\mathbf{r})}{\hbar\omega + (E_{\alpha} - E_0) + i\hbar\eta} \Bigg].
\end{aligned} \tag{5}$$

Here $|\alpha_0\rangle$ and E_0 denote the ground state and ground state energy, respectively. Thus, the dynamic four-component susceptibility tensor is comprised of simple poles at excitation energies $\hbar\omega = E_{\alpha} - E_0$, each weighted by the transition matrix elements $n^{\mu}_{0\alpha}(\mathbf{r}) = \langle \alpha_0 | \hat{n}^{\mu}(\mathbf{r}) | \alpha \rangle$ and $n^{\nu}_{\alpha 0}(\mathbf{r}') = \langle \alpha | \hat{n}^{\nu}(\mathbf{r}') | \alpha_0 \rangle$.

In order to further illustrate the physics embedded in the four-component susceptibility tensor, a single frequency component is considered, $W^{\mu}_{\text{ext}}(\mathbf{r}, t) = W^{\mu}_{\text{ext}}(\mathbf{r}) \cos(\omega_0 t)$. In this case, the real and imaginary parts of the dynamic susceptibility determine the in- and out-of-phase response, respectively [see Eq. (A15)]:

$$\begin{aligned}
\delta n^{\mu}(\mathbf{r}, t) = \sum_{\nu} \int d\mathbf{r}' \, \{ &\text{Re}[\chi^{\mu\nu}(\mathbf{r}, \mathbf{r}', \omega_0)] \cos(\omega_0 t) \\
& + \text{Im}[\chi^{\mu\nu}(\mathbf{r}, \mathbf{r}', \omega_0)] \sin(\omega_0 t) \} W^{\nu}_{\text{ext}}(\mathbf{r}').
\end{aligned} \tag{6}$$

Here it was used that the four-component density operator is Hermitian, $\hat{n}^{\mu}(\mathbf{r})^{\dagger} = \hat{n}^{\mu}(\mathbf{r})$, such that $\chi^{\mu\nu}(\mathbf{r}, \mathbf{r}', -\omega) = $

$\chi^{\mu\nu*}(\mathbf{r}, \mathbf{r}', \omega)$ [see Eq. (A14)]. The rate of energy absorption into the system under the perturbation (2) is given by $Q = d\langle \hat{H} \rangle / dt$, and from (6) it then follows, that only the out-of-phase response contributes to the energy dissipation on average [see Eq. (A16)]:

$$\bar{Q} = -\frac{\omega_0}{2} \sum_{\mu,\nu} \iint d\mathbf{r} d\mathbf{r}' \, W_{\text{ext}}^{\mu}(\mathbf{r})$$

$$\times \text{Im}[\chi^{\mu\nu}(\mathbf{r}, \mathbf{r}', \omega_0)] W_{\text{ext}}^{\nu}(\mathbf{r}'). \quad (7)$$

Now, instead of using $\chi^{\mu\nu}(\mathbf{r}, \mathbf{r}', -\omega) = \chi^{\mu\nu*}(\mathbf{r}, \mathbf{r}', \omega)$ to express the mean rate of energy absorption in terms of the imaginary part of $\chi^{\mu\nu}$, one may instead interchange summation and integration variables, such that it becomes expressed in terms of the dissipative (anti-symmetric) part instead. This is advantageous, because the dissipative part of $\chi^{\mu\nu}$ [defined in Eq. (A5c)] is proportional to the spectral function of induced excitations [see Eqs. (A8) and (A9)]

$$S^{\mu\nu}(\mathbf{r}, \mathbf{r}', \omega) \equiv -\frac{1}{2\pi i}[\chi^{\mu\nu}(\mathbf{r}, \mathbf{r}', \omega) - \chi^{\nu\mu}(\mathbf{r}', \mathbf{r}, -\omega)] \quad (8a)$$

$$= A^{\mu\nu}(\mathbf{r}, \mathbf{r}', \omega) - A^{\nu\mu}(\mathbf{r}', \mathbf{r}, -\omega), \quad (8b)$$

where

$$A^{\mu\nu}(\mathbf{r}, \mathbf{r}', \omega) \equiv \sum_{\alpha \neq \alpha_0} n_{0\alpha}^{\mu}(\mathbf{r}) n_{\alpha 0}^{\nu}(\mathbf{r}') \, \delta(\hbar\omega - (E_\alpha - E_0)). \quad (9)$$

Using these definitions,

$$\bar{Q} = \frac{\pi \omega_0}{2} \sum_{\mu,\nu} \iint d\mathbf{r} \, d\mathbf{r}' \, W_{\text{ext}}^{\mu}(\mathbf{r}) S^{\mu\nu}(\mathbf{r}, \mathbf{r}', \omega_0) W_{\text{ext}}^{\nu}(\mathbf{r}'). \quad (10)$$

In this way, Eqs. (8), (9), and (10) comprise the linear response formulation of the fact, that energy dissipation is directly governed by the spectrum of induced excitations. This also illustrates the direct connection to Fermi's golden rule.

B. The four-component susceptibility tensor in circular coordinates

In a collinear description, magnons are collective quasiparticles carrying a unit of spin angular momentum. With the ground state magnetization aligned along the z-axis ($\mathbf{m}(\mathbf{r}) = \langle \hat{n}^z(\mathbf{r}) \rangle_0 \mathbf{e}_z$), they are generated by the spin-raising and spin-lowering operators,

$$\hat{n}^+(\mathbf{r}) = \frac{1}{2}[\hat{n}^x(\mathbf{r}) + i\hat{n}^y(\mathbf{r})] = \hat{\psi}_\uparrow^\dagger(\mathbf{r})\hat{\psi}_\downarrow(\mathbf{r}), \quad (11)$$

$$\hat{n}^-(\mathbf{r}) = \frac{1}{2}[\hat{n}^x(\mathbf{r}) - i\hat{n}^y(\mathbf{r})] = \hat{\psi}_\downarrow^\dagger(\mathbf{r})\hat{\psi}_\uparrow(\mathbf{r}), \quad (12)$$

which flip the spin of a spin-down and a spin-up electron at position $\mathbf{r}$, respectively. In terms of the external electromagnetic field, spin-raising and spin-lowering excitations are induced by the circular components

$$W_{\text{ext}}^{\pm}(\mathbf{r}, t) = W_{\text{ext}}^x(\mathbf{r}, t) \pm i \, W_{\text{ext}}^y(\mathbf{r}, t), \quad (13)$$

such that the perturbation from Eq. (2) can be written

$$\hat{H}_{\text{ext}}(t) = \int d\mathbf{r} \left[\hat{n}(\mathbf{r}) V_{\text{ext}}(\mathbf{r}, t) + \hat{n}^+(\mathbf{r}) W_{\text{ext}}^-(\mathbf{r}, t) \right.$$

$$\left. + \hat{n}^-(\mathbf{r}) W_{\text{ext}}^+(\mathbf{r}, t) + \hat{\sigma}^z(\mathbf{r}) W_{\text{ext}}^z(\mathbf{r}, t) \right]$$

$$= \int d\mathbf{r} \sum_j \hat{n}^j(\mathbf{r}) \breve{W}_{\text{ext}}^j(\mathbf{r}, t), \quad (14)$$

where $j \in \{0, +, -, z\}$ and the breve accent is introduced to reverse the ordering of $+$ and $-$ components $(\breve{W}^j) = (V, W^-, W^+, W^z)$. Using the relations (11) and (12), one may also write the four-component susceptibility tensor in circular coordinates, where χ^{jk} is given by the *Kubo formula* of Eq. (4). For example, one obtains

$$\chi^{x0} = \chi^{+0} + \chi^{-0},$$

$$\chi^{xx} = \chi^{++} + \chi^{+-} + \chi^{-+} + \chi^{--},$$

$$\chi^{xy} = -i\chi^{++} + i\chi^{+-} - i\chi^{-+} + i\chi^{--},$$

$$\chi^{xz} = \chi^{+z} + \chi^{-z}, \quad (15)$$

where the spatial and temporal arguments have been suppressed. Rewriting Eq. (3) in this manner yields the response relation in circular coordinates:

$$\delta n^j(\mathbf{r}, t) = \sum_k \int_{-\infty}^{\infty} dt' \int d\mathbf{r}' \, \chi^{jk}(\mathbf{r}, \mathbf{r}', t - t') \breve{W}_{\text{ext}}^k(\mathbf{r}', t'). \quad (16)$$

It should be noted that the circular components satisfy $\chi^{-+}(\mathbf{r}, \mathbf{r}', -\omega) = \chi^{+-*}(\mathbf{r}, \mathbf{r}', \omega)$.

If the system is collinear, such that the total electronic spin projection in the z-direction, S_z, can be taken as a good quantum number, the products of transition matrix elements

$$n_{0\alpha}^j(\mathbf{r}) n_{\alpha 0}^k(\mathbf{r}') = \langle \alpha_0 | \hat{n}^j(\mathbf{r}) | \alpha \rangle \langle \alpha | \hat{n}^k(\mathbf{r}') | \alpha_0 \rangle \quad (17)$$

vanish if $\hat{n}^j(\mathbf{r}) \hat{n}^k(\mathbf{r}')$ results in a net change of S_z. Consequently, several of the components vanish from the Lehmann representation (5) for χ^{jk}, and the tensor becomes block diagonal:

$$\chi^{[0,+,-,z]} = \begin{pmatrix} \chi^{00} & 0 & 0 & \chi^{0z} \\ 0 & 0 & \chi^{+-} & 0 \\ 0 & \chi^{-+} & 0 & 0 \\ \chi^{z0} & 0 & 0 & \chi^{zz} \end{pmatrix}, \quad (18)$$

$$\chi^{[0,x,y,z]} = \begin{pmatrix} \chi^{00} & 0 & 0 & \chi^{0z} \\ 0 & \chi^{+-} + \chi^{-+} & i\chi^{+-} - i\chi^{-+} & 0 \\ 0 & -i\chi^{+-} + i\chi^{-+} & \chi^{+-} + \chi^{-+} & 0 \\ \chi^{z0} & 0 & 0 & \chi^{zz} \end{pmatrix}. \quad (19)$$

Thus, in the collinear case, the transverse magnetic response is completely decoupled from the longitudinal magnetic response, given by χ^{zz}, and the longitudinal dielectric response, given by χ^{00}:

$$\delta n^+(\mathbf{r}, t) = \int_{-\infty}^{\infty} dt' \int d\mathbf{r}' \chi^{+-}(\mathbf{r}, \mathbf{r}', t - t') W_{\text{ext}}^+(\mathbf{r}', t'), \quad (20a)$$

$$\delta n^-(\mathbf{r}, t) = \int_{-\infty}^{\infty} dt' \int d\mathbf{r}' \chi^{-+}(\mathbf{r}, \mathbf{r}', t - t') W_{\text{ext}}^-(\mathbf{r}', t'). \quad (20b)$$

For a spin-paired (nonmagnetic) collinear ground state, spin-rotational symmetry implies that $\chi^{xx} = \chi^{yy} = \chi^{zz}$, but also that $\chi^{xy} = \chi^{zx}$, $\chi^{z0} = \chi^{x0}$ and $\chi^{0z} = \chi^{0x}$ where all the latter terms vanish as argued in Eq. (19). Thus, the magnetic response is fully characterized by χ^{zz} for nonmagnetic systems [28].

C. The spectrum of transverse magnetic excitations

In periodic crystals, the linear response of a material may be characterized by the four-component plane wave susceptibility, which is defined in terms of the lattice Fourier transform [see Eq. (A28)]:

$$\chi_{\mathbf{GG'}}^{\mu\nu}(\mathbf{q},\omega) \equiv \iint \frac{d\mathbf{r}\,d\mathbf{r'}}{\Omega} e^{-i(\mathbf{G}+\mathbf{q})\cdot\mathbf{r}} \chi^{\mu\nu}(\mathbf{r},\mathbf{r'},\omega) e^{i(\mathbf{G'}+\mathbf{q})\cdot\mathbf{r'}}$$

$$= \lim_{\eta\to 0^+} \frac{1}{\Omega} \sum_{\alpha\neq\alpha_0} \left[\frac{n_{0\alpha}^{\mu}(\mathbf{G}+\mathbf{q})n_{\alpha 0}^{\nu}(-\mathbf{G'}-\mathbf{q})}{\hbar\omega - (E_\alpha - E_0) + i\hbar\eta} \right.$$

$$\left. - \frac{n_{0\alpha}^{\nu}(-\mathbf{G'}-\mathbf{q})n_{\alpha 0}^{\mu}(\mathbf{G}+\mathbf{q})}{\hbar\omega + (E_\alpha - E_0) + i\hbar\eta} \right]. \quad (21)$$

Here Ω is the crystal volume, $\mathbf{G}$ is a reciprocal lattice vector, and $\mathbf{q}$ is a wave vector within the first Brillouin zone (BZ). The reciprocal space pair densities $n_{\alpha\alpha'}^{\mu}(\mathbf{G}+\mathbf{q})$ are Fourier transforms of the spatial pair densities; see Eqs. (A32)–(A35). The plane wave susceptibility gives the linear order plane wave response $e^{i([\mathbf{G}+\mathbf{q}]\cdot\mathbf{r}-\omega t)}$ in density component μ to a plane wave perturbation $e^{i([\mathbf{G'}+\mathbf{q}]\cdot\mathbf{r}-\omega t)}$ in external field component ν [see Eq. (A31)]. The plane wave response is diagonal in reduced wave vector $\mathbf{q}$ due to the periodicity of the crystal [see Eq. (A29)].

In analogy with the real space response in Eqs. (8), (9), and (10), the energy dissipation in periodic crystals is governed by the dissipative part of $\chi_{\mathbf{GG'}}^{\mu\nu}(\mathbf{q},\omega)$, that is, the plane wave spectrum of induced excitations (A41)

$$S_{\mathbf{GG'}}^{\mu\nu}(\mathbf{q},\omega) = -\frac{1}{2\pi i}\left[\chi_{\mathbf{GG'}}^{\mu\nu}(\mathbf{q},\omega) - \chi_{-\mathbf{G'}-\mathbf{G}}^{\nu\mu*}(-\mathbf{q},-\omega)\right] \quad (22a)$$

$$= A_{\mathbf{GG'}}^{\mu\nu}(\mathbf{q},\omega) - A_{-\mathbf{G'}-\mathbf{G}}^{\nu\mu}(-\mathbf{q},-\omega), \quad (22b)$$

where

$$A_{\mathbf{GG'}}^{\mu\nu}(\mathbf{q},\omega) \equiv \frac{1}{\Omega} \sum_{\alpha\neq\alpha_0} n_{0\alpha}^{\mu}(\mathbf{G}+\mathbf{q})n_{\alpha 0}^{\nu}(-\mathbf{G'}-\mathbf{q})$$

$$\times \delta(\hbar\omega - (E_\alpha - E_0)). \quad (23)$$

For the reciprocal space pair densities $n_{0\alpha}^{\mu}(\mathbf{G}+\mathbf{q})$ to be nonzero, it is necessary that $\mathbf{q}_{\alpha 0} = \mathbf{q}$ [see Eq. (A34)]. Thus, only excited states with a difference in crystal momentum $\hbar\mathbf{q}$ with respect to the ground state have finite weight in the spectral function (23).

Equations (21), (22), and (23) also apply to the susceptibility tensor in circular coordinates, χ^{jk}. Because the spin-flip densities $\hat{n}^+(\mathbf{r})$ and $\hat{n}^-(\mathbf{r})$ are Hermitian conjugates, it follows that $\chi_{\mathbf{GG'}}^{+-*}(\mathbf{q},\omega) = \chi_{-\mathbf{G}-\mathbf{G'}}^{-+}(-\mathbf{q},-\omega)$ and consequently, the dissipative parts of $\chi^{\pm\mp}$ are also the imaginary parts along the diagonal:

$$S_{\mathbf{G}}^{+-}(\mathbf{q},\omega) \equiv S_{\mathbf{GG}}^{+-}(\mathbf{q},\omega) = -\frac{1}{\pi}\mathrm{Im}[\chi_{\mathbf{GG}}^{+-}(\mathbf{q},\omega)]$$

$$= A_{\mathbf{G}}^-(\mathbf{q},\omega) - A_{-\mathbf{G}}^+(-\mathbf{q},-\omega), \quad (24a)$$

$$S_{\mathbf{G}}^{-+}(\mathbf{q},\omega) = A_{\mathbf{G}}^+(\mathbf{q},\omega) - A_{-\mathbf{G}}^-(-\mathbf{q},-\omega), \quad (24b)$$

where the short-hand notation $A_{\mathbf{G}}^{\mp}(\mathbf{q},\omega) \equiv A_{\mathbf{GG}}^{\pm\mp}(\mathbf{q},\omega)$ has been introduced. From Eq. (23) it is clear that $A_{\mathbf{G}}^+(\mathbf{q},\omega)$ and $A_{\mathbf{G}}^-(\mathbf{q},\omega)$ are the spectral functions for spin-raising and spin-lowering magnetic excitations, respectively. These excitations may be associated with quasiparticles of energy $\hbar\omega$,

crystal momentum $\hbar\mathbf{q}$, and spin projections $\pm\hbar$. Depending on the character of the excitations, the quasiparticles are either identified as collective magnon quasiparticles, as single-particle electron-hole (Stoner) pairs, or something in between. Thus, for a ferromagnetic material assumed magnetized along the z-direction, one may read off the full spectrum of magnon excitations from the spectral function $S_{\mathbf{G}}^{+-}(\mathbf{q},\omega)$, with majority-to-minority magnons at positive frequencies and minority-to-majority magnons at negative frequencies.

Finally, the transverse magnetic excitation spectrum does not depend on the reduced wave vector $\mathbf{q}$ only, but also on the reciprocal lattice vector $\mathbf{G}$. The spin-flip pair densities in Eq. (23) represent the local field components of the change in spin orientation from the ground state to the excited state in question. Therefore, different excited states may be visible for different choices of $\mathbf{G}$. As an example, the macroscopic (unit-cell averaged) $\mathbf{G} = \mathbf{0}$ component represents a dynamic change to the magnetization, where the spin orientation at different magnetic atomic sites is precessing according to a long-range phase factor of $e^{i\mathbf{q}\cdot\mathbf{r}}$. This corresponds to an acoustic magnon mode, which will dominate the spectrum at small $\mathbf{q}$ and ω. Excited states where different magnetic atoms inside the unit cell precess with opposite phases will not be present in the macroscopic transverse magnetic excitation spectrum $S^{+-}(\mathbf{q},\omega)$, but in the local field components $\mathbf{G} \neq \mathbf{0}$ that match the spin structure of the given excited state.

D. Linear response time-dependent density functional theory

It is, in general, a prohibitively demanding task to diagonalize the many-body Hamiltonian $\hat{H}_0$ in order to find the eigenstates entering the susceptibility. However, within the framework of time-dependent density functional theory (TDDFT), it is possible to compute $\chi^{\mu\nu}$ without accessing the many-body eigenstates. In particular, it follows from the Runge-Gross theorem [21] that the time-dependent spin-density can be represented by an auxiliary noninteracting Kohn-Sham system defined by the Hamiltonian

$$\hat{H}_{\mathrm{KS}}(t) = \hat{T} + \hat{V}_{\mathrm{nuc}} + \hat{V}_{\mathrm{Hxc}}[n^\mu](t) + \hat{H}_{\mathrm{ext}}(t), \quad (25)$$

where $\hat{H}_{\mathrm{ext}}(t)$ is given by Eq. (2a) and

$$\hat{V}_{\mathrm{Hxc}}[n^\mu](t) = \sum_\mu \int d\mathbf{r}\, \hat{n}^\mu(\mathbf{r}) W_{\mathrm{Hxc}}^\mu[n^\mu](\mathbf{r},t). \quad (26)$$

Here $W_{\mathrm{Hxc}}^\mu(\mathbf{r},t)$ is the four-component time-dependent Hartree-exchange-correlation potential required to reproduce the time-dependent density of the interacting system. It is a functional of the four-component time-dependent density and is typically treated in the adiabatic approximation, where it is evaluated from a given approximation to the static exchange-correlation potential of the electron density at time t.

In the Kohn-Sham system, the induced density resulting from a small external perturbation $\delta W_{\mathrm{ext}}^\mu(\mathbf{r},t)$ can be written as

$$\delta n^\mu(\mathbf{r},t) = \sum_\nu \int_{-\infty}^{\infty} dt' \int d\mathbf{r'}\, \chi_{\mathrm{KS}}^{\mu\nu}(\mathbf{r},\mathbf{r'},t-t')\delta W_s^\nu(\mathbf{r'},t'),$$

$$(27)$$

where $\chi_{\mathrm{KS}}^{\mu\nu}$ is the noninteracting Kohn-Sham susceptibility and $\delta W_s^\mu = \delta W_{\mathrm{ext}}^\mu + \delta W_{\mathrm{Hxc}}^\mu$. Comparing with the response

relation (3) and using that the induced change in Hartree-exchange-correlation potential $\delta W_{\mathrm{Hxc}}^{\mu}$ is a functional of the induced density, one may derive the Dyson equation [22]:

$$
\chi^{\mu\nu}(\mathbf{r}, \mathbf{r}', \omega) = \chi_{\mathrm{KS}}^{\mu\nu}(\mathbf{r}, \mathbf{r}', \omega) + \sum_{\tau_1, \tau_2} \iint d\mathbf{r}_1\, d\mathbf{r}_2
$$
$$
\times\, \chi_{\mathrm{KS}}^{\mu\tau_1}(\mathbf{r}, \mathbf{r}_1, \omega) K_{\mathrm{Hxc}}^{\tau_1\tau_2}(\mathbf{r}_1, \mathbf{r}_2, \omega)
$$
$$
\times\, \chi^{\tau_2\nu}(\mathbf{r}_2, \mathbf{r}', \omega), \tag{28}
$$

where

$$
K_{\mathrm{Hxc}}^{\tau_1\tau_2}(\mathbf{r}_1, \mathbf{r}_2, t_1 - t_2) = \frac{\delta W_{\mathrm{Hxc}}^{\tau_1}(\mathbf{r}_1, t_1)}{\delta n^{\tau_2}(\mathbf{r}_2, t_2)}. \tag{29}
$$

By inverting the Dyson equation (28), the full four-component susceptibility tensor may be computed from the Kohn-Sham susceptibility, which may be obtained directly from quantities that can be extracted from a routine ground state DFT calculation [19,20,29,30]. The main difficulty then resigns in finding a good approximation for the Hartree-exchange-correlation kernel (29). Below, the functional form for the transverse components of $K_{\mathrm{Hxc}}^{\tau_1\tau_2}$ is provided within the adiabatic local density approximation for collinear systems.

E. The Kohn-Sham four-component susceptibility tensor

In the absence of an external time-dependent electromagnetic field, the (four-component) ground state density can be obtained from the auxiliary Kohn-Sham system, whereupon the Kohn-Sham Hamiltonian (25) may be diagonalized. With access to the Kohn-Sham eigenstates, the Kohn-Sham susceptibility may be easily evaluated using the Lehmann representation (5). For periodic crystals, the Kohn-Sham eigenstates are Slater determinants composed of Bloch wave spinors $\psi_{n\mathbf{k}}(\mathbf{r}) = (\psi_{n\mathbf{k}\uparrow}(\mathbf{r}), \psi_{n\mathbf{k}\downarrow}(\mathbf{r}))/\sqrt{N_k}$ where n and $\mathbf{k}$ denotes the band index and k-point, while the Kohn-Sham orbitals have been normalized to the unit cell by dividing with the square root of the number of k-points N_k (number of unit cells in the crystal). By expanding the field operators in Eq. (1) in terms of the Bloch wave spinors, the four-component density operator may be written in terms of the Kohn-Sham orbitals:

$$
\hat{n}^{\mu}(\mathbf{r}) = \sum_{s,s'} \sigma_{ss'}^{\mu} \frac{1}{N_k} \sum_{n\mathbf{k}} \sum_{m\mathbf{k}'} \psi_{n\mathbf{k}s}^{*}(\mathbf{r}) \psi_{m\mathbf{k}'s'}(\mathbf{r}) \hat{c}_{n\mathbf{k}}^{\dagger} \hat{c}_{m\mathbf{k}'}. \tag{30}
$$

Thus, in the Kohn-Sham system, the four-component density operator simply moves an electron from one spinorial orbital to another. As a consequence, the Kohn-Sham susceptibility is easily evaluated in the Lehmann representation (5), which involves only states where a single electron from an occupied orbital has been moved to an unoccupied one. Denoting the Kohn-Sham single-particle energies $\epsilon_{n\mathbf{k}}$ and ground state occupancies $f_{n\mathbf{k}}$, one may write the Kohn-Sham four-component susceptibility tensor as

$$
\chi_{\mathrm{KS}}^{\mu\nu}(\mathbf{r}, \mathbf{r}', \omega) = \lim_{\eta\to 0^+} \frac{1}{N_k^2} \sum_{n\mathbf{k}} \sum_{m\mathbf{k}'} (f_{n\mathbf{k}} - f_{m\mathbf{k}'})
$$
$$
\times\, \frac{n_{n\mathbf{k},m\mathbf{k}'}^{\mu}(\mathbf{r})\, n_{m\mathbf{k}',n\mathbf{k}}^{\nu}(\mathbf{r}')}{\hbar\omega - (\epsilon_{m\mathbf{k}'} - \epsilon_{n\mathbf{k}}) + i\hbar\eta}, \tag{31}
$$

where the Kohn-Sham four-component pair densities are given by

$$
n_{n\mathbf{k},m\mathbf{k}'}^{\mu}(\mathbf{r}) = \sum_{s,s'} \sigma_{ss'}^{\mu} \psi_{n\mathbf{k}s}^{*}(\mathbf{r}) \psi_{m\mathbf{k}'s'}(\mathbf{r}). \tag{32}
$$

Since $\chi^{\mu\nu}(\mathbf{r}, \mathbf{r}', \omega)$, $\chi_{\mathrm{KS}}^{\mu\nu}(\mathbf{r}, \mathbf{r}', \omega)$, and $K_{\mathrm{Hxc}}^{\mu\nu}(\mathbf{r}, \mathbf{r}', \omega)$ are periodic functions under simultaneous translations of $\mathbf{r}$ and $\mathbf{r}'$ [see Eq. (A25)], the Dyson equation (28) can be Fourier transformed to reciprocal space, yielding a matrix equation which is diagonal in crystal momentum $\hbar\mathbf{q}$ as well as in energy $\hbar\omega$:

$$
\chi_{\mathbf{GG}'}^{\mu\nu}(\mathbf{q}, \omega) = \chi_{\mathrm{KS},\mathbf{GG}'}^{\mu\nu}(\mathbf{q}, \omega) + \sum_{\tau_1, \tau_2} \sum_{\mathbf{G}_1, \mathbf{G}_2} \chi_{\mathrm{KS},\mathbf{GG}_1}^{\mu\tau_1}(\mathbf{q}, \omega)
$$
$$
\times\, K_{\mathrm{Hxc},\mathbf{G}_1\mathbf{G}_2}^{\tau_1\tau_2}(\mathbf{q}, \omega) \chi_{\mathbf{G}_2\mathbf{G}'}^{\tau_2\nu}(\mathbf{q}, \omega). \tag{33}
$$

As a matrix equation, Eq. (33) is straightforward to invert in order to obtain the many-body susceptibility, $\chi_{\mathbf{GG}'}^{\mu\nu}(\mathbf{q}, \omega)$, from its Kohn-Sham analog. From Eq. (31), the Kohn-Sham susceptibility is lattice Fourier transformed, yielding

$$
\chi_{\mathrm{KS},\mathbf{GG}'}^{\mu\nu}(\mathbf{q}, \omega) = \lim_{\eta\to 0^+} \frac{1}{\Omega} \sum_{\mathbf{k}} \sum_{n,m} (f_{n\mathbf{k}} - f_{m\mathbf{k}+\mathbf{q}})
$$
$$
\times\, \frac{n_{n\mathbf{k},m\mathbf{k}+\mathbf{q}}^{\mu}(\mathbf{G} + \mathbf{q})\, n_{m\mathbf{k}+\mathbf{q},n\mathbf{k}}^{\nu}(-\mathbf{G}' - \mathbf{q})}{\hbar\omega - (\epsilon_{m\mathbf{k}+\mathbf{q}} - \epsilon_{n\mathbf{k}}) + i\hbar\eta}, \tag{34}
$$

where

$$
n_{n\mathbf{k},m\mathbf{k}+\mathbf{q}}^{\mu}(\mathbf{G} + \mathbf{q}) = \int_{\Omega_{\mathrm{cell}}} d\mathbf{r}\, e^{-i(\mathbf{G}+\mathbf{q})\cdot\mathbf{r}}\, n_{n\mathbf{k},m\mathbf{k}+\mathbf{q}}^{\mu}(\mathbf{r}) \tag{35}
$$

gives the plane wave coefficients of the Kohn-Sham four-component pair density and Ω_{cell} is the unit cell volume. In the above, $\epsilon_{m\mathbf{k}+\mathbf{q}}$, $f_{m\mathbf{k}+\mathbf{q}}$, and $\psi_{m\mathbf{k}+\mathbf{q}}(\mathbf{r})$ are used to denote the eigenvalue, occupancy and single-particle spinorial wave functions corresponding to the Kohn-Sham orbital with a wave vector $\mathbf{k}'$ within the first BZ, satisfying $\mathbf{k}' = \mathbf{k} + \mathbf{q}$ up to a reciprocal lattice vector. The plane wave Hartree-exchange-correlation kernel is simply computed by lattice Fourier transforming Eq. (29).

For collinear systems, Eqs. (18) and (19) also apply to the Kohn-Sham susceptibility tensor. Furthermore, the spinorial orbitals can all be chosen to have one nonzero component, such that the spin polarization may be included in the band index $n \to (ns)$. This leads to a simplification of the Kohn-Sham plane wave susceptibility:

$$
\chi_{\mathrm{KS},\mathbf{GG}'}^{\mu\nu}(\mathbf{q}, \omega) = \lim_{\eta\to 0^+} \frac{1}{\Omega} \sum_{n\mathbf{k}s} \sum_{ms'} (f_{n\mathbf{k}s} - f_{m\mathbf{k}+\mathbf{q}s'}) \sigma_{ss'}^{\mu} \sigma_{s's}^{\nu}
$$
$$
\times\, \frac{n_{n\mathbf{k}s,m\mathbf{k}+\mathbf{q}s'}(\mathbf{G} + \mathbf{q})\, n_{m\mathbf{k}+\mathbf{q}s',n\mathbf{k}s}(-\mathbf{G}' - \mathbf{q})}{\hbar\omega - (\epsilon_{m\mathbf{k}+\mathbf{q}s'} - \epsilon_{n\mathbf{k}s}) + i\hbar\eta}, \tag{36}
$$

where

$$
n_{n\mathbf{k}s,m\mathbf{k}+\mathbf{q}s'}(\mathbf{G} + \mathbf{q}) = \int_{\Omega_{\mathrm{cell}}} d\mathbf{r}\, e^{-i(\mathbf{G}+\mathbf{q})\cdot\mathbf{r}}\, \psi_{n\mathbf{k}s}^{*}(\mathbf{r}) \psi_{m\mathbf{k}+\mathbf{q}s'}(\mathbf{r}). \tag{37}
$$

Writing the product of spin matrix elements $\sigma_{ss}^{\mu}\sigma_{s's}^{\nu}$ of Eq. (36) in terms of the basic matrices

$$\sigma^{\uparrow} = \begin{pmatrix} 1 & 0 \\ 0 & 0 \end{pmatrix}, \quad \sigma^{\downarrow} = \begin{pmatrix} 0 & 0 \\ 0 & 1 \end{pmatrix}, \tag{38a}$$

$$\sigma^{+} = \begin{pmatrix} 0 & 1 \\ 0 & 0 \end{pmatrix}, \quad \sigma^{-} = \begin{pmatrix} 0 & 0 \\ 1 & 0 \end{pmatrix}, \tag{38b}$$

it is straightforward to see that the only nonvanishing components are χ_{KS}^{+-}, χ_{KS}^{-+} and

$$\chi_{\mathrm{KS}}^{00} = \chi_{\mathrm{KS}}^{zz} = \chi_{\mathrm{KS}}^{\uparrow\uparrow} + \chi_{\mathrm{KS}}^{\downarrow\downarrow}, \tag{39a}$$

$$\chi_{\mathrm{KS}}^{0z} = \chi_{\mathrm{KS}}^{z0} = \chi_{\mathrm{KS}}^{\uparrow\uparrow} - \chi_{\mathrm{KS}}^{\downarrow\downarrow}. \tag{39b}$$

Thus, in the collinear case, one needs only to compute $\chi_{\mathrm{KS}}^{\uparrow\uparrow}$, $\chi_{\mathrm{KS}}^{\downarrow\downarrow}$, χ_{KS}^{+-}, and χ_{KS}^{-+} in order to construct the full Kohn-Sham four-component susceptibility tensor.

In the LR-TDDFT formalism described above, one needs in principle all the excited states of the Kohn-Sham system in order to evaluate the Kohn-Sham susceptibility in Eq. (36). It should be noted that the Kohn-Sham construction allows for the calculation of $\chi^{+-}(\mathbf{r}, \mathbf{r}', t - t')$ without explicit use of the excited states of the Kohn-Sham system. Such approaches include propagating the system in real-time for different "transverse magnetic kicks" [31] or using the Sternheimer equation from time-dependent density functional perturbation theory [32,33]. As we will show below, the Kohn-Sham excited states are generally not a main limiting factor for the LR-TDDFT methodology, and we will use these complementing methods only for comparison.

F. Transverse magnetic susceptibility within the adiabatic local spin-density approximation

The Hartree part of the Hartree-exchange-correlation kernel is straightforward to evaluate. In frequency space one obtains $K_{\mathrm{Hxc}}^{\mu\nu} = v_c \delta^{0\mu}\delta^{0\nu} + K_{\mathrm{xc}}^{\mu\nu}$, where v_c is the Coulomb interaction and $K_{\mathrm{xc}}^{\mu\nu}$ needs to be approximated. In the adiabatic local spin-density approximation (ALDA), $K_{\mathrm{xc}}^{\mu\nu}$ is approximated by

$$K_{\mathrm{ALDA}}^{\tau_1\tau_2}(\mathbf{r}_1, \mathbf{r}_2, t_1 - t_2) = f_{\mathrm{LDA}}^{\tau_1\tau_2}[n, \mathbf{m}](\mathbf{r}_1)\delta(\mathbf{r}_1 - \mathbf{r}_2)\delta(t_1 - t_2), \tag{40}$$

where $n(\mathbf{r})$ and $\mathbf{m}(\mathbf{r})$ are the ground state electron density and magnetization, while

$$f_{\mathrm{LDA}}^{\tau_1\tau_2}[n, \mathbf{m}](\mathbf{r}) = \left.\frac{\partial^2[\epsilon_{\mathrm{xc}}(n, |\mathbf{m}|)n]}{\partial n^{\tau_1}\partial n^{\tau_2}}\right|_{n(\mathbf{r}),\mathbf{m}(\mathbf{r})}, \tag{41}$$

where $\epsilon_{\mathrm{xc}}(n, m)$ is the exchange-correlation energy per electron of a homogeneous electron gas of density n and magnetization $m = |\mathbf{m}|$. The derivatives are evaluated using

$$m = \sqrt{(n^x)^2 + (n^y)^2 + (n^z)^2} = \sqrt{4n^+n^- + (n^z)^2}, \tag{42}$$

which yields

$$\frac{\partial}{\partial n^z} = \frac{n^z}{m}\frac{\partial}{\partial m}, \quad \frac{\partial}{\partial n^{\pm}} = \frac{2n^{\mp}}{m}\frac{\partial}{\partial m}. \tag{43}$$

Similar to Eq. (16), the response relation for the Kohn-Sham susceptibility tensor can be rewritten in circular

coordinates:

$$\delta n^j(\mathbf{r}, t) = \sum_k \int_{-\infty}^{\infty} dt' \int d\mathbf{r}' \, \chi_{\mathrm{KS}}^{jk}(\mathbf{r}, \mathbf{r}', t - t')\delta\check{W}_s^k(\mathbf{r}', t'). \tag{44}$$

This results in the Dyson equation

$$\chi^{jk}(\mathbf{r}, \mathbf{r}', \omega) = \chi_{\mathrm{KS}}^{jk}(\mathbf{r}, \mathbf{r}', \omega) + \sum_{l_1, l_2}\iint d\mathbf{r}_1 \, d\mathbf{r}_2 \chi_{\mathrm{KS}}^{jl_1}(\mathbf{r}, \mathbf{r}_1, \omega)$$
$$\times \check{K}_{\mathrm{Hxc}}^{l_1l_2}(\mathbf{r}_1, \mathbf{r}_2, \omega)\chi^{l_2k}(\mathbf{r}_2, \mathbf{r}', \omega), \tag{45}$$

where

$$\check{K}_{\mathrm{Hxc}}^{l_1l_2}(\mathbf{r}_1, \mathbf{r}_2, t_1 - t_2) = \frac{\delta\check{W}_{\mathrm{Hxc}}^{l_1}(\mathbf{r}_1, t_1)}{\delta n^{l_2}(\mathbf{r}_2, t_2)}. \tag{46}$$

In the case of a collinear ground state, spin-polarized in the z-direction, the ALDA Hartree-exchange-correlation kernel becomes block diagonal:

$$\check{K}_{\mathrm{Hxc}}^{[0,+,-,z]} = \begin{pmatrix} v_c + K_{\mathrm{ALDA}}^{00} & 0 & 0 & K_{\mathrm{ALDA}}^{0z} \\ 0 & 0 & \check{K}_{\mathrm{ALDA}}^{+-} & 0 \\ 0 & \check{K}_{\mathrm{ALDA}}^{-+} & 0 & 0 \\ K_{\mathrm{ALDA}}^{z0} & 0 & 0 & K_{\mathrm{ALDA}}^{zz} \end{pmatrix}, \tag{47}$$

with $K_{\mathrm{ALDA}}^{0z} = K_{\mathrm{ALDA}}^{z0}$ and $\check{K}_{\mathrm{ALDA}}^{+-} = \check{K}_{\mathrm{ALDA}}^{-+}$. Since both the many-body susceptibility tensor and the Kohn-Sham analog are block diagonal as well [see Eq. (18)], the transverse components decouple from the remaining components:

$$\chi^{+-}(\mathbf{r}, \mathbf{r}', \omega) = \chi_{\mathrm{KS}}^{+-}(\mathbf{r}, \mathbf{r}', \omega) + \iint d\mathbf{r}_1 \, d\mathbf{r}_2 \chi_{\mathrm{KS}}^{+-}(\mathbf{r}, \mathbf{r}_1, \omega)$$
$$\times \check{K}_{\mathrm{ALDA}}^{-+}(\mathbf{r}_1, \mathbf{r}_2, \omega)\chi^{+-}(\mathbf{r}_2, \mathbf{r}', \omega), \tag{48}$$

where $+$ and $-$ can be interchanged to obtain the Dyson equation for $\chi^{-+}(\mathbf{r}, \mathbf{r}', \omega)$. The transverse LDA kernel itself turns out to be particularly simple,

$$f_{\mathrm{LDA}}^{-+}[n, n^z](\mathbf{r}) = \frac{2W_{\mathrm{xc,LDA}}^z[n, n^z](\mathbf{r})}{n^z(\mathbf{r})}, \tag{49}$$

and in the plane wave representation, the ALDA kernel is independent of $\mathbf{q}$ as well as ω:

$$\check{K}_{\mathrm{ALDA},\mathbf{G}_1\mathbf{G}_2}^{-+} = \frac{1}{\Omega_{\mathrm{cell}}}\int_{\Omega_{\mathrm{cell}}} d\mathbf{r} \, e^{-i(\mathbf{G}_1 - \mathbf{G}_2)\cdot\mathbf{r}} f_{\mathrm{LDA}}^{-+}(\mathbf{r})$$
$$= \frac{1}{\Omega_{\mathrm{cell}}} f_{\mathrm{LDA}}^{-+}(\mathbf{G}_1 - \mathbf{G}_2). \tag{50}$$

To summarize, the many-body transverse magnetic susceptibility can be calculated directly from the Kohn-Sham susceptibility (36) and the kernel (49)–(50). Due to the separation of components, solving the Dyson equation (33) amounts to a simple matrix inversion:

$$\chi_{[\mathbf{G}]}^{+-}(\mathbf{q}, \omega) = [1 - \chi_{\mathrm{KS}}^{+-}(\mathbf{q}, \omega)\check{K}_{\mathrm{ALDA}}^{-+}]_{[\mathbf{G}]}^{-1}\chi_{\mathrm{KS},[\mathbf{G}]}^{+-}(\mathbf{q}, \omega). \tag{51}$$

The structure of the susceptibility tensor for a spin-paired ground state will now be briefly discussed. In this case, it is not sensible to distinguish between transverse magnetic and longitudinal magnetic susceptibilities. It is straightforward to

show that the full ALDA kernel becomes diagonal, such that

$$K_{\text{Hxc}}^{[0,x,y,z]} = \begin{pmatrix} v_c + K_{\text{ALDA}}^{00} & 0 & 0 & 0 \\ 0 & K_{\text{ALDA}}^{zz} & 0 & 0 \\ 0 & 0 & K_{\text{ALDA}}^{zz} & 0 \\ 0 & 0 & 0 & K_{\text{ALDA}}^{zz} \end{pmatrix},$$
(52)

with

$$f_{\text{LDA}}^{00}[n](\mathbf{r}) = \left. \frac{\partial^2[\epsilon_{\text{xc}}(n,m)n]}{\partial n^2} \right|_{n(\mathbf{r}),m(\mathbf{r})=0},$$
(53a)

$$f_{\text{LDA}}^{zz}[n](\mathbf{r}) = \left. \frac{\partial^2[\epsilon_{\text{xc}}(n,m)n]}{\partial m^2} \right|_{n(\mathbf{r}),m(\mathbf{r})=0}.$$
(53b)

Furthermore, one can easily inspect Eq. (36) to conclude that $\chi_{\text{KS}}^{\uparrow\uparrow} = \chi_{\text{KS}}^{\downarrow\downarrow} = \chi_{\text{KS}}^{+-} = \chi_{\text{KS}}^{-+} \equiv \chi_{\text{KS}}/2$, such that the Kohn-Sham four-component susceptibility tensor simplifies significantly: $\chi_{\text{KS}}^{[0,x,y,z]} = \chi_{\text{KS}} I_{4\times4}$. In addition, from the discussion below Eq. (20b), the many-body susceptibility tensor becomes diagonal as well,

$$\chi^{[0,x,y,z]} = \begin{pmatrix} \chi^{00} & 0 & 0 & 0 \\ 0 & \chi^{zz} & 0 & 0 \\ 0 & 0 & \chi^{zz} & 0 \\ 0 & 0 & 0 & \chi^{zz} \end{pmatrix},$$
(54)

and the full magnetic response is contained in a single Dyson equation:

$$\chi^{zz}(\mathbf{r},\mathbf{r}',\omega) = \chi_{\text{KS}}(\mathbf{r},\mathbf{r}',\omega) + \iint d\mathbf{r}_1 d\mathbf{r}_2$$
$$\times \chi_{\text{KS}}(\mathbf{r},\mathbf{r}_1,\omega) K_{\text{ALDA}}^{zz}(\mathbf{r}_1,\mathbf{r}_2) \chi^{zz}(\mathbf{r}_2,\mathbf{r}',\omega).$$
(55)

G. Spectral enhancement and the Goldstone theorem

Although χ^{+-} and χ_{KS}^{+-} are directly related by the Dyson equation (51), the transverse magnetic excitations as described by the corresponding spectral functions $S_{\mathbf{G}}^{+-}(\mathbf{q},\omega)$ and $S_{\text{KS},\mathbf{G}}^{+-}(\mathbf{q},\omega)$ can be quite different. $S_{\text{KS},\mathbf{G}}^{+-}(\mathbf{q},\omega)$ gives the spectrum of Kohn-Sham spin-flip excitations, also referred to as the Stoner spectrum. In the collinear case, the noninteracting Stoner pairs are generated by removing an electron from an occupied band and k-point $\mathbf{k}$, flipping its spin and placing it in an unoccupied band and k-point $\mathbf{k}+\mathbf{q}$. The Stoner pairs form a continuum, which for ferromagnetic materials is gapped by the exchange splitting energy Δ_x at $\mathbf{q}=\mathbf{0}$. Whereas the exchange splitting can have a magnitude of several electron volts, the fully interacting spectrum of transverse magnetic excitations, $S_{\mathbf{G}}^{+-}(\mathbf{q},\omega)$, exhibits a so-called Goldstone mode with $\omega_{\mathbf{q}=\mathbf{0}} = 0$ for spin-isotropic systems. Physically, this mode arises when a rigid rotation of the direction of magnetization does not cost any energy and it is a manifestation of the more general Goldstone theorem. Due to the binding nature of the interaction in Eq. (49), the many-body transverse magnetic excitations generally exist at energies below the Stoner continuum. However, in itinerant ferromagnets, the Stoner gap will close for wave vectors $\mathbf{q}$ connecting the majority and minority spin Fermi surfaces [4,34]. As a magnon branch enters the Stoner continuum, it will be dressed by the single-particle excitations leading to a broadening of the spectral width. The

corresponding shortening in quasiparticle lifetime is called Landau damping [35].

Often χ^{+-} is referred to as the enhanced susceptibility because the Dyson equation (51) can be understood as the formation of collective magnon excitations out of the single-particle Stoner continuum. As it turns out, this procedure preserves the total spectral weight embedded in the susceptibility. For the transverse magnetic susceptibility, the zeroth order sum rule [see (A10)] relates the spectrum of transverse magnetic excitations to the magnetization density of the ground state:

$$\hbar \int_{-\infty}^{\infty} S^{+-}(\mathbf{r},\mathbf{r}',\omega) d\omega = n^z(\mathbf{r})\,\delta(\mathbf{r}-\mathbf{r}').$$
(56)

Because the spin-polarization density is the same in both the Kohn-Sham and the fully interacting system by construction, the total spectral weight is preserved between the two. By performing a lattice Fourier transform, a similar expression for the plane wave susceptibility is obtained:

$$\hbar \int_{-\infty}^{\infty} S_{\mathbf{GG}'}^{+-}(\mathbf{q},\omega) d\omega = \frac{n^z(\mathbf{G}-\mathbf{G}')}{\Omega_{\text{cell}}},$$
(57)

where $n^z(\mathbf{G}-\mathbf{G}')$ denotes the plane wave coefficients of the spin-polarization density, defined similarly to Eq. (A35). As a consequence, the total spectral weight of transverse magnetic excitations at any $\mathbf{G}$ and $\mathbf{q}$ is simply the average spin-polarization density:

$$\hbar \int_{-\infty}^{\infty} S_{\mathbf{G}}^{+-}(\mathbf{q},\omega) d\omega = \frac{\sigma_z}{\Omega_{\text{cell}}},$$
(58)

where σ_z denotes $n^z(\mathbf{r})$ integrated over the unit cell.

III. COMPUTATIONAL IMPLEMENTATION

As described above, the transverse magnetic plane wave susceptibility can be computed within linear response time-dependent density functional theory using only quantities that can be obtained from the auxiliary noninteracting Kohn-Sham system. We have implemented this methodology into the GPAW open-source code [36,37], which uses the projected augmented wave method [23]. The implementation is based on the existing linear response module for GPAW [38], which enables computation of the longitudinal dielectric susceptibility χ^{00} and related material properties. In this section, we present the implementation and make a rigorous performance assessment of the numerical scheme employed.

A. Projected augmented wave method for plane wave susceptibilities

The list of Kohn-Sham quantities needed for calculating the transverse magnetic plane wave susceptibility is relatively short. The Kohn-Sham orbital energies and occupancies, $\epsilon_{n\mathbf{k}s}$ and $f_{n\mathbf{k}s}$, are easily extracted from any DFT ground state calculation, the Kohn-Sham pair densities (37) are calculated from the Kohn-Sham orbitals, and the transverse magnetic plane wave kernel (49)–(50) is calculated from the ground state density and spin-polarization density.

In the projected augmented wave method (PAW), the all-electron Kohn-Sham orbitals $\psi_{n\mathbf{k}s}$ are written in terms of

smooth pseudowaves $\tilde{\psi}_{n\mathbf{k}s}$, which are easy to represent numerically:

$$|\psi_{n\mathbf{k}s}\rangle = \hat{\mathcal{T}}|\tilde{\psi}_{n\mathbf{k}s}\rangle, \tag{59a}$$

$$\hat{\mathcal{T}} = 1 + \sum_{a,i}\left(|\phi_i^a\rangle - |\tilde{\phi}_i^a\rangle\right)\langle\tilde{p}_i^a|. \tag{59b}$$

Inside the so-called augmentation sphere, a spherical region of space centered at the position of the ath atomic nuclei $\mathbf{R}_a$, smooth partial waves $\tilde{\phi}_i^a$, and projector functions $\tilde{p}_i^a$ are constructed to fulfill $\sum_i|\tilde{\phi}_i^a\rangle\langle\tilde{p}_i^a| = 1$, so that the linear operator $\hat{\mathcal{T}}$ effectively maps the smooth pseudowaves onto the all-electron partial waves ϕ_i^a. Outside the augmentation sphere $\tilde{\phi}_i^a(\mathbf{r} - \mathbf{R}_a) = \phi_i^a(\mathbf{r} - \mathbf{R}_a)$, making the smooth pseudowave equal to the all-electron Kohn-Sham orbital in the interstitial region between the augmentation spheres. Due to the linear mapping in Eq. (59), matrix elements between Kohn-Sham orbitals can be evaluated from the smooth pseudowaves using a pseudo-operator, operating on the space of pseudowaves:

$$\langle\psi_{n\mathbf{k}s}|\hat{A}|\psi_{m\mathbf{k}'s'}\rangle = \langle\tilde{\psi}_{n\mathbf{k}s}|\tilde{A}|\tilde{\psi}_{m\mathbf{k}'s'}\rangle, \quad \tilde{A} = \hat{\mathcal{T}}^\dagger\hat{A}\hat{\mathcal{T}}. \tag{60}$$

For any quasilocal operator $\hat{A}$, the effective pseudo-operator can be written [23]

$$\tilde{A} = \hat{A} + \sum_a\sum_{i,i'}|\tilde{p}_i^a\rangle\left[\langle\phi_i^a|\hat{A}|\phi_{i'}^a\rangle - \langle\tilde{\phi}_i^a|\hat{A}|\tilde{\phi}_{i'}^a\rangle\right]\langle\tilde{p}_{i'}^a|. \tag{61}$$

Thus, the evaluation of the Kohn-Sham pair densities in Eq. (37) amounts to a direct evaluation using the pseudowaves and a PAW correction:

$$n_{n\mathbf{k}s,m\mathbf{k}+\mathbf{q}s'}(\mathbf{G} + \mathbf{q}) = \tilde{n}_{n\mathbf{k}s,m\mathbf{k}+\mathbf{q}s'}(\mathbf{G} + \mathbf{q}) \\ + \Delta n_{n\mathbf{k}s,m\mathbf{k}+\mathbf{q}s'}(\mathbf{G} + \mathbf{q}), \tag{62}$$

where

$$\Delta n_{n\mathbf{k}s,m\mathbf{k}+\mathbf{q}s'}(\mathbf{G} + \mathbf{q}) = \sum_a\sum_{i,i'}Q_{ii'}^a(\mathbf{G} + \mathbf{q}) \\ \times \langle\tilde{\psi}_{n\mathbf{k}s}|\tilde{p}_i^a\rangle\langle\tilde{p}_{i'}^a|\tilde{\psi}_{m\mathbf{k}+\mathbf{q}s'}\rangle, \tag{63}$$

with

$$Q_{ii'}^a(\mathbf{G} + \mathbf{q}) = \int_{\Omega_{\text{cell}}}d\mathbf{r}\,e^{-i(\mathbf{G}+\mathbf{q})\cdot\mathbf{r}}\left[\phi_i^{a*}(\mathbf{r} - \mathbf{R}_a)\phi_{i'}^a(\mathbf{r} - \mathbf{R}_a)\right. \\ \left. - \tilde{\phi}_i^{a*}(\mathbf{r} - \mathbf{R}_a)\tilde{\phi}_{i'}^a(\mathbf{r} - \mathbf{R}_a)\right]. \tag{64}$$

In a given DFT calculation, the PAW setups for every atomic species is fixed (fixing ϕ_i^a, $\tilde{\phi}_i^a$, and $\tilde{p}_i^a$), so that the PAW correction tensor, $Q_{ii'}^a(\mathbf{G} + \mathbf{q})$, can be evaluated once and reused for all the Kohn-Sham pair densities as a function of $\mathbf{G}$ and $\mathbf{q}$. As a result, the calculation of pair densities is a fairly cheap procedure in terms of computational power.

Similarly, the ground state spin densities may be written in terms of a smooth contribution from the pseudowaves $\tilde{n}_\sigma(\mathbf{r})$ and atom-centered PAW corrections localized to the augmentation spheres:

$$n_\sigma(\mathbf{r}) = \tilde{n}_\sigma(\mathbf{r}) + \sum_a\left[n_\sigma^a(\mathbf{r} - \mathbf{R}_a) - \tilde{n}_\sigma^a(\mathbf{r} - \mathbf{R}_a)\right]. \tag{65}$$

As a result, ALDA plane wave kernels, such as the transverse magnetic kernel in Eq. (50), can be calculated as a contribution from the smooth density and a PAW correction localized

to the augmentation spheres:

$$\check{K}_{\text{ALDA},\mathbf{G}_1\mathbf{G}_2}^{-+} = \frac{1}{\Omega_{\text{cell}}}\tilde{f}_{\text{LDA}}^{-+}(\mathbf{G}_1 - \mathbf{G}_2) + \Delta\check{K}_{\text{ALDA},\mathbf{G}_1\mathbf{G}_2}^{-+}, \tag{66}$$

where

$$\Delta\check{K}_{\text{ALDA},\mathbf{G}_1\mathbf{G}_2}^{-+} = \sum_a\int_{\Omega_{\text{cell}}}\frac{d\mathbf{r}_1}{\Omega_{\text{cell}}}\,e^{-i(\mathbf{G}_1-\mathbf{G}_2)\cdot\mathbf{r}_1}\Delta f_{\text{LDA}}^{a,-+}(\mathbf{r}_1 - \mathbf{R}_a), \tag{67}$$

with atom-centered PAW corrections to the LDA kernel

$$\Delta f_{\text{LDA}}^{a,-+}(\mathbf{r}) = f_{\text{LDA}}^{-+}[n_\uparrow^a, n_\downarrow^a](\mathbf{r}) - f_{\text{LDA}}^{-+}[\tilde{n}_\uparrow^a, \tilde{n}_\downarrow^a](\mathbf{r}). \tag{68}$$

In principle, the PAW method does not lead to any loss in generality, and the PAW corrected Kohn-Sham pair densities and ALDA plane wave kernels can be regarded as all-electron quantities. In practice, however, generating partial waves with projector functions to match is not a trivial task, and the partial wave expansion will not be complete.

B. Implementation of the PAW method

In GPAW, the pseudowaves $\tilde{\psi}_{n\mathbf{k}s}(\mathbf{r}) = e^{i\mathbf{k}\cdot\mathbf{r}}\tilde{u}_{n\mathbf{k}s}(\mathbf{r})$ are represented on a real-space grid using a plane wave basis set for the periodic parts $\tilde{u}_{n\mathbf{k}s}(\mathbf{r})$. The smooth contributions to the Kohn-Sham pair densities in Eq. (62) and the transverse ALDA plane wave kernel in Eq. (66) are then computed by evaluating the integrand on the real-space grid and performing a fast Fourier transform to reciprocal space:

$$\tilde{n}_{n\mathbf{k}s,m\mathbf{k}+\mathbf{q}s'}(\mathbf{G} + \mathbf{q}) = \mathcal{F}_{\mathbf{G}}[e^{-i\mathbf{q}\cdot\mathbf{r}}\tilde{\psi}_{n\mathbf{k}s}^*(\mathbf{r})\tilde{\psi}_{m\mathbf{k}+\mathbf{q}s'}(\mathbf{r})], \tag{69}$$

$$\tilde{f}_{\text{LDA}}^{-+}(\mathbf{G}_1 - \mathbf{G}_2) = \mathcal{F}_{\mathbf{G}_1-\mathbf{G}_2}\{f_{\text{LDA}}^{-+}[\tilde{n}_\uparrow, \tilde{n}_\downarrow](\mathbf{r})\}. \tag{70}$$

Furthermore, the angular part of the atom-centered partial waves are real spherical harmonics:

$$\phi_i^a(\mathbf{r}) = Y_{l_i}^{m_i}(\hat{\mathbf{r}})\phi_i^a(r), \quad \tilde{\phi}_i^a(\mathbf{r}) = Y_{l_i}^{m_i}(\hat{\mathbf{r}})\tilde{\phi}_i^a(r). \tag{71}$$

Using the plane wave expansion into real spherical harmonics,

$$e^{-i\mathbf{K}\cdot\mathbf{r}} = 4\pi\sum_l\sum_{m=-l}^l(-i)^l j_l(|\mathbf{K}|r)Y_l^m(\hat{\mathbf{K}})Y_l^m(\hat{\mathbf{r}}), \tag{72}$$

where $j_l(|\mathbf{K}|r)$ are spherical Bessel functions, the angular part of the PAW correction tensor integral in Eq. (64) can be carried out analytically:

$$Q_{ii'}^a(\mathbf{K}) = 4\pi e^{-i\mathbf{K}\cdot\mathbf{R}_a}\sum_l\sum_{m=-l}^l(-i)^l Y_l^m(\hat{\mathbf{K}})g_{l_im_i,l_{i'}m_{i'}}^{lm} \\ \times \int_0^{R_c^a}r^2dr\,j_l(|\mathbf{K}|r)\left[\phi_i^a(r)\phi_{i'}^a(r) - \tilde{\phi}_i^a(r)\tilde{\phi}_{i'}^a(r)\right], \tag{73}$$

with $\mathbf{K} = \mathbf{G} + \mathbf{q}$. Here R_c^a is the radius of the ath augmentation sphere and $g_{l_im_i,l_{i'}m_{i'}}^{lm}$ are the Gaunt coefficients. The radial part of each partial wave is stored on the same nonlinear radial grid for a given atom. We use this grid to carry out the radial integral in Eq. (73) by point integration.

For the ALDA plane wave kernel, we approach the PAW correction in a similar fashion. We expand the atom-centered PAW corrections to the LDA kernel in real spherical

harmonics,

$$\Delta f_{\text{LDA}}^{a,-+}(\mathbf{r}) = \sum_{l} \sum_{m=-l}^{l} Y_l^m(\hat{\mathbf{r}}) \Delta f_{\text{LDA}}^{a,lm,-+}(r), \qquad (74)$$

such that the angular integral in the PAW correction to the ALDA plane wave kernel (67) can be carried out analytically:

$$\Delta \check{K}_{\text{ALDA}}^{a,-+}(\mathbf{K}) = \frac{4\pi e^{-i\mathbf{K}\cdot\mathbf{R}_a}}{\Omega_{\text{cell}}} \sum_{l} \sum_{m=-l}^{l} (-i)^l Y_l^m(\hat{\mathbf{K}})$$

$$\times \int_0^{R_c^a} r^2 dr \, j_l(|\mathbf{K}|r) \Delta f_{\text{LDA}}^{a,lm,-+}(r), \quad (75)$$

with $\mathbf{K} = \mathbf{G}_1 - \mathbf{G}_2$. To obtain the expansion into real spherical harmonics in Eq. (74), the atom-centered PAW corrections to the LDA kernel are simply evaluated on an angular grid, a Lebedev quadrature of degree 11, for all radii r on the nonlinear radial grid. Through point integration, the expansion coefficients are calculated for each radii r:

$$\Delta f_{\text{LDA}}^{a,lm,-+}(r) = \int d\hat{\mathbf{r}} \, Y_l^m(\hat{\mathbf{r}}) \Delta f_{\text{LDA}}^{a,-+}(r\hat{\mathbf{r}}). \qquad (76)$$

With a Lebedev quadrature of degree 11, polynomials up to order 11 can be point integrated exactly. This implies that the plane wave expansion remains numerically exact up to $l = 5$. In practice, we truncate the expansion at $l = 4$, which results in a well-converged overall expansion for all the materials covered in this study.

C. Numerical details

In our implementation there are a number of key parameters, with respect to which the calculation needs to be converged. The k-point summation in Eq. (36) is evaluated on the Monkhorst-Pack grid [39] of the ground state calculation:

$$\chi_{\text{KS},\mathbf{GG}'}^{+-}(\mathbf{q}, z) = \frac{1}{\Omega_{\text{cell}}} \frac{1}{N_k} \sum_{\mathbf{k}} \sum_{n,m} (f_{n\mathbf{k}\uparrow} - f_{m\mathbf{k}+\mathbf{q}\downarrow})$$

$$\times \frac{n_{n\mathbf{k}\uparrow,m\mathbf{k}+\mathbf{q}\downarrow}(\mathbf{G}+\mathbf{q}) \, n_{m\mathbf{k}+\mathbf{q}\downarrow,n\mathbf{k}\uparrow}(-\mathbf{G}'-\mathbf{q})}{\hbar\omega - (\epsilon_{m\mathbf{k}+\mathbf{q}\downarrow} - \epsilon_{n\mathbf{k}\uparrow}) + i\hbar\eta},$$

$$(77)$$

where N_k in this case denotes the number of grid points. Because a finite grid is used, the continuum of Kohn-Sham states is discretized. To make up for this fact, we do not take the formal limit $\eta \to 0^+$ in Eq. (77), but leave η as a finite broadening parameter in order to smear out the transition energies $(\epsilon_{m\mathbf{k}+\mathbf{q}\downarrow} - \epsilon_{n\mathbf{k}\uparrow})$ and form a continuum. For a detailed discussion of this procedure, see Sec. III E. Additionally, the band summation in Eq. (77) is truncated to include a finite number of excited states, and a finite plane wave basis set is used to invert the Dyson equation in Eq. (51). The effect of these parameters is investigated in Secs. III D, III F, and III G. Unless otherwise stated, 12 empty shell bands per atom and a plane wave cutoff of 1000 eV are used.

On top of these convergence parameters, the GPAW implementation has two additional simplifications. As mentioned above, the projected augmented wave method is formally exact, but in reality a finite set of partial waves is used in the expansion of the Kohn-Sham orbitals. For a given number of frozen core electrons, GPAW is distributed with a single PAW setup for each atomic species, meaning that the truncation of the expansion is given in advance, it is not a parameter that can be converged. Furthermore, we do not include the frozen core states in the band summation of Eq. (77). For iron, cobalt, and nickel this implies that only transitions from the occupied 4s and 3d electronic orbitals are included. GPAW also supplies an alternative setup for nickel, where also the 3p orbitals are taken as valence states as opposed to being frozen core electronic orbitals. We tested the extended PAW setup, but found it much more difficult to converge the plane wave basis in Eq. (51), only to obtain a small difference in the magnon dispersion. We extract a difference in magnon peak position between the PAW setups of $\Delta\omega_{\mathbf{q}} = 5.2$ meV calculated at the wave vector X/3, where $\omega_{\mathbf{q}} = 305$ meV corresponding to a relative difference of 1.7%. At the wave vector 2X/3 and at the the X-point itself, the relative difference is even smaller. Although including the frozen core states should increase the overall accuracy, the computational cost far exceeds what we seem to stand to gain. The minimal PAW setups are used for the results reported throughout the remainder of this paper.

The crystal structures of the transition metals investigated are described using ASE [40] with experimental lattice constants $a = 2.867$ Å for bcc-Fe, $a = 3.524$ Å for fcc-Ni, $a = 3.539$ Å for fcc-Co and $a = 2.507$ Å for hcp-Co taken from [24,27] and the references therein. We investigate only reduced wave vectors $\mathbf{q}$ commensurate with the Monkhorst-Pack grid of the ground state calculation.

D. Sum rule check

As a check of our implementation, we have computed the average spin polarization from the Kohn-Sham transverse magnetic susceptibility. Inserting the diagonal components of Eq. (36) into the sum rule (58) and performing the frequency integral analytically,

$$\frac{1}{\Omega} \sum_{\mathbf{k}} \sum_{n,m} (f_{n\mathbf{k}\uparrow} - f_{m\mathbf{k}+\mathbf{q}\downarrow}) |n_{m\mathbf{k}+\mathbf{q}\downarrow,n\mathbf{k}\uparrow}(-\mathbf{G} - \mathbf{q})|^2 = \frac{\sigma_z}{\Omega_{\text{cell}}}.$$

$$(78)$$

We refer to the average spin polarization calculated in this manner as the pair spin polarization, $\sigma_z^{\chi_{\text{KS}}}$.

We have computed the pair spin polarization and compared it to the average spin polarization extracted from the ground state for iron, nickel, and cobalt at $\mathbf{q} = \mathbf{0}$ and different reciprocal lattice vectors $\mathbf{G}$. The comparison is presented in Fig. 1 as a function of the number of empty shell bands per atom included in the band summation of Eq. (78). The pair spin polarization is consistently smaller that the average spin polarization of the ground state, $\Delta\sigma_z^{\chi_{\text{KS}}} = \sigma_z^{\chi_{\text{KS}}} - \sigma_z < 0$, but rapidly converges towards it for $\mathbf{G} = \mathbf{0}$ as the number of empty shell bands is increased. Thus, the PAW implementation seems to provide a good description of the macroscopic spatial variation embedded in the transverse magnetic susceptibility.

For $\mathbf{G} \neq \mathbf{0}$ the convergence is orders of magnitude slower. The convergence is governed by the pair densities, which are calculated as simple overlap integrals between two Kohn-Sham orbitals and a plane wave [see Eq. (37)]. We believe
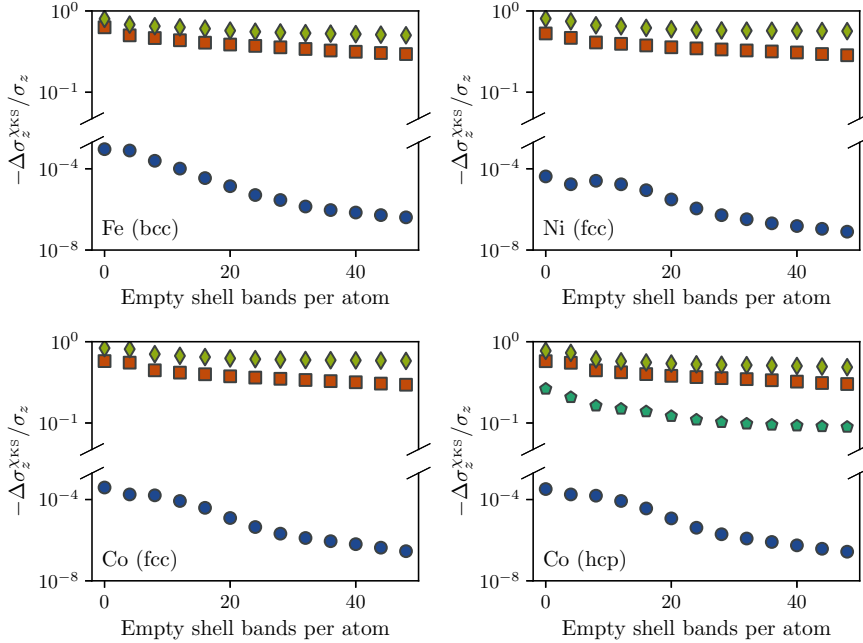
FIG. 1. Relative error in the pair spin polarization of iron, nickel, and cobalt calculated from the sum rule (78) at $\mathbf{q} = \mathbf{0}$ as a function of empty shell bands per atom. The markers represent different reciprocal lattice vectors $\mathbf{G}$: Blue circles represent $(0, 0, 0)$, red squares $(0, 0, 1)$ for Fe, Ni and fcc-Co and $(0, 0, 2)$ for hcp-Co, green rhombi $(1, 1, -1)$ for Fe, $(1, 0, -1)$ for Ni, fcc-Co, and $(1, 0, -2)$ for hcp-Co. The teal pentagons represent the $(0, 0, 1)$ reciprocal lattice vector in hcp-Co.

that this slow convergence arises because many Kohn-Sham orbitals are needed to represent a single plane wave, or conversely, that many plane waves are needed to represent a single Kohn-Sham orbital. This interpretation is supported by the fact, that the $\mathbf{G} = (0, 0, 1)$ pair spin polarization in hcp-Co has an improved convergence with respect to more local reciprocal lattice vectors. The $\mathbf{G} = (0, 0, 1)$ plane wave is better represented in terms of Kohn-Sham orbitals as it gives the two atoms in the unit cell exactly opposite phases. To fully converge the pair spin polarization for all reciprocal lattice vectors, one would also need to include the frozen core states in the band summation. This slow convergence with respect to the number of bands is much less pronounced for the transverse magnetic susceptibility at small frequencies, as we will show in Secs. III F and III G, because transitions to highly excited states are suppressed by a factor $\Delta\epsilon^{-1}$ in Eq. (77). Thus, the pair spin-polarization convergence is generally not a necessary requirement for obtaining an accurate description of the magnons.

E. Convergence of the Kohn-Sham continuum

For the itinerant ferromagnets of this study, the k-point grid refinement of Eq. (77) is an important numerical parameter to converge. Even though the bands of different spin character are split by exchange, there are metallic Kohn-Sham bands of both majority and minority spin character in all four materials. This means that the Stoner continuum will extend downwards from the exchange splitting energy Δ_x to $\omega = 0$ for reduced

wave vectors $\mathbf{q}$ that connect the Fermi surfaces of different spin character. For such $\mathbf{q}$, the collective magnon modes will unavoidably be dressed by these low-frequency Stoner excitations and be Landau damped as a result. Thus, to accurately describe the magnon modes, the discretized Stoner continuum obtained from Eq. (77) must be broadened into a continuum by leaving η as a finite broadening parameter. In the end, one should use a sufficiently dense k-point grid such that η can be chosen small enough not to have an overall influence on the magnon dispersion, yet large enough to effectively broaden the low-frequency spectrum of Stoner excitations into a continuum.

In Fig. 2 we illustrate the effect of the broadening procedure by plotting the macroscopic transverse magnetic excitation spectrum at a fixed k-point density, but with regular and centered Monkhorst-Pack grids and different values for η. For the spectral peak at $\mathbf{q} = \mathbf{0}$, the two grid alignments yield consistent results with a Lorentzian line shape of half-width η, corresponding to a magnon mode free of Landau damping. However, this is not the case for the spectra at finite crystal momentum transfer. With a broadening of $\eta = 20$ meV, spurious finite-grid effects dominate the line shapes, and the magnon peak positions, i.e., the frequencies corresponding to the maximum of the spectral function for a given $\mathbf{q}$, cannot be consistently extracted. At $\eta = 200$ meV the discrepancy between the two grid alignments is more or less cured, as the discrete spectrum of low-frequency Stoner excitations has been broadened into a continuum. Unfortunately, the effect of Landau damping is now hard to discern, and, as will be shown
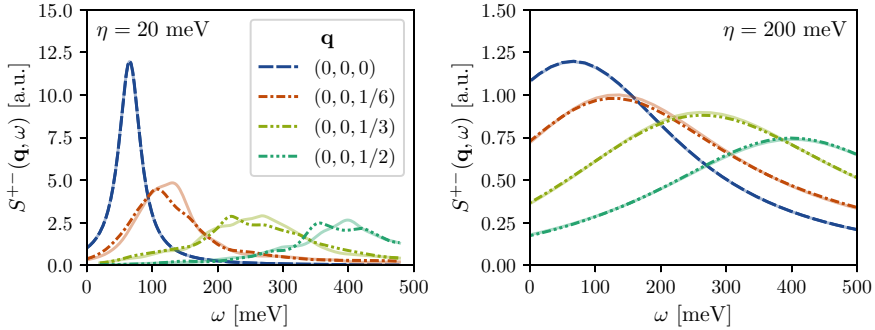
FIG. 2. Macroscopic transverse magnetic excitation spectrum of bcc-Fe in the ALDA [$S_{\mathbf{G}=0}^{+-}(\mathbf{q}, \omega)$; see Eq. (24)] calculated at a range of different wave vectors $\mathbf{q}$. The calculations were performed on (42, 42, 42) k-point grids, where the dash-dotted lines indicate results from a regular Monkhorst-Pack grid, whereas the translucent lines are results from a Γ-centered grid. The panels show the spectra calculated at two different broadening parameters η.

below, the magnon peak positions have been shifted towards higher frequencies.

To study the convergence of the low-frequency Stoner continuum further, it is worthwhile to remark that the macroscopic spectrum of Stoner excitations is much cheaper to compute than the full transverse magnetic excitation spectrum, as no extra plane wave components are needed, when the Dyson equation (51) does not have to be inverted. Thus, it would be of great value if the convergence of the low-frequency Stoner continuum could be assessed from the Kohn-Sham spectral function itself. To that end, we introduce the average frequency displacement $\langle \Delta\omega \rangle$. The idea is to consider the Stoner continuum truly converged when different k-point grid alignments yield the same Kohn-Sham spectral function. The average frequency displacement is defined as the integrated absolute difference between the Kohn-Sham spectral functions calculated on regular and Γ-centered Monkhorst-Pack k-point grids, normalized by the effective absolute change in spectral function intensity over the integration range:

$$\langle \Delta\omega \rangle_{[\omega]} \equiv \frac{1}{|\Delta S_{\mathrm{KS}}^{+-}(\mathbf{q})|_{[\omega]}} \int_{[\omega]} |S_{\mathrm{KS,r}}^{+-}(\mathbf{q}, \omega) - S_{\mathrm{KS,c}}^{+-}(\mathbf{q}, \omega)| d\omega. \tag{79}$$

Here $S_{\mathrm{KS,r/c}}^{+-}$ denotes the macroscopic Kohn-Sham spectral function ($\mathbf{G} = 0$) calculated using a regular/centered Monkhorst-Pack grids and $[\omega]$ denotes a given choice of frequency integration range. The effective absolute change in spectral function intensity, $|\Delta S_{\mathrm{KS}}^{+-}(\mathbf{q})|_{[\omega]}$, is calculated from the gradient of a linear fit to both spectral functions as illustrated in Fig. 3(a). In a similar setup, but where the two spectral functions happened to be straight parallel lines with the same gradient as the linear fit and the same integrated absolute difference between the spectral functions [see Fig. 3(b)], this definition exactly corresponds to the horizontal frequency displacement of the two spectral functions, hence the name. Now, the idea is to choose a frequency integration range that overlaps with the magnon bandwidth (the actual region of interest for Landau damping) and in which the spectral function is approximately a linear function of frequency. Due to the normalization, the average frequency displacement does

not depend on the actual intensity of the low-frequency Stoner continuum, which may vary substantially between different materials. As a consequence of the construction illustrated in Fig. 3, $\langle \Delta\omega \rangle$ quantifies the actual frequency displacement of the spectra calculated on differently aligned grids, which should correlate strongly with the discrepancy in magnon peak position between the grids, that is, the quantity we want to converge. This said, the discrepancies between the spectral functions are spurious in nature, and the computed average frequency displacement will vary with the chosen frequency integration range in actual calculations. However, when calculating $\langle \Delta\omega \rangle$ also as an average over different wave vectors $\mathbf{q}$, the spurious effects can be averaged out sufficiently well to make $\langle \Delta\omega \rangle$ stable enough for comparisons of different k-point densities and values of η. The stability towards changes in the frequency integration range is documented in the Supplemental Material [41]. In this main text a frequency integration range of $[-0.4\,\mathrm{eV}, 0.4\,\mathrm{eV}]$ is used for all materials.

To assess the convergence of the low-frequency Kohn-Sham spectrum and the applicability of $\langle \Delta\omega \rangle$ as a method of quantifying the related convergence in magnon peak positions, we have calculated the magnon peak positions at a range of different wave vectors $\mathbf{q}$ in iron, nickel, and cobalt at different k-point grid densities, using $\eta = 200$ meV. The $\mathbf{q}$ wave vectors are all chosen to lie on the same path through the first BZ, $\Gamma \rightarrow N$ for bcc-Fe, $\Gamma \rightarrow X$ for fcc-Ni and fcc-Co, and $\Gamma \rightarrow A$ for hcp-Co. To accurately obtain the magnon peak position, the transverse magnetic excitation spectrum is calculated on a frequency grid with a spacing $\delta\omega \leqslant \eta/8$ and the peak position is extracted from a parabolic fit to the spectral function maximum. Along with the magnon peak positions, $\langle \Delta\omega \rangle$ has been calculated averaging over (up to 9) wave vectors on the given path starting 1/3 of the way to the first BZ edge, such that the Stoner gap is closed for all the wave vectors in the average. In Fig. 4 the magnon peak positions calculated on a regular and Γ-centered Monkhorst-Pack grid are compared as a function of k-point density, showing also the calculated values for $\langle \Delta\omega \rangle$. Interestingly, the k-point density itself does not seem to influence the overall magnon dispersion. No net change in magnon peak positions is observed as the density is increased, but with increasing grid
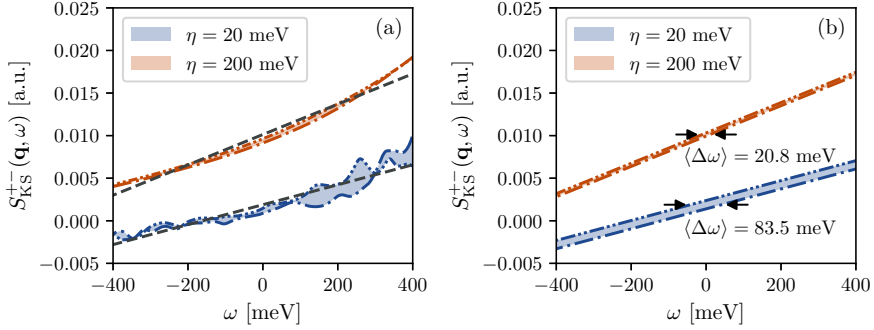
FIG. 3. The average frequency displacement, $\langle \Delta \omega \rangle$, calculated from the macroscopic spectral function of Stoner excitations $S_{\mathrm{KS},\mathbf{G=0}}^{+-}(\mathbf{q}, \omega)$. (a) The Kohn-Sham spectral functions of iron calculated using a $(30, 30, 30)$ k-point grid and two different values for η. Dash-dotted lines represents a Γ-centered grid and the dash-double-dotted lines a regular Monkhorst-Pack grid. A simultaneous fit to the two spectral functions is also shown, which along with the colored area between the functions determines $\langle \Delta \omega \rangle$ as defined in Eq. (79). (b) Linear spectral functions with the gradient from the fit in panel (a) and of the same area between the curves. For these parallel spectral functions, $\langle \Delta \omega \rangle$ gives the horizontal frequency displacement of the curves.

density, the spurious effects seem to disappear as $\eta = 200$ meV becomes sufficient to broaden the low-frequency Stoner spectrum into a continuum. Moreover, the disappearance of spurious effects seems strongly correlated with the average frequency displacement. For all materials, the general trend is that the average displacement frequency drops with increasing k-point grid density, but not in a monotonic way. We believe that the nonmonotonic behavior reflects the fact that the low-

frequency Stoner spectrum is highly sensitive to the sampling of Fermi surfaces, which depends on not only the density of the grid, but also the geometry of the surfaces and how they are situated on the grid. For the same reasons, the spurious displacements of magnon peak positions do not decrease monotonically either and the two trends seem correlated. As an example, both the average frequency displacement and magnon peak position displacement in iron were found to be

FIG. 4. Magnon peak positions relative to the Γ-peak, in color (left axis), and average displacement frequency, in gray (right axis), as a function of k-point density with $\eta = 200$ meV. For hcp-Co, the k-point density along the c-direction is plotted. Red, green, and teal indicate the magnon peaks at wave vectors $1/3$ of the way, $2/3$ of the way, and at the end of the paths $\Gamma \rightarrow \mathrm{N}$, $\Gamma \rightarrow \mathrm{X}$, and $\Gamma \rightarrow \mathrm{A}$ (for bcc, fcc, and hcp). Yellow, purple, and blue indicate similar points on the path $\mathrm{A} \rightarrow \Gamma$ in the second BZ of hcp-Co. The opaque and translucent markers represent results calculated using regular and Γ-centered Monkhorst-Pack grids, respectively.

FIG. 5. Magnon peak positions of iron relative to the Γ-peak, in color (left axis), and average displacement frequency, in gray (right axis), as a function of broadening parameter η. Panels (a), (b), (c), and (d) were calculated using $(18, 18, 18)$, $(42, 42, 42)$, $(54, 54, 54)$, and $(78, 78, 78)$ k-point grids, respectively. Red, green, and teal indicate the magnon peaks at wave vectors $1/3$ of the way, $2/3$ of the way, and at the end of the path $\Gamma \rightarrow$ N. The opaque and translucent markers represent results calculated using regular and Γ-centered Monkhorst-Pack grids, respectively.

larger for k-point densities of 9.7 Å and 11.6 Å compared to the grid with density 7.7 Å. For all materials, k-point densities, which result in an average frequency displacement below 8 meV, yield consistent results.

To further investigate the correlation between the average frequency displacement and the convergence of magnon peak positions, we computed both as a function of broadening parameter η for selected k-point densities in iron and nickel. In Fig. 5 we show a selection of results for iron, whereas the results for nickel are given in the Supplemental Material [41]. For coarse k-point grids, such as in Fig. 5(a), we never obtain consistency of results between the two different grid alignments, but as the k-point density increases, consistency is achieved for a broadening above some threshold η_t. A similar picture is obtained for nickel, but with magnon frequency discrepancies smaller in magnitude below the threshold η_t. For both materials, there is consistency of results for all the k-point grids and broadening parameters η that yield an average frequency displacement $\langle \Delta\omega \rangle \leqslant 5$ meV. Inductively, this may be used as a criterion to guarantee strictly converged low-frequency Stoner spectra.

To illustrate the use of this criterion, we have computed the average frequency displacement as a function of η for a wide selection of k-point grids in iron, nickel, and cobalt using also different frequency integration ranges. All show a smooth monotonic decrease in $\langle \Delta\omega \rangle$ as a function of η, similar to the behavior shown in Fig. 5. In the Supplemental Material [41], we supply a table of threshold values η_t corresponding to the intersection with $\langle \Delta\omega \rangle = 5$ meV found by

linear interpolation. As an example, we find $\eta_t = 126$ meV for iron with the $(54, 54, 54)$ k-point grid shown in Fig. 5(c) and $\eta_t = 87$ meV with the $(78, 78, 78)$ k-point grid shown in Fig. 5(d), both using a frequency integration range of $[-0.4 \text{ eV}, 0.4 \text{ eV}]$. Using $[\omega] = [-0.2 \text{ eV}, 0.2 \text{ eV}]$ and $[\omega] = [-0.6 \text{ eV}, 0.6 \text{ eV}]$ instead, threshold values of $\eta_t = 150$ meV, $\eta_t = 127$ meV and $\eta_t = 92$ meV, $\eta_t = 105$ meV are obtained for the two different k-point densities. The variations with frequency integration range are small enough to make the general approach applicable as a computationally cheap rule of thumb, but in the general case one should mostly use it as a starting point for a more careful analysis. Depending on the desired accuracy, a more relaxed criterion of $\langle \Delta\omega \rangle \leqslant 8$ meV should yield converged magnon peak positions, except for a few cases, and if only the general trends are important, not the actual peak positions themselves, an even larger threshold could be applied to achieve spectra similar to the one shown in Fig. 2(a). In the context at present, we want to eliminate spurious effects in the magnon peak positions all together to enable the conduction of a convergence study in other numerical parameters and to obtain magnon dispersions that are suitable for benchmarking against the literature. To achieve this, we apply the strict $\langle \Delta\omega \rangle \leqslant 5$ meV criterion.

So far, we discussed only the effect of η on the grid alignment consistency, but clearly η also has an effect on the overall magnon dispersion, as seen in Fig. 5. Even though we use a finite $\eta > 0$ to broaden the Stoner spectrum into a continuum, we need also to choose it small enough that η itself does not influence the overall dispersion. To find out how small an η
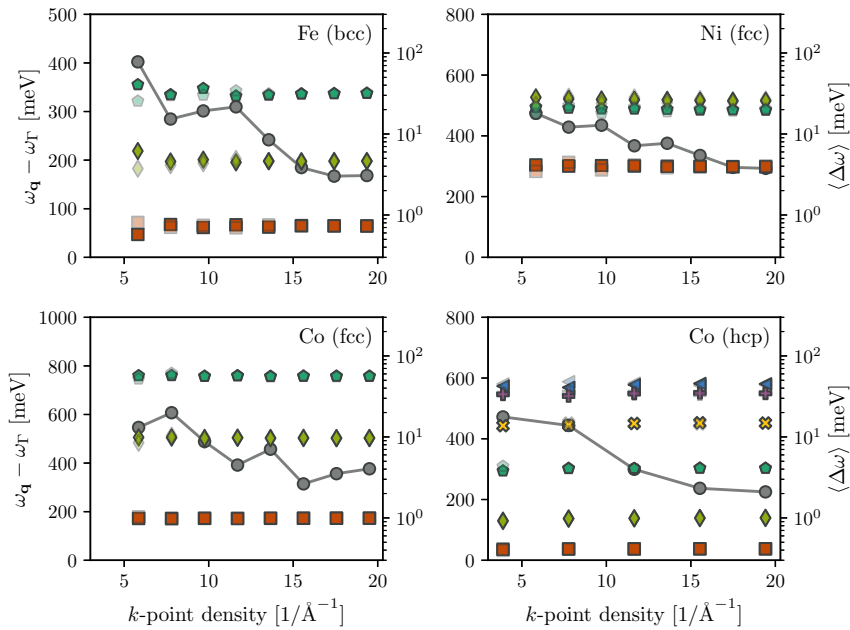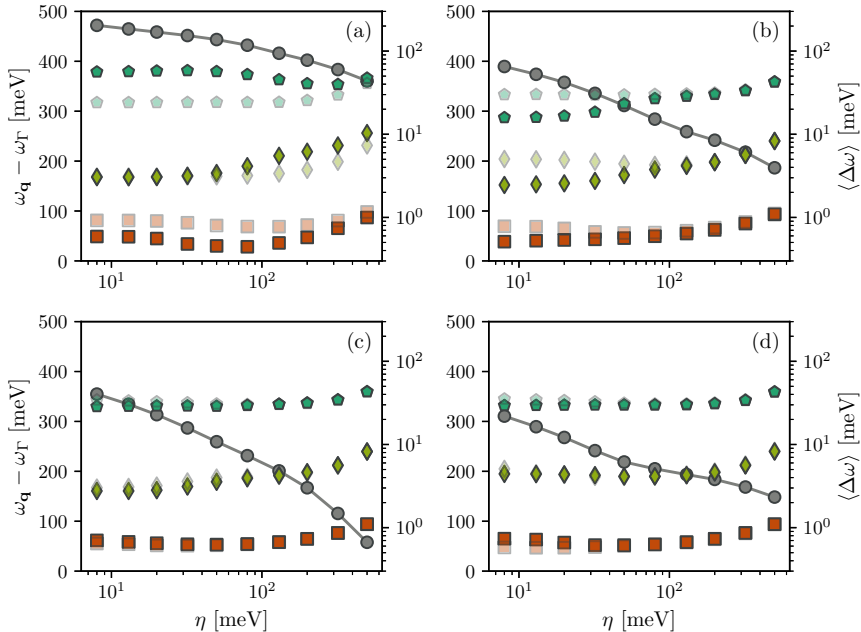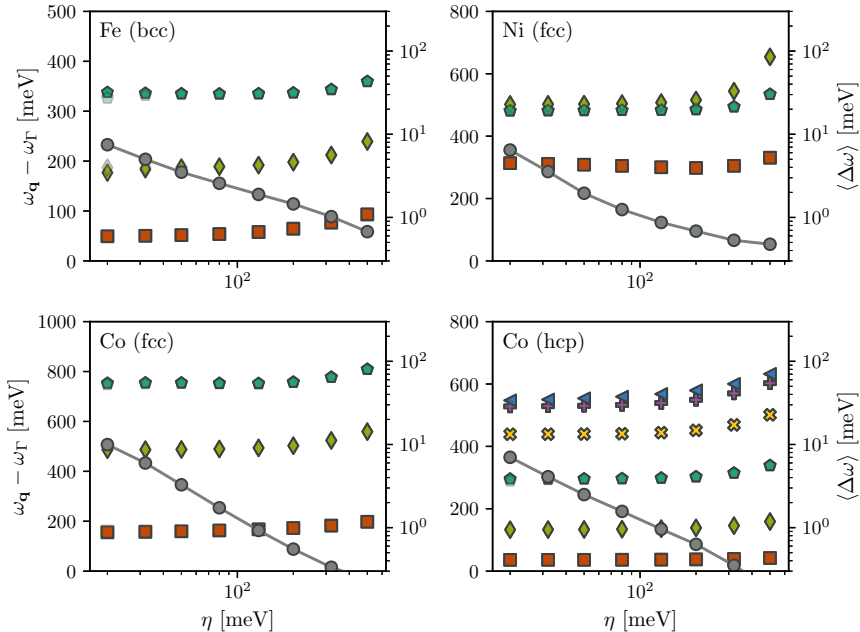
FIG. 6. Magnon peak positions relative to the Γ-peak, in color (left axis), and average displacement frequency, in gray (right axis), as a function of broadening parameter η. Calculations were performed on a (102, 102, 102) k-point grid for bcc-Fe, fcc-Ni, and fcc-Co, and a (84, 84, 48) grid for hcp-Co. Red, green and teal indicate the magnon peaks at wave vectors 1/3 of the way, 2/3 of the way and at the end of the paths $\Gamma \rightarrow N$, $\Gamma \rightarrow X$, and $\Gamma \rightarrow A$ (for bcc, fcc, and hcp). Yellow, purple, and blue indicate similar points on the path $A \rightarrow \Gamma$ in the second BZ of hcp-Co. The opaque and translucent markers represent results calculated using regular and Γ-centered Monkhorst-Pack grids, respectively.

that is, we computed the magnon peak positions as a function of η for all four materials on dense k-point grids, where an $\langle \Delta \omega \rangle \leqslant 5$ meV criterion leads to $\eta_t = 32$ meV, $\eta_t = 26$ meV, $\eta_t = 39$, meV, and $\eta_t = 28$ meV for bcc-Fe, fcc-Ni, fcc-Co, and hcp-Co, respectively. These results are presented in Fig. 6. It seems to be a general trend that the magnon peak positions shift to higher energies as η is increased. In fact, a broadening parameter less than 120 meV is needed in order to achieve a good convergence, except for a few points that require a value as low as $\eta = 50$ meV. Together with the spurious discretization effects, this requires us to use quite dense k-point grids. In order to use $\eta = 50$ meV within the $\langle \Delta \omega \rangle \leqslant 5$ meV criterion, a (90, 90, 90) k-point grid is needed for bcc-Fe, a (84, 84, 84) grid for fcc-Ni and fcc-Co, and a (60, 60, 30) grid for hcp-Co. For the materials investigated here, performing such dense k-point samplings does not itself pose any computational problem, as there are at most two atoms in the unit cell. For larger systems, however, grids that dense will quickly be prohibitive. To circumvent this problem, one can either apply analytic continuation to an alignment consistent calculation performed with a large broadening parameter η or refine the k-point summation in Eq. (77) using methods such as linear tetrahedron interpolation in order to improve the continuum description of the Stoner spectrum.

F. Gap error convergence

As our treatment of the transverse magnetic susceptibility is collinear, all the itinerant ferromagnetic materials of this

study should have a so-called Goldstone mode with a macroscopic magnon peak at $\omega_{\mathbf{q=0}} = 0$. In reality, though, this is not necessarily guaranteed numerically for linear response TDDFT calculations, and transverse magnetic excitation spectra, such as the one shown in Fig. 2, display finite gap errors $\omega_\Gamma \neq 0$. In the literature [24–26], the gap error is usually attributed to numerical approximations as well as inconsistencies between the Kohn-Sham susceptibility and the exchange-correlation kernel. Regarding the latter, one needs to use an exchange-correlation kernel that in the static limit gives the same ground state spin densities as the ground state DFT calculation, on the basis of which the Kohn-Sham susceptibility is computed. Otherwise, $(\delta W_s^\mu(\mathbf{r}, t))$ cannot be considered a perturbative quantity, so that the linear response relation (27) and consequently also the Dyson equation (28) no longer holds. As an example, using an ALDA kernel on top of a GGA ground state calculation will result in a gap error, which is why we are restricted to the use of LDA for the ground state at present. In many-body perturbation theory similar considerations have to be made [17].

For our calculations, we have identified two main numerical parameters that need to be converged in order to minimize the gap error, namely, the truncation in band summation and plane wave representation of the Kohn-Sham susceptibility. Neither the k-point density nor the broadening parameter, η, investigated above had any significant influence on ω_Γ due to the Stoner gap. In Fig. 7 we show the gap error as a function of the number of empty shell bands per atom. For all four

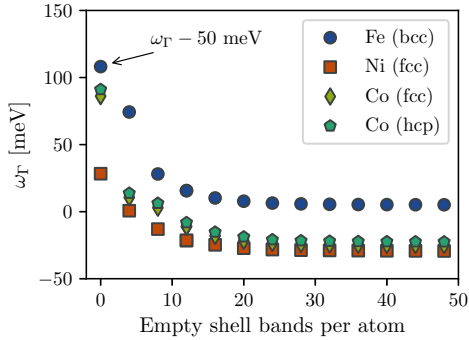FIG. 7. Magnon peak position at the Γ-point in iron, nickel and cobalt as a function of the number of empty shell bands per atom included in the band summation of Eq. (77). Calculations were performed on a $(54, 54, 54)$ regular Monkhorst-Pack grid for bcc and fcc structures and a $(48, 48, 30)$ grid for hcp-Co. For all materials, a broadening parameter of $\eta = 200$ meV was used. For iron, $\omega_\Gamma - 50$ meV is plotted for all the points to be visible on a single axis.

materials the convergence follows a similar pattern in which the gap error falls off as the number of bands is increased and beyond 20 empty shell bands per atom or so, the gap error can be considered to be converged. However, it does not vanish, which in part is due to the plane wave cutoff of 1000 eV used in these calculations. In Fig. 8 we present the gap error dependence on the plane wave representation. Unfortunately, the gap error does not converge even at cutoffs as high as 3600 eV. Extrapolating the trend at high cutoffs, it seems that one in principle would need an infinite cutoff to converge the gap error, and even so, the gap error does not seem to vanish completely, especially in the case of iron. Using the extended PAW setup for nickel, where also the $3p$ electronic orbitals are included as valence states in the band
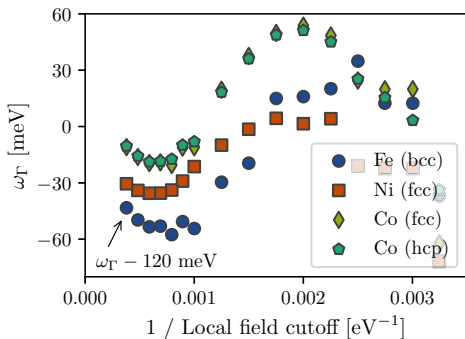

FIG. 8. Magnon peak position at the Γ-point in iron, nickel, and cobalt as a function of the inverse local field cutoff. Calculations were performed on a $(54, 54, 54)$ regular Monkhorst-Pack grid for bcc and fcc structures and a $(48, 48, 30)$ grid for hcp-Co, for all materials using a broadening parameter of $\eta = 200$ meV. For iron, $\omega_\Gamma - 120$ meV is plotted for all the points to be visible on a single axis.

summation of Eq. (77), slows the gap error convergence even more, but yields a smaller gap error for a plane wave cutoff extrapolated to infinity. Based on these results, it would seem that in order to eliminate the gap error altogether, one would need to drop the frozen core approximation, use an infinite plane wave cutoff, and possibly also improve the all-electron partial wave completeness of the PAW data sets. This is bad news, of course, but there are several practical ways to circumvent these limitations. As an example, one can invert the Dyson equation (51) in another basis set than plane waves, a strategy previously shown to yield smaller gap errors than the ones reported here [24]. Additionally, different strategies have been developed to enforce Goldstone's theorem by introducing information about the exchange-correlation kernel into the Kohn-Sham susceptibility [26] or vice versa [24,25] and in that way achieve the consistency needed to guarantee a Goldstone mode.

G. Magnon dispersion convergence

As shown above, we are able to converge the gap error ω_Γ within a finite band summation, but not within a finite plane wave representation. A natural question arises: Can we converge the magnon dispersion itself? To investigate this, we have computed the magnon peak positions for a set of wave vectors in all four materials and as a function of empty shell bands per atom and plane wave cutoff. Generally, the gap error itself should not strongly influence the magnon dispersion. However, it is important for the Landau damping that the transverse magnetic excitation spectrum and the Stoner continuum is appropriately aligned as a function of frequency. For the magnon dispersion convergence, we have used a broadening parameter of $\eta = 200$ meV and applied a $(54, 54, 54)$ regular Monkhorst-Pack grid for the bcc and fcc structures, while a $(48, 48, 30)$ grid has been used for hcp-Co. With these grids, we satisfy the $\langle \Delta \omega \rangle \leqslant 5$ meV criterion. Even though η itself is not converged, the effect of the broadening parameter seen in Fig. 6 is sufficiently smooth that we believe the results to be transferable to lower broadening. After extracting the magnon peak positions from the transverse magnetic excitation spectrum, we shift the peak positions by ω_Γ to minimize the effect of the gap error convergence on the convergence of the full dispersion.

In Fig. 9 the magnon dispersion convergence as a function of empty shell bands per atom is presented. Clearly, the magnon dispersion only weakly depends on inclusion of excited states above the $3d$-shell and above approximately 12 empty shell bands per atom, the magnon dispersion can be considered well converged. Even without empty shell bands, a good description of the overall magnon dispersion is achieved. This is reassuring for the scalability to larger systems and shows that the band summation in excited states is not a practical limitation in linear response TDDFT for magnon spectroscopy.

The magnon dispersion convergence in plane wave representation is presented in Fig. 10. In comparison to the gap error, it is much easier to converge the magnon dispersion in terms of the plane wave cutoff as variations in the relative magnon peak positions become insignificant above a 1000 eV cutoff. For nickel with the extended PAW setups, we need a
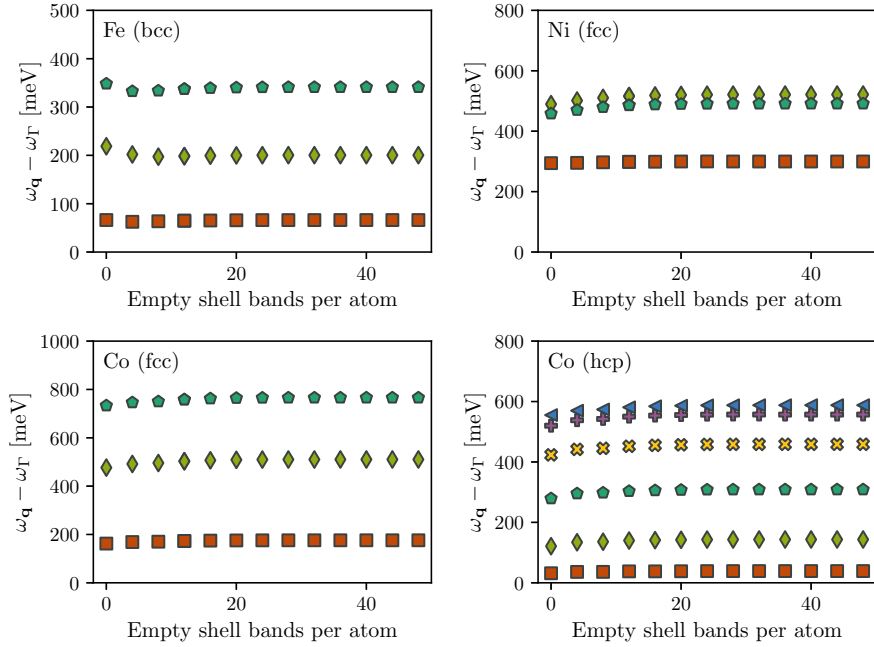
FIG. 9. Magnon peak positions relative to the Γ-peak as a function of the number of empty shell bands per atom included in the band summation of Eq. (77). Red, green, and teal indicate the magnon peaks at wave vectors 1/3 of the way, 2/3 of the way, and at the end of the paths Γ → N, Γ → X, and Γ → A (for bcc, fcc, and hcp). Yellow, purple, and blue indicate similar points on the path A → Γ in the second BZ of hcp-Co.

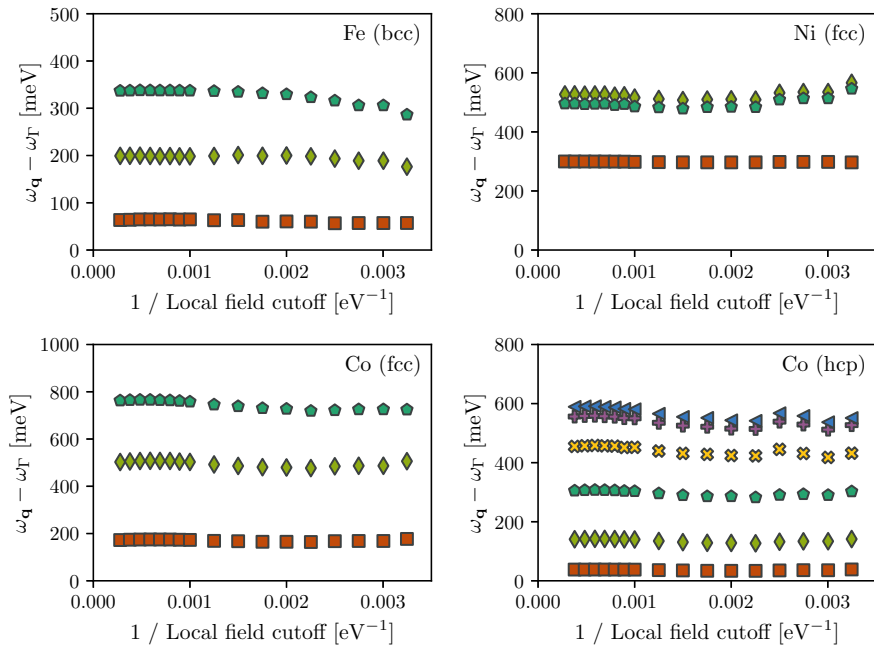

FIG. 10. Magnon peak positions relative to the Γ-peak as a function of inverse local field cutoff. Red, green, and teal indicate the magnon peaks at wave vectors 1/3 of the way, 2/3 of the way, and at the end of the paths Γ → N, Γ → X, and Γ → A (for bcc, fcc, and hcp). Yellow, purple, and blue indicate similar points on the path A → Γ in the second BZ of hcp-Co.

cutoff of 1450 eV to converge the magnon peak positions, yielding only small differences $\leqslant 1.7\%$ from the minimal setup, as previously discussed. This illustrates the usefulness of a gap error correction scheme. For a given cutoff, the spectra can be shifted such that the Goldstone condition of $\omega_{\mathbf{q}} = 0$ is satisfied, and one is then not limited by the slow gap error convergence. This implies that the numerical scheme can be considered exact up to the limitations in PAW projectors and frozen core states discussed above. However, the convergence study also illustrates an important disadvantage of the present implementation. Even though we are able to circumvent the slow convergence of the gap error, a plane wave cutoff of 1000 eV becomes prohibitive for larger structures. The Dyson equation (51) is expressed in matrices that scale in size with the number of plane wave coefficients squared, and as a result, the memory requirements quickly become a computational bottleneck. Nevertheless, the results in Fig. 10 illustrate that less accurate, yet qualitatively correct magnon dispersions can be extracted at significantly smaller plane wave cutoffs, especially when using minimal PAW setups. Once again, a different representation of the spatial coordinates in the Dyson equation may help to overcome this problem, but even within the limitations of the plane wave representation and present computational resources, the ALDA transverse magnetic susceptibility can be calculated for a wide range of collinear materials.

IV. RESULTS

On the basis of the convergence study above, we have computed the transverse magnetic excitation spectrum of bcc-Fe, fcc-Ni, fcc-Co, and hcp-Co within the ALDA. For these calculations, 12 empty shell bands per atom were used in the band summation of Eq. (77) and a 1000 eV plane wave cutoff was used in the plane wave representation of the Dyson equation (51). Furthermore, a constant frequency shift was applied in order to fulfill the Goldstone condition. To converge the magnon dispersion for reduced wave vectors $\mathbf{q}$ inside the low-frequency Stoner continuum, a broadening parameter of $\eta = 50$ meV was used as well as (90, 90, 90), (84, 84, 84), and (60, 60, 30) Γ-centered Monkhorst-Pack k-point grids for the bcc, fcc, and hcp structures, respectively. Below the Stoner continuum, where the acoustic magnon mode is free of Landau damping, the magnon peak positions do not depend on the broadening, and the the limit $\eta \to 0^+$ should be taken. To resolve the full magnon spectrum in a single figure, we do this in an approximate fashion by letting η be $\mathbf{q}$-dependent. We increase η quadratically as a function of $|\mathbf{q}|$ from $\eta = 5$ meV at $\mathbf{q} = 0$ to $\eta = 50$ meV at a threshold q_t. For wave vectors $|\mathbf{q}| > q_\mathrm{t}$, η is held constant. We use a threshold q_t of $|\mathbf{q}_\mathrm{N}|/3$, $|\mathbf{q}_\mathrm{L}|/3$ and $|\mathbf{q}_\mathrm{M}|/3$ for the bcc, fcc, and hcp structures, respectively.

A. Fe (bcc)

For bcc-Fe, applying the LDA and using the experimental lattice constant of $a = 2.867$ Å, we obtain a ferromagnetic ground state with a spatially averaged spin polarization of 2.20 μ_B per iron atom. In Fig. 11(a) we present the calculated macroscopic transverse magnetic excitation spectrum

as a function of wave vector $\mathbf{q}$ and compare it to inelastic neutron scattering (INS) data gathered in the [1$\bar{1}$0] scattering plane [42]. The transverse magnetic excitation spectrum has been corrected for a gap error of $\omega_\Gamma = 65.6$ meV. The experimental comparison is made to the same dataset in both the $\Gamma \to$ N and $\Gamma \to$ H directions, as the experimentally observed magnon dispersion is isotropic for frequencies up to at least 120 meV [43]. For wave vectors shorter than 0.5 Å^{-1}, the magnon dispersion in our transverse magnetic excitation spectrum is completely isotropic. At 0.5 Å^{-1} the dispersion in magnon peak positions flattens out in the $\Gamma \to$ H direction, before making a jump to a plateau around 140 meV, where the magnon dispersion takes a negative slope. The first jump is shortly followed by a second jump to a new plateau, again with a decreasing magnon frequency from 215 meV at 0.88 Å^{-1} to 180 meV at 1.07 Å^{-1}. At this point, the dispersion makes a third jump to 500 meV and the line shape gets severely broadened. There continues to be a well-defined peak position up to $q \sim 1.5$ Å^{-1}, where the magnon frequency is 600 meV, but beyond this point the spectrum becomes dominated by the low-frequency Stoner excitations, and it is not possible to discern a collective magnon mode. This is in contrast to the $\Gamma \to$ N direction, in which the magnon mode remains well defined throughout the entire first BZ with a single plateau around 150 meV and a total bandwidth of 337 meV. The observed jumps in magnon dispersion as well as the disappearance of the magnon mode in the $\Gamma \to$ H direction agree well with previous theoretical results [16,18,24,26,27,33]. The magnon frequency jumps arise because the magnon mode crosses stripe-like features in the Kohn-Sham spectrum corresponding to well-defined Stoner excitations residing below the main Stoner continuum. The appearance of stripe-like features is an itinerant electrons effect and is further discussed in the context of fcc-Ni in the following section as well as in the work of Friedrich and coworkers [18]. Experimentally, a significant intensity drop has been reported for wave vectors longer than 0.6 Å^{-1} [43], but a full experimental picture is not available as the present data is restricted to frequencies below 160 meV. In the frequency range available, the ALDA transverse magnetic excitation spectrum seems to match the experimentally extracted magnon dispersion well.

In Fig. 11(c) the extracted dispersion in magnon peak positions along the $\Gamma \to$ N direction is compared with experimental as well as *ab initio* references. Singh [27], Rousseau [26], Buczek [24], and coworkers use different implementations of the LR-TDDFT methodology in the ALDA, removing the gap error by applying a constant frequency shift, adding a corrective contribution to χ_KS^{+-} and forcing the smallest $\mathbf{q} = \mathbf{0}$ energy eigenvalue of χ^{+-} to zero, respectively. Müller and coworkers [17] apply MBPT in the LDA, but with an *ad hoc* adjustment of the exchange splitting to remove the gap error. Cao and coworkers [33] apply the LDA to TD-DFPT, which does not suffer from any gap error. At short wave vectors, all theoretical dispersion relations agree nicely, but for wave vectors longer than $|\mathbf{q}| = 0.3 |\mathbf{q}_\mathrm{N}|$, the Stoner continuum starts to skew the magnon line shape and discrepancies between results start to form. Similar to the magnon dispersion presented here, Singh, Rousseau, and Cao all report a plateau midway between the Γ and N points, but at lower energies than the

FIG. 11. Transverse magnetic excitation spectrum of bcc-Fe computed within the ALDA. (a) The macroscopic (unit-cell averaged) $\mathbf{G} = 0$ component of the spectrum is shown as a heat map and function of wave vector $\mathbf{q}$ and frequency ω. The spectrum was computed on a N-Γ-H band path and is compared to inelastic neutron scattering data [42]. (b) The spectral intensity is shown as a function of frequency for a range of fixed values for $\mathbf{q}$ along the Γ-N path. (c) The magnon peak positions extracted along the Γ-N path are shown and compared to experimental [42] as well as *ab initio* references [17,24,26,27,33].

plateau we find. The upper plateau frequency seems to match better the experimental dispersion; however, it is unclear from the experimental evidence whether there should be a plateau or not. Buczek and collaborators report an overall magnon dispersion that agrees very well with our results, except that it does not display a frequency plateau. Finally, a wide range of values are reported for the bandwidth among the different theoretical methods.

Most likely, the discrepancies between theoretical (A)LDA results arise from details in the representation of the Stoner continuum. In Fig. 11(b) we present the transverse magnetic excitation spectrum for wave vectors below the plateau and around the onset of the plateau. Just below the plateau, the magnon peak intensity is attenuated as the line shape attains a long tail towards higher frequencies, resembling the magnon line shapes of wave vectors on the plateau itself. On the plateau, the magnon line shape more closely resembles a Lorentzian with a less pronounced Landau damping. In this way, the plateau shape is intimately related to the low-frequency Stoner continuum, which is sensitive to both broadening procedure and k-point sampling, as shown above, as well as details in the DFT ground state calculation. Hopefully, the rigorous convergence analysis presented here can be a step towards resolving some of the discrepancies between different implementations in regards of the former. Concerning the DFT ground states, there are discrepancies already

in the ground state magnetization reported. Singh, Rousseau, Müller, Cao, and collaborators reports values for the LDA average spin polarization of 2.00 μ_B, 2.11 μ_B, 2.20 μ_B, and 2.16 μ_B within their respective ground state methodologies. This implies quantitatively different Fermi surfaces, which will influence the low-frequency Stoner continuum and the magnon modes embedded in it. Furthermore, the gap error correction procedure can affect the frequency alignment of magnon mode and Stoner continuum, which may also influence the magnon dispersion.

B. Ni (fcc)

In Fig. 12(a) we present the transverse magnetic excitation spectrum of ferromagnetic fcc-Ni. The spectrum is based on a LDA ground state calculation with lattice constant $a = 3.524$ Å, resulting in an average spin polarization per nickel atom of 0.627 μ_B. The spectrum is presented as a function of wave vector $\mathbf{q}$ along the X-Γ-L path and is compared to the magnon dispersion as measured by inelastic neutron scattering [44]. A gap error of $\omega_\Gamma = -21.5$ meV was accounted for. The magnon dispersion extracted from the transverse magnetic excitation spectrum is isotropic for small wave vectors, but at $\mathbf{q} = 0.17 \, \mathbf{q}_X$ ($q = 0.3$ Å^{-1}) there is a sudden increase in the magnon frequency, which is not present in the $\Gamma \rightarrow$ L direction. For wave vectors longer than $q = 0.3$ Å^{-1}, the
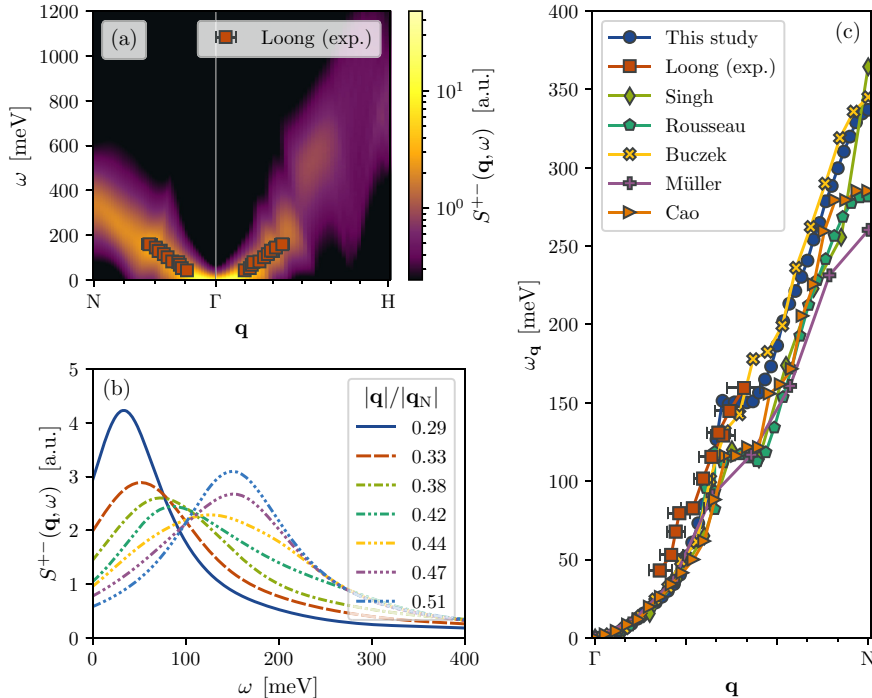
FIG. 12. Transverse magnetic excitation spectrum of fcc-Ni computed within the ALDA. (a) The macroscopic (unit-cell averaged) $\mathbf{G} = 0$ component of the spectrum is shown as a heat map and function of wave vector $\mathbf{q}$ and frequency ω. The spectrum was computed on a X-Γ-L band path and is compared to inelastic neutron scattering data [44]. (b) The spectral intensity is shown as a function of frequency for a range of fixed values for $\mathbf{q}$ along the Γ-X path. The corresponding Kohn-Sham spectrum of Stoner excitations (multiplied in intensity by a factor of 25) is shown as translucent lines. (c) The magnon peak positions extracted along the Γ-X path are shown and compared to experimental [44] as well as *ab initio* references [15,17,24,26,27,33].

magnon dispersion remains slightly anisotropic. The acoustic magnon mode remains well defined in both directions all the way to the first BZ edge, although the spectral width of the mode is more severely broadened due to Landau damping along the Γ → L direction for long wave vectors. Along the Γ → X path, the magnon dispersion attains a maximum frequency of 504 meV at $q = 1.19\,\text{Å}^{-1}$ before decreasing to a value of 484 meV at the BZ edge. Along the Γ → L direction, the magnon frequency is maximal at the BZ edge itself resulting in a bandwidth of 441 meV.

Except for short wave vectors along the Γ → L direction, the computed magnon excitation spectrum fails to reproduce the experimentally observed magnon dispersion. The ALDA treatment results in a significantly more dispersive magnon mode compared to experiment, and where two coexisting modes are observed experimentally along the Γ → X direction, we observe mostly just one. In accordance with previous (A)LDA studies [15,18,24,33], a double-peak line shape is observed around $\mathbf{q} \sim 0.15\,\mathbf{q}_X$, that is, at the point where there is a jump in the magnon frequency, but the coexistence happens only in a very narrow range of wave vectors $\mathbf{q}$. In Fig. 12(b) we present the spectral line shapes around this value, for both the spectrum of transverse magnetic excitations as well as the single-particle Stoner excitations encoded in $S_{\text{KS}}^{+-}(\mathbf{q}, \omega)$. For the wave vectors shorter than $0.17\,|\mathbf{q}_X|$,

the line shape of $S^{+-}(\mathbf{q}, \omega)$ has a shoulder above the main magnon peak, clearly originating from a well-defined single-particle Stoner peak sitting below the main Stoner continuum in $S_{\text{KS}}^{+-}(\mathbf{q}, \omega)$. As the magnon mode and Stoner peak become close in frequency, a new collective peak is developed above the Stoner peak, coexisting with the Goldstone mode only at $\mathbf{q} = 0.14\,\mathbf{q}_X$, where the Stoner peak is wedged in between the two collective peaks. At $\mathbf{q} = 0.17\,\mathbf{q}_X$, the Stoner peak disappears to negative frequencies and the upper collective magnon mode acquires the entire spectral weight. A comprehensive discussion of this phenomena stemming from a stripe-like feature in the single-particle Stoner spectrum can be found in the previous literature [14,15,18,24].

In Fig. 12(c) we compare the extracted magnon dispersion along the Γ → X direction with theoretical literature values as well as the experimental data. Şaşıoğlu and coworkers [15] treat the problem within MBPT, employing the LDA and scaling the screened Coulomb potential in order to remove the gap error. The other theoretical references are described in Sec. IV A. Between different methodologies, there seems to be a good agreement for the (A)LDA magnon dispersion of wave vectors up to $\mathbf{q} \sim 4/9\,\mathbf{q}_X$. Beyond this point there are significant differences in the extracted magnon frequency, resulting once again in a broad range of different values for the bandwidth. However, there seems to be a good agreement
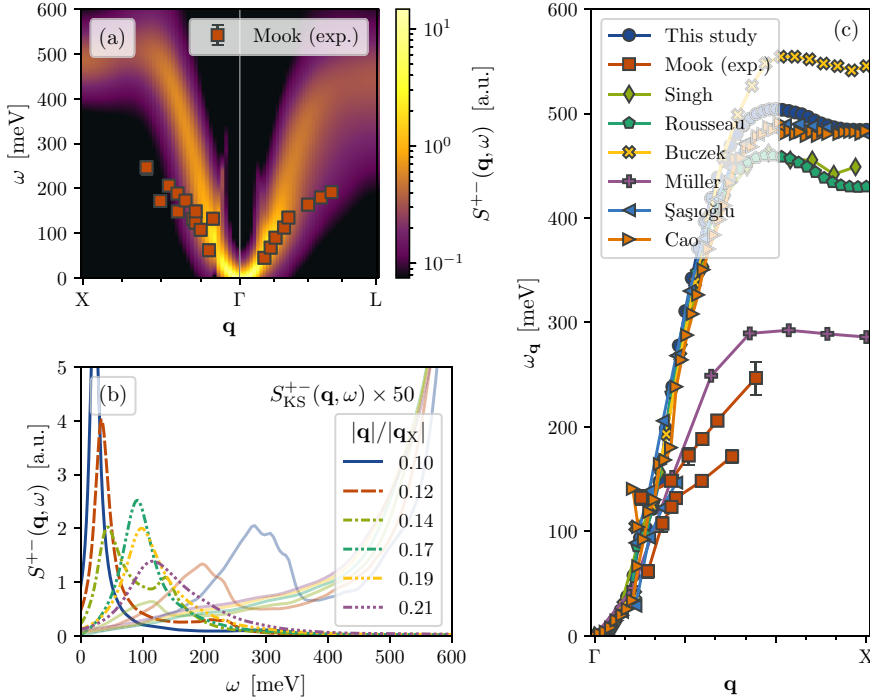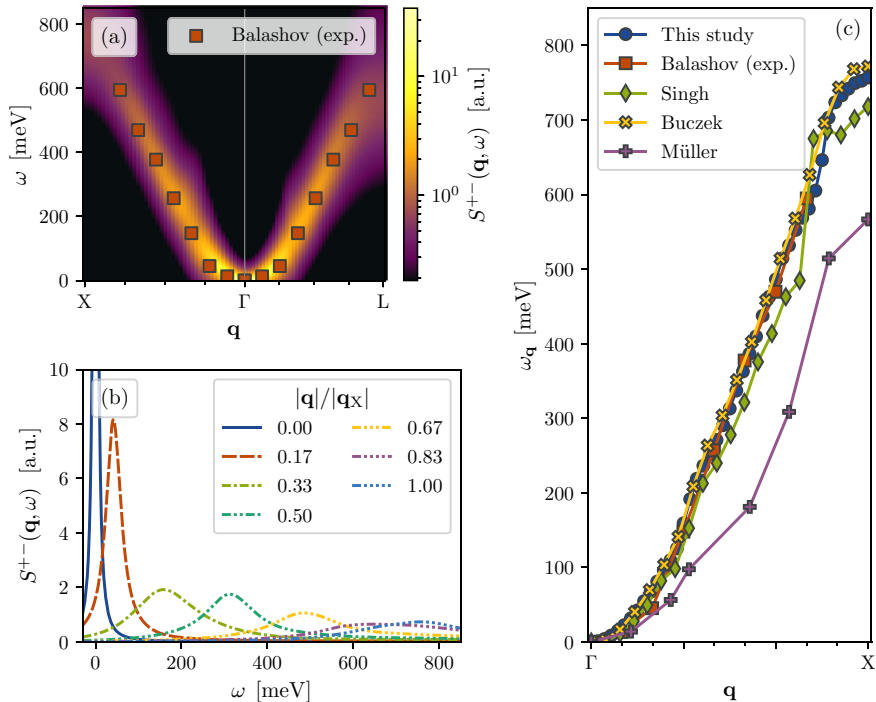
FIG. 13. Transverse magnetic excitation spectrum of fcc-Co computed within the ALDA. (a) The macroscopic (unit-cell averaged) $\mathbf{G} = 0$ component of the spectrum is shown as a heat map and function of wave vector $\mathbf{q}$ and frequency ω. The spectrum was computed on a X-Γ-L band path and is compared to inelastic scanning tunneling spectroscopy data [11]. (b) The spectral intensity is shown as a function of frequency for a range of fixed values for $\mathbf{q}$ along the Γ-X path. (c) The magnon peak positions extracted along the Γ-X path are shown and compared to experimental [11] as well as *ab initio* references [17,24,27].

about the position of the magnon dispersion maxima. As argued in Sec. IV A, at least some of the quantitative discrepancies in the magnon dispersion inside the Stoner continuum can be attributed to differences in the underlying DFT ground states and to improve consistency of ALDA results in the future, one would need to investigate why the different ground state DFT methodologies result in different Stoner spectra. To actually match the experimental dispersion, one would need to go beyond the (A)LDA. The poor performance of (A)LDA in the case of fcc-Ni is known to originate from the exchange splitting being overestimated by roughly a factor of two [15]. As seen in Fig. 12(c), Müller and coworkers obtain an improved description of the magnon dispersion, which is due to their adjustment of the exchange splitting in connection with the removal of the gap error. To get an improved *ab initio* description of fcc-Ni within LR-TDDFT, one would need an exchange-correlation functional that improves the exchange splitting in its own right. Furthermore, one can also expect inclusion of nonlocal effects in the exchange part of the kernel to decrease the magnon (spin-wave) stiffness [45].

C. Co (fcc)

Similar to the treatment of bcc-Fe and fcc-Ni presented above, we have computed the transverse magnetic excitation

spectrum for fcc-Co and compared the extracted magnon peak positions with experimental as well as theoretical references. These results are presented in Fig. 13. The spectrum was computed on the basis of a LDA ground state with average spin polarization per Co atom of $1.62\,\mu_B$, using $a = 3.539\,\text{Å}$ for the lattice constant. The original gap error was $\omega_\Gamma = -10.8$ meV. The computed magnon spectrum in Fig. 13(a) is fairly isotropic even at long wave vectors. For wave vectors longer than $q = 0.44\,\text{Å}^{-1}$, local differences in the dispersion between directions start occurring, but only beyond $q = 1.35\,\text{Å}^{-1}$ do the branches start to split. At this point, ($q = 0.88\,|\mathbf{q}_L|$), the magnon mode approaches the BZ edge in the Γ → L direction and starts to flatten out, whereas the mode continues to disperse towards higher frequencies in the Γ → X direction. As such, we end up with bandwidths of 555 meV and 757 meV in the two directions, respectively.

As evident from Figs. 13(a) and 13(c), the computed magnon dispersion compares very well to the reference experimental dispersion, which itself was inferred from inelastic scanning tunneling spectroscopy data measured on a nine-monolayer Co/Cu(100) film [11]. We compare with the same data set in both directions, as most of the data points lie within the isotropic dispersion range. In addition to the experimental comparison, there is also a good agreement between the entire dispersion computed within ALDA using different
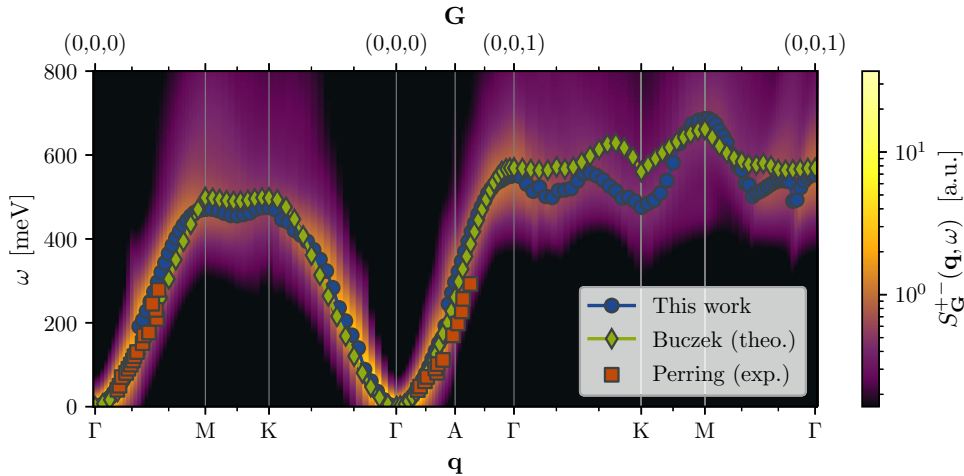
FIG. 14. Transverse magnetic excitation spectrum of hcp-Co computed within the ALDA. The spectrum is shown as a heat map and function of wave vector $\mathbf{G} + \mathbf{q}$ and frequency ω. The spectrum was computed on a Γ-M-K-Γ-A band path for the reduced wave vector $\mathbf{q}$ (lower axis) and is shown in the first and second Brillouin Zones (upper axis). The magnon peak positions are plotted on top of the heat map and compared to inelastic neutron scattering data [46] as well as ALDA results from the literature [24].

implementations of LR-TDDFT. This may be a result of the excitation spectrum having a more trivial dependence of the line shape as a function of $\mathbf{q}$ compared to the cases of bcc-Fe and fcc-Ni. In Fig. 13(b) the spectral line shapes are shown for wave vectors evenly distributed along the Γ → X path. Most of the line shapes are well approximated by Lorentzians of increasing width, meaning that the Stoner continuum mainly broadens the collective magnon mode without altering its shape. If the low-frequency Stoner continuum does not strongly influence the magnon peak positions, this implies that the theoretical magnon dispersion is less susceptible to subtle differences in the DFT ground state calculation on which it is based.

D. Co (hcp)

As the last material investigated in this study, we present the transverse magnetic excitation spectrum of hcp-Co in Fig. 14. Using $a = 2.507$ Å for the lattice constant, we obtain a LDA ground state with an average spin polarization of $1.59 \mu_B$, very close to the value in fcc-Co. The spectrum has been corrected for a gap error of $\omega_\Gamma = -8.1$ meV. Because hcp-Co has two magnetic atoms in the unit cell, the magnon spectrum include an optical mode as well as the acoustic (Goldstone) mode. The spectral function of transverse magnetic excitations, $S_{\mathbf{G}}^{+-}(\mathbf{q}, \omega)$, record excited states where the spin orientation is precessing with a wave vector $\mathbf{G} + \mathbf{q}$ with respect to the ground state. Accordingly, the optical mode manifests itself for wave vectors with which the spin orientation of the two magnetic atoms in the same unit cell are precessing out of phase. This is the case for the second BZ in hcp-Co, and in Fig. 14 we show the spectral function in the second BZ as well as the first. We present also the extracted magnon peak positions and compare them to experimental

INS data [46] as well as reference ALDA values from a literature LR-TDDFT calculation [24].

We obtain well-defined magnon modes for all investigated wave vectors $\mathbf{G} + \mathbf{q}$, although the optical mode is substantially attenuated by Landau damping. The magnon dispersion is isotropic along all three directions up to $q = 0.48$ Å^{-1}. Beyond this point, the magnon dispersion is generally steepest in the Γ → A direction, and at the second BZ center, 1.545 Å^{-1} from the reciprocal space origin, the magnon dispersion attains a maximum with a frequency of 553 meV. The magnon frequencies at the first BZ edge is very similar at the M and K points, with 471 meV and 475 meV, respectively. Because the M-point ($q = 1.447$ Å^{-1}) lies closer to the Γ-point compared to the K-point ($q = 1.671$ Å^{-1}), the upper part of the magnon dispersion is generally slightly steeper along the Γ → M path compared to the Γ → K path.

Overall, hcp-Co has a relatively isotropic magnon dispersion, as is the case of fcc-Co. The extracted magnon peak positions match quite well with experiment along the Γ → M direction, whereas the upper part of the dispersion towards the second BZ center is somewhat overestimated. These conclusions are consistent with previous ALDA results (also plotted). However, we see some discrepancies for the magnon dispersion of the optical branch between the LR-TDDFT implementations. The entire Γ-K-M-Γ optical magnon branch lies in close proximity to a dense region of the Stoner continuum. As such, the magnon dispersion is strongly influenced by local variations in $S_{KS,\mathbf{G}}^{+-}(\mathbf{q}, \omega)$ and at least some of the discrepancies can be attributed to subtle differences in the respective DFT ground states. Meanwhile, the small bumps in the Γ-K-M-Γ optical magnon dispersion might also indicate that the Stoner continuum was not appropriately converged with respect to the k-point density and broadening parameter

η. In the convergence analysis underlying the present choice of parameters, the average frequency displacement, $\langle \Delta \omega \rangle$, was analyzed for $S^{+-}_{\text{KS},\mathbf{G}}(\mathbf{q}, \omega)$ within the first BZ only.

V. SUMMARY AND OUTLOOK

We have applied the Kubo formalism to time-dependent spin-density functional theory and shown how to compute the four-component plane wave susceptibility from first principles. Although the theory is already well known, we have provided a self-contained compilation suitable for plane wave treatments within LR-TDDFT. The methodology has been implemented in the GPAW electronic structure package, enabling accurate computations of the transverse magnetic susceptibility. Within the limitations of the frozen core approximation and a finite set of PAW projector functions, the implemented methodology is formally exact, given that proper convergence in computational parameters is achieved. Thus, all approximations are due to the collinear spin-density functional theory framework and the chosen exchange-correlation functional/kernel.

A detailed convergence analysis was performed regarding spectral broadening, k-point sampling, plane wave representation and truncation of the unoccupied bands. In particular, it was shown that in order to obtain an appropriate description of the low-frequency Stoner continuum, the k-point density and broadening parameter η need to be converged in parallel. To this end, we have introduced the average displacement frequency $\langle \Delta \omega \rangle$, which provides reliable guidance for choosing values of η that result in converged magnon dispersion relations. $\langle \Delta \omega \rangle$ is calculated from the single-particle Stoner spectrum only, which itself is fast to compute. We have assessed the gap error convergence and found that it is not possible to converge ω_Γ within a finite plane wave basis. However, the gap error can be effectively accounted for by applying a constant shift to the spectrum of transverse magnetic excitations, such that the Goldstone condition is fulfilled. As a result, it is possible to attain convergence of the magnon dispersion relation itself within a finite basis set and a modest number of unoccupied bands.

Using the implemented methodology and converged numerical parameters, the transverse magnetic excitation spectrum was computed for 3d transition metals iron, nickel, and cobalt. For bcc-Fe, fcc-Co, and hcp-Co, the ALDA was shown to reproduce experimental magnon dispersions in a satisfactory manner, whereas the magnon dispersion in fcc-Ni is overestimated due to the well-known overestimation of the ground state exchange splitting energy Δ_x with LDA. All results match previous (A)LDA literature well for short wave vectors $\mathbf{q}$, but inside the low-frequency Stoner continuum, literature values for the magnon peak positions vary substantially. These discrepancies were discussed in detail and mostly attributed subtle differences in the underlying DFT ground states.

First principles calculations of magnons are rather scarce in the literature and most studies have focused on iron, nickel, or cobalt. This is likely due to the conspicuous role of these materials when discussing magnetic solids and partly due to the fact that these materials can be described within small unit cells, rendering otherwise prohibitively demanding TDDFT computations feasible. There is, however, a vast experimental literature on transverse magnetic excitations in a wide range of solids, and it is our hope that first principles calculation of the transverse magnetic susceptibility can be carried out routinely in the future. The convergence study of this work implies that the treatment of complex magnetic materials requires additional method development in order to lower the demands on the computational power, but several well-known magnetic materials with small unit cells should be within reach using the present framework [47,48]. To this end, itinerant magnets seem to be the most challenging, as the Stoner spectrum is gapped for insulators and the magnons less sensitive towards k-point sampling and broadening. In addition, the Heisenberg model often provides a rather accurate description for insulators, with parameters that can be obtained directly from ground state DFT calculations [49–51]. Still, it would be of fundamental interest to compare the dispersion relations obtained from a first principles Heisenberg model with a direct computation from TDDFT. Such a comparison could yield valuable insight into the limitations and virtues of both methods.

In this work, we have applied a collinear description of the 3d transition metals, as spin-orbit interactions are nearly negligible for iron, cobalt, and nickel. However, materials with strong spin-orbit coupling may exhibit a wealth of interesting effects. Specifically, spin-orbit effects provide a coupling between the transverse and longitudinal magnetic excitations as well as to the density response. This implies, for example, that magnons can be accessed by perturbing electric fields and that magnons may couple to plasmons and excitons in metals and insulators, respectively. Moreover, spin-orbit coupling may induce topological gaps between magnon branches [52,53], which implies the existence of topological robust surface magnons, or induce nonreciprocity in the magnon dispersion relation [54]. We believe that first principles calculations could help unravel such exotic phenomena in the future.

APPENDIX A: LINEAR RESPONSE THEORY

1. Dynamic susceptibilities and spectral functions

For experimental as well as theoretical spectroscopy, the central object of interest is the susceptibility of the system. In the framework of linear response theory, the retarded susceptibility $\chi_{BA}(t - t')$ gives the change in a system coordinate $\hat{B} = \hat{B}^\dagger$ at time t to a weak external perturbation in the system coordinate $\hat{A} = \hat{A}^\dagger$ at time t', to linear order:

$$\hat{H}(t) = \hat{H}_0 + \hat{H}_{\text{ext}}(t), \quad \hat{H}_{\text{ext}}(t) = \hat{A}f(t), \quad \text{(A1)}$$

$$\langle \delta \hat{B}(t) \rangle = \langle \hat{B}(t) \rangle - \langle \hat{B} \rangle_0 = \int_{-\infty}^{\infty} dt' \, \chi_{BA}(t - t')f(t'). \quad \text{(A2)}$$

Here $\hat{H}_0$ is the time-independent system Hamiltonian, $f(t)$ is a coordinate external to the system, and $\langle \hat{B} \rangle_0$ is the expectation value of the coordinate $\hat{B}$ in the absence of the external perturbation $\hat{H}_{\text{ext}}(t)$.

The retarded susceptibility can be computed from the *Kubo formula* [55]

$$\chi_{BA}(t - t') = -\frac{i}{\hbar}\theta(t - t')\langle [\hat{B}_0(t), \hat{A}_0(t')]\rangle_0, \qquad (A3)$$

where $\theta(t - t')$ is the step function, making the susceptibility retarded, while $\hat{A}_0(t') = e^{i\hat{H}_0 t'/\hbar}\hat{A}\,e^{-i\hat{H}_0 t'/\hbar}$ and $\hat{B}_0(t)$ carry the time dependence in the interaction picture. Due to the step function in Eq. (A3), the retarded susceptibility is analytic in the upper half of the complex frequency plane. Inserting a complete set of energy eigenstates to the system Hamiltonian $\hat{H}_0$ and carrying out the Fourier-Laplace transform (see Appendix B 1 for definitions), one obtains the dynamic susceptibility in the Lehmann representation:

$$\chi_{BA}(z = \omega + i\eta) = \sum_{\alpha,\alpha'} \frac{\langle \alpha|\hat{B}|\alpha'\rangle\langle \alpha'|\hat{A}|\alpha\rangle}{\hbar\omega - (E_{\alpha'} - E_\alpha) + i\hbar\eta}(n_\alpha - n_{\alpha'}),$$
$$(A4)$$

where z is the complex frequency and ω and η are real with $\eta > 0$. $|\alpha\rangle$ denotes an energy eigenstate of $\hat{H}_0$ with energy E_α and population factor n_α (when the system in the absence of the perturbation is in thermal equilibrium with a bath of temperature T).

If $\hat{H}_0$ is known and can be diagonalized, the Lehmann representation (A4) can be used to evaluate the dynamic susceptibility. Conversely, (A4) can be used to interpret a measured or computed susceptibility in terms of the fundamental excitations of the system. In particular, it is useful to split the dynamic susceptibility into its reactive and dissipative parts, $\chi'_{BA}(z)$ and $\chi''_{BA}(z)$ [6]:

$$\chi_{BA}(z) = \chi'_{BA}(z) + i\chi''_{BA}(z), \qquad (A5a)$$

$$\chi'_{BA}(z) = \chi'_{AB}(-z^*) = \frac{1}{2}[\chi_{BA}(z) + \chi_{AB}(-z^*)], \qquad (A5b)$$

$$\chi''_{BA}(z) = -\chi''_{AB}(-z^*) = \frac{1}{2i}[\chi_{BA}(z) - \chi_{AB}(-z^*)]. \qquad (A5c)$$

This operation has the effect of splitting the simple poles in the Lehmann representation (A4) into its real and imaginary parts:

$$\chi'_{BA}(\omega + i\eta) = \sum_{\alpha,\alpha'}\langle \alpha|\hat{B}|\alpha'\rangle\langle \alpha'|\hat{A}|\alpha\rangle(n_\alpha - n_{\alpha'})$$
$$\times \mathrm{Re}\left[\frac{1}{\hbar\omega - (E_{\alpha'} - E_\alpha) + i\hbar\eta}\right], \quad (A6a)$$

$$\chi''_{BA}(\omega + i\eta) = \sum_{\alpha,\alpha'}\langle \alpha|\hat{B}|\alpha'\rangle\langle \alpha'|\hat{A}|\alpha\rangle(n_\alpha - n_{\alpha'})$$
$$\times \mathrm{Im}\left[\frac{1}{\hbar\omega - (E_{\alpha'} - E_\alpha) + i\hbar\eta}\right], \quad (A6b)$$

of which the imaginary part of the simple poles are Lorentzians of width $2\hbar\eta$ and amplitude $-\pi$. In the limit $\eta \to 0^+$, for which the notation $\chi_{BA}(\omega) = \chi_{BA}(\omega + i0^+)$ is used, the Lorentzians become δ functions.

For a system $\hat{H}_0$ with a nondegenerate ground state $|\alpha_0\rangle$ and ground state energy E_0, the Lehmann representation (A4) reduces to a single sum over excited states in the zero temper-

ature limit:

$$\chi_{BA}(\omega + i\eta) = \sum_{\alpha \neq \alpha_0}\left[\frac{\langle \alpha_0|\hat{B}|\alpha\rangle\langle \alpha|\hat{A}|\alpha_0\rangle}{\hbar\omega - (E_\alpha - E_0) + i\hbar\eta}\right.$$
$$\left. - \frac{\langle \alpha_0|\hat{A}|\alpha\rangle\langle \alpha|\hat{B}|\alpha_0\rangle}{\hbar\omega + (E_\alpha - E_0) + i\hbar\eta}\right]. \qquad (A7)$$

Moreover, the dissipative part of the dynamic susceptibility may be expressed as a spectral function for the induced excitations:

$$S_{BA}(\omega) \equiv -\frac{\chi''_{BA}(\omega)}{\pi} = A_{BA}(\omega) - A_{AB}(-\omega), \qquad (A8)$$

$$A_{BA}(\omega) = \sum_{\alpha \neq \alpha_0}\langle \alpha_0|\hat{B}|\alpha\rangle\langle \alpha|\hat{A}|\alpha_0\rangle\,\delta(\hbar\omega - (E_\alpha - E_0)). \quad (A9)$$

Thus, the dissipative part of the dynamic susceptibility contains both the spectrum of excited states generated by $\hat{A}$, reversed by $\hat{B}$, at positive frequencies, and the spectrum generated by $\hat{B}$, reversed by $\hat{A}$, at negative frequencies. In this way, the susceptibility not only is a quantity characterizing the system response to external perturbations, but it also contains valuable information about the eigenstates of the underlying quantum system.

The intimate relation between the underlying quantum system and the dynamic susceptibility is further illustrated by the spectral moments of its dissipative part. The moments generate a range of expectation values of the quantum system, valid also at finite temperatures [6,56]:

$$\int_{-\infty}^{\infty}(\hbar\omega)^n S_{BA}(\omega)\,d\hbar\omega = (-\hbar)^n\langle[\hat{\mathcal{L}}_0^n\hat{B}, \hat{A}]\rangle_0, \qquad (A10)$$

where $\hat{\mathcal{L}}_0$ is the Liouville operator of the system,

$$\hat{\mathcal{L}}_0\hat{B} = \frac{1}{\hbar}[\hat{H}_0, \hat{B}]. \qquad (A11)$$

Equation (A10) is commonly refered to as the *n*th-order sum rule.

2. Linear response theory and spectroscopy

In the context of a spectroscopic experiment, the dissipative part of the dynamic susceptibility, $\chi''_{BA}(\omega)$, gives the spectrum of transitions between energy eigenstates induced by the perturbation in question (A6b). By the virtue of the *fluctuation-dissipation theorem* [55–58], this spectrum is directly related to the fundamental fluctuations of the system as well as the energy dissipation.

More specifically, one may consider the response to a harmonic perturbation [6]

$$f(t) = f_0 \cos(\omega_0 t) = \frac{f_0}{2}(e^{-i\omega_0 t} + \text{c.c.}). \qquad (A12)$$

Insertion into the response relation (A2) and application of the convolution theorem yields

$$\langle \delta\hat{B}(t)\rangle = \frac{f_0}{2}[\chi_{BA}(\omega_0)e^{-i\omega_0 t} + \chi_{BA}(-\omega_0)e^{i\omega_0 t}]. \qquad (A13)$$

Now, using the Lehmann representation (A4), it is straightforward to show that any retarded susceptibility as defined by the

Kubo formula (A3) satisfy

$$\chi_{B^\dagger A^\dagger}(-z^*) = \chi_{BA}^*(z). \tag{A14}$$

Insertion into Eq. (A13) reveals that the real and imaginary parts of the dynamic susceptibility gives the response in- and out-of-phase of the harmonic perturbation, respectively:

$$\langle \delta \hat{B}(t) \rangle = f_0 \{ \text{Re}[\chi_{BA}(\omega_0)] \cos(\omega_0 t)$$
$$+ \text{Im}[\chi_{BA}(\omega_0)] \sin(\omega_0 t) \}. \tag{A15}$$

Finally, only the out-of-phase response contribute to energy dissipation on average. Consequently, the mean rate of energy absorption in the system $(Q = d\langle \hat{H} \rangle / dt = \langle \hat{A}(t) \rangle df/dt)$ is proportional to $\text{Im}[\chi_{AA}(\omega_0)]$:

$$\bar{Q} = -\frac{1}{2} f_0^2 \omega_0 \text{Im}[\chi_{AA}(\omega_0)] = -\frac{1}{2} f_0^2 \omega_0 \chi_{AA}''(\omega_0). \tag{A16}$$

In the last equality, it was used that Eq. (A14) implies $\chi_{AA^\dagger}(-z^*) = \chi_{A^\dagger A}^*(z)$, meaning that

$$\chi_{A^\dagger A}'(z) = \text{Re}[\chi_{A^\dagger A}(z)], \tag{A17a}$$

$$\chi_{A^\dagger A}''(z) = \text{Im}[\chi_{A^\dagger A}(z)]. \tag{A17b}$$

With this in hand, various spectroscopic techniques can directly probe $\chi_{AA}''(\omega)$ by tracking the energy dissipated from the source of the perturbation. Finally, the energy dissipation is related directly to the transitions between system eigenstates through Eq. (A6b) or specific ground state excitations through Eqs. (A8) and (A9).

3. Dynamic susceptibilities of periodic crystals

As discussed, the dynamic susceptibility is a fundamental property of any quantum system $\hat{H}_0$. In particular, it gives the system response to a weak external perturbation and characterizes the spectrum of system excitations that the perturbation generates to linear order. In the case of real life materials, one has to consider a perturbation which varies in both time and space. If the Born-Oppenheimer approximation is employed, such that $\hat{H}_0$ only needs to describe the electronic degrees of freedom in the material, such a perturbation may be written

$$\hat{H}_{\text{ext}}(t) = \int d\mathbf{r} \, \hat{A}(\mathbf{r}) f(\mathbf{r}, t), \tag{A18}$$

where $\hat{A}(\mathbf{r}) = \hat{A}^\dagger(\mathbf{r})$ is taken to be an electronic one-body operator. The Kubo formalism itself is not restricted to the consideration of one-body operators and what follows can be easily generalized if needed. Now the retarded susceptibility gives the electronic system response in some coordinate $\hat{B}$ (also taken to be a one-body operator) at position $\mathbf{r}$ and time t to a weak perturbation of the system coordinate $\hat{A}$ at position $\mathbf{r}'$ and time t':

$$\langle \delta \hat{B}(\mathbf{r}, t) \rangle = \int_{-\infty}^{\infty} dt' \int d\mathbf{r}' \, \chi_{BA}(\mathbf{r}, \mathbf{r}', t - t') f(\mathbf{r}', t'). \tag{A19}$$

The Kubo theory described above can be easily applied to $\chi_{BA}(\mathbf{r}, \mathbf{r}', t - t')$, simply by letting $\hat{A} = \hat{A}(\mathbf{r})$ and $\hat{B} = \hat{B}(\mathbf{r}) = \hat{B}^\dagger(\mathbf{r})$. In particular, the transition matrix elements entering the Lehmann representation (A4) will now depend on position:

$$A_{\alpha'\alpha}(\mathbf{r}) \equiv \langle \alpha' | \hat{A}(\mathbf{r}) | \alpha \rangle. \tag{A20}$$

In the study of periodic crystals, the material in question is represented as a quantum system which is invariant under lattice translations, $[\hat{T}_\mathbf{R}, \hat{H}_0] = 0$. Here $\hat{T}_\mathbf{R}$ denotes the unitary generator of translations $\mathbf{r} \to \mathbf{r} - \mathbf{R}$, where $\mathbf{R}$ is any lattice vector connecting two points on the Bravais lattice of the crystal. The commutation relation implies that the eigenstates of $\hat{T}_\mathbf{R}$ diagonalize $\hat{H}_0$, and, according to Bloch's theorem, the eigenvalues may be written in terms of real wave vectors $\mathbf{k}_\alpha$:

$$\hat{T}_\mathbf{R} | \alpha \rangle = e^{i\mathbf{k}_\alpha \cdot \mathbf{R}} | \alpha \rangle. \tag{A21}$$

This has important consequences for the dynamic susceptibility of the system. It implies that all transition matrix elements transform as Bloch waves under lattice translations:

$$A_{\alpha'\alpha}(\mathbf{r} + \mathbf{R}) = \langle \alpha' | \hat{A}(\mathbf{r} + \mathbf{R}) | \alpha \rangle = \langle \alpha' | \hat{T}_\mathbf{R}^\dagger \hat{A}(\mathbf{r}) \hat{T}_\mathbf{R} | \alpha \rangle$$
$$= e^{-i\mathbf{q}_{\alpha'\alpha} \cdot \mathbf{R}} A_{\alpha'\alpha}(\mathbf{r}). \tag{A22}$$

The reduced wave vector $\mathbf{q}_{\alpha'\alpha} \equiv (\mathbf{k}_{\alpha'} - \mathbf{k}_\alpha) - \mathbf{G}_{\alpha'\alpha}$, represents the difference in crystal momentum between the two states $|\alpha'\rangle$ and $|\alpha\rangle$, where $\mathbf{G}_{\alpha'\alpha}$ is a reciprocal lattice vector chosen such that $\mathbf{q}_{\alpha'\alpha}$ lies within the first BZ. Following Eq. (A22), the transition matrix elements can be written on a Bloch wave form, with periodic parts $a_{\alpha'\alpha}(\mathbf{r} + \mathbf{R}) = a_{\alpha'\alpha}(\mathbf{r})$:

$$A_{\alpha'\alpha}(\mathbf{r}) = \frac{\Omega_{\text{cell}}}{\Omega} e^{-i\mathbf{q}_{\alpha'\alpha} \cdot \mathbf{r}} a_{\alpha'\alpha}(\mathbf{r}). \tag{A23}$$

Here the periodic parts have been normalized by the crystal volume Ω and the unit cell volume Ω_{cell}, so as to make $a_{\alpha'\alpha}(\mathbf{r})$ size intensive, that is, independent of the crystal volume. As a consequence of Eq. (A23),

$$B_{\alpha\alpha'}(\mathbf{r} + \mathbf{R}) A_{\alpha'\alpha}(\mathbf{r}' + \mathbf{R}) = B_{\alpha\alpha'}(\mathbf{r}) A_{\alpha'\alpha}(\mathbf{r}'), \tag{A24}$$

and from Eq. (A4), it is concluded that also the dynamic susceptibility is a periodic function:

$$\chi_{BA}(\mathbf{r} + \mathbf{R}, \mathbf{r}' + \mathbf{R}, z) = \chi_{BA}(\mathbf{r}, \mathbf{r}', z). \tag{A25}$$

The retarded susceptibility as defined by Eq. (A19) describes the system response on all time and length scales simultaneously. $\chi_{BA}(\mathbf{r}, \mathbf{r}_0, t - t_0)$ gives the response at a specific position $\mathbf{r}$ and time t to a perturbation which is completely local in space and time: $f(\mathbf{r}, t) \propto \delta(\mathbf{r} - \mathbf{r}_0)\delta(t - t_0)$. Thus, it describes the microscopic details and mechanisms that can be activated by an external source, but it does not directly describe the macroscopic properties of the material. To investigate the macroscopic properties embedded in the susceptibility, the response to a plane wave perturbation is considered:

$$\hat{H}_{\text{ext}}(t) = \int d\mathbf{r} \, \hat{A}(\mathbf{r}) \frac{f_0}{2} [e^{i(\mathbf{k}_0 \cdot \mathbf{r} - \omega_0 t)} + \text{c.c.}]. \tag{A26}$$

Then one can ask: To linear order in $f_0 \in \mathbb{R}$, what is the strength of induced plane wave fluctuations in the system coordinate $\hat{B}$,

$$\langle \delta \hat{B}(\mathbf{k}, \omega) \rangle = \int_{-\infty}^{\infty} dt \int d\mathbf{r} \, e^{-i(\mathbf{k} \cdot \mathbf{r} - \omega t)} \langle \delta \hat{B}(\mathbf{r}, t) \rangle? \tag{A27}$$

To answer this question, the plane wave susceptibility is introduced as the lattice Fourier transform of the dynamic

susceptibility:

$$\chi_{BA}^{\mathbf{GG}'}(\mathbf{q}, z) \equiv \iint \frac{d\mathbf{r}\, d\mathbf{r}'}{\Omega} e^{-i(\mathbf{G}+\mathbf{q})\cdot\mathbf{r}} \chi_{BA}(\mathbf{r}, \mathbf{r}', z) e^{i(\mathbf{G}'+\mathbf{q})\cdot\mathbf{r}'},$$
(A28)

where $\mathbf{G}$ and $\mathbf{G}'$ are reciprocal lattice vectors, while $\mathbf{q}$ is a wave vector within the first BZ. Now, due to the periodicity of the dynamic susceptibility (A25), its spatial Fourier transform is diagonal in wave vectors $\mathbf{q}$ and $\mathbf{q}'$ (see Appendix B 2):

$$\chi_{BA}(\mathbf{G}+\mathbf{q}, \mathbf{G}'+\mathbf{q}', z) = \frac{(2\pi)^D}{\Omega} \chi_{BA}^{\mathbf{GG}'}(\mathbf{q}, z) \delta(\mathbf{q}-\mathbf{q}'),$$
(A29)

where D is the dimensionality of the problem. With this, Eqs. (A19) and (A26) are inserted into Eq. (A27), and the convolution theorem is used to obtain

$$\frac{\langle \delta \hat{B}(\mathbf{k}, \omega) \rangle}{(2\pi)^{D+1}} = \frac{f_0}{2} \Big[\chi_{BA}^{\mathbf{GG}_0}(\mathbf{q}, \omega) \delta(\mathbf{q}-\mathbf{q}_0) \delta(\omega - \omega_0)$$
$$+ \chi_{BA}^{\mathbf{G}-\mathbf{G}_0}(\mathbf{q}, \omega) \delta(\mathbf{q}+\mathbf{q}_0) \delta(\omega + \omega_0) \Big], \quad (A30)$$

where $\mathbf{k} = \mathbf{G} + \mathbf{q}$ and $\mathbf{k}_0 = \mathbf{G}_0 + \mathbf{q}_0$. Inverting the Fourier transforms of Eq. (A27),

$$\langle \delta \hat{B}(\mathbf{r}, t) \rangle = \frac{f_0}{2} \sum_{\mathbf{G}} \Big[\chi_{BA}^{\mathbf{GG}_0}(\mathbf{q}_0, \omega_0) e^{i([\mathbf{G}+\mathbf{q}_0]\cdot\mathbf{r} - \omega_0 t)}$$
$$+ \chi_{BA}^{-\mathbf{G}-\mathbf{G}_0}(-\mathbf{q}_0, -\omega_0) e^{-i([\mathbf{G}+\mathbf{q}_0]\cdot\mathbf{r} - \omega_0 t)} \Big]. \quad (A31)$$

From this, the physical interpretation of the plane wave susceptibility, $\chi_{BA}^{\mathbf{GG}'}(\mathbf{q}, \omega)$, is clear: It is a fundamental material property, giving the plane wave coefficients of the material response in coordinate $\hat{B}$ to a plane wave perturbation in coordinate $\hat{A}$ with wave vector $\mathbf{G}' + \mathbf{q}$ and frequency ω per source strength f_0, a response which is diagonal in both ω and $\mathbf{q}$.

4. Lehmann representation of the plane wave susceptibility

So far, the retarded susceptibility was introduced and defined in terms of the linear response in system coordinates assumed to be Hermitian $\hat{A}^\dagger = \hat{A}$ and $\hat{B}^\dagger = \hat{B}$; see Eqs. (A1) and (A2). More generally, operators that are not necessarily hermitian may be considered taking the *Kubo formula* (A3) itself as the definition of a retarded susceptibility. Starting from the Kubo formula, the Lehmann representation (A4) and the separation into reactive and dissipative parts (A6) still hold, meaning that also dynamic susceptibilities of non-Hermitian operators are made up out of spectra of excited states in the system.

For the plane wave susceptibility, one may use the field operators in the Fourier basis,

$$\hat{A}(\mathbf{Q}) \equiv \int d\mathbf{r}\, e^{-i\mathbf{Q}\cdot\mathbf{r}} \hat{A}(\mathbf{r}), \quad (A32)$$

with which the susceptibility can be written on a form consistent with Kubo theory:

$$\chi_{BA}^{\mathbf{GG}'}(\mathbf{q}, z) = \frac{1}{\Omega} \chi_{\beta\alpha}(z), \quad (A33a)$$

$$\hat{\beta} = \hat{B}(\mathbf{G}+\mathbf{q}), \quad \hat{\alpha} = \hat{A}(-\mathbf{G}'-\mathbf{q}). \quad (A33b)$$

As a result, the plane wave susceptibility also can be split up in reactive and dissipative parts by applying Eq. (A5) to $\chi_{\beta\alpha}(z)$.

In order to do this, it is used that the transition matrix elements are Bloch waves (A23):

$$\langle \alpha' | \hat{A}(-\mathbf{G}-\mathbf{q}) | \alpha \rangle = a_{\alpha'\alpha}(-\mathbf{G})\, \delta_{\mathbf{q},\mathbf{q}_{\alpha'}}, \quad (A34)$$

where $\delta_{\mathbf{q},\mathbf{q}_{\alpha'}}$ is a Kroenecker-δ counting pairs of energy eigenstates α', α with $\mathbf{q}_{\alpha'\alpha} = \mathbf{q}$ and $a_{\alpha'\alpha}(\mathbf{G})$ is the plane wave coefficient of the periodic part of the transition matrix elements

$$a_{\alpha'\alpha}(\mathbf{G}) = \int_{\Omega_{\text{cell}}} d\mathbf{r}\, e^{-i\mathbf{G}\cdot\mathbf{r}} a_{\alpha'\alpha}(\mathbf{r}). \quad (A35)$$

With this, the Lehmann representation of the plane wave susceptibility may be written directly from Eq. (A4),

$$\chi_{BA}^{\mathbf{GG}'}(\mathbf{q}, z) = \frac{1}{\Omega} \sum_{\alpha,\alpha'} \frac{b_{\alpha\alpha'}(\mathbf{G}) a_{\alpha'\alpha}(-\mathbf{G}')}{\hbar\omega - (E_{\alpha'} - E_\alpha) + i\hbar\eta} (n_\alpha - n_{\alpha'}) \delta_{\mathbf{q},\mathbf{q}_{\alpha'\alpha}},$$
(A36)

which may be seen as a generalization of the results for the dielectric function from Alder [59] and Wiser [60]. Likewise, the reactive and dissipative parts of the plane wave susceptibility can be written directly from Eq. (A6):

$$\chi_{\beta\alpha}'(\omega + i\eta) = \sum_{\alpha,\alpha'} b_{\alpha\alpha'}(\mathbf{G}) a_{\alpha'\alpha}(-\mathbf{G}')(n_\alpha - n_{\alpha'}) \delta_{\mathbf{q},\mathbf{q}_{\alpha'\alpha}}$$
$$\times \text{Re}\left[\frac{1}{\hbar\omega - (E_{\alpha'} - E_\alpha) + i\hbar\eta} \right], \quad (A37a)$$

$$\chi_{\beta\alpha}''(\omega + i\eta) = \sum_{\alpha,\alpha'} b_{\alpha\alpha'}(\mathbf{G}) a_{\alpha'\alpha}(-\mathbf{G}')(n_\alpha - n_{\alpha'}) \delta_{\mathbf{q},\mathbf{q}_{\alpha'\alpha}}$$
$$\times \text{Im}\left[\frac{1}{\hbar\omega - (E_{\alpha'} - E_\alpha) + i\hbar\eta} \right]. \quad (A37b)$$

Thus, in the case of the plane wave susceptibility, $\chi_{BA}^{\mathbf{GG}'}(\mathbf{q}, z)$, the dissipative part is a spectral function for transitions between energy eigenstates with a difference in crystal momentum $\hbar\mathbf{q}$ and energy $\hbar\omega$, transitions which can be induced by $\hat{A}(-\mathbf{G}'-\mathbf{q})$, reversed by $\hat{B}(\mathbf{G}+\mathbf{q})$ and vice versa.

5. Energy dissipation in periodic crystals

In Sec. A 3 it was shown that the plane wave susceptibility, $\chi_{BA}^{\mathbf{GG}'}(\mathbf{q}, z)$, gives the plane wave coefficients of the linear response in system coordinate $\hat{B}$ to a plane wave perturbation in coordinate $\hat{A}$. As in Sec. A 1 the out-of-phase response to the full sinusoidal perturbation (A26) is needed to compute the energy dissipation. Once again, with $\hat{A}^\dagger(\mathbf{r}) = \hat{A}(\mathbf{r})$ and $\hat{B}^\dagger(\mathbf{r}) = \hat{B}(\mathbf{r})$, Eq. (A14) may be used to rewrite

$$\chi_{BA}^{-\mathbf{G}-\mathbf{G}'}(-\mathbf{q}, -z^*) = \frac{1}{\Omega} \chi_{B(-\mathbf{G}-\mathbf{q})A(\mathbf{G}'+\mathbf{q})}(-z^*)$$
$$= \frac{1}{\Omega} \chi_{B(\mathbf{G}+\mathbf{q})^\dagger A(-\mathbf{G}'-\mathbf{q})^\dagger}(-z^*)$$
$$= \frac{1}{\Omega} \chi_{B(\mathbf{G}+\mathbf{q})A(-\mathbf{G}'-\mathbf{q})}^*(z)$$
$$= \chi_{BA}^{\mathbf{GG}'\,*}(\mathbf{q}, z). \quad (A38)$$

With this result, insertion into Eq. (A31) yields

$$
\begin{aligned}
\langle \delta \hat{B}(\mathbf{r}, t) \rangle = f_0 \sum_{\mathbf{G}} \Big\{ & \mathrm{Re}\big[\chi_{BA}^{\mathbf{G}\mathbf{G}_0}(\mathbf{q}_0, \omega_0) \big] \\
& \times \cos([\mathbf{G} + \mathbf{q}_0] \cdot \mathbf{r} - \omega_0 t) \\
& - \mathrm{Im}\big[\chi_{BA}^{\mathbf{G}\mathbf{G}_0}(\mathbf{q}_0, \omega_0) \big] \sin([\mathbf{G} + \mathbf{q}_0] \cdot \mathbf{r} - \omega_0 t) \Big\}.
\end{aligned}
$$
(A39)

In full analogy with Eq. (A15), the real and imaginary parts of the plane wave susceptibility gives the response in- and out-of-phase of the harmonic perturbation, respectively. Using Eqs. (A26) and (A39), the mean rate of energy absorption may be computed:

$$
\bar{Q} = -\tfrac{1}{2} f_0^2 \omega_0 \, \Omega \, \mathrm{Im}\big[\chi_{AA}^{\mathbf{G}_0 \mathbf{G}_0}(\mathbf{q}_0, \omega_0) \big].
$$
(A40)

Compared to Eq. (A16), the plane wave susceptibility has simply been normalized by the crystal volume, such as to make it a size intensive material property, whereas the dynamic susceptibility in Eq. (A16) is a property of the quantum system $\hat{H}_0$.

For a more general perturbation than that of a single plane wave component in Eq. (A26), the energy dissipation will be governed by the full plane wave spectrum of induced transitions

$$
\begin{aligned}
S_{BA}^{\mathbf{G}\mathbf{G}'}(\mathbf{q}, \omega) & \equiv -\frac{1}{\Omega} \frac{\chi_{\beta\alpha}''(\omega)}{\pi} \\
& = -\frac{1}{2\pi i} \big[\chi_{BA}^{\mathbf{G}\mathbf{G}'}(\mathbf{q}, \omega) - \chi_{AB}^{-\mathbf{G}'-\mathbf{G}}(-\mathbf{q}, -\omega) \big].
\end{aligned}
$$
(A41)

From Eq. (A17b) it follows that the imaginary part and the dissipative part of the plane wave susceptibility are the same along the diagonal. Then, using Eq. (A37b), a clear connection from the Kubo theory to the quasiparticle picture can be made:

$$
\begin{aligned}
S_{AA}^{\mathbf{G}\mathbf{G}}(\mathbf{q}, \omega) & = -\frac{\mathrm{Im}\big[\chi_{AA}^{\mathbf{G}\mathbf{G}}(\mathbf{q}, \omega) \big]}{\pi} \\
& = \frac{1}{\Omega} \sum_{\alpha, \alpha'} |a_{\alpha'\alpha}(-\mathbf{G})|^2 (n_\alpha - n_{\alpha'}) \\
& \times \delta_{\mathbf{q}, \mathbf{q}_{\alpha'\alpha}} \delta(\hbar\omega - (E_{\alpha'} - E_\alpha)).
\end{aligned}
$$
(A42)

When various spectroscopic experiments are carried out, energy dissipation is a direct manifestation of transitions between the energy eigenstates of the system. Through Eqs. (A40) and (A42), the rate of energy absorption in a material at momentum transfer $\hbar\mathbf{q}$ and transition energy $\hbar\omega$ is proportional to the spectral density of eigenstate transitions associated with quasiparticles of crystal momentum $\hbar\mathbf{q}_{\alpha'\alpha} = \hbar\mathbf{q}$ and energy $E_{\alpha'} - E_\alpha = \hbar\omega$. The spectrum is weighted by the periodic part of the transition matrix elements associated to the spectroscopic technique in question.

APPENDIX B: FOURIER TRANSFORMS

1. Temporal Fourier transform

We use the following definition for the temporal Fourier-Laplace transform to complex frequencies:

$$
\chi_{BA}(z) = \int_{-\infty}^{\infty} dt \, \chi_{BA}(t) e^{izt}.
$$
(B1)

For retarded susceptibilities, $\chi_{BA}(z)$ is analytic in the upper half complex plane and has the inverse transform

$$
\chi_{BA}(t) = \lim_{\eta \to 0^+} \int_{-\infty}^{\infty} \frac{d\omega}{2\pi} \chi_{BA}(\omega + i\eta) e^{-i\omega t}.
$$
(B2)

2. Spatial Fourier transform

For the spatial Fourier transform, the following definition is used:

$$
f(\mathbf{Q}) = \int d\mathbf{r} \, f(\mathbf{r}) e^{-i\mathbf{Q}\cdot\mathbf{r}}.
$$
(B3)

For two-point functions, $f(\mathbf{r}, \mathbf{r}')$, the spatial Fourier transform is generalized as

$$
f(\mathbf{Q}, \mathbf{Q}') = \frac{1}{\Omega} \iint d\mathbf{r} \, d\mathbf{r}' \, e^{-i\mathbf{Q}\cdot\mathbf{r}} f(\mathbf{r}, \mathbf{r}') e^{i\mathbf{Q}'\cdot\mathbf{r}'},
$$
(B4)

where Ω is the crystal volume.

Considering a crystal with Bravais lattice points $\mathbf{R}$ and unit cell volume Ω_{cell}, we may change the integration variables:

$$
\iint d\mathbf{r} \, d\mathbf{r}' \, g(\mathbf{r}, \mathbf{r}') = \sum_{\mathbf{R}} \int_{\Omega_{\mathrm{cell}}} d\mathbf{r} \int d\mathbf{r}' \, g(\mathbf{r} + \mathbf{R}, \mathbf{r}' + \mathbf{R}).
$$
(B5)

Now take $\mathbf{G}, \mathbf{G}'$ to be reciprocal lattice vectors and $\mathbf{q}, \mathbf{q}'$ to be a wave vectors within the first BZ, then the Fourier transform of a periodic two-point function $f(\mathbf{r} + \mathbf{R}, \mathbf{r}' + \mathbf{R}) = f(\mathbf{r}, \mathbf{r}')$ reduces:

$$
\begin{aligned}
f(\mathbf{G} + \mathbf{q}, \mathbf{G}' + \mathbf{q}) & = \frac{1}{\Omega} \sum_{\mathbf{R}} \int_{\Omega_{\mathrm{cell}}} d\mathbf{r} \int d\mathbf{r}' \, e^{-i(\mathbf{G}+\mathbf{q})\cdot\mathbf{r}} e^{-i\mathbf{q}\cdot\mathbf{R}} f(\mathbf{r} + \mathbf{R}, \mathbf{r}' + \mathbf{R}) e^{i(\mathbf{G}'+\mathbf{q})\cdot\mathbf{r}'} e^{i\mathbf{q}\cdot\mathbf{R}} \\
& = \frac{1}{\Omega_{\mathrm{cell}}} \int_{\Omega_{\mathrm{cell}}} d\mathbf{r} \int d\mathbf{r}' \, e^{-i(\mathbf{G}+\mathbf{q})\cdot\mathbf{r}} f(\mathbf{r}, \mathbf{r}') e^{i(\mathbf{G}'+\mathbf{q})\cdot\mathbf{r}'},
\end{aligned}
$$
(B6)

$$
\begin{aligned}
f(\mathbf{G} + \mathbf{q}, \mathbf{G}' + \mathbf{q}') & = \frac{1}{\Omega} \sum_{\mathbf{R}} \int_{\Omega_{\mathrm{cell}}} d\mathbf{r} \int d\mathbf{r}' \, e^{-i(\mathbf{G}+\mathbf{q})\cdot\mathbf{r}} f(\mathbf{r} + \mathbf{R}, \mathbf{r}' + \mathbf{R}) e^{i(\mathbf{G}'+\mathbf{q}')\cdot\mathbf{r}'} e^{-i(\mathbf{q}-\mathbf{q}')\cdot\mathbf{R}} \\
& = \frac{1}{\Omega_{\mathrm{cell}}} \int_{\Omega_{\mathrm{cell}}} d\mathbf{r} \int d\mathbf{r}' \, e^{-i(\mathbf{G}+\mathbf{q})\cdot\mathbf{r}} f(\mathbf{r}, \mathbf{r}') e^{i(\mathbf{G}'+\mathbf{q}')\cdot\mathbf{r}'} \frac{\Omega_{\mathrm{cell}}}{\Omega} \sum_{\mathbf{R}} e^{-i(\mathbf{q}-\mathbf{q}')\cdot\mathbf{R}} \\
& = f(\mathbf{G} + \mathbf{q}, \mathbf{G}' + \mathbf{q}) \frac{(2\pi)^D}{\Omega} \delta(\mathbf{q} - \mathbf{q}').
\end{aligned}
$$
(B7)

For the periodic two-point functions, the notation $f_{\mathbf{GG'}}(\mathbf{q}) \equiv f(\mathbf{G} + \mathbf{q}, \mathbf{G'} + \mathbf{q})$ is introduced and referred to as the lattice Fourier transform.

[1] P. Monthoux, D. Pines, and G. G. Lonzarich, Nature (London) **450**, 1177 (2007).

[2] D. J. Scalapino, Rev. Mod. Phys. **84**, 1383 (2012).

[3] S. Neusser and D. Grundler, Adv. Mater. **21**, 2927 (2009).

[4] T. Moriya, *Spin Fluctuations in Itinerant Electron Magnetism*, Springer Series in Solid-State Sciences, Vol. 5 (Springer-Verlag, Berlin, 1985).

[5] L. Van Hove, Phys. Rev. **95**, 1374 (1954).

[6] J. Jensen and A. R. Mackintosh, *Rare Earth Magnetism: Structures and Excitations*, International Series of Monographs on Physics (Clarendon Press, Oxford, 1991).

[7] H. J. Qin, K. Zakeri, A. Ernst, L. M. Sandratskii, P. Buczek, A. Marmodoro, T. H. Chuang, Y. Zhang, and J. Kirschner, Nat. Commun. **6**, 6126 (2015).

[8] K. Zakeri, Phys. Rep. **545**, 47 (2014).

[9] C. F. Hirjibehedin, C. P. Lutz, and A. J. Heinrich, Science **312**, 1021 (2006).

[10] T. Balashov, A. F. Takács, W. Wulfhekel, and J. Kirschner, Phys. Rev. Lett. **97**, 187201 (2006).

[11] T. Balashov, Ph.D. thesis, Karlsruher Institut für Technologie, 2009.

[12] N. B. Brookes, D. Betto, K. Cao, Y. Lu, K. Kummer, and F. Giustino, Phys. Rev. B **102**, 064412 (2020).

[13] F. Aryasetiawan and K. Karlsson, Phys. Rev. B **60**, 7419 (1999).

[14] K. Karlsson and F. Aryasetiawan, Phys. Rev. B **62**, 3006 (2000).

[15] E. Şaşıoğlu, A. Schindlmayr, C. Friedrich, F. Freimuth, and S. Blügel, Phys. Rev. B **81**, 054434 (2010).

[16] C. Friedrich, E. Şaşıoğlu, M. Müller, A. Schindlmayr, and S. Blügel, in *First Principles Approaches to Spectroscopic Properties of Complex Materials*, edited by C. Di Valentin, S. Botti, and M. Cococcioni (Springer, Berlin, 2014), pp. 259–301.

[17] M. C. T. D. Müller, C. Friedrich, and S. Blügel, Phys. Rev. B **94**, 064433 (2016).

[18] C. Friedrich, M. C. T. D. Müller, and S. Blügel, in *Handbook of Materials Modeling: Methods: Theory and Modeling*, edited by W. Andreoni and S. Yip (Springer International Publishing, Cham, 2020), pp. 919–956.

[19] P. Hohenberg and W. Kohn, Phys. Rev. **136**, B864 (1964).

[20] W. Kohn and L. J. Sham, Phys. Rev. **140**, A1133 (1965).

[21] E. Runge and E. K. U. Gross, Phys. Rev. Lett. **52**, 997 (1984).

[22] E. K. U. Gross and W. Kohn, Phys. Rev. Lett. **55**, 2850 (1985).

[23] P. E. Blöchl, Phys. Rev. B **50**, 17953 (1994).

[24] P. Buczek, A. Ernst, and L. M. Sandratskii, Phys. Rev. B **84**, 174418 (2011).

[25] S. Lounis, A. T. Costa, R. B. Muniz, and D. L. Mills, Phys. Rev. B **83**, 035109 (2011).

[26] B. Rousseau, A. Eiguren, and A. Bergara, Phys. Rev. B **85**, 054305 (2012).

[27] N. Singh, P. Elliott, T. Nautiyal, J. K. Dewhurst, and S. Sharma, Phys. Rev. B **99**, 035151 (2019).

[28] A. L. Wysocki, A. Kutepov, and V. P. Antropov, Phys. Rev. B **94**, 140405(R) (2016).

[29] U. von Barth and L. Hedin, J. Phys. C **5**, 1629 (1972).

[30] A. K. Rajagopal and J. Callaway, Phys. Rev. B **7**, 1912 (1973).

[31] N. Tancogne-Dejean, F. G. Eich, and A. Rubio, J. Chem. Theory Comput. **16**, 1007 (2020).

[32] S. Y. Savrasov, Phys. Rev. Lett. **81**, 2570 (1998).

[33] K. Cao, H. Lambert, P. G. Radaelli, and F. Giustino, Phys. Rev. B **97**, 024420 (2018).

[34] M. Niesert, Ph.D. thesis, RWTH Aachen University, 2011.

[35] L. D. Landau, On the vibrations of the electronic plasma, in *Collected Papers of L. D. Landau*, edited by D. T. Haar (Pergamon, 1965), Vol. 2, pp. 445–460.

[36] J. J. Mortensen, L. B. Hansen, and K. W. Jacobsen, Phys. Rev. B **71**, 035109 (2005).

[37] J. Enkovaara, C. Rostgaard, J. J. Mortensen, J. Chen, M. Dułak, L. Ferrighi, J. Gavnholt, C. Glinsvad, V. Haikola, H. A. Hansen, H. H. Kristoffersen, M. Kuisma, a. H. Larsen, L. Lehtovaara, M. Ljungberg, O. Lopez-Acevedo, P. G. Moses, J. Ojanen, T. Olsen, V. Petzold *et al.*, J. Phys.: Condens. Matter **22**, 253202 (2010).

[38] J. Yan, J. J. Mortensen, K. W. Jacobsen, and K. S. Thygesen, Phys. Rev. B **83**, 245122 (2011).

[39] H. J. Monkhorst and J. D. Pack, Phys. Rev. B **13**, 5188 (1976).

[40] A. Hjorth Larsen, J. J. Mortensen, J. Blomqvist, I. E. Castelli, R. Christensen, M. Dułak, J. Friis, M. N. Groves, B. Hammer, C. Hargus, E. D. Hermes, P. C. Jennings, P. Bjerre Jensen, J. Kermode, J. R. Kitchin, E. Leonhard Kolsbjerg, J. Kubal, K. Kaasbjerg, S. Lysgaard, J. Bergmann Maronsson *et al.*, J. Phys.: Condens. Matter **29**, 273002 (2017).

[41] See Supplemental Material at http://link.aps.org/supplemental/10.1103/PhysRevB.103.245110 for additional figures and tables documenting convergence of the low-frequency Stoner spectrum.

[42] C. Loong, J. M. Carpenter, J. W. Lynn, R. A. Robinson, and H. A. Mook, J. Appl. Phys. **55**, 1895 (1984).

[43] H. A. Mook and R. M. Nicklow, Phys. Rev. B **7**, 336 (1973).

[44] H. A. Mook and D. M. Paul, Phys. Rev. Lett. **54**, 227 (1985).

[45] F. G. Eich, S. Pittalis, and G. Vignale, Eur. Phys. J. B **91**, 173 (2018).

[46] T. Perring, A. Taylor, and G. Squires, Phys. B: Condens. Matter **213–214**, 348 (1995).

[47] P. Buczek, A. Ernst, P. Bruno, and L. M. Sandratskii, Phys. Rev. Lett. **102**, 247206 (2009).

[48] M. M. Odashima, A. Marmodoro, P. Buczek, A. Ernst, and L. Sandratskii, Phys. Rev. B **87**, 174420 (2013).

[49] H. Xiang, C. Lee, H.-J. Koo, X. Gong, and M.-H. Whangbo, Dalton Trans. **42**, 823 (2013).

[50] D. Torelli and T. Olsen, 2D Mater. **6**, 015028 (2018).

[51] D. Torelli, H. Moustafa, K. W. Jacobsen, and T. Olsen, npj Comput. Mater. **6**, 158 (2020).

[52] A. Mook, J. Henk, and I. Mertig, Phys. Rev. B **90**, 024412 (2014).

[53] A. T. Costa, D. L. R. Santos, N. M. R. Peres, and J. Fernández-Rossier, 2D Mater. **7**, 045031 (2020).

[54] M. Costa, N. M. R. Peres, J. Fernández-Rossier, and A. T. Costa, Phys. Rev. B **102**, 014450 (2020).

[55] R. Kubo, J. Phys. Soc. Jpn. **12**, 570 (1957).

[56] R. Kubo, Rep. Prog. Phys. **29**, 255 (1966).

[57] H. Nyquist, Phys. Rev. **32**, 110 (1928).

[58] H. B. Callen and T. A. Welton, Phys. Rev. **83**, 34 (1951).

[59] S. L. Adler, Phys. Rev. **126**, 413 (1962).

[60] N. Wiser, Phys. Rev. **129**, 62 (1963).

Dynamic transverse magnetic susceptibility in the projected augmented wave method.
Application to Fe, Ni, and Co.

Thorbjørn Skovhus[1] and Thomas Olsen[1, *]

[1]*CAMD, Department of Physics, Technical University of Denmark, 2820 Kgs. Lyngby Denmark*
(Dated: March 9, 2021)

I.   SELECTING THE BROADENING PARAMETER
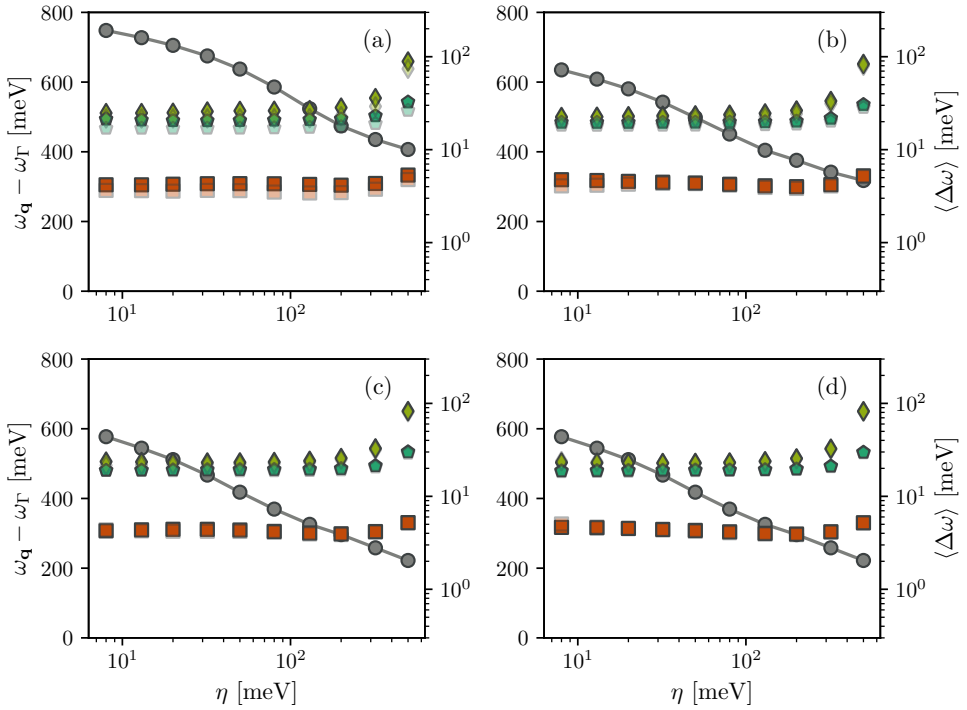
FIG. 1. Magnon peak positions of nickel relative to the Γ-peak, in color (left axis), and average displacement frequency, in grey (right axis), as a function of broadening parameter η. The panels (a), (b), (c) and (d) were calculated using $(18, 18, 18)$, $(42, 42, 42)$, $(54, 54, 54)$ and $(78, 78, 78)$ k-point grids respectively. The colors red, green and turquoise indicate the magnon peaks at wave vectors 1/3 of the way, 2/3 of the way and at the end of the path $\Gamma \to X$. The opaque and translucent markers represent results calculated using regular and Γ-centered Monkhorst-Pack grids respectively.

TABLE I. Table of threshold broadening parameters η_t calculated using a $\langle \Delta\omega \rangle \leq 5$ meV criterion. Each field in the table represents a k-point grid density for the given material. In the first row of each field, the number of grid points and grid density is given. For hcp-Co, the density is along the c-direction. In the second row, η_t is given for frequency integration ranges $[-0.2\,\mathrm{eV}, 0.2\,\mathrm{eV}]$, $[-0.4\,\mathrm{eV}, 0.4\,\mathrm{eV}]$ and $[-0.6\,\mathrm{eV}, 0.6\,\mathrm{eV}]$.

Fe (bcc) grid		density	Ni (fcc) grid		density	Co (fcc) grid		density	Co (hcp) grid		density
± 0.2	± 0.4	± 0.6	± 0.2	± 0.4	± 0.6	± 0.2	± 0.4	± 0.6	± 0.2	± 0.4	± 0.6
									(12, 12, 6)		3.9
									>500	>500	>500
(18, 18, 18)		5.8	(18, 18, 18)		5.8	(18, 18, 18)		5.9			
>500	>500	>500	>500	>500	>500	433	472	>500			
(24, 24, 24)		7.7	(24, 24, 24)		7.8	(24, 24, 24)		7.8	(18, 18, 12)		7.8
>500	>500	>500	>500	>500	>500	>500	>500	>500	>500	>500	>500
(30, 30, 30)		9.7	(30, 30, 30)		9.7	(30, 30, 30)		9.8			
>500	>500	>500	>500	>500	>500	465	410	357			
(36, 36, 36)		11.6	(36, 36, 36)		11.7	(36, 36, 36)		11.7	(30, 30, 18)		11.6
>500	>500	>500	385	328	374	213	191	179	160	173	170
(42, 42, 42)		13.6	(42, 42, 42)		13.6	(42, 42, 42)		13.7			
437	412	387	467	442	453	389	333	312			
(48, 48, 48)		15.5	(48, 48, 48)		15.5	(48, 48, 48)		15.6	(36, 36, 24)		15.5
180	160	156	268	235	273	148	122	121	79.8	105	97.2
(54, 54, 54)		17.4	(54, 54, 54)		17.5	(54, 54, 54)		17.6			
150	126	127	159	130	183	181	129	113			
(60, 60, 60)		19.4	(60, 60, 60)		19.4	(60, 60, 60)		19.5	(48, 48, 30)		19.4
95	99.3	112	142	126	182	185	143	119	71.7	73.6	72.5
(66, 66, 66)		21.3	(66, 66, 66)		21.4	(66, 66, 66)		21.5			
325	298	275	128	100	122	74.4	69	68.4			
(72, 72, 72)		23.2	(72, 72, 72)		23.3	(72, 72, 72)		23.4	(60, 60, 36)		23.3
40.1	52.8	65.3	59.9	60.7	66.1	73.4	68.4	60.3	46.5	45.6	46.2
(78, 78, 78)		25.2	(78, 78, 78)		25.3	(78, 78, 78)		25.4			
92.3	86.6	105	60.5	53.8	62.9	59	56.2	50			
(84, 84, 84)		27.1	(84, 84, 84)		27.2	(84, 84, 84)		27.3	(78, 78, 42)		27.2
45.5	54.1	60.7	49	47.4	68.9	44.2	46.4	44.1	33.3	40.7	33.7
(90, 90, 90)		29.0	(90, 90, 90)		29.1	(90, 90, 90)		29.3			
33.4	35.9	40.2	29.3	35.2	32.2	43.9	45.4	40.5			
(96, 96, 96)		31.0	(96, 96, 96)		31.1	(96, 96, 96)		31.2	(84, 84, 48)		31.1
28	32.8	40.8	19.2	27.8	20.5	39.8	42.2	36.3	26	28.3	27.1
(102, 102, 102)		32.9	(102, 102, 102)		33.0	(102, 102, 102)		33.2			
27.8	32	32.6	18.4	26	19.5	35.1	38.6	32.7			

5.2 Publication B: Interplay between static and dynamic correlation in itinerant magnets - a first principles study of magnons in MnBi

In Publication [B], we study the magnon excitations of the itinerant ferromagnet MnBi. MnBi is an interesting system to address with theoretical magnon spectroscopy for several reasons. First of all, the electronic structure of MnBi is quite different than what we are used to for Fe, Ni and Co. Most of the itinerancy is derived from a number of dispersive bands of mixed orbital character, whereas the $3d$ electronic orbitals, which mainly carry the Mn magnetic moment, form narrow bands gaped by the exchange splitting. Due to the exchange gap, only the metallic bands of mixed orbital character give rise to low frequency Stoner pair excitations and the experimental magnon spectrum [69] is without distinct itinerant electron effects. However, for an appropriate description of the material, there is still a need for treating localized and itinerant electrons on the same footing. To this end, an *ab initio* treatment of the system can better elucidate the interplay of effects with different physical origins as compared to a localized spin model Hamiltonian. More concretely, the Mn atoms are subject to a strongly correlated nearest-neighbour antiferromagnetic exchange interaction, which gives rise to inherent magnetic frustration in competition with the long range ferromagnetic exchange. Lastly, there is excellent single-crystal experimental data available for the full magnon dispersion as well as a long range of different magnetic properties of MnBi [69, 70]. For this reason, it provides an unambiguous test bed to showcase the advantages and drawbacks of the LR-TDDFT methodology, in particular with regards to the inclusion of correlation effects. In particular, it seems that the LSDA underestimates the exchange splitting by a factor of two, and it is necessary to include a Hubbard correction to the ground state, not only to appropriately describe the magnon dynamics, but also to capture ground state magnetic moments, structural properties as well as magnetic anisotropy and magneto-optical effects [71, 72].

5.2.1 The inverse enhancement function

To characterize the collective enhancement of magnon quasi-particles out of the single-particle Stoner continuum and to better understand the breakdown of the Dyson equation (3.40) when used on a LSDA+U ground state, we introduce in Publication [B] the so-called inverse enhancement function (IEF):

$$\kappa_{\mathbf{G}}^{+-}(\mathbf{q}, \omega) = \mathrm{Re}\left[\frac{\chi_{\mathrm{KS},\mathbf{G}\mathbf{G}}^{+-}(\mathbf{q}, \omega)}{\chi_{\mathbf{G}\mathbf{G}}^{+-}(\mathbf{q}, \omega)}\right]. \tag{5.1}$$

In the homogeneous electron gas limit, the IEF exactly determines the enhancement of the many-body spectrum, that is, the spectrum is enhanced when $\kappa^{+-}(q, \omega) = 1 - \mathrm{Re}\left[\chi_{\mathrm{KS}}^{+-}(q, \omega)\right] f_{\mathrm{LSDA}}^{-+}$ has a root. In periodic crystals, the collective enhancement is instead governed by the matrix $\left(1 - \chi_{\mathrm{KS}}^{+-}(\mathbf{q}, \omega) f_{\mathrm{LSDA}}^{-+}\right)_{[\mathbf{G}]}^{-1}$ (see the Dyson equation (3.40)), whereto the IEF provides a post hoc characterization in terms of a simple

scalar quantity. In frequency dependence, the IEF resembles the real part of the Kohn-Sham susceptibility with pole-like features at peaks in the Kohn-Sham Stoner spectrum. Furthermore, also for periodic crystals, the IEF attains a root whenever the many-body spectrum is maximally enhanced outside the Kohn-Sham Stoner spectrum, that is, one may essentially characterize the dispersion of undamped magnons in terms of the IEF roots. In addition, it is our experience that the picture of maximal enhancement at the IEF roots also holds approximately for Landau damped magnons.

We envision that the IEF can provide a transparent tool for analysis of the itinerant electron effects in theoretical magnon spectroscopy. In particular, we have found it extremely useful in order to understand why the stripe-like features in the Kohn-Sham Stoner spectrum of Fe and Ni make the magnon dispersion jump. For magnon frequencies below the given Stoner peak, the Stoner pair excitations contribute attractively to the collective enhancement, but for frequencies above the Stoner resonance, this is no longer the case as the stripe's contribution to the reactive (real) part of $\chi_{KS,\mathbf{GG}}^{+-}(\mathbf{q}, \omega)$ has changed sign. In turn, this forces the magnon dispersion to make a discontinuous jump to higher frequencies as it crosses the Stoner spectral peak. This is most clearly visualized by the third and largest jump in the magnon dispersion of Fe along the $\Gamma \to H$ direction, shown in Figure 5.1. Because the IEF inherits a pole-like feature from the Stoner peak, the IEF attains a new root several hundreds of meV above the old as the Stoner peak center passes through $\kappa^{+-}(\mathbf{q}, \omega) = 0$. This leads to an equally large discontinuous jump in the point of maximal enhancement and hence the magnon dispersion. Due to the change in sign of the Stoner peak's contribution to the collective enhancement, we view the magnon modes below and above the Stoner peak as *separate*
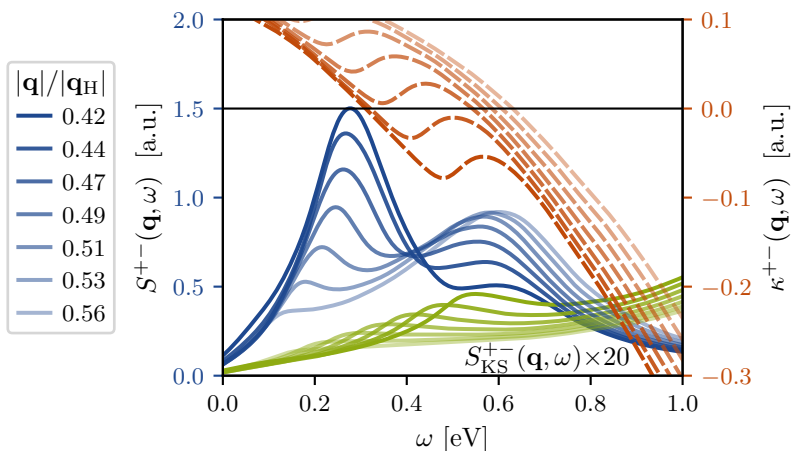
Figure 5.1: Collective magnon enhancement in bcc-Fe along the $\Gamma \to H$ high-symmetry path. Left axis: The macroscopic (unit-cell averaged, $\mathbf{G} = \mathbf{0}$) Kohn-Sham Stoner spectrum and many-body spectrum of transverse magnetic excitations shown in green and blue respectively, with color intensities decreasing with $|\mathbf{q}|$ according to the legend. Right axis: Inverse enhancement function (5.1) plotted in red for each set of noninteracting/many-body spectra.

modes of excitation. Furthermore, as the stripe-like feature is a direct consequence of the spin inversion of the given Stoner pair for specific wave vectors $\mathbf{q}$, the multitude of magnon modes, that such features imply, is an itinerant electron effect.

5.2.2   Summary of results

In the case of MnBi, we use the IEF to find an appropriate scaling of the ALDA kernel in order to satisfy the Goldstone condition for LR-TDDFT calculations on the basis of LSDA+U ground states. However, it is in no way certain that a flat scaling of the ALDA kernel should provide a physical magnon spectrum. In fact, it scales both kernel contributions from the Mn $3d$ electrons targeted by the Hubbard correction as well as contributions from the dispersive bands of mixed orbital character. Furthermore, the corresponding scaled LSDA xc potential most certainly does not reproduce the LSDA+U ground state, thus breaking the consistency of the Dyson equation (3.40). Therefore, it is not a trivial result, that a Hubbard correction included in this way consistently improves on the ALDA accuracy for the magnon dispersion when compared to experiment, resulting in an excellent qualitative agreement using $U_{\mathrm{eff}} = 3$ eV in the Dudarev Hubbard correctional scheme [61].

The chosen value of $U_{\mathrm{eff}} = 3$ eV for the Hubbard correction is not only an appropriate choice based on the constrained random phase approximation and constrained LSDA methods [71], it also provides the best overall match to the experimental magnon dispersion in our calculations. Interestingly, there is an upper bound for the choice of U_{eff}, above which the ferromagnetic state becomes dynamically unstable, resulting in a magnetic phase transition to helical order. In Publication [B], we discuss this transition and is relation to the inherent magnetic frustration in detail. In experiment however, U_{eff} cannot be tuned. Instead we show that a similar phase transition can be induced with hole doping and uniaxial strain, at least in simulation. Because it requires much less effort to adjust such parameters in simulation compared to experiment, we believe that theoretical magnon spectroscopy over time can become a valuable tool for screening the effect of different material variables on quantum phase transitions in particular and magnetic interactions in general. In essence, Publication [B] provides a first step in this direction for the material family of transition metal pnictides.

Interplay between static and dynamic correlation in itinerant magnets - a first principles study of magnons in MnBi

Thorbjørn Skovhus,[1] Thomas Olsen,[1, *] and Henrik M. Rønnow[2]

[1] CAMD, Department of Physics, Technical University of Denmark, 2800 Kgs. Lyngby, Denmark
[2] LQM, Institute of Physics, École Polytechnique Fédérale de Lausanne, CH-1015 Lausanne, Switzerland

We present first principles calculations of the dynamic susceptibility in strained and doped ferromagnetic MnBi using time-dependent density functional theory. In spite of being a metal, MnBi exhibits signatures of strong correlation and a proper description in the framework of density functional theory requires Hubbard corrections to the Mn d-orbitals. Here we develop a consistent rescaling of the exchange-correlation kernel that permits calculations of the dynamic susceptibility that includes Hubbard corrections without deteriorating the delicate balance between the magnon dispersion and the Stoner continuum. We find excellent agreement with the experimentally observed magnon dispersion for pristine MnBi and show that the material undergoes a phase transition to helical order under application of either doping or strain. The presented methodology pave the way for susceptibility calculations of a wide range of magnetic materials that require Hubbard corrections for a proper description of the ground state in the framework of density functional theory.

I. INTRODUCTION

MnBi has been proposed as a promising alternative to permanent magnets based on rare-earth elements [1–3]. This is primarily due to the large spontaneous magnetization at room temperature [4], strong uniaxial magnetic anisotropy [5] and the abundance of its constituent elements [6]. Moreover, it exhibits an extraordinarily large Kerr rotation [7], which makes it an ideal candidate for magnetooptical data storage applications [8, 9]. From a fundamental point of view MnBi is an intriguing material since it can be regarded as a member of the transition metal pnictides AX (A=V/Cr/Mn/Fe/Co/Ni, X=P/As/Sb), which realize a wide variety of spiral magnetic orders depending on the composition, pressure and temperature [10–12]. In particular, MnP and CrAs have recently been demonstrated to exhibit unconventional superconductivity below 1 K [13] and 2 K [14] respectively. The superconducting state emerges at the critical pressure for magnetic order and has been argued to imply an unconventional mechanism for Cooper pairing associated with magnetic quantum fluctuations [14]. The possibility of tayloring the magnetic order by pressure or doping in transition metal pnictides thus facilitates exploration of unconventional superconductivity in proximity of spiral magnetic order, but the microscopic origin of different spiral ordering is complex and still not completely understood. For example, at low temperatures MnP exhibits helical order at ambient pressure, becomes ferromagnetic at ∼ 1 GPa, makes a transition to a second helical phase at ∼ 1.5 GPa and finally becomes paramagnetic at 6.7 GPa with a superconducting window at pressures $6.7 < P < 8$ GPa [10]. While MnBi has not been reported to exhibit phase transitions involving helical order, a phase transition from ferromagnetic to helical order has has been observed for the isostructural MnAs

upon doping with Cr [15] and it is not unlikely that a similar transition may occur in MnBi.

At room temperature, MnBi crystallizes in the hexagonal NiAs structure with space group $P6_3/mmc$. Upon cooling, MnBi undergoes a structural phase transition at 90 K, where the in-plane hexagonal symmetry is slightly broken and the crystal structure becomes orthorhombic (space group $Cmcm$) [16]. It is ferromagnetic up to 630 K where is segregates into $Mn_{1.08}Bi$ and Bi [17], which are both paramagnetic. The true Curie temperature is thus unknown, but the lower bound of 630 K indicates strong magnetic interactions in the material. At room temperature, MnBi exhibits a large uniaxial magnetic anisotropy along the c-axis of the NiAs crystal structure. The anisotropy decreases with decreasing temperature and aligns with the ab-plane of the orthorhombic phase below 90 K [16]. For thin film [18, 19] and nanocrystalline [20] MnBi, it has been shown that Cr doping lowers the Curie temperature below the segregation temperature for $Mn_{1-x}Cr_xBi$ doping levels down to at least $x = 0.03$. For Cr doping in the range of 3-15%, Curie temperatures have been recorded to lie in the 520-560 K range. Moreover, the coercivity has been shown increase significantly by Cr doping [20], while the beneficial magneto-optical properties are retained. To our knowledge there has so far not been attempts to study the low-temperature magnetic structure of Cr-doped MnBi.

The magnon spectrum of MnBi at 5 K was been measured by Williams et al. using inelastic neutron scattering [21]. The hexagonal phase was assumed in the analysis of results, which is likely to be a good approximation due to the strong similarity with the orthorhombic phase expected at low temperatures [21]. The magnon band width is on the order of 100 meV and the spectrum was found to be gapless as expected from the easy-plane anisotropy at low temperatures. It was shown that the spectrum is well reproduced by fitting to an isotropic Heisenberg model with 6 exchange parameters. While such a fit may not be unique, the nearest neigh-

bor interaction was unambiguously shown to be anti-ferromagnetic having the largest magnitude of all interactions. The inherent magnetic frustration thus makes it highly plausible that a magnetic phase transition may be induced by external strain or doping, which will inevitable influence the individual exchange parameters differently.

From a computational perspective the magnetic excitation spectrum can be accessed at various levels of accuracy. The simplest approach is to assume a Heisenberg model description and extract the exchange parameters by a total energy mapping approach in the framework of Density Functional Theory (DFT) [22–24]. This will yield the spin-wave spectrum directly in the noninteracting magnon approximation to the model. Alternatively, one can obtain the dispersion relation directly from the magnetic force theorem [25–27], which is more practical when long range interactions are involved although the method explicitly assumes a *classical* Heisenberg model description. For itinerant magnets, the model assumption becomes somewhat dubious although it is often possible to fit spin-wave spectra to Heisenberg models if enough exchange parameters are included in the fit [28]. However, certain qualitative aspects, such as Landau damping cannot be obtained from Heisenberg models and magnon spectra calculated without reference to models strongly facilitate comparison and analysis of experimental results. Linear Response Time-Dependent Density Functional Theory (LR-TDDFT) provides such a first principles framework [29, 30] and has been successfully applied to extract magnon dispersion relations and magnon lifetimes for several simple itinerant ferromagnets [31–35]. While formally exact, LR-TDDFT in practice relies on approximations for the exchange-correlation kernel such as the Adiabatic Local Density Approximation (ALDA). The accuracy of this approach is strongly dependent of the system at hand. For example, ALDA LR-TDDFT captures the magnon spectrum of bcc-Fe and hcp-Co rather accurately, whereas the bandwidth of the magnon spectrum of fcc-Ni is overestimated by a factor of two [35, 36]. The main reason for the inaccuracy is likely related to the inability of ALDA to correct for the Kohn-Sham exchange splitting, which is overestimated in LDA.

In the context of static DFT, the disagreement between the Kohn-Sham spectrum and the quasi-particle spectrum may often be alleviated by the DFT+U approach [37–39] where an on-site Hubbard repulsion is added, which tends to localize orbitals and typically increase the band gap as well as the exchange splitting. In particular, Antropov et al. [40] have shown that DFT+U is crucial to describe the ground state magnetic moments as well as the temperature-dependent magnetic anisotropy correctly in MnBi. Similarly, a Hubbard correction is also needed to reach an appropriate description of the structural properties of MnBi [41]. However, in the context of LR-TDDFT it is not obvious how to include the Hubbard correction at the level of the exchange-correlation

kernel, which introduces a mismatch between the kernel and the orbitals. This has severe consequences for the calculations since the delicate balance between the magnon spectrum and single-particle excitations is lost, leading to a gross violation of the Goldstone theorem in the combination of DFT+U and ALDA LR-TDDFT.

In the present work, we introduce a simple rescaling of the exchange-correlation kernel that eliminates the mismatch between single-particle Stoner spectrum and magnon spectrum. The rescaling is fixed by the requirement of a gap-less acoustic magnon mode and does not introduce any new free parameters apart from the ground state Hubbard correction. It is shown that the experimentally measured magnon spectrum is accurately captured within λALDA+U LR-TDDFT, whereas the neglect of Hubbard corrections leads to an overestimation of the optical magnon frequencies by at least a factor of two. In this way, it is demonstrated, that dynamic correlation effects are essential to include in order to correctly capture the inherent magnetic frustration in MnBi. Inclusion of the Hubbard correction strengthens the out-of-plane anti-ferromagnetic exchange interaction, and when artificially increasing the Hubbard correction beyond the experimental match, MnBi is imposed a phase transition to helical order. We demonstrate that MnBi undergoes a similar phase transition upon the introduction of either hole-doping (as one would expect in a Cr-alloy) or under uniaxial compressive strain in the out-of-plane direction.

The paper is organized as follows. In Sec. II we outline the theoretical concepts underlying the LR-TDDFT framework for theoretical magnon spectroscopy. In Sec. III we show how the Hubbard correction is included and how to determine the rescaled exchange-correlation kernel that is required when combing LDA+U with ALDA LR-TDDFT. In addition, we also supply the computational details. In Sec. IV we present the results of our study, including static correlation effects in the ground state, dynamic correlation effects in the magnon spectrum of pristine MnBi as well as the effect of hole doping and uniaxial compressive strain on magnon dynamics. Finally, in Sec. V we discuss how the results fit in as another piece in the puzzle of the complex magnetic phases in the transition metal pnictide family and in Sec. VI we summarize our conclusions.

II. THEORY

A. The transverse magnetic susceptibility

As exploited experimentally in inelastic neutron scattering and similar spectroscopic techniques, one may probe the fundamental excitations of a material by studying its response to external perturbations. In a collinear treatment, the linear order response in the transverse magnetic degrees of freedom can be fully characterized by a single response function, namely the transverse magnetic susceptibility. The susceptibility is given by the

Kubo formula,

$$\chi^{+-}(\mathbf{r}, \mathbf{r}', t - t') = -\frac{i}{\hbar}\theta(t - t')\langle\,[\hat{n}_0^+(\mathbf{r}, t), \hat{n}_0^-(\mathbf{r}', t')]\,\rangle_0,$$
(1)

where $\langle\cdot\rangle_0$ is the expectation value with respect to the ground state, $\theta(t - t')$ is the step function and $\hat{n}^\pm$ are the spin-raising and spin-lowering density operators respectively:

$$\hat{n}^+(\mathbf{r}) = \hat{\psi}_\uparrow^\dagger(\mathbf{r})\hat{\psi}_\downarrow(\mathbf{r}), \quad \hat{n}^-(\mathbf{r}) = \hat{\psi}_\downarrow^\dagger(\mathbf{r})\hat{\psi}_\uparrow(\mathbf{r}).$$
(2)

In Eq. (1), the operators carry the time-dependence of the interaction picture, $\hat{n}_0^\pm(\mathbf{r}, t) \equiv e^{i\hat{H}_0 t/\hbar}\,\hat{n}^\pm(\mathbf{r})\,e^{-i\hat{H}_0 t/\hbar}$, where $\hat{H}_0$ is the Hamiltonian of the unperturbed system, which in the case of MnBi has a ferromagnetic ground state. Furthermore, one may interchange the $+$ and $-$ indices in Eq. (1) to define the susceptibility χ^{-+}, but thanks to the relation $\chi^{-+}(\mathbf{r}, \mathbf{r}', -\omega) = \chi^{+-*}(\mathbf{r}, \mathbf{r}', \omega)$, it is sufficient to consider only χ^{+-}.

From the dissipative (anti-symmetric) part of the susceptibility, one may extract the spectrum of induced excitations [35]:

$$S^{+-}(\mathbf{r}, \mathbf{r}', \omega) = -\frac{1}{2\pi i}\left[\chi^{+-}(\mathbf{r}, \mathbf{r}', \omega) - \chi^{-+}(\mathbf{r}', \mathbf{r}, -\omega)\right].$$
(3)

For a ferromagnet (assumed spin-polarized along the z-direction), this spectrum determines the energy dissipation from weak perturbations in the transverse magnetic field $B_\text{ext}^{x/y}(\mathbf{r}, t)$. Furthermore, $S^{+-}(\mathbf{r}, \mathbf{r}', \omega)$ constitutes a spectral function for the excited states which differ by a single unit of spin angular momentum compared to the ground state. In this way, one may use various spectroscopic techniques to extract $S^{+-}(\mathbf{r}, \mathbf{r}', \omega)$, permitting direct access to the transverse magnetic excitations of the system. Alternatively, $S^{+-}(\mathbf{r}, \mathbf{r}', \omega)$ may be computed by theoretical spectroscopy techniques, which may aid the interpretation of measurements significantly. More importantly, calculations of the transverse susceptibility allow one to rapidly scrutinize the effect of material modifications such as strain and doping, which may be time-consuming and costly to investigate experimentally.

B. Computing the transverse magnetic susceptibility within LR-TDDFT

As a consequence of the Runge-Gross theorem [29], the time-dependent electronic structure of any material may be characterized in terms of an auxiliary Kohn-Sham system of non-interacting electrons where the electronic Coulomb repulsion is replaced by an effective (electromagnetic) potential. The susceptibility of the Kohn-Sham system can be evaluated using only quantities from a routine ground state DFT calculation [42–45],

$$\chi_\text{KS}^{+-}(\mathbf{r}, \mathbf{r}', \omega) = \lim_{\eta \to 0^+}\frac{1}{N_k^2}\sum_{n\mathbf{k}}\sum_{m\mathbf{k}'}(f_{n\mathbf{k}\uparrow} - f_{m\mathbf{k}'\downarrow})$$
$$\times\frac{\psi_{n\mathbf{k}\uparrow}^*(\mathbf{r})\psi_{m\mathbf{k}'\downarrow}(\mathbf{r})\,\psi_{m\mathbf{k}'\downarrow}^*(\mathbf{r}')\psi_{n\mathbf{k}\uparrow}(\mathbf{r}')}{\hbar\omega - (\epsilon_{m\mathbf{k}'\downarrow} - \epsilon_{n\mathbf{k}\uparrow}) + i\hbar\eta},$$
(4)

where N_k is the number of k-points, $\psi_{n\mathbf{k}s}(\mathbf{r})$ the Kohn-Sham orbital of band index n, k-point $\mathbf{k}$ and spin s, $f_{n\mathbf{k}s}$ the ground state occupancy and $\epsilon_{n\mathbf{k}s}$ the single-particle energy. In the adiabatic local density approximation (ALDA), the transverse magnetic susceptibility is directly related to the corresponding Kohn-Sham susceptibility through a single Dyson equation [30],

$$\chi^{+-}(\mathbf{r}, \mathbf{r}', \omega) = \chi_\text{KS}^{+-}(\mathbf{r}, \mathbf{r}', \omega) + \int d\mathbf{r}_1$$
$$\times\chi_\text{KS}^{+-}(\mathbf{r}, \mathbf{r}_1, \omega)f_\text{LDA}^{-+}(\mathbf{r}_1)\chi^{+-}(\mathbf{r}_1, \mathbf{r}', \omega),$$
(5)

where $f_\text{LDA}^{-+}(\mathbf{r}_1) = 2W_\text{xc,LDA}^z(\mathbf{r})/n^z(\mathbf{r})$ is the transverse LDA kernel. Similar to the Kohn-Sham susceptibility, the kernel is given solely in terms of ground state quantities, namely the magnetic contribution to the LDA exchange-correlation potential, $W_\text{xc,LDA}^z(\mathbf{r})$ (equal to the effective magnetic field up to a factor of μ_B), and the spin-polarization density $n^z(\mathbf{r})$. In this way, one can compute the many-body susceptibility of a given material within LR-TDDFT by computing $\chi_\text{KS}^{+-}(\mathbf{r}, \mathbf{r}', \omega)$ and $f_\text{LDA}^{-+}(\mathbf{r})$ for the LDA ground state and inverting the Dyson equation (5) within a suitable basis.

C. Magnons and the plane wave susceptibility

For periodic crystals (where $\hat{H}_0$ is invariant under lattice transformations $\hat{T}_\mathbf{R}$), one may characterize the transverse magnetic response in terms of the plane wave susceptibility,

$$\chi_{\mathbf{G}\mathbf{G}'}^{+-}(\mathbf{q}, \omega) = \iint\frac{d\mathbf{r}d\mathbf{r}'}{\Omega}e^{-i(\mathbf{G}+\mathbf{q})\cdot\mathbf{r}}\chi^{+-}(\mathbf{r}, \mathbf{r}', \omega)e^{i(\mathbf{G}'+\mathbf{q})\cdot\mathbf{r}'},$$
(6)

where Ω is the crystal volume, $\mathbf{G}$ and $\mathbf{G}'$ are reciprocal lattice vectors and $\mathbf{q}$ is a wave vector within the first Brillouin Zone (BZ). The plane wave susceptibility determines the coefficients for the linear order plane wave response $\propto e^{i([\mathbf{G}+\mathbf{q}]\cdot\mathbf{r} - \omega t)}$ to an external plane wave perturbation $\propto e^{i([\mathbf{G}'+\mathbf{q}]\cdot\mathbf{r} - \omega t)}$, a response which is diagonal in the reduced wave vector $\mathbf{q}$, thanks to the periodicity of the crystal.

In full analogy with Eq. (3), one can compute the plane wave spectrum of induced excitations [35]:

$$S_{\mathbf{G}\mathbf{G}'}^{+-}(\mathbf{q}, \omega) = -\frac{1}{2\pi i}\left[\chi_{\mathbf{G}\mathbf{G}'}^{+-}(\mathbf{q}, \omega) - \chi_{-\mathbf{G}'-\mathbf{G}}^{-+}(-\mathbf{q}, -\omega)\right].$$
(7)

This spectrum can be decomposed into contributions from spin-lowering and spin-raising excitations encoded in the spectral functions $A_{\mathbf{GG}'}^{+-}(\mathbf{q}, \omega)$ and $A_{\mathbf{GG}'}^{-+}(\mathbf{q}, \omega)$ respectively:

$$S_{\mathbf{GG}'}^{+-}(\mathbf{q}, \omega) = A_{\mathbf{GG}'}^{+-}(\mathbf{q}, \omega) - A_{-\mathbf{G}'-\mathbf{G}}^{-+}(-\mathbf{q}, -\omega). \quad (8)$$

Both of these spectral functions have peaks at frequencies $\hbar\omega = E_\alpha - E_0$ corresponding to the transition energies between the excited states $|\alpha\rangle$ and the ground state $|\alpha_0\rangle$. The contribution from each excited state is weighted by the reciprocal space pair densities $n_{\alpha\alpha'}^j(\mathbf{G} + \mathbf{q})$,

$$A_{\mathbf{GG}'}^{jk}(\mathbf{q}, \omega) = \frac{1}{\Omega} \sum_{\alpha \neq \alpha_0} n_{0\alpha}^j(\mathbf{G} + \mathbf{q}) n_{\alpha 0}^k(-\mathbf{G}' - \mathbf{q})$$
$$\times \delta(\hbar\omega - (E_\alpha - E_0)), \quad (9)$$

where $\delta(\hbar\omega - \Delta E)$ denotes the Dirac delta-function. The reciprocal space pair densities are Fourier transforms of the real-space pair densities $n_{\alpha\alpha'}^j(\mathbf{r}) = \langle\alpha|\hat{n}^j(\mathbf{r})|\alpha'\rangle$. As the effect of the spin-lowering and spin-raising operators is to remove a spin-up or a spin-down electron at the position $\mathbf{r}$ respectively and replace it with an electron of the opposite spin, the A^{+-} and A^{-+} spectral functions include only excited states for which the spin angular momentum has been either lowered or raised by a single unit compared to the ground state. Furthermore, the reciprocal space pair densities are only non-zero for excited states which differ in crystal momentum by $\hbar\mathbf{q}$ compared to the ground state. In this way, $A_{\mathbf{GG}'}^{+-}(\mathbf{q}, \omega)$ and $A_{\mathbf{GG}'}^{-+}(\mathbf{q}, \omega)$ encode quasi-particle excitations of energy $\hbar\omega$ and crystal momentum $\hbar\mathbf{q}$, excitations that carry a single unit of spin angular momentum. In turn, the plane wave spectrum $S_{\mathbf{GG}'}^{+-}(\mathbf{q}, \omega)$ of a ferromagnet assumed spin-polarized in the z-direction encodes majority-to-minority magnons at positive frequencies and minority-to-majority magnons at negative frequencies. Concerning the reciprocal lattice vectors, it is useful to focus on the diagonal $S_{\mathbf{G}}^{+-}(\mathbf{q}, \omega) = S_{\mathbf{GG}}^{+-}(\mathbf{q}, \omega)$. As the reciprocal lattice vector $\mathbf{G}$ represents the local field component of the spin-flipping pair densities, it also represents the local spin texture of the excitations within the unit cell. Accordingly, the acoustic magnon mode will appear in the spectrum $S_{\mathbf{G}}^{+-}(\mathbf{q}, \omega)$ for values of $\mathbf{G}$ for which the magnetic atoms of the unit cell are in phase. Likewise, the optical mode of MnBi will be visible in $S_{\mathbf{G}}^{+-}(\mathbf{q}, \omega)$ for values of $\mathbf{G}$, for which the two Mn atoms in the unit cell are out of phase.

III. METHODOLOGY

A. Ground state Hubbard correction

Although one would not normally expect strong correlation effects in metals, previous *ab initio* studies of MnBi have shown that the LDA provides an insufficient description of properties ranging from lattice constants and equilibrium magnetic moments to the temperature dependent magnetic anisotropy and magneto-optical effects [40, 41]. For these properties, a significant improvement is obtained when including a Hubbard-like on-site correction to the $3d$ electronic orbitals of Mn. In this study, we apply the rotationally invariant Dudarev LDA+U scheme [39], where the Coulomb interaction amongst the $3d$ electrons is corrected with a single effective Hubbard parameter $U_{\text{eff}} = U - J$. The Hubbard correction favors idempotency and splits the localized majority and minority $3d$ bands by a value similar to U_{eff}.

B. Hubbard correction and LR-TDDFT

In order to relate the Kohn-Sham susceptibility to the many-body susceptibility by means of the Dyson equation (5), the xc-kernel needs to be derived from a time-dependent xc-potential that reproduces the correct ground state spin densities and effective potentials in the static limit (in the absence of an external perturbation). This implies, that the ALDA xc-kernel cannot be used to calculate the transverse magnetic susceptibility based on a LDA+U ground state calculation.

1. Collective enhancement

To elaborate on how the Dyson equation (5) breaks down in practice, we invert it in the plane wave basis,

$$\chi_{[\mathbf{G}]}^{+-}(\mathbf{q}, \omega) = \left(1 - \chi_{\text{KS}}^{+-}(\mathbf{q}, \omega) f_{\text{LDA}}^{-+}\right)_{[\mathbf{G}]}^{-1} \chi_{\text{KS},[\mathbf{G}]}^{+-}(\mathbf{q}, \omega), \quad (10)$$

and compare it to the Dyson equation for a homogeneous electron gas (HEG), for which the susceptibility in reciprocal space is a scalar function of the wave number q [46, 47]:

$$\chi^{+-}(q, \omega) = \frac{\chi_{\text{KS}}^{+-}(q, \omega)}{1 - \chi_{\text{KS}}^{+-}(q, \omega) f_{\text{LDA}}^{-+}}. \quad (11)$$

For $\chi^{+-}(q, \omega)$, $\chi_{\text{KS}}^{+-}(q, \omega)$ and the diagonal elements of $\chi_{\mathbf{GG}'}^{+-}(\mathbf{q}, \omega)$, the spectrum of induced excitations is proportional to the imaginary part of the susceptibility [35]: $S_{\mathbf{G}}^{+-}(\mathbf{q}, \omega) = -\text{Im}[\chi_{\mathbf{GG}}^{+-}(\mathbf{q}, \omega)]/\pi$. The Kohn-Sham spectrum $S_{\text{KS}}^{+-}(q, \omega)$ forms a continuum of Stoner pair excitations, that is, single-particle electron-hole pairs involving a single spin-flip. Through Eq. (11), the Stoner excitations are carried over to the many-body spectrum $S^{+-}(q, \omega)$ at a renormalized spectral intensity determined by the real part of the denominator. Apart from the Stoner excitations, Eq. (11) also permits a new type of excitation at the roots of the real part of the denominator. Inspired by this fact, we introduce the inverse enhancement function (IEF):

$$\kappa^{+-}(q, \omega) \equiv \text{Re}\left[\frac{\chi_{\text{KS}}^{+-}(q, \omega)}{\chi^{+-}(q, \omega)}\right] = 1 - \text{Re}\left[\chi_{\text{KS}}^{+-}(q, \omega)\right] f_{\text{LDA}}^{-+}. \quad (12)$$

This function determines the collective enhancement of the many-body spectrum due to the electron-electron interaction described by f_{LDA}^{-+}. Outside the Stoner continuum, where $\mathrm{Im}\big[\chi_{\mathrm{KS}}^{+-}(q,\omega)\big] = 0$, collective magnon excitations appear at roots of the IEF. Furthermore, if the IEF vanishes (or nearly vanishes) inside the Stoner continuum, the Stoner pair excitations in the vicinity are enhanced. Whereas the Stoner continuum for the spin-polarized HEG is gapped at $q = 0$ by the exchange splitting energy Δ_{x}, the many-body spectrum exhibits a so-called Goldstone magnon mode with $\omega_{q=0} = 0$. As the IEF defines the magnon dispersion exactly outside the Stoner continuum, the Goldstone theorem thus dictates that $\kappa^{+-}(0,0) = 0$ for the spin-polarized HEG. In a similar spirit, we may introduce the following expression as the inverse enhancement function for periodic crystals:

$$\kappa_{\mathbf{G}}^{+-}(\mathbf{q},\omega) \equiv \mathrm{Re}\left[\frac{\chi_{\mathrm{KS},\mathbf{GG}}^{+-}(\mathbf{q},\omega)}{\chi_{\mathbf{GG}}^{+-}(\mathbf{q},\omega)}\right]. \qquad (13)$$

Whereas the IEF for the HEG *determines* the collective enhancement in the Dyson equation (11), $\kappa_{\mathbf{G}}^{+-}(\mathbf{q},\omega)$ provides a post hoc *characterization* of the enhancement. Nevertheless, we find that the magnon condition $\kappa_{\mathbf{G}}^{+-}(\mathbf{q},\omega) = 0$ provides a good approximation for the peak position of magnon excitations away from dense parts of the Stoner continuum for MnBi as well as for the simpler itinerant ferromagnets Fe, Ni and Co. More generally, it is the matrix $\big(1 - \chi_{\mathrm{KS}}^{+-}(\mathbf{q},\omega)f_{\mathrm{LDA}}^{-+}\big)^{-1}_{[\mathbf{G}]}$ that determines the enhancement in the Dyson equation (10). Thus, it is somewhat surprising that the collective enhancement can be effectively characterized using a scalar function for each local field component. We attribute this success to the fact that the definition in Eq. (13) involves the fully enhanced $\chi_{\mathbf{GG}}^{+-}(\mathbf{q},\omega)$, thus implicitly accounting for the contribution of all plane wave components.

2. Gap error and rescaling of the ALDA kernel

In Fig. 1(a) the collective enhancement is illustrated for the Goldstone mode of MnBi at $\mathbf{q} = 0$, calculated using the ALDA kernel on the LDA ground state. The Kohn-Sham spectrum has a well-defined peak at 2.9 eV, corresponding to the LDA exchange splitting. At the Kohn-Sham peak position, the IEF exhibits a pole-like feature with a shape that closely resembles $\mathrm{Re}\big[\chi_{\mathrm{KS},\mathbf{GG}}^{+-}(\mathbf{q},\omega)\big]$, which in turn forms a Kramers-Kronig pair with the Kohn-Sham spectrum. In this way, the plane wave IEF behaves exactly as one would expect from the HEG, where $\mathrm{Re}\big[\chi_{\mathrm{KS}}^{+-}(q,\omega)\big]$ carries all the frequency dependence in $\kappa^{+-}(q,\omega)$, as seen from Eq. (12). Far away from the Stoner continuum, the Kohn-Sham susceptibility vanishes and the IEF goes to unity. Because the IEF takes negative values for frequencies just below the exchange splitting energy, it also obtains a root below the Kohn-Sham peak, which in the macro-scopic case ($\mathbf{G} = \mathbf{0}$) gives rise to the acoustic (Goldstone) magnon mode. For the ALDA kernel applied to the the LDA ground state shown in Fig. 1(a), the acoustic magnon frequency goes to zero in the long-range limit, thus fulfilling the Goldstone theorem (at least within some tenths of meV using the applied computational parameters).

When applying the ALDA kernel to the LDA+U ground state however, the Goldstone theorem is violated. As shown in Fig. 1(b), including a Hubbard correction of $U_{\mathbf{eff}} = 3$ eV increases the Kohn-Sham peak position to 6.2 eV, i.e. the effective exchange splitting increases by a value $\simeq U_{\mathbf{eff}}$. However, the ALDA kernel does not change sufficiently to accommodate the increased exchange splitting, resulting in a gap error of $\omega_{\Gamma} = 2.6$ eV. In the HEG limit, the ALDA kernel amounts to a scalar entity giving the effective interaction strength amongst the single-particle Stoner excitations. Furthermore, the HEG magnon spectrum consist of a single mode, i.e. only a unique root in $\kappa^{+-}(q,\omega)$ corresponds to a collective excitation. Consequently, the Goldstone condition $\kappa^{+-}(0,0) = 0$ fixes the scalar ALDA kernel f_{LDA}^{-+} in Eq. (11). Conversely, if the Goldstone condition is violated, it is consistent with the ALDA to simply scale the value of f_{LDA}^{-+} to satisfy $\kappa^{+-}(0,0) = 0$. In a similar spirit, we rescale the plane wave kernel $f_{\mathrm{LDA},[\mathbf{G}]}^{-+} \to \lambda f_{\mathrm{LDA},[\mathbf{G}]}^{-+}$ such as to satisfy the approximate Goldstone condition $\kappa_{\mathbf{G}=\mathbf{0}}^{+-}(\mathbf{q} = \mathbf{0},\omega = 0) = 0$ whenever a Hubbard correction has been applied. Henceforward, we will refer to the kernel calculated in this way as the λALDA+U kernel. As seen in Fig. 1(b), this rescaling increases the intensity of the pole-like feature in $\kappa_{\mathbf{G}}^{+-}(\mathbf{q},\omega)$ stemming from the Stoner continuum and thus effectively moves the root as well as the magnon peak position to zero frequency. Since the Hubbard correction mainly affects the $3d$ electrons, it is a somewhat naive approach to rescale the entire ALDA kernel, but as we will show in Sec. IV B, the inclusion of a Hubbard correction in the λALDA+U approach leads to significant improvements of the magnon dispersion when compared to experiment. As a result, it seems that the λALDA+U approach can be a valuable tool for including correlation effects within LR-TDDFT in a simple and transparent way.

C. Computational details

All calculations in this study have been carried out using the open-souce GPAW code [48, 49], with which the plane wave susceptibility $\chi_{\mathbf{GG}'}^{+-}(\mathbf{q},\omega)$ can be computed within LR-TDDFT [35]. In principle, the PAW implementation yields all-electron accuracy, but in practise it is not possible to construct a complete basis of projector functions. In the applied PAW-setups, only the Mn $4s$ and $3d$ as well as the Bi $6s$, $6p$ and $5d$ orbitals are included as valence states in the band summation of Eq. (4). In addition to the valence states, 8 empty shell bands per atom are included as well. Furthermore, a (30, 30,
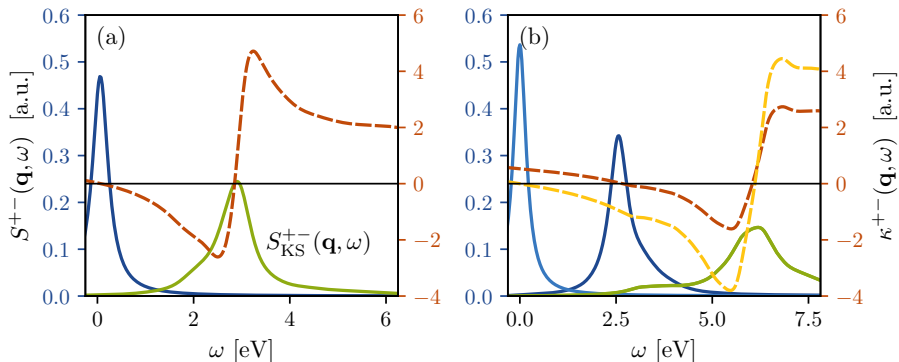
FIG. 1. Collective enhancement of the Goldstone mode in MnBi at $\mathbf{q} = \mathbf{0}$. The macroscopic Stoner spectrum $S_{\mathrm{KS}}^{+-}(\mathbf{q}, \omega) = S_{\mathrm{KS}, \mathbf{G}=0}^{+-}(\mathbf{q}, \omega)$ is shown in green, the inverse enhancement function $\kappa_{\mathbf{G}=0}^{+-}(\mathbf{q}, \omega)$ in red and the macroscopic many-body spectrum $S_{\mathbf{G}=0}^{+-}(\mathbf{q}, \omega)$ in blue. (a) ALDA collective enhancement. (b) ALDA+U collective enhancement. Red and dark blue show the enhancement using the bare ALDA kernel calculated for the LDA+U ground state using $U_{\mathrm{eff}} = 3$ eV. The yellow and light blue colors shows the enhancement using the λALDA kernel scaled to fulfill the Goldstone condition $\kappa_{\mathbf{0}}^{+-}(\mathbf{0}, 0) = 0$.

18) Γ-centered Monkhorst-Pack (MP) grid is used along with a plane wave cutoff of 750 eV for the plane wave basis in Eq. (10). These parameters were chosen based of an extensive convergence study of the magnon dispersion in the itinerant ferromagnets Fe, Ni and Co [35] and we have checked that these parameters lead to well converged results for MnBi as well.

Calculations have been carried out in the NiAs-type crystal structure, using the experimental room temperature lattice constants ($a = 4.287$ Å, $c = 6.117$ Å) for LR-TDDFT calculations. It should be noted that the reference inelastic neutron scattering data available is taken at 5 K [21] and that the MnBi structure is contracting when cooling, all the way from 293 K, through the structural phase transition at 90 K, down to at least 20 K [16]. Nevertheless, we expect a fair comparison between theory and experiment, when using the room temperature crystal structure for the simulations. Occasional comparisons of magnon dispersion relations with calculations performed in the orthorhombic crystal structure reported at 80 K [16] have been carried out, without any noteworthy qualitative differences as a result.

In order to reliably extract the magnon dispersion, the Kohn-Sham continuum, which is sampled on a finite k-point mesh, needs to be broadened into a continuum. In practise this is done by leaving η as a small, but finite parameter in Eq. (4). Through the average frequency displacement technique described in [35], it was found that the low frequency Kohn-Sham spectrum of MnBi is effectively broadened into a continuum for values of $\eta \geq 100$ meV using the chosen k-point grid. Unfortunately, the broadening parameter η not only dictates the minimum width of features in the Kohn-Sham spectrum, but in the many-body spectrum as well. Using $\eta = 100$ meV, the spectral width of the magnons will be of the same order

of magnitude as the MnBi magnon bandwidth. Consequently, it becomes difficult for the human eye to discern the magnon dispersion directly from the spectrum, as illustrated in Fig. 2(a), and it is not possible to extract a physical lineshape for the magnons. However, it is still possible to extract the magnon dispersion. To do this, we sample the spectrum on a frequency grid with a spacing $\delta\omega \leq \eta/8$ and compute the magnon frequency as the maximum in a parabolic fit to the magnon spectral peak. In Fig. 2(a), the magnon peak positions extracted from the (30, 30, 18) k-point grid are compared to similarly extracted peak positions on a (60, 60, 36) grid, where it was possible to reduce η to a value of 40 meV without compromising the Kohn-Sham continuum. Clearly, it is not necessary to go beyond the (30, 30, 18) k-point grid in order to converge the magnon dispersion and a value of $\eta = 100$ meV will be used throughout the remainder of the paper.

As a final note, we extract the magnon stiffness D along a given direction in reciprocal space by performing a biquadratic fit to the magnon peak positions of the 4 shortest $\mathbf{q}$-vectors along the path in question (excluding the Γ-point). This procedure is illustrated in Fig 2(b) for the $\Gamma \to M$ direction.

IV. RESULTS

A. Correlation effects in the ground state

As argued in Refs. [40, 41], it is necessary to include a Hubbard correction in the DFT ground state description of MnBi in order to capture both structural and magnetic properties. In Fig. 3(a) we compare the lattice constants in the NiAs-type crystal structure calculated
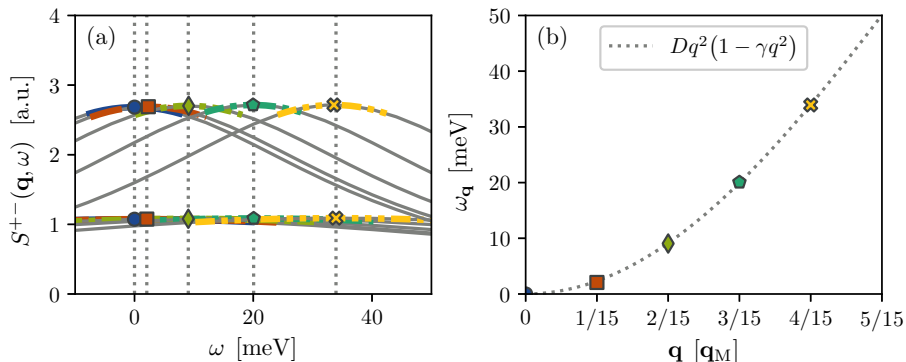
FIG. 2. Extraction of the magnon stiffness from the λALDA+U transverse magnetic excitation spectrum with $U_{\text{eff}} = 3\,\text{eV}$. (a) Magnon spectrum along the $\Gamma \to M$ path calculated on a $(30, 30, 18)$ Γ-centered MP-grid using $\eta = 100\,\text{meV}$ (lower set of lineshapes) and a $(60, 60, 36)$ Γ-centered MP-grid using $\eta = 40\,\text{meV}$ (upper set of lineshapes). Magnon energies (scatter points) are identified as peak positions from a quadratic fit to the maximum of each Lorentzian lineshape (colored lines). Vertical dotted lines indicate the magnon energies from the sparse k-point grid for visual comparison. (b) Extracted magnon dispersion from the calculation using the sparse k-point grid along with a biquadratic fit, $\omega_{\mathbf{q}} = Dq^2(1 - \gamma q^2)$, to the dispersion.
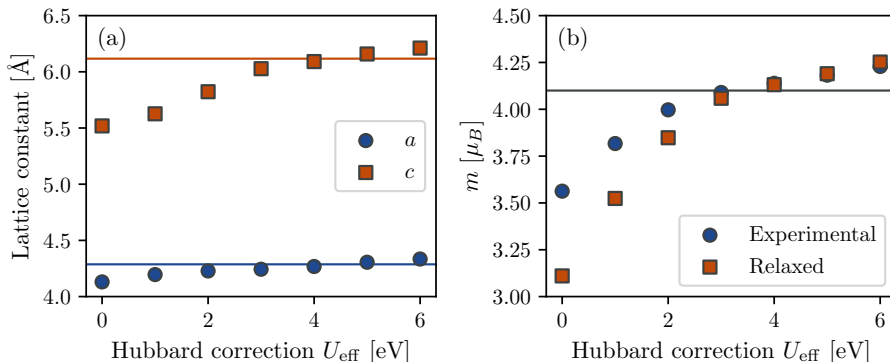
FIG. 3. Effects of Hubbard corrections on lattice parameters and magnetization. (a) LDA+U lattice constants as a function of U_{eff}, calculated using the Atomic Simulation Recipes (ASR) [50]. Solid lines indicate the experimental lattice constants at room temperature [16]. (b) Magnetization per Mn atom as a function of U_{eff} using the experimental and LDA+U crystal structures respectively. The experimental magnetization at 5 K [16] is shown as a reference.

with LDA(+U) to the experimental room temperature crystal structure. Without a Hubbard correction, we find the lattice constants $a = 4.131\,\text{Å}$ and $c = 5.519\,\text{Å}$, which are both underestimated compared to the experimental lattice constants at room temperature, differing by $\Delta a = 0.156\,\text{Å}$ and $\Delta c = 0.598\,\text{Å}$ respectively. The temperature effect only provides a minor contribution to this difference. Experimentally, a and c are found to contract $< 0.02\,\text{Å}$ and $< 0.06\,\text{Å}$ respectively when the material is cooled down from room temperature to 20 K [16]. Thus, the error mainly resides within the exchange-correlation functional, which in the case of LDA significantly underestimates the lattice constants, especially

the out-of-plane lattice constant c, which determines the nearest neighbour distance between the Mn atoms. In the case of LDA+U however, reasonable lattice constants are obtained for values of U_{eff} within the range of $3 - 5$ eV, with $U_{\text{eff}} = 4$ eV providing the best match to experiment. In Fig. 3(b), we show the LDA(+U) ground state magnetization per Mn atom calculated for the experimental and relaxed DFT crystal structures respectively. In LDA, the magnetization is significantly underestimated with a value of $3.56\,\mu_{\text{B}}$ (to be compared with the experimental value of $4.1\,\mu_{\text{B}}$ [16]). If we instead use the LDA lattice constants, the situation is even worse as the magnetization takes a value of $3.11\,\mu_{\text{B}}$. Again,
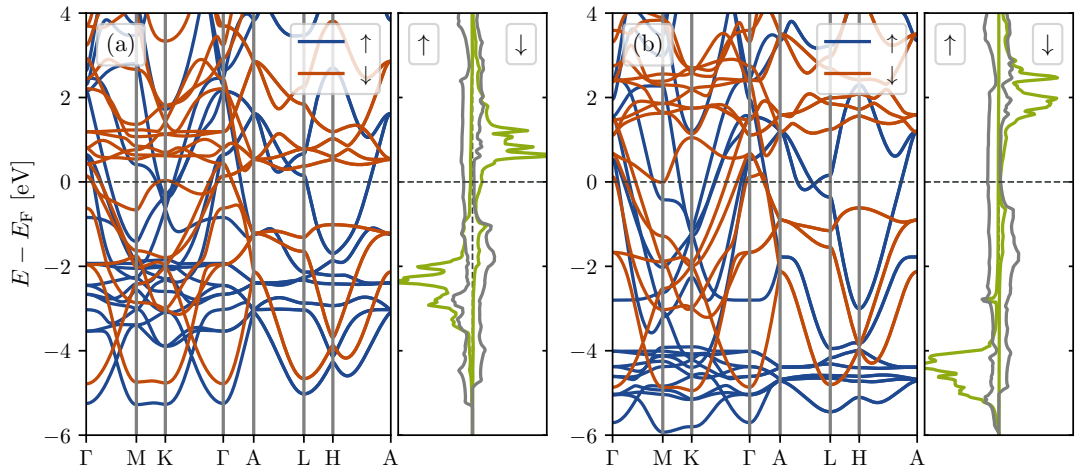
FIG. 4. Kohn-Sham electronic band structure and projected density of states (PDOS). Projections in green indicate the Mn $3d$ orbitals, whereas the grey projections show the sum of contributions from the Mn $4s$, Mn $4p$, Bi $6s$ and Bi $6p$ orbitals. (a) LDA band structure and PDOS. (b) LDA+U band structure and PDOS ($U_{\text{eff}} = 3$ eV).

this deficiency is amended upon the inclusion of a Hubbard correction and a reasonable agreement with experiment is found for values of U_{eff} in the range of 2-5 eV. Similar to the lattice constant c in Fig. 3(a), the magnetization increases monotonically with U_{eff}, but most rapidly so for values of U_{eff} up to 3 eV. This can be understood based on the band structures and projected density of states shown in Fig. 4. Generally speaking, the Hubbard correction increases the exchange splitting, moving the minority bands up in energy and the majority bands down in energy compared to the Fermi level, hence the monotonic increase in magnetization. For the Kohn-Sham band structure in the vicinity of the Fermi level, one may separate the bands into two groups based on the orbital projections. There is a group of narrow bands consisting mainly of Mn $3d$ orbitals as well as a group of more dispersive bands of mixed orbital character. Due to the nature of the Hubbard correction, it mostly affects the narrow Mn $3d$ bands. For $U_{\text{eff}} = 3$ eV, the Mn $3d$ minority bands are moved ~ 1 eV up and the Mn $3d$ majority bands are moved ~ 2 eV down in energy with respect to the Fermi level. That is, the Mn $3d$ exchange splitting is increased by a value $\sim U_{\text{eff}}$. For the Mn $3d$ majority bands, the energy shift is not associated with a change in the occupancies, as the bands are placed 2-4 eV below the Fermi level in the LDA band structure. In contrast, there are Mn $3d$ minority states situated around the Fermi level of the LDA band structure, some of them partially occupied. Since the Hubbard correction increases the exchange splitting, the Mn $3d$ minority bands are shifted away from the Fermi level and become fully occupied at $U_{\text{eff}} = 3$. Thus, for values

of U_{eff} above 3 eV, the increasing magnetization is determined solely from the more dispersive bands of mixed orbital character, which are less affected by the correction. As a consequence, the magnetization increases only slowly with U_{eff} above 3 eV.

B. Dynamic correlation effects

While the effect of Hubbard corrections on the ground state properties have been discussed in Refs. [40, 41], we extend the discussion to include also the influence on the dynamic susceptibility of MnBi. As shown above, the LDA Kohn-Sham spectrum in Fig. 1(a) has a well-defined Stoner peak at 2.9 eV. From the band structure and projected density of states shown in Fig. 4(a), we see that the origin of this peak is the narrow Mn $3d$ bands, which dominate the spin dynamics of the system as expected. However, as reflected in Fig. 1(b), the Fermi surface includes large contributions from the dispersive bands of mixed orbital character and these will have an important influence on the fundamental spin excitations as well. As the exchange splitting between the Mn $3d$ bands grows, a non-negligible contribution from the dispersive bands becomes visible below the main Stoner peak. For values of U_{eff} above 3 eV, it would be tempting to apply a localized (half-)integer spin model based on the gapped Mn $3d$ bands, but this would largely neglect the itinerant effects introduced by the dispersive bands crossing the Fermi level. For example, the magnon dispersion is expected to exhibit Landau damping, which originates from the coupling of the collective Mn d-band excita-
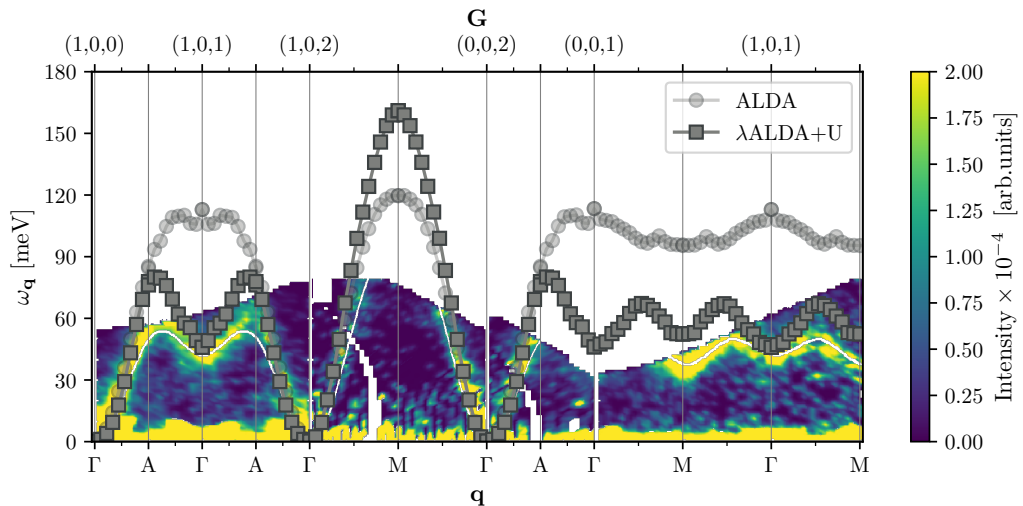
FIG. 5. Theoretical ALDA and λALDA+U ($U_{\mathrm{eff}} = 3\,\mathrm{eV}$) magnon dispersion relations plotted on top of a heat map of the transverse magnetic structure factor as probed by inelastic neutron scattering [21].

tions to the Stoner continuum originating from states in the vicinity of the Fermi level. In contrast, LR-TDDFT includes contributions from all bands on the same footing and is expected to capture both the Landau damping as well as the associated renormalization of the magnon dispersion.

In Fig. 5, we show the experimental magnon spectrum as measured by inelastic neutron scattering on single-crystalline MnBi [21] and compare it to the theoretical magnon dispersion relations computed within LR-TDDFT. The magnon dispersion is quite anisotropic, differing substantially between the in-plane ($\Gamma \to M$) direction and the out-of-plane ($\Gamma \to A$) direction. This difference arises, as the nearest neighbour exchange interaction (which is out-of-plane) is strongly anti-ferromagnetic, while all other couplings are ferromagnetic. In order to fit the magnon spectrum to a Heisenberg model, it is necessary to include interactions up to the 6th nearest neighbours (such that each Mn-site is directly coupled to 40 other Mn sites), and even in this case, the magnon stiffness (short wave vector dispersivity) is underestimated in the model [21]. The long-range exchange interactions are attributed the itinerant nature of MnBi and when calculating the magnon dispersion within the ALDA (which is parameter free), we get a better match of magnon stiffnesses (and thus the long-range spin wave excitations) to experiment than it is the case with the fitted Heisenberg model. However, the ALDA completely fails to describe the optical magnon mode (short-range magnon excitations outside the first BZ), both quantitatively and qualitatively. Throughout most of the second BZ, magnon frequencies are more than doubled compared to exper-

iment, and whereas the experimental dispersion attains a minimum at the center of the second BZ, the ALDA dispersion attains a maximum. This short-coming of the ALDA is to a large extend amended by the inclusion of a Hubbard correction and both the acoustic and optical magnon modes agree reasonably well with the experimental spectrum within the λALDA+U approach with $U_{\mathrm{eff}} = 3$ eV. Thus, an appropriate description of correlation effects seems essential for capturing the short-range anti-ferromagnetic exchange interaction between neighbouring Mn atoms. At the same time, it is crucial to incorporate the itinerant nature of MnBi in order to capture the long-range ferromagnetic exchange interactions. This makes the inherent magnetic frustation of MnBi a highly non-trivial problem to treat theoretically. Therefore, it is a noteworthy achievement that we are able to reproduce the experimental magnon dispersion in LR-TDDFT.

C. Correlation effects and the Hubbard parameter

So far, we have presented excited state quantities calculated using the effective Hubbard parameter $U_{\mathrm{eff}} = 3$ eV. However, the "correct" magnitude of the Hubbard correction cannot be uniquely defined, and in Fig. 6(a) we show the magnon stiffness as a function of U_{eff}. We have extracted the experimental magnon stiffness from a biquadratic fit to the inelastic neutron scattering data available [21], obtaining values $D_{\mathrm{M}} = 683 \pm 75\,\mathrm{meV\,\mathring{A}}^2$ and $D_{\mathrm{A}} = 426 \pm 54\,\mathrm{meV\,\mathring{A}}^2$ for the in-plane and out-of-plane magnon stiffnesses respectively. Using the ALDA
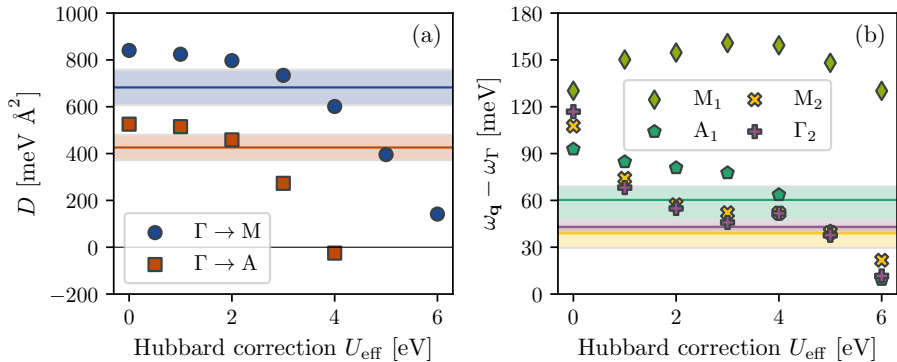
FIG. 6. MnBi magnon dispersion as a function of Hubbard U_{eff}. (a) Extracted magnon stiffness along the $\Gamma \to M$ and $\Gamma \to A$ directions. Horizontal lines and colored areas indicate the experimental best estimates and 1σ uncertainty intervals of biquadratic fits to the transverse magnetic structure factor as probed by inelastic neutron scattering [21]. (b) Extracted magnon energies at a selected number of high-symmetry points. The experimentally determined magnon energies are shown by horizontal lines and the colored areas indicate their uncertainties.

kernel, the magnon stiffnesses are slightly overestimated to values of $D_{\text{M}} = 841 \, \text{meV} \, \text{Å}^2$ and $D_{\text{A}} = 526 \, \text{meV} \, \text{Å}^2$, clearly reproducing the stiffness anisotropy of experiment. Adding an increasing amount of Hubbard correction, as shown in Fig. 6(a), the magnon stiffness decreases along both directions, but more so in the out-of-plane direction than it does in-plane. For the $\Gamma \to A$ direction, the magnon stiffness reaches negative values for $U_{\text{eff}} \geq 4$ eV, implying that the ferromagnetic ground state becomes dynamically unstable beyond this point, a fact which will be discussed in further detail below. Because the MnBi ground state is indeed ferromagnetic, this sets an upper bound on appropriate values for U_{eff}. Overall, it seems that values of $U_{\text{eff}} \leq 3$ eV provide a reasonable agreement with experiment for the magnon stiffnesses, with the best fit being somewhere in the range of 2-3 eV.

As mentioned previously, it is especially the optical magnon frequencies, for which ALDA falls short. In Fig. 6(b) we show the magnon energy at the first BZ M-point and A-point, $(1/2, 0, 0)$ and $(0, 0, 1/2)$ in relative reciprocal coordinates, as well as the second BZ M-point and Γ-point, $(1/2, 0, 1)$ and $(0, 0, 1)$, as a function of U_{eff}. Using the ALDA kernel, the magnon frequencies at the three high-symmetry points of the second BZ (this includes the A-point) are significantly overestimated. Generally speaking, the three optical magnon frequencies decrease with increasing U_{eff}, coinciding with the experimental reference for values in the 4-5 eV range. As a result, it is not possible to obtain a complete simultaneous match to experiment of both magnon stiffnesses and optical magnon frequencies using the λALDA+U approach. From the results in Fig. 6, it seems that in order to reproduce the observed optical magnon frequencies as well as possible, U_{eff} should be chosen as large as the magnon stiffnesses permit.

Considering all the preceding results, ranging from lattice constants and magnetization to the magnon dispersion relation, it seems that a choice of $U_{\text{eff}} \sim 3$ eV provides the best compromise between various material properties. This finding agrees quite well with the previous efforts of Antropov et al. to determine U and J [40]. Using the constrained local spin-density approximation (cLSDA) and constrained random phase approximation (cRPA) methods, they obtain values for U of 4.57 eV and 3.6 eV respectively. As these methods generally tend to overestimate/underestimate the value for U, the authors deem a value of $U \sim 4$ eV the most appropriate choice, which along with the cLSDA value for $J = 0.97$ eV gives $U_{\text{eff}} = U - J \sim 3$ eV.

Finally, we return to the dynamic instability of the ferromagnetic ground state, which occurs for $U_{\text{eff}} \geq 4$ eV. In Fig. 7(a) we show the magnon dispersion close to the Γ-point for values of U_{eff} below, on and above the onset of the instability. At the onset itself ($U_{\text{eff}} \sim 4$ eV), the magnon stiffness vanishes and the dispersion becomes flat along the $\Gamma \to A$ direction, meaning that the low-frequency magnons disperse with some power larger than q^2 in this direction. Above the onset however, the magnon stiffness is finite and negative, such that the magnon dispersion attains its global minimum away from the Γ-point and at negative magnon frequencies. This implies that a selection of magnon quasi-particle excitations with finite wave vectors $\mathbf{q} \propto \mathbf{q}_{\text{A}}$ place the system in an energetically more favorable state, than the ferromagnetic starting point, thus rendering the ferromagnetic state dynamically unstable. There is no reason to believe that the correlation effects included in the Hubbard correction quench magnetic order as a whole, rather they seem to enhance the nearest neighbour exchange in-
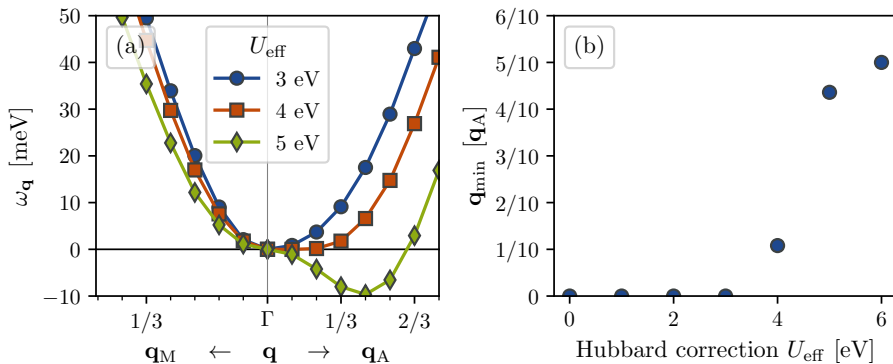
FIG. 7. (a) Magnon dispersion in the ferromagnetic state at different values for the Hubbard parameter U_{eff}. (b) $\mathbf{q}$-point (in the $\Gamma \to A$ direction) where the ferromagnetic magnon dispersion has its minimum as a function of the Hubbard parameter.

teraction, which is out-of-plane and anti-ferromagnetic. Thus it is more likely, that the new (hypothetical) ground state would be a helically ordered state. As a first estimate of the helical wave vector, we give in Fig. 7(b) the wave vector at which the ferromagnetic magnon frequency attains its minimum along the $\Gamma \to A$ direction, determined from a fit to the λALDA+U dispersion using gaussian process regression.

D. Hole doping and uniaxial compressive strain

Although the Hubbard parameter U_{eff} encodes real physical correlations in MnBi, it is not an actual parameter, which can be tuned in experiments. However, as previously hypothesized, the main role of the Hubbard correction regarding a possible phase transition to helical magnetic order seems to be, that it enhances the nearest neighbour anti-ferromagnetic exchange interaction to such an extent, that the ferromagnetic state becomes dynamically unstable. Whereas we cannot tune U_{eff} in real life, we can try to enhance the anti-ferromagnetic exchange and possibly realize a magnetic phase transition to helical order in this way. To this end, we investigate two different approaches: Hole doping and uniaxial compressive strain. Investigating the effect of hole doping is motivated by the fact that Mn sits to the right of Cr in the periodic table. Cr is well-known for exhibiting strong anti-ferromagnetic exchange interactions and by substituting a small amount of Mn with Cr it may be possible to induce a phase transition into a helically ordered ground state. Because large supercell LR-TDDFT computations currently are out-of-scope, we simulate this scenario by introducing holes into the electronic structure of MnBi (moving the Fermi level down). We do this with U_{eff} fixed to a value of 3 eV. The motivation for investigating strain effects on the magnon dynamics is more straightforward. If we can compress the nearest neigh-

bour bond length, the anti-ferromagnetic exchange interaction should be enhanced. However, if we apply a hydrostatic pressure and reduce the crystal volume from all directions, also the ferromagnetic exchange interactions are expected to increase in strength. Thus, to simplify the picture, we compress the crystal along the c-axis, while keeping the volume constant through an expansion of the in-plane lattice constant. In experiment, this would to some extent correspond to applying a uniaxial pressure.

In Fig. 8, we show the magnon stiffness as a function of hole doping and uniaxial compressive strain. In both cases, the magnon stiffness decreases more or less linearly along the $\Gamma \to A$ direction and the ferromagnetic state becomes unstable at 0.12 holes per formula unit and 4.4% compressive strain along the c-axis (determined from linear interpolation). When hole-doping the system, also the in-plane magnon stiffness along the $\Gamma \to M$ direction decreases. This fits well with the intention of simulating a substitution of Mn with Cr, as one would also expect a weakening of the long-range ferromagnetic exchange interactions in this case. For the uniaxial compressive strain, it is less clear what to expect for the in-plane magnon stiffness. With the expansion of the in-plane lattice constant, the in-plane ferromagnetic exchange interactions are expected to become weaker, leading to a reduction in the frequency scale for D_{M}. At the same time however, the length scale for D_{M} increases with an expanding a lattice constant. Seemingly, these opposite sided effects cancel out, as the in-plane magnon stiffness in Fig. 8(b) is seen to be largely unaffected by the uniaxial compressive strain, at least for strains below 10% (which are really 5% strains in-plane). The weakening of in-plane ferromagnetic exchange interactions is more clear from the in-plane magnon band width (i.e. the magnon frequency at the first BZ M-point), for which there is a decrease with *both* hole doping and uniaxial compressive strain, as seen in Fig. 9. In addition, also
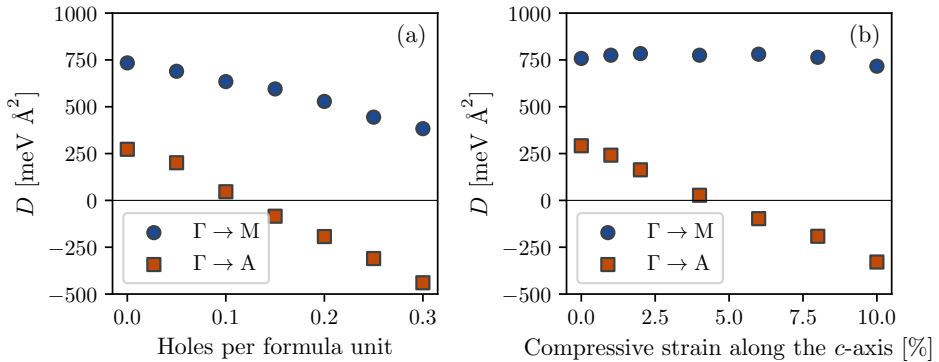
FIG. 8. Theoretical magnon stiffness along the $\Gamma \to M$ and $\Gamma \to A$ directions as (a) a function of removed electrons, (b) a function of uniaxial compressive strain in the c-direction. Calculated with the λALDA+U kernel and $U_{\mathrm{eff}} = 3$ eV.
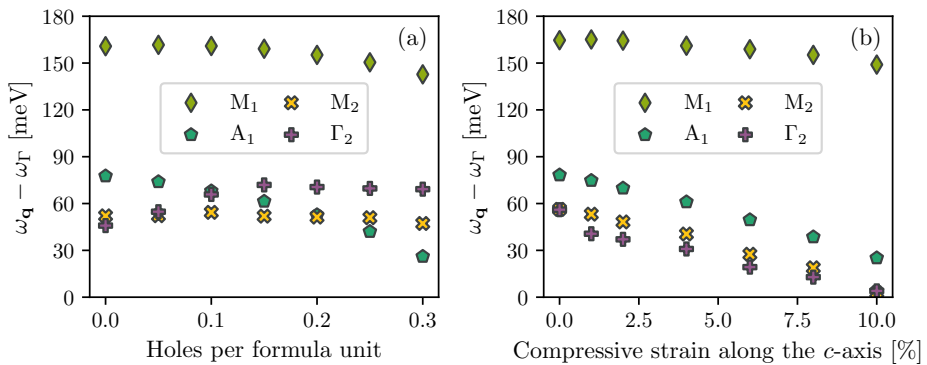
FIG. 9. Theoretical magnon energies at a selected number of high-symmetry points as (a) a function of removed electrons, (b) a function of uniaxial compressive strain in the c-direction. Calculated with the λALDA+U kernel and $U_{\mathrm{eff}} = 3$ eV.

the magnon frequency in the A-point decreases with both hole-doping and uniaxial compressive strain. However, this is not the case for the second BZ M-point and Γ-point for which the magnon frequencies only decrease with strain. On the contrary, the magnon frequency in the second BZ center actually increases with hole doping. This is somewhat of a surprise, since the second BZ Γ-point magnons correspond to spin wave excitations where the nearest neighbour Mn atoms acquire opposite phases. Once again, this emphasizes that the magnetic frustration in MnBi is a highly non-trivial problem, due to the fact that the long-range ferromagnetic exchange interactions cannot be boiled down to a simple set of short-range couplings.

Experimental studies have shown that it is indeed possible to dope MnBi with Cr, at least for thin films [18, 19] and melt-spun ribbons [20]. It may even be an advantage for the synthesis to add Cr, as it helps to stabilize

the formation of ferromagnetic MnBi as opposed to a decomposition into paramagnetic $Mn_{1.08}Bi$ and Bi [20]. For both thin films and ribbons, the Curie temperatures of the investigated $Mn_{1-x}Cr_xBi$ alloys lie below the segregation temperature of 630 K. Based on these studies, it is not completely clear how the Curie temperature depends on Cr doping levels, since the samples are rather inhomogeneous. As an example, the Cr content of the thin films was shown to depend on depth, with Cr concentrated at the surface [19]. With 10% Cr in the overall composition (comparable to the critical doping level for the helical phase transition according to the results of Fig. 8(a)), the Curie temperature was decreased to 523 K and 546 K for the thin films and ribbons respectively. The fact that Cr doping lowers the Curie temperature is in good agreement with our results, but a confirmation of the calculated trends and existence of a magnetic phase transition requires further experimental studies.
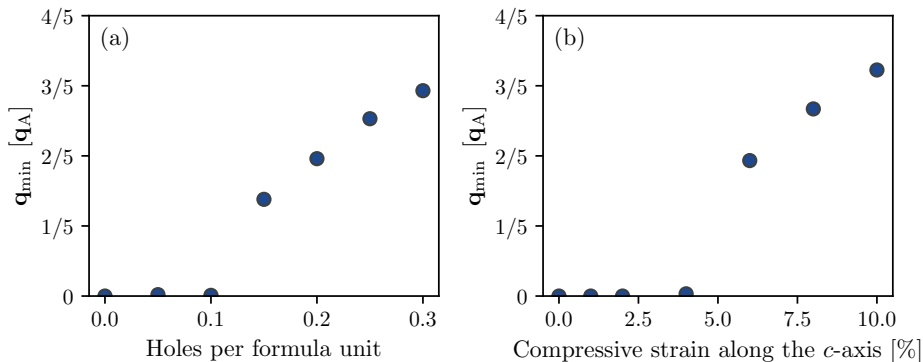
FIG. 10. $\mathbf{q}$-point where the ferromagnetic magnon dispersion has its minimum as (a) a function of removed electrons, (b) a function of uniaxial compressive strain in the c-direction. Calculated with the λALDA+U kernel and $U_{\mathrm{eff}} = 3$ eV.

To our knowledge, it is an open question, how MnBi behaves under uniaxial pressure. From the present theoretical investigations, it does not seem realistic to induce a phase transition to helical magnetic order in a uniaxial pressure cell, as one would expect the crystal to break long before obtaining a 4.4% uniaxial compressive strain. However, based on the fact that D_{A} decreases linearly with both hole-doping and strain, as seen in Fig. 8, one could hope to combine the two effects, such that the hypothetical helical phase transition of the $\mathrm{Mn}_{1-x}\mathrm{Cr}_x\mathrm{Bi}$ alloys could be induced by pressure for Cr-doping levels close to the phase transition. Indeed, it seems that both effects produce similar trends for the minimal frequency magnon wave vectors beyond the magnetic phase transition, as seen in Fig. 10.

V. DISCUSSION

In this paper, we have mainly discussed the magnon dynamics of pristine MnBi and Cr doped alloys. However, the results can be regarded as an initial step in a broader context, since many of the quantum magnetic phenomena studied here are shared by the family of transition metal pnictides. Among the Mn and Cr based compounds, helical magnetic order is quite common and the helical wave vectors have also previously been shown to depend on the relative concentrations of Mn and Cr [10]. As an example, the $\mathrm{Mn}_{1-x}\mathrm{Cr}_x\mathrm{As}$ phase diagram includes a phase transition from ferromagnetic MnAs to helically ordered CrAs [15]. In addition, MnP has been shown to exhibit pressure induced magnetic phase transitions between ferromagnetic and helical order as well as pressure induced super-conductivity [10, 13], which is also found in CrAs [14].

Also the inherent magnetic frustration in the transition metal pnictide family has been the subject of several previous studies. Based on analysis of the band structure

and partial occupation of orbitals in MnP, Goodenough provided a qualitative explanation for the existence of both anti-ferromagnetic and ferromagnetic order at different temperatures [11]. He argued that the half-filling of the localized Mn t_{2g} orbital directed towards the nearest Mn neighbours calls for an anti-ferromagnetic ordering while the three-fourths filling of the collective, yet narrow, $3d$ bands representing the remaining t_{2g} orbitals calls for ferromagnetic ordering. Similar considerations have also been explored for MnAs, where exchange striction also plays a role in the competition between the NiAs and MnP structural phases [12].

In this context, the theoretical prediction that magnetic order in MnBi is characterized by a competition between nearest neighbour anti-ferromagnetic exchange and long-range ferromagnetic exchange has some precedent, as similar effects have been observed in closely related members of the transition metal pnictide family. Similarly, it seems likely that the prediction of a phase transition to helical magnetic order in Cr doped MnBi could be correct and that the phase transition would be strain sensitive.

The coupling between structural and magnetic degrees of freedom may also help to explain, why the Hubbard correction has such a strong influence on the out-of-plane lattice constant c, as show in Fig. 3(a). As the appropriate correlation effects are included with increasing U_{eff} and the anti-ferromagnetic exchange interaction between nearest neighbours is increased, it becomes favorable to increase the nearest neighbour distance as a compensation for the ground state remaining ferromagnetic. Similarly, a magnetic phase transition to helical order could be accompanied by a structural compression in the c-direction, as the anti-ferromagnetic nearest neighbour exchange interaction does no longer need to be compensated to the same extent. Another possibility is that MnBi undergoes a structural phase transition from the hexagonal NiAs structure into the orthorhom-

bic MnP structure with Cr doping, as it is the case in the $Mn_{1-x}Cr_xAs$ phase diagram.

Although the occurrence of similar phenomena in other transition metal pnictides inspire confidence in the qualitative predictions made on the basis of this study, the quantitative predictions may depend somewhat on the details in the theoretical representation of doping and strain. The by-hand introduction of hole-doping and uniaxial compressive strain should be viewed as efforts to study the underlying physical mechanisms and not to provide accurate estimates for e.g. the critical Cr doping level for the magnetic phase transition. Actually, the critical doping levels and strains for the phase transition are likely to be underestimated, as the Hubbard parameter $U_{eff} = 3$ eV used here leads to an underestimate of the out-of-plane magnon stiffness D_A, as seen in Fig. 6(a). In this sense, the undoped an unstrained MnBi is closer to a helical phase transition in our simulations, than the experiments predict (based on magnon stiffness).

VI. CONCLUSION

MnBi has a long history of experimental as well as theoretical investigations based on its attractive properties for technological applications. As we have shown in this study, MnBi exhibits a non-trivial inherent magnetic frustration, which makes it an intriguing subject for theoretical studies, but also implies a potential for future discovery of new magnetic phases. The nearest neighbour exchange interactions between Mn $3d$ electrons are strongly anti-ferromagnetic and highly susceptible to correlation effects, but despite the strength of these interactions, the ground state magnetic order is determined by the long-range ferromagnetic exchange. Because the competing magnetic interactions arise from electrons of localized and itinerant character respectively, it is a substantial theoretical challenge to provide an appropriate description of the magnetic frustration in MnBi.

In this study, we have shown that it is in fact possible to capture the magnetic frustration from the perspective of (LR-TD)DFT calculations, both for the ground state properties of MnBi, but also for the magnon dynamics. The itinerant and localized correlations in MnBi have been described at the LDA+U level and for the LR-TDDFT calculations, we have introduced a rescaled ALDA kernel based on considerations of the Goldstone criterion for the homogeneous electron gas. With the rescaled λALDA+U kernel, we are able to reproduce the experimental magnon dispersion using a Hubbard correction of $U_{eff} = 3$ eV, which in turn also provides ground state properties that are in accordance with experiment. In this way, the present study may pave the way for future theoretical studies of magnon dynamics in the transition metal pnictide family. To this end, we hope that first principles calculations can provide a new angle of insight into the wide range of phenomena driven by magnetic frustration and magnetic fluctuations.

With a proper *ab initio* description of the magnon dynamics of MnBi in place, we have explored some of the phenomena that arise from the magnetic frustration. We have shown that an increase of the local electronic correlations gives rise to a decrease in the magnon stiffness out-of-plane (D_A) due to an increased strength of the anti-ferromagnetic exchange interactions between the nearest neighbours. At $U_{eff} \sim 4$ eV, the magnon stiffness changes sign, meaning that a phase transition takes place, most likely in the favor of a phase of helical order. Whereas the increase in electronic correlations is an artificial one, we have shown that a similar increase in anti-ferromagnetic interaction strength may be imposed using hole-doping or uniaxial compressive strain, in both cases leading to a similar phase transition. In particular, it seems realistic to realize this phase transition by substituting 10-20% of the Mn content with Cr. Similarly, it may be possible to induce the transition by applying uniaxial pressure, but only for compositions of $Mn_{1-x}Cr_xBi$ close to the critical Cr doping level. Furthermore, we predict the helical wave vector **q** to be sensitive to the Cr doping level and strain, especially for doping levels and strains close to the phase transition.

To further unravel the inherent magnetic frustration in MnBi, additional experiments on single-crystaline MnBi are highly desirable. Especially investigations of the effect of Cr doping and a possible phase transition to helical magnetic order are of great interest. Such investigations could potentially provide an improved understanding of the physical mechanisms underlying a wide range of members in the family of transition metal pnictides.

[1] E. Adams, W. M. Hubbard, and A. M. Syeles, Journal of Applied Physics **23**, 1207 (1952).
[2] J. B. Yang, K. Kamaraju, W. B. Yelon, W. J. James, Q. Cai, and A. Bollero, Applied Physics Letters **79**, 1846 (2001).
[3] V. Ly, X. Wu, L. Smillie, T. Shoji, A. Kato, A. Manabe, and K. Suzuki, Journal of Alloys and Compounds **615**, S285 (2015).
[4] B. W. Roberts, Phys. Rev. **104**, 607 (1956).
[5] H. J. Williams, R. C. Sherwood, and O. L. Boothby, Journal of Applied Physics **28**, 445 (1957).
[6] J. M. D. Coey, IEEE Transactions on Magnetics **47**, 4671 (2011).
[7] G. Di, S. Iwata, S. Tsunashima, and S. Uchiyama, Journal of Magnetism and Magnetic Materials **104-107**, 1023 (1992).
[8] H. J. Williams, R. C. Sherwood, F. G. Foster, and E. M. Kelley, Journal of Applied Physics **28**, 1181 (1957).
[9] Di Chen, G. Otto, and F. Schmit, IEEE Transactions on Magnetics **9**, 66 (1973).

[10] Y. Wang, Y. Feng, J.-G. Cheng, W. Wu, J. L. Luo, and T. F. Rosenbaum, Nature Communications **7**, 13037 (2016).

[11] J. B. Goodenough, Journal of Applied Physics **35**, 1083 (1964).

[12] J. B. Goodenough and J. A. Kafalas, Physical Review **157**, 389 (1967).

[13] J.-G. Cheng, K. Matsubayashi, W. Wu, J. P. Sun, F. K. Lin, J. L. Luo, and Y. Uwatoko, Physical Review Letters **114**, 117001 (2015).

[14] W. Wu, J. Cheng, K. Matsubayashi, P. Kong, F. Lin, C. Jin, N. Wang, Y. Uwatoko, and J. Luo, Nature Communications **5**, 5508 (2014).

[15] J. Luo and J. Cheng, Journal of Physics: Condensed Matter **29**, 440301 (2017).

[16] M. A. McGuire, H. Cao, B. C. Chakoumakos, and B. C. Sales, Physical Review B **90**, 174425 (2014).

[17] T. Chen, Journal of Applied Physics **45**, 2358 (1974).

[18] P. R. Bandaru, T. D. Sands, Y. Kubota, and E. E. Marinero, Applied Physics Letters **72**, 2337 (1998).

[19] P. R. Bandaru, T. D. Sands, D. Weller, and E. E. Marinero, Journal of Applied Physics **86**, 1596 (1999).

[20] K. Anand, N. Christopher, and N. Singh, Applied Physics A **125**, 870 (2019).

[21] T. J. Williams, A. E. Taylor, A. D. Christianson, S. E. Hahn, R. S. Fishman, D. S. Parker, M. A. McGuire, B. C. Sales, and M. D. Lumsden, Applied Physics Letters **108**, 192403 (2016).

[22] H. Xiang, C. Lee, H.-J. Koo, X. Gong, and M.-H. Whangbo, Dalton Trans. **42**, 823 (2013).

[23] T. Olsen, Physical Review B **96**, 125143 (2017).

[24] D. Torelli and T. Olsen, Journal of Physics: Condensed Matter **32**, 335802 (2020).

[25] A. Liechtenstein, M. Katsnelson, V. Antropov, and V. Gubanov, Journal of Magnetism and Magnetic Materials **67**, 65 (1987).

[26] P. Bruno, Physical Review Letters **90**, 087205 (2003).

[27] M. I. Katsnelson and A. I. Lichtenstein, Journal of Physics Condensed Matter **16**, 7439 (2004).

[28] M. Pajda, J. Kudrnovský, I. Turek, V. Drchal, and P. Bruno, Physical Review B **64**, 174402 (2001).

[29] E. Runge and E. K. U. Gross, Physical Review Letters **52**, 997 (1984).

[30] E. K. U. Gross and W. Kohn, Physical Review Letters **55**, 2850 (1985).

[31] P. Buczek, A. Ernst, and L. M. Sandratskii, Physical Review B , 174418 (2011).

[32] S. Lounis, A. T. Costa, R. B. Muniz, and D. L. Mills, Physical Review B **83**, 035109 (2011).

[33] B. Rousseau, A. Eiguren, and A. Bergara, Physical Review B **85**, 054305 (2012).

[34] N. Singh, P. Elliott, T. Nautiyal, J. K. Dewhurst, and S. Sharma, Physical Review B **99**, 035151 (2019).

[35] T. Skovhus and T. Olsen, Physical Review B **103**, 245110 (2021).

[36] E. Şaşıoğlu, A. Schindlmayr, C. Friedrich, F. Freimuth, and S. Blügel, Phys. Rev. B **81**, 054434 (2010).

[37] V. I. Anisimov, J. Zaanen, and O. K. Andersen, Physical Review B **44**, 943 (1991).

[38] A. I. Liechtenstein, V. I. Anisimov, and J. Zaanen, Physical Review B **52**, R5467 (1995).

[39] S. L. Dudarev, G. A. Botton, S. Y. Savrasov, C. J. Humphreys, and A. P. Sutton, Physical Review B **57**, 1505 (1998).

[40] V. P. Antropov, V. N. Antonov, L. V. Bekenov, A. Kutepov, and G. Kotliar, Physical Review B **90**, 054404 (2014).

[41] K. V. Shanavas, D. Parker, and D. J. Singh, Scientific Reports **4**, 7222 (2015).

[42] P. Hohenberg and W. Kohn, Physical Review **136**, B864 (1964).

[43] W. Kohn and L. J. Sham, Physical Review **140**, A1133 (1965).

[44] U. von Barth and L. Hedin, Journal of Physics C: Solid State Physics **5**, 1629 (1972).

[45] A. K. Rajagopal and J. Callaway, Physical Review B **7**, 1912 (1973).

[46] M. Niesert, *Ab initio calculations of spin-wave spectra from time-dependent density-functional theory*, Ph.D. thesis, RWTH Aachen University (2011).

[47] C. Friedrich, M. C. T. D. Müller, and S. Blügel, in *Handbook of Materials Modeling: Methods: Theory and Modeling*, edited by W. Andreoni and S. Yip (Springer International Publishing, Cham, 2020) pp. 919–956.

[48] J. J. Mortensen, L. B. Hansen, and K. W. Jacobsen, Physical Review B **71**, 035109 (2005).

[49] J. Enkovaara, C. Rostgaard, J. J. Mortensen, J. Chen, M. Dułak, L. Ferrighi, J. Gavnholt, C. Glinsvad, V. Haikola, H. a. Hansen, H. H. Kristoffersen, M. Kuisma, a. H. Larsen, L. Lehtovaara, M. Ljungberg, O. Lopez-Acevedo, P. G. Moses, J. Ojanen, T. Olsen, V. Petzold, N. a. Romero, J. Stausholm-Møller, M. Strange, G. a. Tritsaris, M. Vanin, M. Walter, B. Hammer, H. Häkkinen, G. K. H. Madsen, R. M. Nieminen, J. K. Nørskov, M. Puska, T. T. Rantala, J. Schiøtz, K. S. Thygesen, and K. W. Jacobsen, Journal of Physics: Condensed Matter **22**, 253202 (2010).

[50] M. Gjerding, T. Skovhus, A. Rasmussen, F. Bertoldo, A. H. Larsen, J. J. Mortensen, and K. S. Thygesen, Computational Materials Science **199**, 110731 (2021).

CHAPTER 6

Results: Magnons in antiferromagnets

In the work leading to this thesis, we have mainly focused on the study of itinerant ferromagnets. Such materials comprise a natural starting point for the emerging field of theoretical magnon spectroscopy due to the simplicity of the ferromagnetic ground state and because itinerant electron effects are seamlessly included in an *ab initio* treatment, on the contrary to the frequently used localized spin models. However, the fundamental theory is not restricted to ferromagnetic states of matter, and in the case of antiferromagnets, first principles calculations could provide a new angle of attack on subjects such as the pressure induced superconductivity in the transition metal pnictide family [7–9]. In Publication [C], we take some initial steps in this direction by considering two prototypical antiferromagnetic (AFM) systems: bulk Cr (metallic) and Cr_2O_3 (insulating). Of these systems, bulk Cr is probably the most interesting due to its itinerant electron physics. However, there is little experimental data to compare a theoretical magnon dispersion of Cr's commensurate spin-density wave phase to. For this reason, we treat also the localized electron antiferromagnetism in Cr_2O_3 and compare our *ab initio* treatment to a classic Heisenberg model.

Now, in order to facilitate the extraction of AFM magnon energies from a transverse magnetic susceptibility calculated within LR-TDDFT, we have analysed the symmetries of $\chi^{+-}_{\mathbf{GG'}}(\mathbf{q},\omega)$ implied by the antiferromagnetic ground state in particular, but also for symmetries of the system Hamiltonian $\hat{H}_0$ in general. The extraction is not as straight-forward as in ferromagnets, because the vanishing total magnetic moment implies that excitations increasing and decreasing the spin angular momentum have equal weight in the spectrum $S^{+-}_{\mathbf{GG'}}(\mathbf{q},\omega)$ [C]. In practice this means that the low frequency magnons in both bcc-Cr and Cr_2O_3 are obscured by a symmetry related magnon of opposite spin. Based on the quantum mechanical Onsager relation (1.22), we show that the spectral functions for the spin-lowering and spin-raising excitations entering $S^{+-}_{\mathbf{GG'}}(\mathbf{q},\omega)$ are not just related in a centrosymmetric antiferromagnet, they are identical in the nonrelativistic limit. Along with an assumption for the magnon lineshape, one can then extract the magnon energies from the spectrum.

It is important to emphasize that the Onsager relation (1.22) is not new. In fact, Kubo immediately recognized that the generalized susceptibilities in systems with opposite static magnetic fields are related by an Onsager relation [41]. However, we hope that the formulation of the relation given in Appendix A of Publication [C] is sufficiently concrete, so that the relation can gain a more widespread use. As an illustrative

example of the relation's significance, we use it to show that the magnon dispersion in a material with a collinear magnetic ground state is reciprocal in the nonrelativistic limit, $S^{+-}_{\mathbf{GG'}}(\mathbf{q}, \omega) = S^{+-}_{-\mathbf{G'}-\mathbf{G}}(-\mathbf{q}, \omega)$. Using the Onsager relation, this result simply falls out as a direct consequence of the fact that the system commutes with the complex conjugation operator.

6.1 Publication C: Magnons in antiferromagnetic bcc-Cr and Cr_2O_3 from time-dependent density functional theory

Due to the spin symmetry of a centrosymmetric antiferromagnet, it is not appropriate to fix the Goldstone error with a constant shift of the spectrum. At the Γ-point, where $\omega_{\mathbf{q}} = 0$ in the nonrelativistic limit, the spin-raising and spin-lowering magnons instead completely cancel each other out, $S^{+-}(\mathbf{q} = \mathbf{0}, \omega) = 0$, given that the magnon lineshape is an even function of frequency. In Publication [C], we use this as the Goldstone criterion and scale the ALDA kernel $f^{-+}_{\mathrm{LSDA}} \rightarrow \lambda f^{-+}_{\mathrm{LSDA}}$ in order to fulfil it. When computing the ALDA spectrum based on a LSDA ground state, only a small scaling of $\sim 1\%$ is needed in order to overcome the numerical approximations and fulfil the Goldstone criterion.

Applying the described gap error correction scheme and carefully extracting the low frequency magnons from the obscured magnon lineshapes in $S^{+-}_{\mathbf{GG'}}(\mathbf{q}, \omega)$, we show in Publication [C], that the ALDA directly yields the characteristic linear dispersion of the acoustic magnon mode in both AFM Cr and Cr_2O_3.

For Cr_2O_3, there is a good overall qualitative agreement with the experimental dispersion as well as the dispersion predicted from a Heisenberg model fitted to experiment [73]. However, the ALDA overestimates the magnon velocity and bandwidth by roughly a factor of two and whereas the experimental magnon velocity is anisotropic, the ALDA long wavelength dispersion is completely isotropic. The latter is somewhat surprising since the anisotropy of the magnon stiffness was well described at the level of ALDA for MnBi. As a test, we show in Publication [C] also the Cr_2O_3 magnon dispersion with a Hubbard correction included in the ground state. With $U_{\mathrm{eff}} = 1$ eV, this results in an excellent agreement in terms of the magnon velocity and long wavelength anisotropy, but in all other regards, comparison to experiment and the fitted Heisenberg model deteriorates. For this reason, we believe that new methods are needed in order to accurately treat the dynamic correlation effects in Cr_2O_3.

For AFM Cr, ALDA predicts the acoustic magnon mode to disperse linearly up to 300-400 meV, where it rapidly broadens due to Landau damping and complete disappears inside the collectively enhanced Stoner pair continuum. Interestingly, we also observe an additional collective mode, which seems somewhat unaffected by the Landau damping, as it resides *inside* the Stoner continuum along the $\Gamma \rightarrow R$ direction. Finally, the ALDA magnon velocity seems to be somewhat overestimated, but a final accuracy assessment cannot be made due to the lack of comparable experimental data.

Magnons in antiferromagnetic bcc-Cr and Cr_2O_3 from time-dependent density functional theory

Thorbjørn Skovhus[1] and Thomas Olsen[1, *]

[1]*CAMD, Department of Physics, Technical University of Denmark, 2800 Kgs. Lyngby, Denmark*

We apply time-dependent density functional theory to calculate the transverse magnetic susceptibility of bcc-Cr and Cr_2O_3, which constitute prototypical examples of antiferromagnets with itinerant and localized magnetic moments respectively. The exchange-correlation kernel is rescaled in order to enforce the Goldstone condition and the magnon dispersion relations are extracted based on a symmetry analysis relying on the generalized Onsager relation. Doing so, our calculations yield the characteristic linear magnon dispersion of antiferromagnets in the long wavelength limit. In the case of Cr_2O_3, we find that the adiabatic local density approximation yields a good qualitative agreement with the measured dispersion, but overestimates the magnon velocity and band width by a factor of two. Including a Hubbard correction improves the magnon velocity, but at the expense of the overall qualitative agreement with the experimental magnon dispersion. For bcc-Cr we find a sharp acoustic magnon mode at low energies with a velocity in agreement with previously reported values. At higher energies, the acoustic magnon mode becomes subject to strong Landau damping and rapidly vanishes once it enters the Stoner continuum. In addition to the acoustic magnon mode, we also observe an additional collective mode along the $\Gamma \rightarrow R$ direction which is located inside the Stoner continuum with an energy of ~ 1 eV, but appears to elude the effect of Landau damping.

I. INTRODUCTION

The far majority of theoretical works on magnetic excitations in solids are based on Heisenberg models, which may be derived as a low energy approximation of the full many-body Hamiltonian [1]. In particular, for materials exhibiting simple magnetic order, the fundamental magnetic excitations - the magnons - can be obtained straightforwardly from linear spin wave theory. At small wavevectors this results in the characteristic quadratic and linear dispersion relations of the acoustic magnon modes in ferromagnets and antiferromagnets respectively. Moreover, the parameters entering the Heisenberg model can often be fitted to a measured dispersion, resulting in excellent quantitative agreement between experiments and theory, while providing crucial insight into the microscopic magnetic interactions [2]. Although such an approach largely corroborate the use of Heisenberg models for a theoretical description of magnons in insulating magnetic materials, it is a fundamental challenge to understand and compute the basic magnetic interactions (the Heisenberg parameters) from first principles. To this end, the simplest methods are to apply either an energy mapping analysis [3–7] or the magnetic force theorem [8–11] to obtain the parameters from ground state density functional theory (DFT). The mapping from the DFT electronic structure problem to a given model Hamiltonian is in principle unique, but in practice it is often not clear, whether deviations from experiments originate from the choice of model or inaccuracies in the applied functional. For example, four-spin interactions [12, 13] are typically neglected in the mapping, but may be crucial for an accurate description and

can lead to wrong predictions for the strength of two-spin interactions [14]. In addition, the calculation of magnetic interactions based on DFT is nearly always based on a mapping to a *classical* Heisenberg model, which may give rise to significant inaccuracies in the predicted Heisenberg parameters [6]. An even more fundamental problem arises for the case of itinerant magnets, where the Heisenberg model description itself becomes dubious. In particular, Heisenberg models do not capture effects stemming from the low frequency Stoner excitations of metals, which give rise to e.g. Landau damping (finite lifetimes) of magnons. In general, it is not obvious that one can construct a reliable model of localized spins for such materials. A first principles treatment that is independent of underlying models thus seems pertinent for the study of magnons in itinerant magnets.

In general, the spectrum of magnetic excitations are encoded in the dissipative part of the transverse magnetic susceptibility χ^{+-}. For insulating magnetic materials, as well as in the Heisenberg model, χ^{+-} is characterized by a discrete set of poles mapping out the magnon dispersion of the material. In an itinerant magnet however, the magnons will be accompanied by a continuum of (renormalized) Stoner pair excitations and acquire a finite width due to Landau damping. In the framework of first principles calculations, there is essentially two distinct approaches for computing the susceptibility [15]. The first is many-body perturbation theory (MBPT), in which the perturbative expansion of the susceptibility is approximated by an infinite series of ladder diagrams. Summing up the series amounts to solving the Bethe-Salpeter equation. MBPT has been shown to yield reasonable results for the basic ferromagnetic metals Fe, Ni and Co [16, 17], although the approach contains certain inconsistencies when using wave functions and eigenvalues from DFT as a starting point [18]. The second approach (and the approach of this

work) is time-dependent DFT (TDDFT), which relies on a time-dependent exchange-correlation potential that needs to be approximated. The simplest approximation is comprised by the adiabatic local density approximation (ALDA), which has previously been shown to yield a good account of the magnon dispersion as well as the Landau damping of simple ferromagnetic metals [19–22].

To the best of our knowledge, there has not yet been any attempts to calculate the transverse magnetic susceptibility in antiferromagnetic (AFM) materials from first principles. This is likely due to the fact that antiferromagnets introduce additional complications for the spectral analysis and fulfilment of the Goldstone criteria in comparison to ferromagnetic (FM) materials. Even for the Heisenberg model, the antiferromagnetic ground state is a complicated correlated state, which is not known exactly. Instead, magnons are typically calculated with respect to the so-called non-interacting magnon state [1], which does not have a simple classical interpretation. Moreover, the fact that the magnon dispersion is linear at small wave vectors implies that the zone center constitutes a non-analytical point for the magnon dispersion. Such a feature is generally expected to be non-trivial to capture in a first principles treatment.

In the present work, we apply the ALDA to calculate the transverse magnetic susceptibility of bcc-Cr and Cr_2O_3, which are two prototypical antiferromagnets representing itinerant antiferromagnetism and local moment antiferromagnetism respectively. At small wave vectors, the extraction of magnon energies is complicated by the spectral interference between degenerate spin-lowering and spin-raising excitations. We show how to resolve this issue using the generalized Onsager relation. Numerically, it is non-trivial to satisfy the Goldstone criterion exactly, but it can be enforced by a slight rescaling of the ALDA kernel. Within this approach, we recover the linear dispersion relation expected for antiferromagnets and the magnon velocity can be directly extracted and compared with experimental values. For Cr_2O_3, we investigate the effect of Hubbard corrections in the LDA+U scheme and find that magnon velocities can be improved compared to bare LDA, but at the cost of deteriorating some qualitative features of the dispersion relation. For bcc-Cr, we find that the acoustic magnon mode is completely washed out once it enters the Stoner continuum. Furthermore, we identify an additional collective mode at high energies that seems to be partly protected from Landau damping.

The paper is organized as follows. In Sec. II we present the basic theory that allow us to calculate the transverse magnetic susceptibility in the framework of TDDFT and explain how the Onsager relation can be used to extract the magnon dispersion. In Sec. III we outline the computational details and in Sec. IV we present our results for Cr_2O_3 and bcc-Cr. Sec. V provides a summary of results and an outlook.

II. THEORY

A. Transverse magnetic susceptibility

The spectrum of transverse magnetic excitations is closely related to the linear transverse magnetic susceptibility, which is given by the *Kubo formula*:

$$\chi^{+-}(\mathbf{r}, \mathbf{r}', t - t') = -\frac{i}{\hbar}\theta(t - t')\langle\, [\hat{n}_0^+(\mathbf{r}, t), \hat{n}_0^-(\mathbf{r}', t')]\,\rangle_0,$$
(1)

where the time-dependency of the spin-raising and spin-lowering density operators, $\hat{n}^+(\mathbf{r}) = \hat{\psi}_\uparrow^\dagger(\mathbf{r})\hat{\psi}_\downarrow(\mathbf{r})$ and $\hat{n}^-(\mathbf{r}) = \hat{\psi}_\downarrow^\dagger(\mathbf{r})\hat{\psi}_\uparrow(\mathbf{r})$, is given in the interaction picture. For magnetic crystals, the Fourier transform of the real-space susceptibility (1) yields the transverse magnetic plane wave susceptibility,

$$\chi_{\mathbf{G}\mathbf{G}'}^{+-}(\mathbf{q}, \omega) = \iint \frac{d\mathbf{r}d\mathbf{r}'}{\Omega}e^{-i(\mathbf{G}+\mathbf{q})\cdot\mathbf{r}}\chi^{+-}(\mathbf{r}, \mathbf{r}', \omega)e^{i(\mathbf{G}'+\mathbf{q})\cdot\mathbf{r}'},$$
(2)

which determines the plane wave response in the transverse magnetization $\propto e^{i([\mathbf{G}+\mathbf{q}]\cdot\mathbf{r}-\omega t)}$ to an external perturbation in the transverse magnetic field $\propto e^{i([\mathbf{G}'+\mathbf{q}]\cdot\mathbf{r}-\omega t)}$, to linear order. Here, Ω is the crystal volume, and each plane wave component is separated in a reciprocal lattice vector $\mathbf{G}/\mathbf{G}'$ and a wave vector $\mathbf{q}$ within the first Brillouin Zone (BZ). Furthermore, it should be noted that the linear response is diagonal both in the frequency ω as well as the wave vector $\mathbf{q}$. We refer to Ref. [22] for more details.

From the plane wave susceptibility, one may calculate the spectrum of induced excitations [22]:

$$S_{\mathbf{G}\mathbf{G}'}^{+-}(\mathbf{q}, \omega) = -\frac{1}{2\pi i}\left[\chi_{\mathbf{G}\mathbf{G}'}^{+-}(\mathbf{q}, \omega) - \chi_{-\mathbf{G}'-\mathbf{G}}^{-+}(-\mathbf{q}, -\omega)\right].$$
(3)

This spectrum is composed of spin-lowering excitations at positive frequencies and spin-raising excitations at negative frequencies. As a result, it can be decomposed into quasi-particle spectral functions that are associated with either a raised or lowered spin angular momentum,

$$S_{\mathbf{G}\mathbf{G}'}^{+-}(\mathbf{q}, \omega) = A_{\mathbf{G}\mathbf{G}'}^{+-}(\mathbf{q}, \omega) - A_{-\mathbf{G}'-\mathbf{G}}^{-+}(-\mathbf{q}, -\omega),$$
(4)

where (assuming zero temperature):

$$A_{\mathbf{G}\mathbf{G}'}^{jk}(\mathbf{q}, \omega) = \frac{1}{\Omega}\sum_{\alpha \neq \alpha_0} n_{0\alpha}^j(\mathbf{G} + \mathbf{q})n_{\alpha 0}^k(-\mathbf{G}' - \mathbf{q})$$
$$\times \delta(\hbar\omega - (E_\alpha - E_0)).$$
(5)

The so-called spin-lowering and spin-raising spectral functions are made up of δ-function peaks at excitations energies $\hbar\omega = (E_\alpha - E_0)$, where E_α is the energy of an excited state $|\alpha\rangle$ with lowered/raised spin angular momentum with respect to the ground state $|\alpha_0\rangle$ with energy E_0. Each quasi-particle excitation is weighted by reciprocal space pair densities $n_{\alpha\alpha'}^j(\mathbf{G} + \mathbf{q})$, which are Fourier transforms of the real-space pair densities

$n_{\alpha\alpha'}^j(\mathbf{r}) = \langle\alpha|\hat{n}^j(\mathbf{r})|\alpha'\rangle$. In the non-relativistic limit, where the total spin-projection along the z-axis can be taken as a good quantum number, A^{+-} is the spectral function for quasi-particle excitations where S^z has been lowered by a single unit, whereas A^{-+} is the spectral function for quasi-particle excitations where S^z has been raised by a single unit. $S_{\mathbf{G}}^{+-}(\mathbf{q},\omega) \equiv S_{\mathbf{GG}}^{+-}(\mathbf{q},\omega)$ thus fully characterizes the spectrum of magnon quasi-particle excitations of a given material, where the diagonals $A_{\mathbf{G}}^{+-}(\mathbf{q},\omega)$ and $A_{\mathbf{G}}^{-+}(\mathbf{q},\omega)$ are real functions of frequency due to the fact that $[\hat{n}^+(\mathbf{r})]^\dagger = \hat{n}^-(\mathbf{r})$.

B. Onsager relations for centrosymmetric antiferromagnets

Both bcc-Cr and Cr_2O_3 are centrosymmetric antiferromagnets, meaning that the Hamiltonians are invariant under parity inversion, $[\hat{H}_0, \hat{P}] = 0$. In the antiferromagnetic ground states, time-reversal symmetry is broken, and for Cr_2O_3, parity inversion is broken as well. For both systems however, application of time-reversal *and* parity inversion maps the ground state onto itself, $\hat{P}\hat{T}|\alpha_0\rangle \to |\alpha_0\rangle$ [23]. This implies that the spectrum of induced transverse magnetic excitations follows the symmetry relation

$$S_{\mathbf{GG}'}^{+-}(\mathbf{q},\omega) = S_{\mathbf{G}'\mathbf{G}}^{-+}(\mathbf{q},\omega), \qquad (6)$$

which is an instance of the generalized Onsager relation (see Appendix A). Furthermore, as the ground state of both systems is collinear, the spectrum also follows the Onsager relation

$$S_{\mathbf{GG}'}^{+-}(\mathbf{q},\omega) = S_{-\mathbf{G}'-\mathbf{G}}^{+-}(-\mathbf{q},\omega) \qquad (7)$$

in the non-relativistic limit (see Sec. A 4), meaning that the magnon dispersion is reciprocal in $\pm(\mathbf{G}+\mathbf{q})$. Combining both of these Onsager relations, it is concluded that the spin-raising and spin-lowering spectral functions are identical upon reversing the wave vector $\mathbf{G}+\mathbf{q}$,

$$S_{\mathbf{GG}'}^{+-}(\mathbf{q},\omega) = S_{-\mathbf{G}-\mathbf{G}'}^{-+}(-\mathbf{q},\omega), \qquad (8)$$

implying that $A_{\mathbf{G}}^{+-}(\mathbf{q},\omega) = A_{-\mathbf{G}}^{-+}(-\mathbf{q},\omega)$.

C. Magnon spectral functions in centrosymmetric antiferromagnets

Due to the PT-symmetry, the AFM spectral functions considered here are different in a few crucial aspects from the familiar FM spectral functions. Assuming that the spin-lowering spectrum for a given $\mathbf{q}$ and $\mathbf{G} = \mathbf{G}'$ is dominated by a single magnon excitation of frequency $\omega_{\mathbf{q}}$, lorentzian lineshape and half-width-half-maximum (HWHM) $\eta > 0$, we may write

$$A_{\mathbf{G}}^{+-}(\mathbf{q},\omega) = \frac{M}{\hbar}\frac{\eta/\pi}{(\omega-\omega_{\mathbf{q}})^2 + \eta^2}, \qquad (9)$$

where $M/\hbar$ denotes the spectral intensity. For a material with multiple magnon modes, Eq. (9) should also include a weighted sum over mode indices, with mode weights depending on the reciprocal lattice vector $\mathbf{G}$. For the acoustic mode in a ferromagnet, one can typically neglect minority-to-majority excitations at short wave vectors $\mathbf{q}$, and as a result, the transverse magnetic spectrum will simply be given as $S_{\mathbf{G}}^{+-}(\mathbf{q},\omega) = A_{\mathbf{G}}^{+-}(\mathbf{q},\omega)$. For a PT-symmetric antiferromagnet however, where $A_{-\mathbf{G}}^{-+}(-\mathbf{q},\omega) = A_{\mathbf{G}}^{+-}(\mathbf{q},\omega)$, the two magnon modes of opposite spin angular momentum will destructively interfere in the spectrum of induced excitations:

$$S_{\mathbf{G}}^{+-}(\mathbf{q},\omega) = \frac{M}{\hbar}\left[\frac{\eta/\pi}{(\omega-\omega_{\mathbf{q}})^2 + \eta^2} - \frac{\eta/\pi}{(\omega+\omega_{\mathbf{q}})^2 + \eta^2}\right]. \qquad (10)$$

For magnon excitations where the frequency is comparable to or smaller than the spectral width, this means that the magnon spectral function is obscured by its degenerate partner of opposite spin as illustrated in Fig. 1(a). In particular, the spectrum completely vanishes for $\omega_{\mathbf{q}} = 0$.

More generally, an AFM spectrum of induced excitations will always have a vanishing zeroth moment, due to the sum rule [22]

$$\hbar\int_{-\infty}^{\infty} S_{\mathbf{G}}^{+-}(\mathbf{q},\omega)\,d\omega = \frac{n_z}{\Omega_{\text{cell}}}, \qquad (11)$$

where n_z/Ω_{cell} gives the magnetization per unit cell. Because the total magnetization vanishes in antiferromagnets, the spin-raising and spin-lowering excitations will always have equal weight in $S_{\mathbf{G}}^{+-}(\mathbf{q},\omega)$, independently of lineshape, inversion symmtry etc. In addition, this also implies, that the AFM magnon spectral weight M will generally vary both as a function $\mathbf{G}$ and $\mathbf{q}$.

D. Transverse magnetic susceptibility from LR-TDDFT

The transverse magnetic susceptibility can be computed from first principles within the framework of linear response time-dependent density functional theory (LR-TDDFT), using only quantities which can be extracted from a routine DFT calculation [24, 25]. For a collinear DFT ground state, the non-interacting susceptibility of the Kohn-Sham system is given by

$$\chi_{\text{KS}}^{+-}(\mathbf{r},\mathbf{r}',\omega) = \lim_{\eta\to 0^+}\frac{1}{N_k^2}\sum_{n\mathbf{k}}\sum_{m\mathbf{k}'}(f_{n\mathbf{k}\uparrow} - f_{m\mathbf{k}'\downarrow})$$
$$\times \frac{\psi_{n\mathbf{k}\uparrow}^*(\mathbf{r})\psi_{m\mathbf{k}'\downarrow}(\mathbf{r})\,\psi_{m\mathbf{k}'\downarrow}^*(\mathbf{r}')\psi_{n\mathbf{k}\uparrow}(\mathbf{r}')}{\hbar\omega - (\epsilon_{m\mathbf{k}'\downarrow} - \epsilon_{n\mathbf{k}\uparrow}) + i\hbar\eta}, \qquad (12)$$

where $\epsilon_{n\mathbf{k}s}$ and $f_{n\mathbf{k}s}$ are the single-particle energies and ground state occupations of the Kohn-Sham Bloch waves $\psi_{n\mathbf{k}s}(\mathbf{r})$, while N_k denotes the number of k-points. As
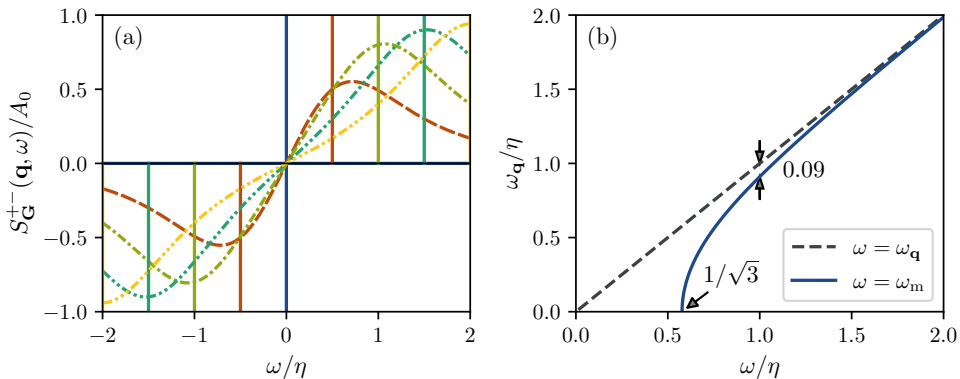
FIG. 1. Characteristics of a PT-symmetric AFM spectrum of transverse magnetic excitations. (a) AFM spectral function in Eq. (10) plotted as a function of frequency for different magnon energies $\hbar\omega_{\mathbf{q}}$. The vertical lines indicate the energy of the spin-lowering (at positive frequencies) and spin-rasing (negative frequencies) magnon excitations. The spectra are normalized by the magnon peak intensity $A_0 = M/(\pi\hbar\eta)$, see Eq. (9). (b) Magnon frequency as a function of the spectral function maximum ω_{m}, as given in Eq. (15). The magnon frequency is also plotted versus itself in dashed gray for visual comparison.

seen in Eq. (12), the transverse magnetic Kohn-Sham spectrum is made up of single-particle Stoner excitations, where an electron is removed from an occupied Kohn-Sham orbital and inserted in an unoccupied orbital of opposite spin. The Stoner pair excitations form a continuum, which is referred to as the Stoner continuum, and give rise to Landau damping of a given collective magnon mode, whenever the mode overlaps with the Stoner continuum. In the ALDA, the full many-body susceptibility is obtained from the Kohn-Sham counterpart through a single Dyson equation

$$
\chi^{+-}(\mathbf{r}, \mathbf{r}', \omega) = \chi_{\mathrm{KS}}^{+-}(\mathbf{r}, \mathbf{r}', \omega) + \int d\mathbf{r}_1 \\
\times \chi_{\mathrm{KS}}^{+-}(\mathbf{r}, \mathbf{r}_1, \omega) f_{\mathrm{LDA}}^{-+}(\mathbf{r}_1) \chi^{+-}(\mathbf{r}_1, \mathbf{r}', \omega),
\tag{13}
$$

where $f_{\mathrm{LDA}}^{-+}(\mathbf{r}) = 2W_{\mathrm{xc,LDA}}^z(\mathbf{r})/n^z(\mathbf{r})$ is the transverse LDA kernel, depending only on the local exchange-correlation magnetic field and spin-polarization of the ground state. For additional details, the reader is referred to Ref. [22].

III. METHODOLOGY

A. Gap error in antiferromagnets

In a collinear LR-TDDFT description of ferromagnets as well as antiferromagnets, there should in principle always exist a gapless magnon mode, thanks to the Goldstone theorem. In the absence of spin-orbit coupling, the so-called Goldstone mode is gapless at the Γ-point, $\omega_\Gamma = 0$, because the energy is invariant towards rigid

rotations of the spins. For LR-TDDFT calculations in practise, however, it has been widely established that numerical approximations such as basis truncation result in a finite gap error [19, 20, 22, 26, 27]. For a plane wave basis in particular, it seems very difficult to converge the Γ-point magnon frequency [22] and in practise a gap error correction scheme is needed in order to provide a converged magnon dispersion.

For ferromagnets, simple correction schemes are sufficient. Due to the limited weight of spin-raising excitations, one can simply shift the transverse magnetic excitation spectrum so as to fulfill $\omega_\Gamma = 0$ [22]. For antiferromagnets however, the spin degeneracy of the Goldstone mode implies that $S_{\mathbf{G}}^{+-}(\mathbf{q}, \omega)$ should vanish at the Γ-point, which cannot be satisfied through a frequency shift of the excitation spectrum, as a finite ω_Γ results in a finite spectral function, see Eq. (10). Instead, we rescale the ALDA kernel, $f_{\mathrm{LDA}}^{-+} \to \lambda f_{\mathrm{LDA}}^{-+}$, such as to fulfill the Goldstone criteria for antiferromagnets, $S_{\mathbf{G}=\mathbf{0}}^{+-}(\mathbf{q} = \mathbf{0}, \omega) = 0$. With otherwise converged numerical parameters, this amounts to a small rescaling of about 1% percent when applied on top of a LSDA ground state calculation, with $\lambda = 1.0096$ for Cr_2O_3 and $\lambda = 1.0124$ for Cr. For this reason, we consider the rescaling a numerical detail rather than a change of exchange-correlation kernel.

B. Extracting the AFM magnon dispersion

As illustrated in Fig. 1(a), it is not only the spin-lowering magnon excitations that contribute to the positive frequency transverse magnetic excitation spectrum, $S_{\mathbf{G}}^{+-}(\mathbf{q}, \omega)$, but also the spin-raising magnon excita-

tions of finite width. As a result, the spectral function maximum will not correspond directly to the magnon frequency. For a spin-lowering PT-symmetric AFM magnon excitation of lorentzian lineshape, see Eqs. (9) and (10), the spectral function maximum is instead located at:

$$\omega_{\mathrm{m}} = \pm \frac{1}{\sqrt{3}} \left(\omega_{\mathbf{q}}^2 + 2\sqrt{\omega_{\mathbf{q}}^4 + \eta^2 \omega_{\mathbf{q}}^2 + \eta^4} - \eta^2 \right)^{1/2}. \quad (14)$$

In the limit $|\omega_{\mathbf{q}}| \gg \eta$, it is a good approximation to identify the magnon frequency as the spectral function maximum, $\omega_{\mathrm{m}} \simeq \omega_{\mathbf{q}}$, but for $|\omega_{\mathbf{q}}| \ll \eta$, such an identification fails catastrophically as ω_{m} is determined mostly from the magnon spectral width, $\omega_{\mathrm{m}} \simeq \eta/\sqrt{3}$, and not the frequency. Consequently, a more careful analysis is needed in order to identify the energy of low frequency AFM magnons.

In the simplest case, the low frequency magnons are undamped, and the lineshape is formally a Dirac δ-function. However, to converge the Stoner continuum in LR-TDDFT calculations (or simply because δ-functions are impossible to resolve numerically), η in Eq. (12) is typically left as a finite broadening parameter. For magnons that do not overlap with the Stoner continuum (free of Landau damping), this means that the lineshape is lorentzian and with HWHM η, as assumed in Eq. (9). Thus, knowing the magnon spectral width, magnon frequencies below the Stoner continuum may be calculated directly from the spectral function maximum of Eq. (10):

$$\omega_{\mathbf{q}} = \pm \left(2\sqrt{\omega_{\mathrm{m}}^4 + \eta^2 \omega_{\mathrm{m}}^2} - \omega_{\mathrm{m}}^2 - \eta^2 \right)^{1/2}. \quad (15)$$

The AFM magnon frequency that results from this equation is illustrated as a function of the spectral function maximum in Fig. 1(b). First of all, we see that $\omega_{\mathbf{q}} \simeq \omega_{\mathrm{m}}$ is a good approximation already at $\omega_{\mathrm{m}} = 2\eta$, where $\omega_{\mathbf{q}} = 0.993\,\omega_{\mathrm{m}}$. For values of $\omega_{\mathrm{m}} < 2\eta$ however, it becomes increasingly important to account for the finite width of the excitations to accurately extract the magnon dispersion. For $\omega_{\mathrm{m}} \in [\eta, 2\eta]$, the spectral function maximum slightly exceeds the magnon frequency, with $\omega_{\mathbf{q}} = 0.910\,\omega_{\mathrm{m}}$ at $\omega_{\mathrm{m}} = \eta$, and for $\omega_{\mathrm{m}} < \eta$ the spectral function maximum is no longer a good indicator of the magnon dispersion, see e.g. the red, green and teal curves in Fig. 1(a). In fact, the linear magnon dispersion of antiferromagnets will appear quadratic at short wave vectors q and with a finite gap of $\eta/\sqrt{3}$, if only the spectral function maximum is considered, see Eq. (14) and Fig. 1(b). As a more practical matter, it becomes a substantial numerical challenge to determine ω_{m} precisely enough to infer $\omega_{\mathbf{q}}$ through Eq. (15) for values of $\omega_{\mathrm{m}} < \eta$. In the limit $\omega_{\mathrm{m}} \to \eta/\sqrt{3}$, the gradient $\partial\omega_{\mathbf{q}}/\partial\omega_{\mathrm{m}}$ diverges, meaning that the inferred magnon frequency around $\omega_{\mathbf{q}} = 0$ is sensitive to infinitesimal changes in ω_{m}. This implies that an increasingly dense frequency grid is needed in order to determine $\omega_{\mathbf{q}}$ from ω_{m} as $\omega_{\mathrm{m}} \to \eta/\sqrt{3}$. If ω_{m} is determined from a parabolic fit to the spectral

peak sampled on a linear frequency grid, Eq. (15) ceases to provide accurate magnon frequencies with a frequency sampling of $\delta\omega = \eta/8$ already for $\omega_{\mathrm{m}} \lesssim \eta$. Instead, it turns out to be much more efficient to fit the entire spectral function in Eq. (10) directly to the calculated spectrum and extract the magnon frequency from the fit. In this case, a $\delta\omega = \eta/8$ frequency sampling provides sufficient accuracy for magnon frequencies as small as $\omega_{\mathbf{q}} = \eta/40$.

For Landau damped magnons, it is a more complicated issue to extract the magnon dispersion, because the exact magnon lineshape is not known beforehand and cannot be directly extracted from $S_{\mathbf{G}}^{+-}(\mathbf{q}, \omega)$ due to the spin degeneracy. To make progress, we take another look at the double-lorentzian spectral function (10), with the aim of establishing some heuristics that may generalize to other lineshapes as well. Firstly, we note that the curvature always vanishes at zero frequency, $\partial^2 S_{\mathbf{G}}^{+-}(\mathbf{q}, \omega)/\partial\omega^2 = 0\big|_{\omega=0}$. Because $\partial^3 S_{\mathbf{G}}^{+-}(\mathbf{q}, \omega)/\partial\omega^3\big|_{\omega=0}$ changes sign from negative to positive at $\omega_{\mathbf{q}} = \eta$, one can then use the low frequency curvature as a simple visual heuristic to determine the relative sizes of the magnon frequency and spectral width. If the spectral function has positive curvature at low frequencies, $\omega_{\mathbf{q}} > \eta$ and $\omega_{\mathbf{q}} \simeq \omega_{\mathrm{m}}$ should at least provide a decent approximation. Of course, the error will depend somewhat on the exact lineshape, but it should be comparable to that of a lorentzian one, which has a maximum error of 7.5% for $\omega_{\mathbf{q}} > \eta$. If the AFM spectral function has negative curvature at low frequencies, one is instead forced to guess a functional form for the lineshape and fit it to the spectrum. To exemplify the use of this heuristic, one would conclude that $\omega_{\mathbf{q}} \simeq \omega_{\mathrm{m}}$ is a decent approximation for the teal and yellow lineshapes in Fig. 1(a), but not for the red and green. To get a better grasp of the error made in approximating $\omega_{\mathbf{q}} \simeq \omega_{\mathrm{m}}$, one can go a step further. For the lorentzian magnon lineshape, a magnon frequency of $\omega_{\mathbf{q}} > 2\eta$ is enough to guarantee that the error is smaller than 1%. For the full spectral function, $S_{\mathbf{G}}^{+-}(\mathbf{q}, \omega)$, this criteria is met when $\omega_{\mathrm{m}} > 2.25\,\mathrm{HWHM}_1$, where HWHM_1 denotes the HWHM below the peak at positive frequency. Thus, one can be reasonably confident that $\omega_{\mathbf{q}} \simeq \omega_{\mathrm{m}}$ is a good approximation, for lineshapes where the spectral function maximum exceeds 2.25 times the lower HWHM.

C. Computational details

In this study, we compute the spectrum of transverse magnetic excitations, $S_{\mathbf{G}}^{+-}(\mathbf{q}, \omega)$, using the GPAW open-source code [28, 29] as described in [22]. We use the experimental room temperature crystal structures (Cr_2O_3: $a = 4.957\,\text{Å}$, $c = 13.592\,\text{Å}$, Cr-$z = 0.3473\,\text{Å}$, O-$x = 0.3057\,\text{Å}$ [30], Cr: $a = 2.884\,\text{Å}$ [31]) and compute ground state properties using the LSDA exchange-correlation functional, with and without Hubbard corrections (in the Dudarev LSDA+U scheme [32]). We neglect core level excitations and include only Cr $4s$, $3d$ and O

2s, 2p orbitals as valence states in the Kohn-Sham susceptibility (12). To converge the summation over Kohn-Sham states, we include also 12 additional empty shell bands per atom, and in order to invert the Dyson equation in a plane wave basis, a plane wave cutoff of 1000 eV is used. Based on a previous convergence study for itinerant ferromagnets Fe, Ni and Co, the applied computational parameters should provide a benchmark-level accuracy of results [22].

When inverting the Dyson equation (13), the scaled ALDA exchange-correlation kernel is used both for LSDA and LSDA+U ground states. However, when a Hubbard correction has been applied in the ground state, the kernel scaling is no longer a numerical detail, as it would also be needed in the limit of an infinite basis representation. Thus, the resulting kernel is formally a new kernel, which we will denote λALDA+U. Usage of such a scaled kernel is justified for ferromagnetic ground states, based on the homogeneous electron gas limit, and λALDA+U has previously proved effective in describing essential correlation effects in the itinerant ferromagnet MnBi [33]. Whether or not the λALDA+U approach is a viable scheme for antiferromagnets remains to be seen.

For magnetic response calculations in the GPAW code, we are currently restricted to computing the transverse magnetic plane wave susceptibility $\chi_{\mathbf{GG'}}^{+-}(\mathbf{q}, \omega)$ at wave vectors $\mathbf{q}$ that are commensurate with the k-point grid of the ground state calculation. The k-point summation in Eq. (12) is approximated as a sum over the Kohn-Sham states on the ground state k-point grid and thus a finite artificial broadening parameter η is needed in order broaden the single-particle Stoner excitations into a continuum. For itinerant ferromagnets as well as antiferromagnets, this implies that the convergence of the k-point grid density and artificial broadening η is intertwined for the magnon dispersion inside the Stoner continuum [22]. Providing such a convergence analysis on the basis of magnon frequencies is a very computationally expensive task, why a method for inferring convergence on the basis on the single-particle Stoner spectrum alone is highly desirable. We have previously developed such a method for itinerant ferromagnets [22], but as it relies on the low frequency Stoner continuum, it is not transferable to antiferromagnets where the low frequency Stoner continuum is obscured due to spin degeneracy. Instead, we choose the k-point grid density and artificial broadening to match converged values for the itinerant ferromagnets Fe, Ni and Co. For metallic Cr we apply a $(60, 60, 60)$ Γ-centered Monkhorst-Pack (MP) grid, resulting in a 27.5 Å k-point density. We use an artificial broadening of $\eta = 50$ meV and sample the susceptibility on a linear frequency grid with a $\delta\omega = 6$ meV spacing.

For insulating Cr_2O_3, the magnon modes never enter the Stoner continuum and broadening of the Stoner spectrum is irrelevant to the magnon dispersion as a result. Instead, the spectral broadening may be chosen as small as possible, while still supporting reliable extraction of the magnon dispersion on a reasonably spaced frequency
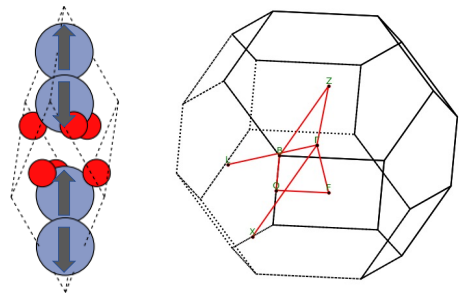
FIG. 2. Structure of Cr_2O_3. Left: Minimal unit cell with the ground state magnetic configuration indicated. Right: Brillouin zone highlighting the high-symmetry path of our computed magnon spectra.

grid. For Cr_2O_3 we use a linear frequency spacing of $\delta\omega = 4$ meV and an artificial broadening of $\eta = 32$ meV. The insulating nature of Cr_2O_3 also significantly relaxes the requirements on k-point sampling. For calculations without empty shell bands and a plane wave cutoff of 500 meV, a $(12, 12, 12)$ (k-point density of 8.8 Å) and a $(24, 24, 24)$ Γ-centered MP-grid (k-point density of 17.5 Å) result in identical magnon frequencies down to the fifth significant digit. As a result, one could probably use an even more sparse k-point sampling, but to compute more than just a few points of the Cr_2O_3 magnon dispersion, we apply the $(12, 12, 12)$ Γ-centered MP-grid. Furthermore, in order to extract accurate magnon velocities we use a $(24, 24, 24)$ Γ-centered MP-grid to compute one additional magnon frequency for each direction $\hat{\mathbf{q}}$ close to the Γ-point.

IV. RESULTS

A. Cr_2O_3

1. Basic properties

Chromium sesquioxide (Cr_2O_3) is an antiferromagnetic insulator with a trigonal corundum crystal structure (space group $R\bar{3}c$), occurring naturally in the form of the eskolaite mineral. The Cr^{3+} atoms are situated at octahedral sites of an O^{2-} hcp array, resulting in a rhombohedral primitive cell containing four Cr atoms located along the [111] diagonal (corresponding to the c-axis of the hexagonal cell) [30]. The Cr magnetic moments align antiferromagnetically in a ↑↓↑↓ spin configuration [34, 35] as shown in Fig. 2, which is consistent with the prediction from Goodenough that all the direct Cr-Cr couplings (along octahedral faces and edges) are antiferromagnetic [36]. Due to its broken inversion symmetry in the ground state, Cr_2O_3 has been thoroughly studied as a prototypical material exhibiting magnetoelectric cou-

pling [23, 37, 38] and has recently been demonstrated to host magnon polarons, that is, hybridized excitations of magnons and phonons [39, 40].

The Cr^{3+} local magnetic moments are slightly reduced from the ionic value of $3\,\mu_B$, with experimental values reported in the range of $2.48 - 2.76\,\mu_B$, where the lower and upper values originate from neutron polarimetry and neutron powder diffraction experiments respectively [30, 35, 41].

In DFT, Cr_2O_3 is consistently predicted to order antiferromagnetically in accordance with experiment. An antiferromagnetic ground state is preferred over the ferromagnetic and paramagnetic states using both the local spin-density approximation (LSDA), the Hubbard corrected LSDA (LSDA+U) and generalized gradient approximations (GGA+U) as well as the hybrid screened exchange (sX) functional [42–46]. Furthermore, a preference for the ↑↓↑↓ spin configuration has been confirmed for both the LSDA+U, GGA+U and sX functionals [43–45]. The band gap is, however, significantly underestimated in the LSDA compared to the experimental value of 3.4 eV [47, 48]. While the Kohn-Sham band gap is not formally required to match the experimental gap, a deviation by approximately a factor of three implies the presence of strong static correlation effects, which are typically not well described by local functionals. This observation is in line with the experimental characterization of Cr_2O_3 as an intermediate between a charge-transfer insulator and a Mott-Hubbard insulator [48, 49]. A similar characterization results from DFT using either of the LSDA+U, GGA+U, sX and B3LYP functionals [43–46, 50, 51].

In the ↑↓↑↓ spin configuration of Cr_2O_3, we find a local magnetic moment of $2.56\,\mu_B$ for the Cr atoms using the LSDA functional (here defined as the integrated moment inside the Cr PAW sphere of radius $2.3\,a_0$). When including a Hubbard correction, the local magnetic moments increase with U_{eff}, although not exceeding the ionic value of $3\,\mu_B$ for $U_{eff} < 5$ eV. The effect of the Hubbard correction is in good agreement with previous LSDA+U literature [44, 52] and is illustrated in Fig. 3(a). Given the ambiguous definition of a local magnetic moment, we find the LSDA(+U) Cr moments to be in reasonable agreement with the experimental range of observed values [30, 35, 41], at least for values of $U_{eff} \lesssim 4$ eV.

In contrast to the local magnetic moments, the band gap is highly sensitive to the inclusion of a Hubbard correction. This is illustrated in Fig. 3(b) as well as in previous literature [43, 44]. We find the LSDA Kohn-Sham band gap to be 1.2 eV (with a direct gap of 1.3 eV), that is, about a third of the experimental gap. When including a Hubbard correction, the gap is widens and it is possible to reproduce the experimental gap with a suitable choice of U_{eff}. However, it should be stressed, that the agreement between the experimental gap and the calculated Kohn-Sham gap is not a figure of merit in itself and cannot be used as a criterion for finding the optimal value for U_{eff}. Rather, a large disagreement simply in-
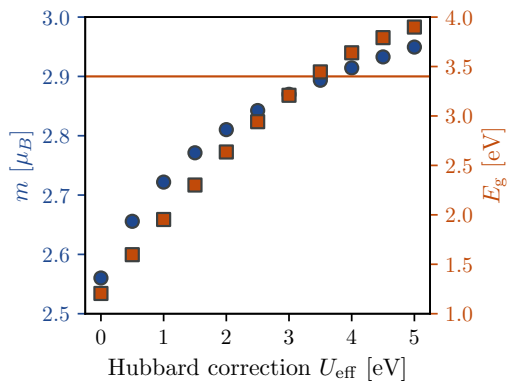
FIG. 3. LSDA+U ground state properties of Cr_2O_3 as a function of the Hubbard correction U_{eff}. Left axis (blue): Local magnetic moment of the Cr atoms. Right axis (red): Kohn-Sham band gap. The horizontal line indicates the experimental gap [47, 48].

dicates the presence of strong correlation, which implies that Hubbard corrections are likely needed in order to describe various material properties accurately. Alternatively, the U and J Hubbard parameters may also be determined using e.g. the constrained occupations method or unrestricted Hartree-Fock theory. Within these approaches, $U_{eff} = U - J$ has previously been demonstrated to fall in the range of 2.5-3.5 eV [44, 52].

2. Magnetic excitations

The magnon excitations of Cr_2O_3 have been investigated experimentally by several authors. Samuelsen [54, 55] provided early short wave vector inelastic neutron scattering (INS) data and estimated the magnon velocity along the $[110]^*$ and $[211]^*$ directions, where square brackets with an asterisk indicate directions in terms of the reciprocal lattice vectors of the rhombohedral lattice. In a similar study, Alikhanov et al. [56] investigated the magnon dispersion in a wide selection of directions in the $(1\bar{1}0)$ plane, still at short wave vectors, and fitted their data to a Heisenberg model including only the exchange couplings between neighbouring Cr occupied octahedra, i.e. exchange parameters up to J_4. They found the magnon dispersion to be anisotropic, with magnon velocities being larger in-plane (in the $[2\bar{1}\bar{1}]$ direction) than out-of-plane (the [111] direction). Finally, Samuelsen et al. [53] reported magnon frequencies throughout the entire $(1\bar{1}0)$ plane of the magnetic BZ, that is, including also the excitations at long wave vectors. Upon including a fifth exchange parameter (J_5), they were able to provide a satisfactory fit of the Heisenberg model to the experimental magnon dispersion.

FIG. 4. Magnon dispersion of Cr_2O_3 as a function of $\mathbf{q}$ inside the first BZ of the rhombohedral lattice. The ALDA acoustic and optical magnon modes are extracted at the $(0,0,0)$ and $(\bar{1},\bar{1},\bar{1})$ reciprocal lattice points respectively and compared to experimental INS data and a J_5 Heisenberg model fitted to experiment [53].

Based on the LSDA ground state, we have employed the ALDA to compute the low frequency spectrum of transverse magnetic excitations for a wide selection of wave vectors in and out of the $(1\bar{1}0)$ plane. The spectrum at a given wave vector is dominated by a single magnon peak and its degenerate partner of opposite spin. By fitting the spectrum to the lorentzian AFM spectral function (10), we obtain a practically ideal fit and extract the Cr_2O_3 magnon dispersion, which is presented in Fig. 4. Qualitatively, the ALDA is seen to reproduce the experimental magnon dispersion. However, both the band width and the magnon velocity are overestimated by roughly a factor of two. Also for wave vectors where there is no experimental data, there is a good qualitative agreement between the ALDA magnon dispersion and that of the Heisenberg model fitted to experiment. As an example, the optical magnon mode seems to be more dispersive along the $\Gamma \to L$ path compared to the $\Gamma \to F$ path in both the ALDA and the Heisenberg model.

Given that Cr_2O_3 is a strongly correlated material, it is not all too surprising that the ALDA fails to yield a good quantitative agreement with experiment. In Fig. 5, we present magnon velocities computed by finite difference on LSDA+U ground states as a function of U_{eff}, including the Hubbard correction by means of the λALDA+U method. Indeed, the magnon velocity seems to steadily decrease with U_{eff}. However, the best correspondence with experiment seems to occur already around $U_{\text{eff}} \sim 1$ eV and at $U_{\text{eff}} = 2.0$ eV, the magnon dispersion has turned completely flat along all directions. In Fig. 6, we show the full magnon dispersion obtained with $U_{\text{eff}} = 1.0$ eV and $U_{\text{eff}} = 2.0$ eV respectively. Whereas the magnon velocity seems to agree well with experiment for $U_{\text{eff}} = 1.0$ eV, the magnon dispersion as a whole
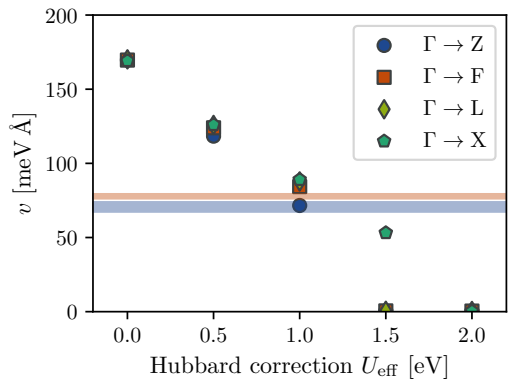
FIG. 5. Cr_2O_3 magnon velocities calculated within the ALDA and the λALDA+U method as a function of Hubbard correction U_{eff}. For reference the 1σ experimental range is shown, extracted as the slope of a linear fit to the INS data [53] of wave numbers in the range $aq \in [0.4, 1.2]$, where a is the rhombohedral lattice constant.

does not. The magnon band width is still overestimated, and some of the features that were qualitatively reproduced in the ALDA, such as the flat optical band between the Γ and F high-symmetry points, are no longer reproduced. Thus, the λALDA+U method proves insufficient for including Hubbard corrections in a meaningful way that consistently improves the Cr_2O_3 magnon dispersion. Nevertheless, it is still a striking feature, that the λALDA+U method yields a completely flat magnon dispersion for short wave vectors at $U_{\text{eff}} = 2.0$ eV. In
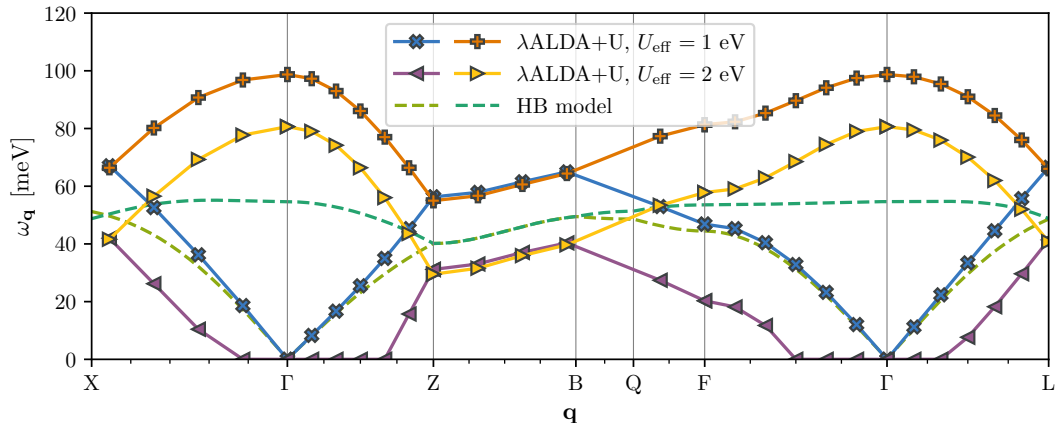
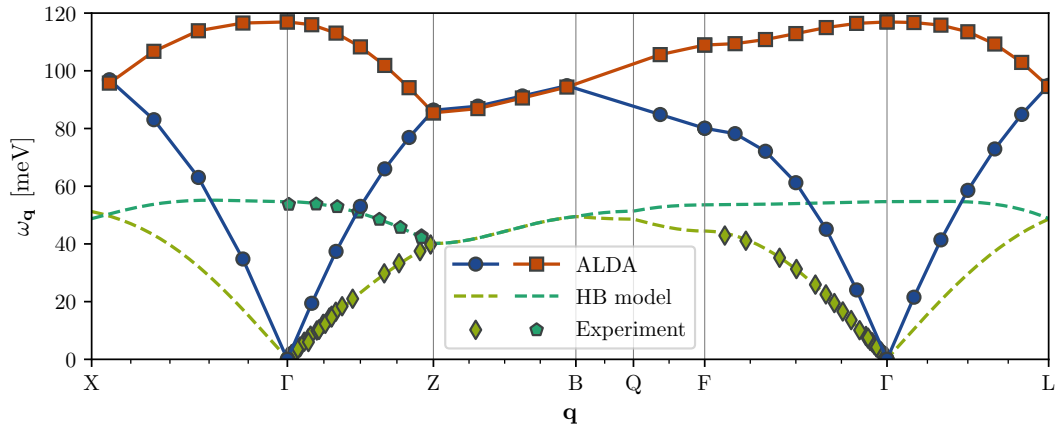FIG. 6. λALDA+U magnon dispersion of Cr_2O_3 as a function $\mathbf{q}$ inside the first BZ of the rhombohedral lattice. The acoustic and optical magnon modes are extracted at the $(0,0,0)$ and $(\bar{1},\bar{1},\bar{1})$ reciprocal lattice points respectively and compared to a J_5 Heisenberg model fitted to experimental INS data [53].

contrast to the Γ-point itself, the transverse magnetic excitation spectrum does not vanish at short, but finite, wave vectors. Instead, the spectrum is peaked more or less exactly at the resolution limit, $\eta/\sqrt{3}$. The physical significance of this, if any, is not clear at present.

In Table I, we present the actual values for the computed LR-TDDFT magnon velocities along with fitted INS reference values and analytical velocities calculated within the J_5 Heisenberg model [53]. The experimental dispersion was fitted only to data in the range $aq \in [0.4, 1.2]$, that is, the range of wave numbers where the magnon dispersion is approximately linear. There is a lower bound to this range due to relativistic effects (not included in our calculations) resulting in an anisotropy gap of $\omega_\Gamma = 0.68$ meV [53, 57]. Clearly, the ALDA yields a completely isotropic magnon dispersion at short wave vectors, which is in sharp contrast to the out-of-plane vs. in-plane anisotropy observed experimentally. In addition, the computed ALDA magnon velocities is overestimated by more than a factor of two. Interestingly, the isotropy is broken by the Hubbard correction and with $U_{\text{eff}} = 1.0$

$\hat{q}$	BZ line	v (ALDA)	v (λALDA+U)	v (Exp.)	v (HB)
$[111]^*$	$\Gamma \to Z$	170	72	70.6 ± 3.2	71.0
$[110]^*$	$\Gamma \to F$	170	84	77.8 ± 1.5	80.7
$[100]^*$	$\Gamma \to L$	170	88		83.1
$[\bar{1}01]^*$	$\Gamma \to X$	169	89		84.2

TABLE I. Cr_2O_3 magnon velocities in units of meV Å. The λALDA+U values were calculated with $U_{\text{eff}} = 1$ eV. The values extracted from the experimental INS data are shown as reference along with values computed analytically from the J_5 Heisenberg model fitted to experiment [53].

eV, the experimental magnon velocities are accurately reproduced, matching also the Heisenberg model values for directions out of the $(1\bar{1}0)$ plane.

B. Bulk Cr

1. Basic properties

Chromium is a metallic antiferromagnetic material with a bcc crystal structure. It is widely accepted to have an incommensurate longitudinal spin-density wave (SDW) as its ground state [58] with a SDW vector of $q_{\text{SDW}} = 0.95 \times 2\pi/a$, directed towards one of the cubic axes [59, 60]. With increasing temperature, pristine Cr first undergoes a spin-flip phase transition to a transverse SDW at $T_{\text{SF}} \simeq 123$ K before becoming paramagnetic at $T_{\text{N}} \simeq 311$ K [58]. Furthermore, in a wide range of dilute Cr alloys, the SDW becomes commensurate with the cubic lattice [61] and the local magnetic moments of the Cr corner and center atoms (which are anti-aligned) become equal in size, see e.g. illustration in Ref. [62]. As an example, the $Cr_{1-x}Mn_x$ system transitions into the commensurate SDW for $x \gtrsim 0.4$ at.% at room temperature [61]. Due to its simplicity, commensurate AFM Cr provides the most basic realization of itinerant antiferromagnetism in a real material and has been used for initial discoveries with emerging first principles methodologies since the advent of the LSDA [62–64]. In addition, the similarity between the commensurate-incommensurate phase transition in Cr and the AFM-superconducting phase transition in doped cuprates has spurred hope that the study of AFM Cr may contribute to a better understanding of the mechanism responsible
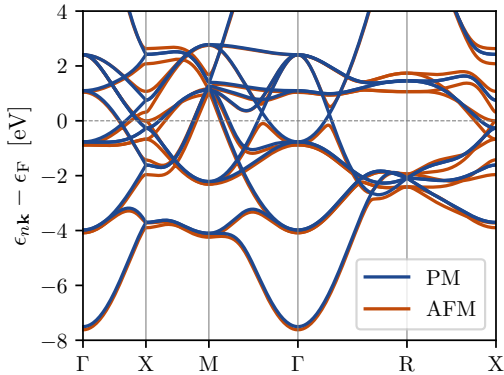
FIG. 7. LSDA band structure of bcc-Cr in the commensurate SDW phase, plotted relative to the Fermi level. The paramagnetic (PM) bands evaluated in the cubic unit cell are shown for reference. All AFM bands are two-fold degenerate, but the paramagnetic fourfold degeneracy at the Brillouin zone boundary (originating from downfolding) is lifted in the antiferromagnetic state.

for unconventional superconductivity [61].

Within the LSDA, we obtain a local magnetic moment of $0.82 \, \mu_{\mathrm{B}}$ for the commensurate SDW in Cr. In literature, the reported LSDA values at the experimental lattice constant range from $0.33 \, \mu_{\mathrm{B}}$ to $0.71 \, \mu_{\mathrm{B}}$ depending on numerical scheme and implementation [62–64]. Given the ill-defined nature of the local magnetic moment, we find our result to be in fair agreement with the PAW value of $0.67 \, \mu_{\mathrm{B}}$ reported in [64] as well as the experimental average moment at $T = 4.2$ K of the commensurate SDW phase in the 2.1 at.% Mn and 7.0 at.% Mn alloys of $0.67 \, \mu_{\mathrm{B}}$ and $0.81 \, \mu_{\mathrm{B}}$ respectively [65]. In Fig. 7, we show the band structure of bcc-Cr in the commensurate SDW and compare it to the paramagnetic (spin-paired) band structure. The antiferromagnetic bands are seen to be highly similar to the paramagnetic ones, which is also reflected in a rather small total energy difference of 4 meV per atom. Nevertheless, the degeneracy of the paramagnetic bands is partially lifted in the AFM phase and give rise to a reduction in the area of the Fermi surface (most clearly seen around the X point and along the $M - \Gamma - R$ path). This is in line with the picture of Fermi surface nesting as the driving mechanism for antiferromagnetism in bcc-Cr.

2. Magnetic excitations

Previously, first principles studies of the magnetic excitations in Cr have been restricted to the paramagnetic phase [21, 66], focusing on the Fermi surface nesting and its relation to the incommensurate SDW ground state. Experimentally, the SDW vector is equal to the nest-

ing vector as measured by angle-resolved photoemission spectroscopy and positron annihilation [67, 68]. In comparison, the nesting vector of the Kohn-Sham band structure has been determined to a value of $q_{\mathrm{F}} = 0.92 \times 2\pi/a$ using the LSDA [21]. Whereas this value is extracted as the maximum of the slowly varying nesting function, the theoretical SDW vector is determined from the well-defined peak in the paramagnetic excitation spectrum at zero frequency. Using the LSDA and PBE exchange-correlation functionals, the SDW vector has been theoretically determined to values of $q_{\mathrm{SDW}} = 0.86 \times 2\pi/a$ and $q_{\mathrm{SDW}} = 0.92 \times 2\pi/a$ respectively [21, 66]. In the present study, we supplement the previous studies of the PM phase by exploring instead the transverse magnetic excitations of the commensurate SDW.

In Fig. 8, we show the ALDA magnon spectrum calculated on the basis of the LSDA ground state. At short wave vectors, the many-body spectrum is characterized by an acoustic magnon mode, which follows a linear dispersion. For wave vectors $q \gtrsim 0.65 \, \text{Å}^{-1}$ along the $\Gamma \to X$ and $\Gamma \to M$ directions, the magnon mode becomes indistinguishable from the background of Stoner-pair excitations, which start to dominate the spectrum. For the $\Gamma \to R$ direction, this happens already for $q \gtrsim 0.45 \, \text{Å}^{-1}$. In contrast to the case of itinerant ferromagnets, the spectral broadening does not imply a decrease in scattering intensity, allowing AFM Cr to exhibit intense Stoner-pair scattering over a frequency range of several eV. For comparison, we show the Kohn-Sham spectrum of transverse magnetic excitations in Fig. 9.

In the many-body spectrum (Fig. 8), the single-particle Stoner excitations of the LSDA Kohn-Sham spectrum (Fig. 9) have been renormalized by the electron-electron interaction as dictated by the Dyson equation (13). The renormalization favors the low-frequency Stoner excitations that lie in the continuation of the collective magnon mode, why these excitations are said to be collectively enhanced. In addition to the acoustic magnon mode, we also observe a new parabolic feature in the many-body spectrum on the $\Gamma \to R$ path. The parabolic feature seems to be a collective mode, not an enhanced Stoner excitation, as it appears only in the many-body spectrum and not in the Kohn-Sham spectrum. In contrast to the acoustic magnon mode, the parabolic mode is clearly distinguishable from the Stoner excitations, even though it resides inside an intense part of the Stoner continuum. This suggests that the parabolic mode is less influenced by Landau damping in comparison to the acoustic mode. A more detailed investigation of this mode is left for future work.

In regions where the acoustic magnon mode is well-defined, we show the magnon frequencies calculated from the spectral function maximum using Eq. (15) and the artificial broadening parameter $\eta = 50$ meV. In doing so, we assume a lorentzian magnon lineshape with HWHM η. For magnon frequencies below ~ 200 meV, this is a valid approximation as the many-body spectral function $S^{+-}(\mathbf{q}, \omega)$ is more less free of Landau damping (the
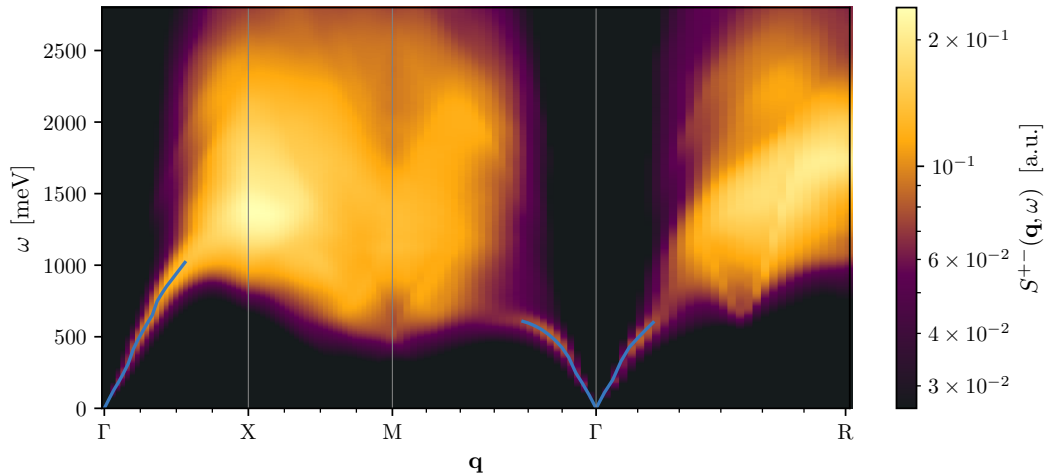
FIG. 8. Magnon spectrum of commensurate AFM Cr calculated within the ALDA (evaluated at $\mathbf{G} = \mathbf{0}$). The light blue line indicate the magnon frequencies determined from the spectral maximum via Eq. (15).
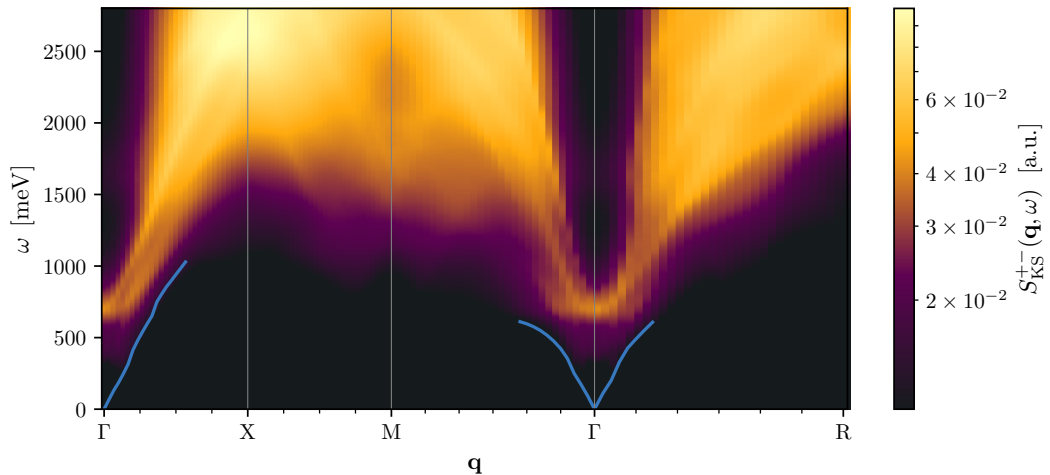
FIG. 9. Kohn-Sham Stoner spectrum of commensurate AFM Cr calculated within the ALDA (evaluated at $\mathbf{G} = \mathbf{0}$). For comparison, the ALDA magnon dispersion is shown in light blue.

magnons reside below the Stoner continuum). Above 200 meV, ω_{m} exceeds 2.25 times the lower HWHM of $S^{+-}(\mathbf{q}, \omega)$ and thus application of Eq. (15) with $\eta = 50$ meV still remains a good approximation, as it simply yields the magnon frequency to coincide with the spectral function maximum (see discussion in Sec. III B). To provide a continuous magnon dispersion, we thus use Eq. (15) for all well-defined magnon excitations. It should be noted that the used frequency sampling is sufficient to

identify ω_{m} for all the calculated wave vectors $\mathbf{q}$ only because we do not sample magnons with frequencies smaller than the artificial broadening η.

The resulting magnon dispersion is isotropic and linear up to magnon frequencies of 300-400 meV. For the identified magnon frequencies below 400 meV, we fit a gapless linear dispersion, $\omega_{\mathbf{q}} = vq$, producing an ALDA magnon velocity of $\hbar v = (1702 \pm 16)$ meV Å (1σ uncertainty of the fit). This result agrees quite well with pre-

vious literature, where a magnon velocity of 1.8 eV Å has been reported for a mean-field treatment of the multi-band Hubbard Hamiltonian that results from computing model parameters based on a paramagnetic GGA band structure [69]. When comparing to the experimental values for the $Cr_{1-x}Mn_x$ alloys as inferred from inelastic neutron scattering, the ALDA magnon velocity seems to be of the correct order of magnitude, but also to constitute an overestimate. The 2 at.% and 5 at.% Mn alloys yield magnon velocities of $\hbar v = (856 \pm 100)$ meV Å and $\hbar v = (1020 \pm 100)$ meV Å respectively, in both cases measured at the reduced temperature $T \sim 0.5 T_N$ [58, 70, 71]. The alloy and finite temperature effects of the available data entails that one cannot make a direct comparison of magnon velocities, and a quantitative performance assessment of the ALDA values will have to be settled in future studies.

V. SUMMARY AND OUTLOOK

To summarize, we have demonstrated that ALDA LR-TDDFT comprises a suitable framework for performing first principles calculations of AFM magnon dispersion relations. To our knowledge the method has only been applied to ferromagnets in the past, but aided by the Onsager relations and a slight rescaling of the ALDA kernel (to satisfy the Goldstone condition) one seamlessly obtains the characteristic linear magnon dispersion for antiferromagnets. In addition, the calculated magnon velocities are at least comparable to experiments. We have exemplified this by two prototypical antiferromagnets: Cr_2O_3 and bcc-Cr, which constitute generic examples of localized moment and itinerant antiferromagnets respectively. In the case of Cr_2O_3, the predicted magnon dispersivity is approximately a factor of two larger than in experiments. Part of this discrepancy can be remedied by adding a Hubbard correction to account for the strong static correlation. Using a value of $U_{eff} = 1.0$ eV, we obtain magnon velocities in very good agreement with experiments. This, however, comes at the expense of introducing spurious dispersion in the optical magnon branch and it appears that approximations beyond the λALDA+U are required to obtain accurate magnon spectra. For bcc-Cr in the commensurate SDW phase, we obtain an acoustic magnon mode with a velocity that seems to be in reasonable agreement with experiments, although a direct comparison cannot be made at the current stage. More importantly, we have shown that there is no natural bound on the intensity of the Stoner continuum (in contrast to ferromagnets) resulting in a almost complete damping of the acoustic magnon in bcc-Cr.

The fact that ALDA appears capable of describing magnetic fluctuations in (possibly strongly correlated) antiferromagnets significantly enlarges the classes of materials and properties that can be accessed by first principles methods. For example, both quantum spin liquids and unconventional superconductors typically exist in close proximity or in coexistance with antiferromagnetic phases. It is far from clear, if LR-TDDFT can be used to gain insight into such exotic phases, but it is possible that the spin fluctuations in proximate antiferromagnetic phases may be unravelled by first principles methods. This could provide an easy way to investigate the influence of external parameters such as pressure and doping. In particular, superconductivity in cuprates typically arises at particular doping concentrations and a simple model of doping can be implemented in LR-TDDFT by a mere shift of the Fermi level without any additional effort. In contrast, the systematic study of doping effects is a highly tedious process in experiments. We thus hope that future LR-TDDFT studies can help to unveil the role of antiferromagnetic fluctuations in exotic quantum phases of matter.

Appendix A: Symmetry relations of the generalized susceptibility

In linear response theory, the aim is to describe how a system in thermal equilibrium responds to external perturbations, to linear order. The system is characterized by the Hamiltonian $\hat{H}_0$ and the perturbation enters the problem through the system coordinate $\hat{A} = \hat{A}^\dagger$, $\hat{H}_{ext}(t) = \hat{A}f(t)$, where $f(t)$ is a coordinate external to the system. The response in system coordinate $\hat{B} = \hat{B}^\dagger$ is then characterized by the retarded susceptibility $\chi_{BA}(t - t')$,

$$\langle \delta \hat{B}(t) \rangle = \langle \hat{B}(t) \rangle - \langle \hat{B} \rangle_0 = \int_{-\infty}^{\infty} dt' \, \chi_{BA}(t - t') f(t'),$$
(A1)

where $\langle \cdot \rangle_0$ denotes the expectation value in absence of the external perturbation. The retarded susceptibility is given by the *Kubo formula* [72],

$$\chi_{BA}(t - t') = -\frac{i}{\hbar}\theta(t - t')\langle [\hat{B}_0(t - t'), \hat{A}] \rangle_0, \quad \text{(A2)}$$

where $\theta(t - t')$ is the step function and the time-dependence is described in the interaction picture, $\hat{B}_0(t) = e^{i\hat{H}_0 t/\hbar}\hat{B}e^{-i\hat{H}_0 t/\hbar}$. Fourier-Laplace transforming the Kubo formula (A2) defines the generalized susceptibility, $\chi_{BA}(\omega)$, where $\hat{A}$ and $\hat{B}$ are allowed to be non-Hermitian. For a definition of the Fourier-Laplace transform and notation in general, the reader is referred to [22]. The aim of Appendix A is to show how symmetry relations can be derived for the generalized susceptibility based on the symmetries of $\hat{H}_0$, including also instances where a given symmetry is spontaneously broken in thermal equilibrium.

1. Non-causal response functions and complex conjugation

Before investigating the symmetries of $\hat{H}_0$, it is worth noting that the retarded susceptibility is directly related to the non-causal response function [73],

$$K_{BA}(t) = -\frac{i}{\hbar}\langle\, [\hat{B}_0(t), \hat{A}]\,\rangle_0, \tag{A3}$$

with $\chi_{BA}(t-t') = \theta(t-t')K_{BA}(t-t')$. This is significant because the non-causal response function can be written in terms of correlation functions $C_{BA}(t) = \langle\hat{B}_0(t)\hat{A}\rangle_0 - \langle\hat{B}\rangle_0\langle\hat{A}\rangle_0$, with $K_{BA}(t) = -i/\hbar\,(C_{BA}(t) - C_{AB}(-t))$. This equivalence between system correlations and the susceptibility leads to the famous *fluctuation-dissipation theorem* [74–76] and entails the following symmetry relation for the non-causal response function:

$$K_{BA}(-t) = -K_{AB}(t). \tag{A4}$$

Furthermore, complex conjugating the non-causal response function (A3), leads to [73]

$$K_{BA}^*(t) = K_{B^\dagger A^\dagger}(t), \tag{A5}$$

meaning that the generalized susceptibility follows the symmetry relation:

$$\chi_{BA}^*(\omega) = \chi_{B^\dagger A^\dagger}(-\omega). \tag{A6}$$

2. Time-reversal symmetry and Onsager's relation

In the absence of external magnetic fields one may characterize the electronic structure of a given material in terms of a Hamiltonian, which is invariant under time-reversal symmetry, $[\hat{H}_0, \hat{T}] = 0$. However, such a Hamiltonian may still permit ground states, $|\alpha_0\rangle$, with spontaneously broken time-reversal symmetry, meaning that $\hat{T}|\alpha_0\rangle$ represents *another* ground state of the system. One such example is ferromagnets, where $\hat{T}$ reverses the sign of the magnetization $\mathbf{m}(\mathbf{r}) \to -\mathbf{m}(\mathbf{r})$. Even though several degenerate ground states exit, the system might be in thermal equilibrium around a single one of them at low temperatures, $T \simeq 0$, meaning that the probability of observing any other ground state vanishes on all relevant time-scales. As a result, the generalized susceptibility at zero temperature is given with reference to a specific ground state in cases of degeneracy:

$$K_{BA}(\alpha_0, t) = -\frac{i}{\hbar}\langle\alpha_0|\,[\hat{B}_0(t), \hat{A}]\,|\alpha_0\rangle, \tag{A7}$$

with $\chi_{BA}(\alpha_0, t-t') = \theta(t-t')K_{BA}(\alpha_0, t-t')$.

Before proceeding, it should be noted that $\hat{T}$ is an anti-unitary operator. In the notation used here, it acts only to the right and for a given ket state $\hat{T}|u\rangle = |\hat{T}u\rangle$, the corresponding bra is written $\langle\hat{T}u|$. Anti-unitary operators are anti-linear, $\hat{T}(c_1|u\rangle + c_2|v\rangle) = c_1^*|\hat{T}u\rangle + c_2^*|\hat{T}v\rangle$,

and preserves the norm of the states on which they act, such that $\langle\hat{T}u|\hat{T}v\rangle = \langle u|v\rangle^*$ [77].

For an arbitrary operator $\hat{A}$, the time-reversed operator $\hat{A}^T$ is defined $\hat{A}^T \equiv \hat{T}\hat{A}\hat{T}^{-1}$. Furthermore, using that $[\hat{H}_0, \hat{T}] = 0$,

$$\begin{aligned}\hat{T}\hat{B}_0(t)\hat{T}^{-1} &= \hat{T}e^{i\hat{H}_0 t/\hbar}\hat{B}\hat{T}^{-1}\hat{T}e^{-i\hat{H}_0 t/\hbar}\hat{T}^{-1}\\ &= e^{-i\hat{H}_0 t/\hbar}\hat{T}\hat{B}\hat{T}^{-1}e^{i\hat{H}_0 t/\hbar} = \hat{B}_0^T(-t). \end{aligned} \tag{A8}$$

Using the symmetry relation (A5), one may then write:

$$\begin{aligned}K_{B^\dagger A^\dagger}(\alpha_0, t) &= \frac{i}{\hbar}\langle\hat{T}\alpha_0|\,\hat{T}[\hat{B}_0(t), \hat{A}]\,|\alpha_0\rangle\\ &= \frac{i}{\hbar}\langle\hat{T}\alpha_0|\Big[\hat{T}\hat{B}_0(t)\hat{T}^{-1}\hat{T}\hat{A}\hat{T}^{-1}\\ &\qquad - \hat{T}\hat{A}\hat{T}^{-1}\hat{T}\hat{B}_0(t)\hat{T}^{-1}\Big]\hat{T}|\alpha_0\rangle\\ &= \frac{i}{\hbar}\langle\hat{T}\alpha_0|\,[\hat{B}_0^T(-t), \hat{A}^T]\,|\hat{T}\alpha_0\rangle\\ &= -K_{B^T A^T}(\hat{T}\alpha_0, -t) = K_{A^T B^T}(\hat{T}\alpha_0, t). \end{aligned} \tag{A9}$$

where the symmetry relation (A4) was used in the last step. Fourier-Laplace transforming Equation (A9) yields the following relation for the generalized susceptibility:

$$\chi_{B^\dagger A^\dagger}(\alpha_0, \omega) = \chi_{A^T B^T}(\hat{T}\alpha_0, \omega). \tag{A10}$$

This relation generalizes Onsager's relation for correlation functions in statistical mechanics [78–80], why it is often referred to simply as the *Onsager relation*. It defines a reciprocal relation between the generalized susceptibility in a given set of coordinates and their time-reversed equivalents.

To concretise the kinds of symmetries implied by the *Onsager relation*, the four-component susceptibility tensor is considered. The tensor defines the linear response of an electronic system to an external electromagnetic field (neglecting orbital current contributions) and is given in terms of the four-component density variables

$$\hat{n}^\mu(\mathbf{r}) = \sum_{s,s'}\sigma_{ss'}^\mu\,\hat{\psi}_s^\dagger(\mathbf{r})\hat{\psi}_{s'}(\mathbf{r}), \tag{A11}$$

where $\mu \in \{0, x, y, z\}$ and $\sigma_{ss'}^\mu$ yields the Pauli matrices augmented by the 2×2 identity matrix for $\mu = 0$ (refer e.g. to [22] for more details). The four-component density is hermitian and transforms as even/odd variables under time-reversal, $\hat{T}\hat{n}^\mu(\mathbf{r})\hat{T}^{-1} = \varepsilon_T^\mu\hat{n}^\mu(\mathbf{r})$, where $\varepsilon_T^\mu = 1$ for $\mu = 0$ and $\varepsilon_T^\mu = -1$ for $\mu \in \{x, y, z\}$. With this, the Onsager relation can be written in the more familiar form [72, 81, 82]:

$$\chi^{\mu\nu}(\alpha_0, \mathbf{r}, \mathbf{r}', \omega) = \varepsilon_T^\nu\varepsilon_T^\mu\chi^{\nu\mu}(\hat{T}\alpha_0, \mathbf{r}', \mathbf{r}, \omega). \tag{A12}$$

For a non-magnetic system with a ground state that is invariant under time-reversal, the Onsager relation (A12) implies that e.g. the dielectric susceptibility is symmetric

in real-space, $\chi^{00}(\mathbf{r}, \mathbf{r}', \omega) = \chi^{00}(\mathbf{r}', \mathbf{r}, \omega)$, meaning that an external scalar potential in $\mathbf{r}'$ induces the same electron density fluctuations at position $\mathbf{r}$, as a potential in $\mathbf{r}$ induces in $\mathbf{r}'$. This is a non-trivial statement, which gets even less trivial in cases where time-reversal symmetry is broken in the ground state. Take for example a ferromagnet of magnetization $\mathbf{m}(\mathbf{r})$. In this case, the Onsager relation (A12) implies that a magnetic field along the y-direction at $\mathbf{r}'$ induces similar fluctuations in the magnetization in the x-direction at $\mathbf{r}$, as a magnetic field along the x-direction at $\mathbf{r}$ induces in the y-magnetization at $\mathbf{r}'$ for the ground state with *opposite* magnetization $-\mathbf{m}(\mathbf{r})$: $\chi^{xy}(\alpha_0, \mathbf{r}, \mathbf{r}', \omega) = \chi^{yx}(\hat{T}\alpha_0, \mathbf{r}', \mathbf{r}, \omega)$.

3. The generalized Onsager relation

Although the Onsager relation (A10) relies on one of the most fundamental symmetries in physics, that is, time-reversal symmetry, the derivation is quite general and can be extended to any symmetry of the system.

Theorem. For any unitary or anti-unitary operator $\hat{U}$ with inverse $\hat{U}^{-1}$ that commutes with the system Hamiltonian, $[\hat{H}_0, \hat{U}] = 0$, the generalized susceptibility is subject to one of the following Onsager relations:

$$\chi_{BA}(\alpha_0, \omega) = \chi_{B^U A^U}(\hat{U}\alpha_0, \omega), \quad \text{if } \hat{U} \text{ is unitary,} \tag{A13a}$$

$$\chi_{B^\dagger A^\dagger}(\alpha_0, \omega) = \chi_{A^U B^U}(\hat{U}\alpha_0, \omega), \quad \text{if } \hat{U} \text{ is anti-unitary,} \tag{A13b}$$

where $\hat{A}^U \equiv \hat{U}\hat{A}\hat{U}^{-1}$.

Proof. The proof for anti-unitary operators was already given in the preceding section, exemplified using the time-reversal operator $\hat{T}$. For a unitary operator $\hat{U}$, that commutes with the system Hamiltonian:

$$\hat{U}\hat{B}_0(t)\hat{U}^{-1} = \hat{U}e^{i\hat{H}_0 t/\hbar}\hat{B}\hat{U}^{-1}e^{-i\hat{H}_0 t/\hbar}\hat{U}^{-1}$$
$$= e^{i\hat{H}_0 t/\hbar}\hat{U}\hat{B}\hat{U}^{-1}e^{-i\hat{H}_0 t/\hbar} = \hat{B}_0^U(t), \tag{A14}$$

and so:

$$K_{BA}(\alpha_0, t) = -\frac{i}{\hbar}\langle\hat{U}\alpha_0|\,\hat{U}[\hat{B}_0(t), \hat{A}]\,|\alpha_0\rangle$$
$$= -\frac{i}{\hbar}\langle\hat{U}\alpha_0|\Big[\hat{U}\hat{B}_0(t)\hat{U}^{-1}\hat{U}\hat{A}\hat{U}^{-1}$$
$$- \hat{U}\hat{A}\hat{U}^{-1}\hat{U}\hat{B}_0(t)\hat{U}^{-1}\Big]\hat{U}|\alpha_0\rangle$$
$$= -\frac{i}{\hbar}\langle\hat{U}\alpha_0|\,[\hat{B}_0^U(t), \hat{A}^U]\,|\hat{U}\alpha_0\rangle$$
$$= K_{B^U A^U}(\hat{U}\alpha_0, t). \tag{A15}$$

Fourier-Laplace transforming the relation (A15) then yields the generalized Onsager relation (A13a).

4. Onsager relations for non-relativistic systems

For systems with spontaneously broken time-reversal symmetry, it is in general hard to make good use of the Onsager relation (A10), as it relates the susceptibility of two *different* ground states. For non-relativistic system in absence of external magnetic fields however, the situation simplifies. Take as an example the electronic Hamiltonian:

$$\hat{H}_0 = \hat{T}_{\text{kin}} + \hat{V} + \hat{U}_{\text{ee}}, \tag{A16}$$

where $\hat{T}_{\text{kin}}$ is the kinetic energy operator, $\hat{V}$ is the interaction with the electrostatic potential (set up by the atomic nuclei) and $\hat{U}_{\text{ee}}$ is the electron-electron Coulomb interaction. In the non-relativistic limit, this Hamiltonian commutes with the complex conjugation operator, $[\hat{H}_0, \hat{K}] = 0$, meaning that the generalized susceptibility is subject to the Onsager relation:

$$\chi_{B^\dagger A^\dagger}(\alpha_0, \omega) = \chi_{A^K B^K}(\hat{K}\alpha_0, \omega). \tag{A17}$$

Assuming that the only ground state degeneracy arises from the rotational symmetry of the spinor degrees of freedom, complex conjugation of a collinear magnetic ground state must map the state onto itself, $\hat{K}|\alpha_0\rangle \rightarrow |\alpha_0\rangle$, such that the non-relativistic Onsager relation (A17) describes symmetries of a *single* generalized susceptibility.

For the four-component susceptibility tensor, one may use that the electronic creation/annihilation operators are invariant under complex conjugation, $\hat{K}\hat{\psi}_s^\dagger(\mathbf{r})\hat{\psi}_{s'}(\mathbf{r})\hat{K}^{-1} = \hat{\psi}_s^\dagger(\mathbf{r})\hat{\psi}_{s'}(\mathbf{r})$ [83], such that for collinear materials,

$$\chi^{\mu\nu}(\mathbf{r}, \mathbf{r}', \omega) = \varepsilon_K^\nu \varepsilon_K^\mu \chi^{\nu\mu}(\mathbf{r}', \mathbf{r}, \omega), \tag{A18}$$

where $\varepsilon_K^\mu = -1$ for $\mu = y$ and $\varepsilon_K^\mu = 1$ for $\mu \in \{0, x, z\}$. For the transverse magnetic susceptibility, the Onsager relation (A17) yields

$$\chi^{+-}(\mathbf{r}, \mathbf{r}', \omega) = \chi^{+-}(\mathbf{r}', \mathbf{r}, \omega) \tag{A19}$$

for collinear ground states $|\alpha_0\rangle$. This implies that magnon quasi-particles are reciprocal in the non-relativistic limit,

$$\chi_{\mathbf{G}\mathbf{G}'}^{+-}(\mathbf{q}, \omega) = \chi_{-\mathbf{G}'-\mathbf{G}}^{+-}(-\mathbf{q}, \omega), \tag{A20}$$

that is, the spectrum of transverse magnetic excitations is identical for $\mathbf{Q} = \pm(\mathbf{G} + \mathbf{q})$ in reciprocal space. Thus, for ferromagnets and antiferromagnets, a nonreciprocal magnon dispersion is strictly a relativistic effect. Indeed, it has been demonstrated that spin-orbit effects can lead to nonreciprocal magnon dispersions via the the Dzyaloshinskii-Moriya interaction [84–87].

5. Onsager relations for PT-symmetric systems

For centrosymmetric antiferromagnets in absence of external magnetic fields, the system Hamiltonian is invariant both under time-reversal, $[\hat{H}_0, \hat{T}] = 0$, and parity inversion $[\hat{H}_0, \hat{P}] = 0$. In the antiferromagnetic ground

state, both symmetries can be spontaneously broken at the same time, meaning that both $\hat{P}$ and $\hat{T}$ maps the ground state $|\alpha_0\rangle$ into a *different* ground state. However, application of *both* operators may still map the ground state onto itself, $\hat{P}\hat{T}|\alpha_0\rangle \rightarrow |\alpha_0\rangle$. As an example, one can think of the Néel state on a 1D chain of magnetic sites with an inversion center between two magnetic sites: Successive applications of parity inversion and time-reversal maps the antiferromagnetic ground state into a similar state with all local magnetic moments reversed, meaning that $\hat{P}\hat{T}$ maps the ground state onto itself. As $\hat{P}$ is a unitary operator, $\hat{P}\hat{T}$ is anti-unitary, and for ground states invariant under applications of $\hat{P}\hat{T}$, the generalized susceptibility is thus subject to the Onsager relation:

$$\chi_{B^\dagger A^\dagger}(\omega) = \chi_{A^{PT}B^{PT}}(\omega). \qquad (A21)$$

For the four-component susceptibility tensor, the four-component density transforms as

$$\hat{P}\hat{T}\hat{n}^\mu(\mathbf{r})\hat{T}^{-1}\hat{P}^{-1} = \varepsilon_T^\mu \hat{n}^\mu(-\mathbf{r}), \qquad (A22)$$

and with this, one obtains the following Onsager relation for ground states invariant under applications of $\hat{P}\hat{T}$:

$$\chi^{\mu\nu}(\mathbf{r}, \mathbf{r}', \omega) = \varepsilon_T^\nu \varepsilon_T^\mu \chi^{\nu\mu}(-\mathbf{r}', -\mathbf{r}, \omega). \qquad (A23)$$

Similarly, the transverse magnetic susceptibility is subject to the following Onsager relation,

$$\chi^{+-}(\mathbf{r}, \mathbf{r}', \omega) = \chi^{-+}(-\mathbf{r}', -\mathbf{r}, \omega), \qquad (A24)$$

meaning that the spectrum of spin-raising and spin-lowering excitations are related by a simple exchange of local field components in reciprocal space:

$$\chi^{+-}_{\mathbf{G}\mathbf{G}'}(\mathbf{q}, \omega) = \chi^{-+}_{\mathbf{G}'\mathbf{G}}(\mathbf{q}, \omega). \qquad (A25)$$

[1] K. Yosida, *Theory of magnetism* (Springer Berlin, 1996).
[2] A. T. Boothroyd, *Principles of Neutron Scattering from Condensed Matter* (Oxford University Press, 2020).
[3] F. Illas and R. L. Martin, The Journal of Chemical Physics **108**, 2519 (1998).
[4] H. Xiang, C. Lee, H.-J. Koo, X. Gong, and M.-H. Whangbo, Dalton Trans. **42**, 823 (2013).
[5] T. Olsen, Physical Review B **96**, 125143 (2017).
[6] D. Torelli, H. Moustafa, K. W. Jacobsen, and T. Olsen, npj Computational Materials **6**, 158 (2020).
[7] T. Olsen, Journal of Physics D: Applied Physics **54**, 314001 (2021).
[8] Journal of Magnetism and Magnetic Materials **67**, 65 (1987).
[9] S. Frota-Pessôa, R. B. Muniz, and J. Kudrnovský, Physical Review B **62**, 5293 (2000).
[10] V. V. Mazurenko and V. I. Anisimov, Physical Review B - Condensed Matter and Materials Physics **71**, 1 (2005).
[11] H. Ebert and S. Mankovsky, Physical Review B - Condensed Matter and Materials Physics **79**, 1 (2009).
[12] S. Brinker, M. dos Santos Dias, and S. Lounis, Physical Review Research **2**, 1 (2020).
[13] M. Hoffmann and S. Blügel, Physical Review B **101**, 024418 (2020).
[14] A. Kartsev, M. Augustin, R. F. L. Evans, K. S. Novoselov, and E. J. G. Santos, npj Computational Materials **6**, 150 (2020).
[15] G. Onida, L. Reining, and A. Rubio, Rev. Mod. Phys. **74**, 601 (2002).
[16] F. Aryasetiawan and K. Karlsson, Physical Review B **60**, 7419 (1999).
[17] E. Şaşıoğlu, A. Schindlmayr, C. Friedrich, F. Freimuth, and S. Blügel, Physical Review B **81**, 054434 (2010).
[18] M. C. Müller, C. Friedrich, and S. Blügel, Physical Review B **94**, 1 (2016).
[19] P. Buczek, A. Ernst, and L. M. Sandratskii, Physical Review B , 174418 (2011).

[20] B. Rousseau, A. Eiguren, and A. Bergara, Physical Review B **85**, 054305 (2012).
[21] K. Cao, H. Lambert, P. G. Radaelli, and F. Giustino, Physical Review B **97**, 024420 (2018).
[22] T. Skovhus and T. Olsen, Physical Review B **103**, 245110 (2021).
[23] S. Coh, D. Vanderbilt, A. Malashevich, and I. Souza, Physical Review B **83**, 085108 (2011).
[24] E. Runge and E. K. U. Gross, Physical Review Letters **52**, 997 (1984).
[25] E. K. U. Gross and W. Kohn, Physical Review Letters **55**, 2850 (1985).
[26] S. Lounis, A. T. Costa, R. B. Muniz, and D. L. Mills, Physical Review B **83**, 035109 (2011).
[27] N. Singh, P. Elliott, T. Nautiyal, J. K. Dewhurst, and S. Sharma, Physical Review B **99**, 035151 (2019).
[28] J. J. Mortensen, L. B. Hansen, and K. W. Jacobsen, Physical Review B **71**, 035109 (2005).
[29] J. Enkovaara, C. Rostgaard, J. J. Mortensen, J. Chen, M. Dułak, L. Ferrighi, J. Gavnholt, C. Glinsvad, V. Haikola, H. a. Hansen, H. H. Kristoffersen, M. Kuisma, a. H. Larsen, L. Lehtovaara, M. Ljungberg, O. Lopez-Acevedo, P. G. Moses, J. Ojanen, T. Olsen, V. Petzold, N. a. Romero, J. Stausholm-Møller, M. Strange, G. a. Tritsaris, M. Vanin, M. Walter, B. Hammer, H. Häkkinen, G. K. H. Madsen, R. M. Nieminen, J. K. Nørskov, M. Puska, T. T. Rantala, J. Schiøtz, K. S. Thygesen, and K. W. Jacobsen, Journal of Physics: Condensed Matter **22**, 253202 (2010).
[30] A. H. Hill, A. Harrison, C. Dickinson, W. Zhou, and W. Kockelmann, Microporous and Mesoporous Materials **130**, 280 (2010).
[31] R. Jaramillo, Y. Feng, J. C. Lang, Z. Islam, G. Srajer, H. M. Rønnow, P. B. Littlewood, and T. F. Rosenbaum, Physical Review B **77**, 184418 (2008).
[32] S. L. Dudarev, G. A. Botton, S. Y. Savrasov, C. J. Humphreys, and A. P. Sutton, Physical Review B **57**,

1505 (1998).

[33] T. Skovhus, T. Olsen, and H. M. Rønnow, Interplay between static and dynamic correlation in itinerant magnets – a first principles study of magnons in mnbi (2021), arXiv:2110.07282 [cond-mat.mtrl-sci].

[34] B. N. Brockhouse, The Journal of Chemical Physics **21**, 961 (1953).

[35] L. M. Corliss, J. M. Hastings, R. Nathans, and G. Shirane, Journal of Applied Physics **36**, 1099 (1965).

[36] J. B. Goodenough, Physical Review **117**, 1442 (1960).

[37] J. Íñiguez, Physical Review Letters **101**, 117201 (2008).

[38] A. Malashevich, S. Coh, I. Souza, and D. Vanderbilt, Physical Review B **86**, 094430 (2012).

[39] J. Li, C. B. Wilson, R. Cheng, M. Lohmann, M. Kavand, W. Yuan, M. Aldosary, N. Agladze, P. Wei, M. S. Sherwin, and J. Shi, Nature **578**, 70 (2020).

[40] J. Li, H. T. Simensen, D. Reitz, Q. Sun, W. Yuan, C. Li, Y. Tserkovnyak, A. Brataas, and J. Shi, Physical Review Letters **125**, 217201 (2020).

[41] P. J. Brown, J. B. Forsyth, E. Lelièvre-Berna, and F. Tasset, Journal of Physics: Condensed Matter **14**, 1957 (2002).

[42] A. Y. Dobin, W. Duan, and R. M. Wentzcovitch, Physical Review B **62**, 11997 (2000).

[43] A. Rohrbach, J. Hafner, and G. Kresse, Physical Review B **70**, 125426 (2004).

[44] S. Shi, A. L. Wysocki, and K. D. Belashchenko, Physical Review B **79**, 104404 (2009).

[45] Y. Guo, S. J. Clark, and J. Robertson, Journal of Physics: Condensed Matter **24**, 325504 (2012).

[46] F. Maldonado, C. Novillo, and A. Stashans, Chemical Physics **393**, 148 (2012).

[47] D. Adler, in *Solid State Physics - Advances in Research and Applications*, Vol. 21 (1968) pp. 1–113.

[48] R. Zimmermann, P. Steiner, and S. Hüfner, Journal of Electron Spectroscopy and Related Phenomena **78**, 49 (1996).

[49] T. Uozumi, K. Okada, and A. Kotani, Journal of Electron Spectroscopy and Related Phenomena **78**, 103 (1996).

[50] F. Lebreau, M. M. Islam, B. Diawara, and P. Marcus, The Journal of Physical Chemistry C **118**, 18133 (2014).

[51] E. A. Moore, Physical Review B **76**, 195107 (2007).

[52] N. J. Mosey, P. Liao, and E. A. Carter, The Journal of Chemical Physics **129**, 014103 (2008).

[53] E. Samuelsen, M. Hutchings, and G. Shirane, Physica **48**, 13 (1970).

[54] E. Samuelsen, Physics Letters A **26**, 160 (1968).

[55] E. Samuelsen, Physica **45**, 12 (1969).

[56] R. A. Alikhanov, Ž. Dimitrijević, A. Kowalska, S. Kraśnicki, H. Rżany, J. Todorović, and A. Wanic, physica status solidi (b) **32**, 41 (1969).

[57] S. Foner, Physical Review **130**, 183 (1963).

[58] E. Fawcett, Reviews of Modern Physics **60**, 209 (1988).

[59] S. A. Werner, A. Arrott, and H. Kendrick, Physical Review **155**, 528 (1967).

[60] D. Gibbs, K. M. Mohanty, and J. Bohr, Physical Review B **37**, 562 (1988).

[61] E. Fawcett, H. L. Alberts, V. Y. Galkin, D. R. Noakes, and J. V. Yakhmi, Reviews of Modern Physics **66**, 25 (1994).

[62] J. Kübler, Journal of Magnetism and Magnetic Materials **20**, 277 (1980).

[63] H. L. Skriver, Journal of Physics F: Metal Physics **11**, 97 (1981).

[64] R. Hafner, D. Spišák, R. Lorenz, and J. Hafner, Physical Review B **65**, 184432 (2002).

[65] W. C. Koehler, R. M. Moon, A. L. Trego, and A. R. Mackintosh, Physical Review **151**, 405 (1966).

[66] S. Y. Savrasov, Physical Review Letters **81**, 2570 (1998).

[67] E. Rotenberg, B. K. Freelon, H. Koh, A. Bostwick, K. Rossnagel, A. Schmid, and S. D. Kevan, New Journal of Physics **7**, 114 (2005).

[68] J. Laverock, T. D. Haynes, M. A. Alam, and S. B. Dugdale, Physical Review B **82**, 125127 (2010).

[69] K. Sugimoto, Z. Li, E. Kaneshita, K. Tsutsui, and T. Tohyama, Physical Review B **87**, 134418 (2013).

[70] J. Als-Nielsen, J. D. Axe, and G. Shirane, Journal of Applied Physics **42**, 1666 (1971).

[71] S. K. Sinha, G. R. Kline, C. Stassis, N. Chesser, and N. Wakabayashi, Physical Review B **15**, 1415 (1977).

[72] R. Kubo, Journal of the Physical Society of Japan **12**, 570 (1957).

[73] J. Jensen and A. R. Mackintosh, *Rare Earth Magnetism: Structures and excitations*, The International Series of Monographs on Physics (Clarendon Press, Oxford, 1991).

[74] H. Nyquist, Physical Review **32**, 110 (1928).

[75] H. B. Callen and T. A. Welton, Physical Review **83**, 34 (1951).

[76] R. Kubo, Rep. Prog. Phys. **29**, 255 (1966).

[77] L. E. Ballentine, *Quantum Mechanics - A Modern Development* (World Scientific Publishing Co. Pte. Ltd., Singapore, 2015).

[78] L. Onsager, Physical Review **37**, 405 (1931).

[79] L. Onsager, Physical Review **38**, 2265 (1931).

[80] H. B. G. Casimir, Reviews of Modern Physics **17**, 343 (1945).

[81] L. D. Landau and E. M. Lifshitz, *Statistical Physics*, Course of Theoretical Physics (Pergamon Press, Oxford, 1969).

[82] N. Nagaosa, J. Sinova, S. Onoda, A. H. MacDonald, and N. P. Ong, Reviews of Modern Physics **82**, 1539 (2010).

[83] A. Bernevig, *Topological insulators and topological superconductors* (Princeton University Press, 2013).

[84] L. Udvardi and L. Szunyogh, Physical Review Letters **102**, 207204 (2009).

[85] K. Zakeri, Y. Zhang, J. Prokop, T.-H. Chuang, N. Sakr, W. X. Tang, and J. Kirschner, Physical Review Letters **104**, 137203 (2010).

[86] A. T. Costa, R. B. Muniz, S. Lounis, A. B. Klautau, and D. L. Mills, Physical Review B **82**, 014428 (2010).

[87] M. Costa, N. M. R. Peres, J. Fernández-Rossier, and A. T. Costa, Physical Review B **102**, 014450 (2020).

Theory: Exchange and correlation - a deeper look

As has been illustrated in the preceding results chapters, the most fundamental obstacle for the applicability of theoretical magnon spectroscopy is the lack of consistent exchange-correlation functionals and kernels that improve the accuracy of LR-TDDFT beyond the ALDA. For ferromagnetic Ni, neither the inclusion of gradient or Hubbard corrections improve the overall accuracy, and whereas a scaled ALDA kernel on top of a Hubbard corrected ground state did improve the description of dynamic correlation effects in ferromagnetic MnBi, it did not consistently improve the magnon dispersion in antiferromagnetic Cr_2O_3.

Thus, within the field of theoretical magnon spectroscopy alone, one can find plenty of motivation to look for new ways of developing consistent approximations beyond the ALDA. In chapter 8, we will present a new class of exchange-correlation functionals, developed with the specific purpose of approaching an accurate description of the *dynamic* homogeneous electron gas. We hope, that this new class of functionals can be of general use for the electronic structure community, but also for the field of theoretical magnon spectroscopy in particular. In order to put the functional development into context, this chapter will serve as a theoretical background.

7.1   The exchange-correlation hole

Thanks to the Hohenberg-Kohn theorems, the ground state electronic structure problem may be formulated as the constrained minimization of the energy functional $E[n]$, see Equation (2.5). The difficulty arises in coming up with appropriate approximations for energy contributions, to which many-body correlations are important. At first glance, the apparent success of such approximations is itself surprising, since the electron density, $n(\mathbf{r})$, is a continuous variable without reference to the individual electrons. However, a closer inspection of the energy functional $E[n]$ reveals, that it can easily be rewritten in terms of the one-body and two-body density matrices [53, 74],

$$\rho_1(\mathbf{r}, \mathbf{r}') = \sum_s \langle \psi_0 | \hat{\psi}_s^\dagger(\mathbf{r}) \hat{\psi}_s(\mathbf{r}') | \psi_0 \rangle, \tag{7.1}$$

$$\rho_2(\mathbf{r}, \mathbf{r}') = \sum_{s,s'} \langle \psi_0 | \hat{\psi}_s^\dagger(\mathbf{r}) \hat{\psi}_{s'}^\dagger(\mathbf{r}') \hat{\psi}_{s'}(\mathbf{r}') \hat{\psi}_s(\mathbf{r}) | \psi_0 \rangle, \tag{7.2}$$

where $|\psi_0\rangle$ is the many-body ground state, which is a unique functional of the ground state electron density, and $\rho_1(\mathbf{r}, \mathbf{r}) = n(\mathbf{r})$. In particular, the kinetic energy and Coulomb repulsion functionals are given by:

$$T[n] = \langle\psi_0| \sum_s \int d\mathbf{r}\, \hat{\psi}_s^\dagger(\mathbf{r}) \left(\frac{-\hbar^2 \nabla_\mathbf{r}^2}{2m}\right) \hat{\psi}_s(\mathbf{r})|\psi_0\rangle$$

$$= \iint d\mathbf{r}d\mathbf{r}'\, \delta(\mathbf{r} - \mathbf{r}') \left(\frac{-\hbar^2 \nabla_\mathbf{r}^2}{2m}\right) \rho_1(\mathbf{r}', \mathbf{r}), \tag{7.3}$$

and

$$U[n] = \langle\psi_0|\frac{1}{2} \sum_{s,s'} \iint d\mathbf{r}d\mathbf{r}'\, \hat{\psi}_s^\dagger(\mathbf{r})\hat{\psi}_{s'}^\dagger(\mathbf{r}')v_\mathrm{c}(\mathbf{r} - \mathbf{r}')\hat{\psi}_{s'}(\mathbf{r}')\hat{\psi}_s(\mathbf{r})|\psi_0\rangle$$

$$= \frac{1}{2} \iint d\mathbf{r}d\mathbf{r}'\, v_\mathrm{c}(\mathbf{r} - \mathbf{r}')\rho_2(\mathbf{r}, \mathbf{r}'). \tag{7.4}$$

Thus, the exact energy functional can readily be evaluated based on the *continuous* correlations embodied in the density matrices, without the need of an explicit notion of the individual electron degrees of freedom.

From Equation (7.4), it is clear that the Hartree energy, defined in Equation (2.9), corresponds to the Coulomb repulsion in an uncorrelated continuous system, where $\rho_2(\mathbf{r}, \mathbf{r}') \to n(\mathbf{r})n(\mathbf{r}')$. Thus, the exchange-correlation functional has to account for the correlation effects

$$U[n] - E_\mathrm{H}[n] = \frac{1}{2} \iint d\mathbf{r}d\mathbf{r}'\, v_\mathrm{c}(\mathbf{r} - \mathbf{r}') \left[\rho_2(\mathbf{r}, \mathbf{r}') - n(\mathbf{r})n(\mathbf{r}')\right] \tag{7.5}$$

$$= \frac{1}{2} \iint d\mathbf{r}d\mathbf{r}'\, n(\mathbf{r})v_\mathrm{c}(\mathbf{r} - \mathbf{r}')n(\mathbf{r}') \left[g(\mathbf{r}, \mathbf{r}') - 1\right], \tag{7.6}$$

which are embodied by the pair correlation function $g(\mathbf{r}, \mathbf{r}')$:

$$\rho_2(\mathbf{r}, \mathbf{r}') = n(\mathbf{r})n(\mathbf{r}')g(\mathbf{r}, \mathbf{r}'). \tag{7.7}$$

Expressed reversely, the correlation related contributions to the Coulomb repulsion may be written in terms of the so-called exchange-correlation hole density $n_\mathrm{xc}(\mathbf{r}, \mathbf{r}') = n(\mathbf{r}')[g(\mathbf{r}, \mathbf{r}') - 1]$:

$$U[n] - E_\mathrm{H}[n] = \frac{1}{2} \iint d\mathbf{r}d\mathbf{r}'\, n(\mathbf{r})v_\mathrm{c}(\mathbf{r} - \mathbf{r}')n_\mathrm{xc}(\mathbf{r}, \mathbf{r}'). \tag{7.8}$$

The xc hole density is then responsible for cancelling the self-interaction error of the Hartree energy, which arises because an electron at position $\mathbf{r}$ is repulsed by the entire electron density $n(\mathbf{r})$, including contributions from the electron itself. Thus, in the xc contribution (7.8), an electron at position $\mathbf{r}$ should be repulsed by an effective electron density $n_\mathrm{xc}(\mathbf{r}, \mathbf{r}')$ that corresponds to a single electron hole:

$$\int d\mathbf{r}'\, n_\mathrm{xc}(\mathbf{r}, \mathbf{r}') = -1. \tag{7.9}$$

In this way, $n_\mathrm{xc}(\mathbf{r}, \mathbf{r}')$ describes the electron depletion around an electron at position $\mathbf{r}$, i.e. the reduced probability of finding another electron at a position $\mathbf{r}'$ close by.

7.2 Electron density fluctuations and the exchange-correlation hole

As the exchange-correlation hole provides an effective description of the many-body correlations of the electronic system, it is directly related to its fundamental fluctuations. By the virtue of the fluctuation-dissipation theorem, this implies that the xc hole is related also to the dynamic susceptibility of the electronic system.

Using the anti-commutation rules for the fermionic creation/annihilation operators, the two-body density matrix (7.2) can be rewritten in terms of the electron density operator [66, 75, 76]:

$$\rho_2(\mathbf{r}, \mathbf{r}') = \sum_{s,s'} \langle \psi_0 | \hat{\psi}_s^\dagger(\mathbf{r}) \left(\hat{\psi}_s(\mathbf{r}) \hat{\psi}_{s'}^\dagger(\mathbf{r}') - \delta_{s,s'} \delta(\mathbf{r} - \mathbf{r}') \right) \hat{\psi}_{s'}(\mathbf{r}') | \psi_0 \rangle$$

$$= \langle \psi_0 | \hat{n}(\mathbf{r}) \hat{n}(\mathbf{r}') | \psi_0 \rangle - \delta(\mathbf{r} - \mathbf{r}') n(\mathbf{r}). \qquad (7.10)$$

In turn, the exchange-correlation contribution to the Coulomb repulsion is written in terms of the electron density fluctuation operator $\delta \hat{n}(\mathbf{r}) = \hat{n}(\mathbf{r}) - n(\mathbf{r})$,

$$n(\mathbf{r}) n_{\text{xc}}(\mathbf{r}, \mathbf{r}') = \rho_2(\mathbf{r}, \mathbf{r}') - n(\mathbf{r}) n(\mathbf{r}') = \langle \psi_0 | \delta \hat{n}(\mathbf{r}) \delta \hat{n}(\mathbf{r}') | \psi_0 \rangle - \delta(\mathbf{r} - \mathbf{r}') n(\mathbf{r}), \quad (7.11)$$

where it is used that $\langle \psi_0 | \delta \hat{n}(\mathbf{r}) | \psi_0 \rangle = 0$. Ultimately, the two-body density fluctuations $\langle \psi_0 | \delta \hat{n}(\mathbf{r}) \delta \hat{n}(\mathbf{r}') | \psi_0 \rangle$ are directly related to the density-density correlation function $C(\mathbf{r}, \mathbf{r}', t) = \langle \hat{n}_0(\mathbf{r}, t) \hat{n}(\mathbf{r}') \rangle_0 - n(\mathbf{r}) n(\mathbf{r}')$, which at zero temperature is given by the frequency representation

$$C(\mathbf{r}, \mathbf{r}', \omega) = 2\pi\hbar \sum_{\psi_i \neq \psi_0} \langle \psi_0 | \hat{n}(\mathbf{r}) | \psi_i \rangle \langle \psi_i | \hat{n}(\mathbf{r}') | \psi_0 \rangle \, \delta\big(\hbar\omega - (E_i - E_0)\big), \qquad (7.12)$$

see Equation (1.18). Assuming that there is zero overlap, $\langle \psi_i | \hat{n}(\mathbf{r}) | \psi_0 \rangle = 0$, for any degenerate eigenstate $\hat{H}_0 | \psi_i \rangle = E_i | \psi_i \rangle$ to the ground state $| \psi_0 \rangle$, then $C(\mathbf{r}, \mathbf{r}', \omega) = 0$ for $\omega \leq 0$ and:

$$\langle \psi_0 | \delta \hat{n}(\mathbf{r}) \delta \hat{n}(\mathbf{r}') | \psi_0 \rangle = \frac{1}{2\pi\hbar} \int_0^\infty d\hbar\omega \, C(\mathbf{r}, \mathbf{r}', \omega)$$

$$= -\frac{\hbar}{\pi} \int_0^\infty d\omega \, \chi''(\mathbf{r}, \mathbf{r}', \omega), \qquad (7.13)$$

where the fluctuation-dissipation theorem (1.16) was used in the last equality. Thus, the exchange-correlation hole density is formally given by the electron density $n(\mathbf{r})$ and the dissipative part of the dielectric susceptibility $\chi(\mathbf{r}, \mathbf{r}', \omega)$ (the 00 component of the four-component susceptibility tensor). Although illuminating, χ still remains an unknown functional of the electron density. However, as will be described in the following sections, Equation (7.13) offers important insights into the requirements for fulfilling the normalization condition (7.9) and it provides an essential ingredient in the adiabatic connection fluctuation-dissipation (ACFD) framework that follows.

7.2.1   Charge conservation and xc hole normalization

The exchange-correlation hole normalization condition (7.9) is naturally connected to the charge conservation (electron number conservation) of the system. In terms of the system's linear response, one might consider a harmonic perturbation on the form

$$\hat{H}_{\text{ext}}(t) = \int d\mathbf{r}\, \hat{n}(\mathbf{r}) V_{\text{ext}}(\mathbf{r}) \cos(\omega_0 t). \tag{7.14}$$

Applying the convolution theorem to the linear response relation (1.25), the induced electron density fluctuations are then given by:

$$\langle \delta \hat{n}(\mathbf{r}, t) \rangle = \int d\mathbf{r}'\, \text{Re}\left[\chi(\mathbf{r}, \mathbf{r}', \omega_0) e^{-i\omega_0 t} \right] V_{\text{ext}}(\mathbf{r}'). \tag{7.15}$$

Now, the considered external perturbation can only redistribute the electrons, not add or remove them from the system. Thus, in order to uphold charge conservation in the linear response, one has to require that:

$$\int d\mathbf{r}\, \langle \delta \hat{n}(\mathbf{r}, t) \rangle = 0 \quad \text{for any time } t. \tag{7.16}$$

Thanks to the relation (7.15), charge is therefore only conserved for any general external potential $V_{\text{ext}}(\mathbf{r})$ and frequency ω_0, if the dielectric susceptibility satisfies:

$$\int d\mathbf{r}\, \chi(\mathbf{r}, \mathbf{r}', \omega) = 0 \quad \text{for any } \mathbf{r}' \text{ and } \omega. \tag{7.17}$$

Furthermore, for a collinear system in the nonrelativistic limit, the dielectric response is reciprocal [C],

$$\chi(\mathbf{r}, \mathbf{r}', \omega) = \chi(\mathbf{r}', \mathbf{r}, \omega), \tag{7.18}$$

meaning that the charge conservation requirement (7.17) carries over to the dissipative part of the susceptibility:

$$\int d\mathbf{r}\, \chi''(\mathbf{r}, \mathbf{r}', \omega) = \int d\mathbf{r}'\, \chi''(\mathbf{r}, \mathbf{r}', \omega) = 0. \tag{7.19}$$

Thus, in order for the xc hole to be normalized, it is sufficient to require that the underlying dielectric susceptibility respects charge conservation,

$$\int d\mathbf{r}' n(\mathbf{r}) n_{\text{xc}}(\mathbf{r}, \mathbf{r}') = \int d\mathbf{r}' \left[\langle \psi_0 | \delta \hat{n}(\mathbf{r}) \delta \hat{n}(\mathbf{r}') | \psi_0 \rangle - \delta(\mathbf{r} - \mathbf{r}') n(\mathbf{r}) \right]$$
$$= \int d\mathbf{r}' \left[-\frac{\hbar}{\pi} \int_0^\infty d\omega\, \chi''(\mathbf{r}, \mathbf{r}', \omega) - \delta(\mathbf{r} - \mathbf{r}') n(\mathbf{r}) \right] = -n(\mathbf{r}), \tag{7.20}$$

where Equations (7.11) and (7.13) were used for the first two equalities. That charge conservation is a sufficient requirement for xc hole normalization is of course only natural, since $n_{\text{xc}}(\mathbf{r}, \mathbf{r}')$ represents the depletion charge from the fixation of a single electron. A more general argument for the relation between charge conservation and xc hole normalization based on the imaginary frequency dielectric susceptibility can be found in Reference [75].

7.3   Adiabatic connection and the ACFD framework

In the Kohn-Sham construction, one considers the auxiliary system of *noninteracting* electrons which shares its ground state density with the fully interacting system $\hat{H}_0$. This construction may be generalized to an auxiliary system of *interacting* electrons, but where the electron-electron interaction has been scaled by a factor $\lambda \in [0, 1]$:

$$\hat{H}_{\mathrm{KS}}^{\lambda} = \hat{T} + \hat{V}_{\mathrm{s}}^{\lambda} + \lambda\hat{U}. \tag{7.21}$$

The effective potential $\hat{V}_{\mathrm{s}}^{\lambda}$ is then defined such that $\langle\psi|\hat{H}_{\mathrm{KS}}^{\lambda}|\psi\rangle$ is minimal using $|\psi\rangle = |\psi_0^{\lambda}\rangle$ with $\langle\psi_0^{\lambda}|\hat{n}(\mathbf{r})|\psi_0^{\lambda}\rangle = n(\mathbf{r})$. In the limit $\lambda = 0$, the usual Kohn-Sham system is recovered, to which the ground state is a single Slater determinant $|\phi_0\rangle$, and for $\lambda = 1$, one obtains the fully interacting system. This construction, which is called the adiabatic connection, may seem somewhat arbitrary, but thanks to the Hellmann-Feynmann theorem, one can use it to write the Hartree-exchange-correlation energy as a coupling-constant average over the Coulomb repulsion (see e.g. [66] and the references therein):

$$\begin{aligned} E_{\mathrm{Hxc}}[n] &= \langle\psi_0|\hat{T} + \hat{U}|\psi_0\rangle - \langle\phi_0|\hat{T}|\phi_0\rangle \\ &= \int_0^1 d\lambda \, \frac{d}{d\lambda}\langle\psi_0^{\lambda}|\hat{T} + \lambda\hat{U}|\psi_0^{\lambda}\rangle \\ &= \int_0^1 d\lambda \, \langle\psi_0^{\lambda}|\hat{U}|\psi_0^{\lambda}\rangle. \end{aligned} \tag{7.22}$$

Using equations (7.4), (7.10) and (7.13), one may therefore in turn write the Hxc energy in terms of the coupling-constant averaged dissipative part of the dielectric susceptibility [76–78],

$$E_{\mathrm{Hxc}}[n] = \frac{1}{2} \iint d\mathbf{r}d\mathbf{r}' \, v_{\mathrm{c}}(\mathbf{r} - \mathbf{r}') \int_0^1 d\lambda \, \rho_2^{\lambda}(\mathbf{r}, \mathbf{r}'), \tag{7.23}$$

where

$$\begin{aligned} \rho_2^{\lambda}(\mathbf{r}, \mathbf{r}') &= \langle\psi_0^{\lambda}|[n(\mathbf{r}) + \delta\hat{n}(\mathbf{r})][n(\mathbf{r}') + \delta\hat{n}(\mathbf{r}')]|\psi_0^{\lambda}\rangle - \delta(\mathbf{r} - \mathbf{r}')n(\mathbf{r}) \\ &= n(\mathbf{r})n(\mathbf{r}') - \frac{\hbar}{\pi}\int_0^{\infty} d\omega \, \chi_{\lambda}''(\mathbf{r}, \mathbf{r}', \omega) - \delta(\mathbf{r} - \mathbf{r}')n(\mathbf{r}), \end{aligned} \tag{7.24}$$

and it was used that $\langle\psi_0^{\lambda}|\delta\hat{n}(\mathbf{r})|\psi_0^{\lambda}\rangle = 0$. The first term in Equation (7.24) yields the Hartree energy functional, meaning that the xc energy functional within the adiabatic connection fluctuation-dissipation framework is given by

$$E_{\mathrm{xc}}[n] = \frac{1}{2} \iint d\mathbf{r}d\mathbf{r}' n(\mathbf{r})v_{\mathrm{c}}(\mathbf{r} - \mathbf{r}')n(\mathbf{r}') \left[\bar{g}(\mathbf{r}, \mathbf{r}') - 1\right] \tag{7.25}$$

$$= \frac{1}{2} \iint d\mathbf{r}d\mathbf{r}' n(\mathbf{r})v_{\mathrm{c}}(\mathbf{r} - \mathbf{r}')\bar{n}_{\mathrm{xc}}(\mathbf{r}, \mathbf{r}'), \tag{7.26}$$

where $\bar{g}(\mathbf{r}, \mathbf{r}')$ is the coupling-constant averaged pair distribution function and the coupling-constant averaged exchange-correlation hole density is given by:

$$\bar{n}_{\text{xc}}(\mathbf{r}, \mathbf{r}') = -\frac{\hbar}{\pi} \frac{1}{n(\mathbf{r})} \int_0^1 d\lambda \int_0^\infty d\omega \, \chi''_\lambda(\mathbf{r}, \mathbf{r}', \omega) - \delta(\mathbf{r} - \mathbf{r}'). \qquad (7.27)$$

With this definition, it is clear that also $\bar{n}_{\text{xc}}(\mathbf{r}, \mathbf{r}')$ is normalized according to Equation (7.9), provided that $\chi_\lambda(\mathbf{r}, \mathbf{r}', \omega)$ respects charge conservation for all $\lambda \in [0, 1]$, in full analogy with the discussion of Section 7.2.1 [75]. For more details on the coupling-constant averaged exchange-correlation hole, the reader is referred to relevant literature, such as [79].

7.3.1 LDA in the ACFD framework

In the ACFD framework, the local density approximation corresponds to the replacement of $\bar{n}_{\text{xc}}[n](\mathbf{r}, \mathbf{r}')$ in Equation (7.26) with the xc hole density of an homogeneous electron gas of density $n(\mathbf{r})$,

$$\bar{n}_{\text{xc}}^{\text{LDA}}[n](\mathbf{r}, \mathbf{r}') = \bar{n}_{\text{xc}}^{\text{HEG}}\big(\mathbf{r} - \mathbf{r}', n(\mathbf{r})\big) = n(\mathbf{r})\bar{g}^{\text{HEG}}\big(\mathbf{r} - \mathbf{r}', n(\mathbf{r})\big) - n(\mathbf{r}), \qquad (7.28)$$

where $\bar{g}^{\text{HEG}}(r, n)$ is the coupling-constant averaged pair distribution function of an HEG of density n. The exchange-correlation energy per electron, that enters the LDA definition (2.30), is then given by:

$$\epsilon_{\text{xc}}(n) = \frac{1}{2} \int d\mathbf{r}' v_{\text{c}}(\mathbf{r} - \mathbf{r}') \bar{n}_{\text{xc}}^{\text{HEG}}(\mathbf{r} - \mathbf{r}', n). \qquad (7.29)$$

In this formulation, it becomes clear, that the LDA not only is exact in the homogeneous electron gas limit, but it also inherits an exact xc hole normalization (7.9) for a general nonuniform density $n(\mathbf{r})$, thanks to the exactness of the used HEG xc hole. At least some of the success of the LDA can be attributed this remarkable feature.

7.3.2 The weighted density approximation

Whereas the LDA completely neglects the nonlocality of the exchange-correlation functional, i.e. by substituting $n(\mathbf{r}') [\bar{g}(\mathbf{r}, \mathbf{r}') - 1] \to n(\mathbf{r})[\bar{g}^{\text{HEG}}(\mathbf{r} - \mathbf{r}', n(\mathbf{r})) - 1]$ in Equation (7.25), the weighted density approximation (WDA) is designed to retain the nonlocality of the functional form. In the WDA, only $\bar{g}(\mathbf{r}, \mathbf{r}')$ is replaced, and with some model distribution function $\bar{g}^{\text{eff}}(\mathbf{r} - \mathbf{r}', \bar{n}(\mathbf{r}))$ which depends locally on the so-called weighted density $\bar{n}(\mathbf{r})$ [80]. The weighted density is then determined, such that the WDA xc hole density,

$$\bar{n}_{\text{xc}}^{\text{WDA}}[n](\mathbf{r}, \mathbf{r}') = n(\mathbf{r}')\bar{g}^{\text{eff}}\big(\mathbf{r} - \mathbf{r}', \bar{n}(\mathbf{r})\big) - n(\mathbf{r}'), \qquad (7.30)$$

is normalized according to Equation (7.9). Although more of the nonlocal information is retained compared to the LDA, the WDA functional is also substantially more expensive to compute, because the weighted density is a nonlocal property of the system that has to be evaluated as a function of position $\mathbf{r}$.

7.4 Exchange and correlation

So far, the distinction between exchange and correlation has not been discussed. Exchange is generally defined as the correlation effects induced solely from the antisymmetry of the many-particle electron wave function, that is, the correlation that arises from Pauli's exclusion principle alone, without correlations induced by the actual electron-electron repulsion [81]. The concrete implications of this, rather vague, definition is somewhat context dependent.

7.4.1 Hartree-Fock exchange

In Hartree-Fock theory, see e.g. [82], the energy functional $\langle \hat{T} + \hat{V} + \hat{U} \rangle$ is minimized assuming that the ground state can be written as a single Slater determinant. Using such an ansatz, only the effects of Hartree and exchange are included, and the Hartree-Fock exchange functional may be defined as the correlation effects captured by inserting $\rho_2^{\mathrm{KS}}(\mathbf{r}, \mathbf{r}')$ instead of $\rho_2(\mathbf{r}, \mathbf{r}')$ in Equation (7.4). Of course, $\rho_2^{\mathrm{KS}}(\mathbf{r}, \mathbf{r}') = \rho_2^{\mathrm{KS}}[n](\mathbf{r}, \mathbf{r}')$ is still some complicated functional of the ground state electron density $n(\mathbf{r})$, but because the Kohn-Sham system is noninteracting and its ground state, $|\phi_0\rangle$, is a single Slater determinant, the two-body density matrix of the Kohn-Sham system is readily expanded into the single-particle Kohn-Sham eigenstates:

$$
\begin{aligned}
\rho_2^{\mathrm{KS}}(\mathbf{r}, \mathbf{r}') = & \sum_{s,s'} \langle \phi_0 | \left(\sum_{n_1} \psi_{n_1 s}^*(\mathbf{r}) \hat{c}_{n_1 s}^\dagger \right) \left(\sum_{m_1} \psi_{m_1 s'}^*(\mathbf{r}') \hat{c}_{m_1 s'}^\dagger \right) \\
& \times \left(\sum_{m_2} \psi_{m_2 s'}(\mathbf{r}') \hat{c}_{m_2 s'} \right) \left(\sum_{n_2} \psi_{n_2 s}(\mathbf{r}) \hat{c}_{n_2 s} \right) |\phi_0\rangle \\
= & \left(\sum_s \sum_n f_{ns} |\psi_{ns}(\mathbf{r})|^2 \right) \left(\sum_{s'} \sum_m f_{ms'} |\psi_{ms'}(\mathbf{r}')|^2 \right) \\
& - \sum_s \sum_{n,m} f_{ns} f_{ms} \psi_{ns}^*(\mathbf{r}) \psi_{ms}^*(\mathbf{r}') \psi_{ns}(\mathbf{r}') \psi_{ms}(\mathbf{r}).
\end{aligned}
\tag{7.31}
$$

The first term yields the Hartree energy functional, and upon insertion into Equation (7.4), the Hartree-Fock (HF) exchange functional is obtained:

$$
E_{\mathrm{x}}^{\mathrm{HF}}[n] = -\frac{1}{2} \sum_s \sum_{n,m} f_{ns} f_{ms} \iint d\mathbf{r} d\mathbf{r}' \, \psi_{ns}^*(\mathbf{r}) \psi_{ms}^*(\mathbf{r}') v_{\mathrm{c}}(\mathbf{r} - \mathbf{r}') \psi_{ns}(\mathbf{r}') \psi_{ms}(\mathbf{r}). \tag{7.32}
$$

In this formulation, it is clear that the orbital self-interaction of the Hartree energy,

$$
\frac{1}{2} \sum_s \sum_n f_{ns}^2 \iint d\mathbf{r} d\mathbf{r}' \, |\psi_{ns}(\mathbf{r})|^2 \, v_{\mathrm{c}}(\mathbf{r} - \mathbf{r}') \, |\psi_{ns}(\mathbf{r}')|^2, \tag{7.33}
$$

is cancelled exactly by the (n, m) diagonal of the exchange energy, which is also called the self-exchange. In nominal values, the self-exchange energy is generally larger than the remaining inter-electronic exchange, which in turn is larger than the correlation

energy. However, a great deal of the nominal energy contributions are due to the tightly bound core electrons of the heavier elements, and in order to obtain an appropriate description of valence electron physics, the correlation contribution is essential [83].

Whereas the exact HF exchange cancels the self-interaction completely, semi-local approximations, such as the LSDA, do not generally do so. One way to compensate for the self-interaction error in semi-local functionals is to mix in a fraction of HF exchange, resulting in the hybrid class of functionals [84], with examples such as the B3LYP functional [85]. However, the mixing parameter between the semi-local exchange and the HF exchange is not a uniquely defined quantity, and in addition, the HF exchange is computationally very demanding to evaluate. For this reason, there is plenty of room for the development of new functionals, that are either more consistent or have similar/improved performance, but at a lower computational cost than the hybrid functionals.

7.4.2   The exchange hole

The HF exchange energy (7.32), can easily be rewritten in terms of the spin-specific one-body density matrix [74],

$$\rho_s^{\mathrm{KS}}(\mathbf{r}, \mathbf{r}') = \langle \phi_0 | \hat{\psi}_s^\dagger(\mathbf{r}) \hat{\psi}_s(\mathbf{r}') | \phi_0 \rangle = \sum_n f_{ns} \psi_{ns}^*(\mathbf{r}) \psi_{ns}(\mathbf{r}'). \tag{7.34}$$

such that:

$$E_{\mathrm{x}}^{\mathrm{HF}}[n] = -\frac{1}{2} \sum_s \iint d\mathbf{r} d\mathbf{r}' \, \rho_s^{\mathrm{KS}}(\mathbf{r}, \mathbf{r}') v_{\mathrm{c}}(\mathbf{r} - \mathbf{r}') \rho_s^{\mathrm{KS}}(\mathbf{r}', \mathbf{r}). \tag{7.35}$$

Comparison with (7.6) and (7.8) then implies that the exchange hole density is given by [83, 86]:

$$n_{\mathrm{x}}(\mathbf{r}, \mathbf{r}') = -\sum_s \frac{\rho_s^{\mathrm{KS}}(\mathbf{r}, \mathbf{r}') \rho_s^{\mathrm{KS}}(\mathbf{r}', \mathbf{r})}{n(\mathbf{r})} = -\sum_s \frac{\left| \rho_s^{\mathrm{KS}}(\mathbf{r}, \mathbf{r}') \right|^2}{n(\mathbf{r})}, \tag{7.36}$$

and that the exchange depletion, or exchange hole, may be defined as the exchange contribution to the pair correlation function [74]:

$$g_{\mathrm{x}}(\mathbf{r}, \mathbf{r}') = 1 - \sum_s \frac{\left| \rho_s^{\mathrm{KS}}(\mathbf{r}, \mathbf{r}') \right|^2}{n(\mathbf{r}) n(\mathbf{r}')}. \tag{7.37}$$

7.4.3   ACFD exchange and correlation

Because the exchange interaction relates to correlation effects that can be described on the Kohn-Sham level, where the ground state is a Slater determinant, the coupling-constant average in e.g. Equation (7.23) only targets the correlation interaction. In particular, one may within the ACFD framework identify the exchange energy as the correlation effects captured by the fluctuations of the Kohn-Sham system, (see Equation (7.24)),

$$\rho_2^{\mathrm{KS}}(\mathbf{r}, \mathbf{r}') = n(\mathbf{r}) n(\mathbf{r}') - \frac{\hbar}{\pi} \int_0^\infty d\omega \, \chi_{\mathrm{KS}}''(\mathbf{r}, \mathbf{r}', \omega) - \delta(\mathbf{r} - \mathbf{r}') n(\mathbf{r}), \tag{7.38}$$

such that

$$E_{\mathrm{x}}^{\mathrm{ACFD}}[n] = -\frac{1}{2} \iint d\mathbf{r}d\mathbf{r}' \, v_{\mathrm{c}}(\mathbf{r} - \mathbf{r}') \left[\frac{\hbar}{\pi} \int_0^\infty d\omega \, \chi_{\mathrm{KS}}''(\mathbf{r}, \mathbf{r}', \omega) + \delta(\mathbf{r} - \mathbf{r}')n(\mathbf{r}) \right]. \quad (7.39)$$

It should be noted, that the difference between the HF and the ACFD exchange is a subtle one, finite only for systems with fractional occupations [87]. With the ACFD exchange defined, the correlation energy functional can be identified as the correlation effects induced by the electron-electron interaction, that is, the interaction associated with the *difference* in density-density fluctuations between the many-body system and the noninteracting Kohn-Sham system:

$$E_{\mathrm{c}}^{\mathrm{ACFD}}[n] = E_{\mathrm{Hxc}}[n] - E_{\mathrm{Hx}}[n] = \frac{1}{2} \iint d\mathbf{r}d\mathbf{r}' \, v_{\mathrm{c}}(\mathbf{r} - \mathbf{r}') \int_0^1 d\lambda \left[\rho_2^\lambda(\mathbf{r}, \mathbf{r}') - \rho_2^{\mathrm{KS}}(\mathbf{r}, \mathbf{r}') \right]$$

$$= -\frac{\hbar}{2\pi} \iint d\mathbf{r}d\mathbf{r}' \, v_{\mathrm{c}}(\mathbf{r} - \mathbf{r}') \int_0^1 d\lambda \int_0^\infty d\omega \left[\chi_\lambda''(\mathbf{r}, \mathbf{r}', \omega) - \chi_{\mathrm{KS}}''(\mathbf{r}, \mathbf{r}', \omega) \right]. \quad (7.40)$$

Thus, within the ACFD framework, the total energy functional, $E[n]$, may be evaluated on the basis of the dielectric susceptibility of the Kohn-Sham system along with the coupling-constant averaged many-body susceptibility, which can be computed from the Dyson equation (3.28). For a spin-paired system in particular, one is left with a single Dyson equation to solve [36],

$$\chi_\lambda(\mathbf{r}, \mathbf{r}', \omega) = \chi_{\mathrm{KS}}(\mathbf{r}, \mathbf{r}', \omega) + \iint d\mathbf{r}_1 d\mathbf{r}_2 \, \chi_{\mathrm{KS}}(\mathbf{r}, \mathbf{r}_1, \omega) K_{\mathrm{Hxc}}^\lambda(\mathbf{r}_1, \mathbf{r}_2, \omega) \chi_\lambda(\mathbf{r}_2, \mathbf{r}', \omega), \quad (7.41)$$

where the interaction scaled kernel is given by [40, 88, 89]

$$K_{\mathrm{Hxc}}^\lambda(\mathbf{r}_1, \mathbf{r}_2, \omega) = \lambda v_{\mathrm{c}}(\mathbf{r} - \mathbf{r}') + K_{\mathrm{xc}}^\lambda(\mathbf{r}_1, \mathbf{r}_2, \omega), \quad (7.42)$$

with

$$K_{\mathrm{xc}}^\lambda(\mathbf{r}_1, \mathbf{r}_2, \omega) = \lambda^2 K_{\mathrm{xc}}[n_\lambda](\lambda\mathbf{r}, \lambda\mathbf{r}', \omega/\lambda^2) \quad (7.43)$$

where $n_\lambda(\mathbf{r}, t) = n(\mathbf{r}/\lambda, t/\lambda^2)/\lambda^3$. Lastly, it is worth noting that the frequency integration in Equation (7.40) usually is performed along the imaginary frequency axis, where the susceptibility is smooth, instead of the real one. For more details, the reader is referred to literature such as [66] or [75].

7.4.4 The ACFD exchange and correlation holes

Once the exchange and correlation contributions have been separated in the ACFD framework, also the exchange and correlation holes may be understood as separate entities. The exchange hole describes the electron depletion of the Kohn-Sham system, i.e. the correlation due to the anti-symmetry of the Kohn-Sham wave function,

$$E_{\mathrm{x}}[n] = \frac{1}{2} \iint d\mathbf{r}d\mathbf{r}' n(\mathbf{r}) v_{\mathrm{c}}(\mathbf{r} - \mathbf{r}') n(\mathbf{r}') \left[g_{\mathrm{x}}(\mathbf{r}, \mathbf{r}') - 1 \right] \quad (7.44)$$

$$= \frac{1}{2} \iint d\mathbf{r}d\mathbf{r}' n(\mathbf{r}) v_{\mathrm{c}}(\mathbf{r} - \mathbf{r}') n_{\mathrm{x}}(\mathbf{r}, \mathbf{r}'), \quad (7.45)$$

where comparison with Equation (7.39) yields the exchange hole density:

$$n_{\mathrm{x}}(\mathbf{r}, \mathbf{r}') = -\frac{\hbar}{\pi} \frac{1}{n(\mathbf{r})} \int_0^\infty d\omega\, \chi''_{\mathrm{KS}}(\mathbf{r}, \mathbf{r}', \omega) - \delta(\mathbf{r} - \mathbf{r}'). \tag{7.46}$$

In full analogy with Equations (7.20) and (7.27), the exchange hole is itself normalized according to (7.9), given that the Kohn-Sham susceptibility respects charge conservation. This is essentially a reflection of the fact, that the exchange interaction identically cancels the Hartree self-interaction.

In a similar fashion, the correlation energy functional may be written in terms of the coupling-constant averaged correlation hole:

$$E_{\mathrm{c}}[n] = \frac{1}{2} \iint d\mathbf{r} d\mathbf{r}'\, n(\mathbf{r}) v_{\mathrm{c}}(\mathbf{r} - \mathbf{r}') n(\mathbf{r}') \bar{g}_{\mathrm{c}}(\mathbf{r}, \mathbf{r}') \tag{7.47}$$

$$= \frac{1}{2} \iint d\mathbf{r} d\mathbf{r}'\, n(\mathbf{r}) v_{\mathrm{c}}(\mathbf{r} - \mathbf{r}') \bar{n}_{\mathrm{c}}(\mathbf{r}, \mathbf{r}'), \tag{7.48}$$

where

$$\bar{n}_{\mathrm{c}}(\mathbf{r}, \mathbf{r}') = -\frac{\hbar}{\pi} \frac{1}{n(\mathbf{r})} \int_0^1 d\lambda \int_0^\infty d\omega \left[\chi''_\lambda(\mathbf{r}, \mathbf{r}', \omega) - \chi''_{\mathrm{KS}}(\mathbf{r}, \mathbf{r}', \omega) \right], \tag{7.49}$$

meaning that the coupling-constant averaged correlation hole essentially is charge neutral, $\int d\mathbf{r}'\, \bar{n}_{\mathrm{c}}(\mathbf{r}, \mathbf{r}') = 0$, given that also $\chi_\lambda(\mathbf{r}, \mathbf{r}', \omega)$ respects charge conservation.

7.5   Correlation hole of the homogeneous electron gas

For the homogeneous electron gas, the noninteracting susceptibility of the Kohn-Sham system has a well-known analytical functional form, known as the Lindhard function [90]. Thus, one may use the correlation energy, or the correlation hole, of the HEG as an exact limit to compare a given approximation for the exchange-correlation kernel to. For the HEG, the Dyson equation (7.41) becomes a scalar one in reciprocal space, which can be trivially inverted, yielding

$$\chi_\lambda(q, \omega) = \frac{\chi_0(q, \omega)}{1 - \chi_0(q, \omega) \left[\lambda v_{\mathrm{c}}(q) + K^\lambda_{\mathrm{xc}}(q, \omega) \right]}, \tag{7.50}$$

where $\chi_0(q, \omega)$ denotes the Lindhard function for an HEG of density n. Thus, in reciprocal space, the correlation energy per electron can then be written on a simple closed form in terms of the Lindhard function at imaginary frequencies u [40]:

$$\epsilon_{\mathrm{c}}(n) = -\frac{\hbar}{\pi^2 n} \int_0^\infty \frac{q^2}{4\pi} dq\, v_{\mathrm{c}}(q) \int_0^1 d\lambda \int_0^\infty du \frac{[\chi_0(q, iu)]^2 K^\lambda_{\mathrm{Hxc}}(q, iu)}{1 - \chi_0(q, iu) K^\lambda_{\mathrm{Hxc}}(q, iu)}. \tag{7.51}$$

Similarly, a simple expression for the coupling-constant averaged correlation hole is obtained,

$$\bar{g}_{\mathrm{c}}(q) = -\frac{\hbar}{\pi n^2} \int_0^1 d\lambda \int_0^\infty du \frac{[\chi_0(q, iu)]^2 K^\lambda_{\mathrm{Hxc}}(q, iu)}{1 - \chi_0(q, iu) K^\lambda_{\mathrm{Hxc}}(q, iu)}, \tag{7.52}$$

where the only unknown ingredient is the exchange-correlation kernel. Given an approximation of $K_{xc}^{\lambda}(q,\omega)$, one can then compare the resulting correlation hole (7.52) to the exact one, for which an accurate analytical functional form is known [91]. For additional details on Fourier transform definitions and derivations for the HEG, the reader is referred to Appendices A.1 and A.2.

7.5.1 HEG correlation hole in the RPA and ALDA

In the ALDA, the Hartree-exchange-correlation kernel is independent of the frequency ω and in the HEG limit, the static kernel also becomes a simple function of the electron density n and the wave number q,

$$f_{Hxc}^{ALDA}(n,q) = v_c(q) + f_{xc}^{LDA}(n), \tag{7.53}$$

where the Coulomb kernel only depends on the wave number q and the LDA kernel, see Equation (3.34), depends only on the density n. In Figure 7.1, we show the HEG coupling-constant averaged correlation hole (7.52), calculated within the RPA (neglecting K_{xc} completely), the ALDA and ALDAx (including only the LDA exchange contribution to f_{xc}). The HEG correlation hole is presented as a function of the wave number q in units of the Fermi wave number,

$$k_F = \left(3\pi^2 n\right)^{1/3}, \tag{7.54}$$
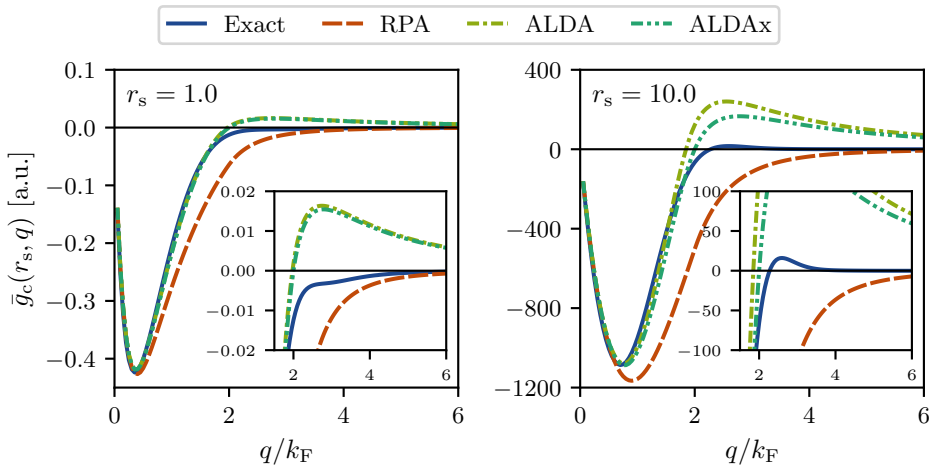
Figure 7.1: Reciprocal space coupling-constant averaged correlation hole of the homogeneous electron gas, with insets highlighting the short wavelength limit. An accurate analytical representation of the exact correlation hole [91] is compared to holes calculated within the RPA, ALDA and ALDAx approximations, using Equation (7.52). Each respective panel shows the correlation hole calculated with a given electron density $n = 3/(4\pi r_s^3)$.

and shown for two different electron densities n, listed in terms of the corresponding Wigner radius,

$$r_{\mathrm{s}} = \left(\frac{3}{4\pi n} \right)^{1/3}. \tag{7.55}$$

For all three kernels, the HEG correlation hole is well described for wave numbers q up to the reciprocal space minimum of the exact hole. For wave numbers beyond the minimum, the RPA underestimates the correlation hole, which also vanishes too slowly in the short wavelength limit $q \to \infty$. Reversely, the ALDA(x) kernels overestimates the correlation hole for values of q where the exact hole is small or vanishing. This means that the HEG correlation energy calculated within the RPA is underestimated and that the ALDA(x) kernels over-correct for this fact [40].

7.5.2   The renormalized ALDA

Due to the deficiencies of the RPA and ALDA kernels in the short wavelength limit of the homogeneous electron gas, it is not an unequivocal advantage to evaluate the correlation energy of real materials within the ACFD framework, even though nonlocality is seamlessly included through the Kohn-Sham susceptibility $\chi_{\mathrm{KS}}(\mathbf{r}, \mathbf{r}', \omega)$. As an example, both the correlation energies of the single-electron and two-electron systems H, H_2 and He as well as the atomization energies of a range of diatomic molecules are better described with the PBE functional [92] than within the RPA or ALDA [93, 94].

One may on the basis of Figure 7.1 notice that the HEG correlation hole has a root exactly at $q = 2k_{\mathrm{F}}$, independent of the density n, when using the ALDAx kernel. At the same time, the exact correlation hole more or less vanishes for $q > 2k_{\mathrm{F}}$, which is region where the ALDA(x) kernels perform poorly. For these reasons, a renormalized ALDA kernel has been proposed [93, 94], simply truncating the ALDAx kernel in reciprocal space for $q > 2k_{\mathrm{F}}$:

$$f_{\mathrm{Hxc}}^{\mathrm{rALDA}}(n, q) = \theta(2k_{\mathrm{F}} - q) \left[v_{\mathrm{c}}(q) + f_{\mathrm{x}}^{\mathrm{LDA}}(n) \right]. \tag{7.56}$$

Using this kernel in combination with HF exchange, accurate absolute correlation energies were obtained and a consistent improvement over PBE for properties ranging from atomization energies of diatomic molecules and cohesive energies of solids to lattice constants and H_2 dimer dissociation was achieved [66, 93–95].

However, whereas the rALDA results are encouraging, the calculations, on which they are based, are not completely self-consistent in the sense that, the Kohn-Sham susceptibility entering the ACFD framework is computed on the basis of the LDA ground state. Whereas the LDA xc potential provides a consistent starting point for the ALDA kernel, see Equation (3.31), the reciprocal space truncation of the rALDA kernel implies that the corresponding xc potential is strictly a nonlocal one. In the subsequent chapter, we will investigate a new class of nonlocal exchange-correlation functionals with the aim of producing an ALDA based kernel which is naturally truncated in reciprocal space, in the spirit of the rALDA. It is the hope, that such a functional in itself can improve the ground state properties in comparison with LDA, and that a more consistent treatment of the xc potential/kernel will lead to improved accuracy also within the ACFD framework.

Weighted local density approximation

The local density approximation (2.30) is not only one of the simplest approximations to the exchange-correlation functional, it is also a common starting point for more advanced approximations. In the traditional Jacob's ladder of DFT, one starts at the Hartree level of theory (earth) and approaches chemical accuracy (heaven) by climbing the rungs of a ladder one at a time, and at each rung include more information into the functional. LDA comprises the first rung of the ladder and forms the basis for all further approximations in this picture. At the second rung, the local electron spin-density gradient, $|\boldsymbol{\nabla} n_s(\mathbf{r})|$, is included in the functional, resulting in the generalized gradient approximation (GGA) class of functionals to which e.g. PBE [92] belongs. At the third rung, the meta-GGA functionals, also the local orbital positive kinetic energy density, $\tau_s(\mathbf{r}) = \sum_n f_n| - i\hbar\boldsymbol{\nabla}\psi_{ns}(\mathbf{r})|^2/(2m)$, is included with examples such as TPSS [96] or SCAN [97]. Further up the ladder, the functionals are no longer semi-local. At the fourth rung, a semi-local functional is mixed with HF exchange to create hybrid functionals [84] such as the B3LYP [85], and at the final fifth rung, the fully nonlocal functionals, which includes the WDA [80], the functional form is completely unrestricted.

However, when climbing Jacob's ladder of DFT, one is not guaranteed an improved description across all properties and materials. In fact, it has been shown that the magnon dispersion of Fe, Ni and Co actually worsens in comparison with experiment when including density gradients at the (adiabatic) GGA level in LR-TDDFT [31]. Similarly, it is often an insurmountable challenge to describe the electronic structure of highly correlated electron systems at the semi-local level, where one instead has to rely on Hubbard corrections, see Section 2.4.3, or advance to a higher level of theory.

Interestingly, as illustrated in the preceding chapter, the ACFD framework offers an alternative view on the functional development process. Even though the LDA ground state functional is exact in the homogeneous electron gas limit, the associated ALDA kernel does not reproduce exactly the density fluctuations described by the HEG correlation hole. Instead of proceeding up the ladder from the LDA to GGAs or meta-GGAs, one may instead, based on the LDA, seek to develop functionals that also capture the *dynamic* correlation effects of the HEG, that is, that improve the description of the coupling-constant averaged correlation hole.

In the present chapter, we will therefore take inspiration in the rALDA kernel [93, 94] and explore a new class of functionals that produce an xc kernel for the HEG, which

is truncated in reciprocal space,

$$f_{\mathrm{Hxc}}(n,q) = \Theta(2k_{\mathrm{F}} - q)\left[v_{\mathrm{c}}(q) + f_{\mathrm{xc}}^{\mathrm{LDA}}(n)\right], \tag{8.1}$$

where $\Theta(2k_{\mathrm{F}} - q)$ is a some smooth truncation function that resembles a step function. As discussed in Section 7.5, such a kernel entails that the corresponding xc functional is a fully nonlocal one. In this sense, we will skip the middle rungs of Jacob's ladder, not to directly improve the description of nonuniform systems, but to improve the description of the dynamic fluctuations of a uniform one (the HEG). Because the functional development of the present chapter relies on observations of the HEG correlation hole, the reader is expected to be familiar with the contents of Section 7.5.

The work presented in this chapter was conducted in close collaboration with fellow PhD student Asbjørn Rasmussen. For additional information and a different view on the work, the reader is therefore referred to his thesis [98].

8.1   Definition

In the ACFD framework, the Hartree-exchange-correlation energy of any xc functional may be written in terms of the Hxc energy per electron, see Equation (7.25):

$$E_{\mathrm{Hxc}}[n] = \int d\mathbf{r}\, \epsilon_{\mathrm{Hxc}}[n](\mathbf{r})\, n(\mathbf{r}). \tag{8.2}$$

For the LDA functional (2.30), this formulation is especially simple, as the Hxc energy per electron is given by:

$$\epsilon_{\mathrm{Hxc}}^{\mathrm{LDA}}[n](\mathbf{r}) = \frac{1}{2}\int d\mathbf{r}'\, v_{\mathrm{c}}(\mathbf{r} - \mathbf{r}')n(\mathbf{r}') + \epsilon_{\mathrm{xc}}\big(n(\mathbf{r})\big). \tag{8.3}$$

The idea, of what we will refer to as the generalized weighted local density approximation (GWLDA), is to replace the true electron density $n(\mathbf{r})$ with a weighted density $n^{*}(\mathbf{r})$ in one or more places of Equations (8.2) and (8.3). The weighted density is calculated on the basis of the true density using a predefined weight function $\phi(r,n)$,

$$n^{*}(\mathbf{r}) = \int d\mathbf{r}'\, \phi\big(\left|\mathbf{r} - \mathbf{r}'\right|, n(\mathbf{r}')\big)n(\mathbf{r}'), \tag{8.4}$$

such that the LDA is recovered in the limit where $\phi(r,n) = \delta(r)$. We restrict ourselves to consider weight functions that respect charge conservation, or even more specifically, the effective density $n^{*}(\mathbf{r})$ should simply compose a redistribution of the electrons. In order to be useful, the weight function should then effectively spread out localized charges and in this way compensate for the delocalization error of the LDA.

8.1.1   The WLDA functional form

As a first look into the GWLDA class of functionals, we consider the following three:

$$E_{\text{Hxc}}^{\text{WLDA}_1}[n] = \int d\mathbf{r}\, \epsilon_{\text{Hxc}}[n](\mathbf{r})\, n^*(\mathbf{r}), \tag{8.5a}$$

$$E_{\text{Hxc}}^{\text{WLDA}_2}[n] = \int d\mathbf{r}\, \epsilon_{\text{Hxc}}[n^*](\mathbf{r})\, n(\mathbf{r}), \tag{8.5b}$$

$$E_{\text{Hxc}}^{\text{WLDA}_3}[n] = \int d\mathbf{r}\, \epsilon_{\text{Hxc}}[n^*](\mathbf{r})\, n^*(\mathbf{r}), \tag{8.5c}$$

each of which have reasonable physical interpretations. In the first functional, the electron distribution of the true electron density $n(\mathbf{r})$ defines the Hxc energy per electron, but the energy is assigned according to the delocalized effective density $n^*(\mathbf{r})$. Reversely, the effective density sets up the Hxc energy per electron, which is then assigned to the true electron density in the second functional. Lastly, the third functional corresponds simply to evaluating the LDA Hxc energy using the effective density instead instead of the true.

The next step is to see, whether the functional forms (8.5) allow for an appropriate reciprocal space truncation of the ALDA Hxc kernel according to Equation (8.1). We start with the Hartree contribution, which we define as terms in the kernel arising from the Hartree term of Equation (8.3),

$$
\begin{aligned}
f_{\text{H}}^{\text{WLDA}_1}[n](\mathbf{r}, \mathbf{r}') &= f_{\text{H}}^{\text{WLDA}_2}[n](\mathbf{r}, \mathbf{r}') \\
&= \frac{1}{2} \iint d\mathbf{r}_1 d\mathbf{r}_2 \left[\frac{\delta n^*(\mathbf{r}_1)}{\delta n(\mathbf{r})} \delta(\mathbf{r}_2 - \mathbf{r}') + \delta(\mathbf{r}_1 - \mathbf{r}) \frac{\delta n^*(\mathbf{r}_2)}{\delta n(\mathbf{r}')} \right. \\
&\qquad\qquad \left. + n(\mathbf{r}_1) \frac{\delta^2 n^*(\mathbf{r}_2)}{\delta n(\mathbf{r})\delta n(\mathbf{r}')} \right] v_{\text{c}}(\mathbf{r}_1 - \mathbf{r}_2),
\end{aligned}
\tag{8.6a}
$$

$$
\begin{aligned}
f_{\text{H}}^{\text{WLDA}_3}[n](\mathbf{r}, \mathbf{r}') &= \iint d\mathbf{r}_1 d\mathbf{r}_2 \left[\frac{\delta n^*(\mathbf{r}_1)}{\delta n(\mathbf{r})} \frac{\delta n^*(\mathbf{r}_2)}{\delta n(\mathbf{r}')} \right. \\
&\qquad\qquad \left. + n^*(\mathbf{r}_1) \frac{\delta^2 n^*(\mathbf{r}_2)}{\delta n(\mathbf{r})\delta n(\mathbf{r}')} \right] v_{\text{c}}(\mathbf{r}_1 - \mathbf{r}_2).
\end{aligned}
\tag{8.6b}
$$

At this point, we make a halt in order to make two important observations. For all three functional forms, the usual Hartree/Coulomb kernel is recovered simply by letting $n^*(\mathbf{r}) = n(\mathbf{r})$, for which $\delta n^*(\mathbf{r}'')/\delta n(\mathbf{r}') = \delta(\mathbf{r}'' - \mathbf{r}')$ and the second order functional derivative vanishes. In short, the idea of the GWLDA is then to use a weight function of finite width to replace the δ-function and obtain a q-truncated kernel. However, there is a major issue with the Hartree kernels of Equation (8.6). The term including the second order functional derivative can be written in terms of the Hartree potential (2.12) of the true/weighted density:

$$\int d\mathbf{r}'' \frac{\delta^2 n^*(\mathbf{r}'')}{\delta n(\mathbf{r})\delta n(\mathbf{r}')} V_{\text{H}}[\tilde{n}](\mathbf{r}''),$$

where $\tilde{n} = n$ for WLDA$_1$ and WLDA$_2$, while $\tilde{n} = n^*$ for WLDA$_3$. This is a problem, because the Hartree potential diverges in the homogeneous electron gas, and for physically meaningful weight functions $\phi(r, n)$, the second order functional derivative does not prevent the Hxc kernel in inheriting this divergence[1]. Consequently, we must discard the functionals (8.5) as physically irrelevant. At this point, it could seem that all hope is lost for the GWLDA class of functionals, but in fact the issue may be solved by introducing the combined functional,

$$E_{\text{Hxc}}^{\text{WLDA}}[n] = E_{\text{Hxc}}^{\text{WLDA}_1}[n] + E_{\text{Hxc}}^{\text{WLDA}_2}[n] - E_{\text{Hxc}}^{\text{WLDA}_3}[n], \tag{8.7}$$

such that the Hartree kernel only depends on the Hartree potential of the *difference* between the true and the effective electron density, $V_{\text{H}}[n - n^*](\mathbf{r}'')$. In the homogeneous electron gas limit, $n^*(\mathbf{r}) = n(\mathbf{r}) = n$ thanks to the assumed charge conservation of the weighting procedure (8.4), and the Hartree potential term in the kernel completely cancels out for the HEG. Henceforward, we shall refer to the functional (8.7), simply as the weighted local density approximation (WLDA).

8.1.2 WLDA as a correction

Whereas we first introduced the WLDA as an Hxc functional, the Hartree functional is itself well-known and should not be approximated. Rather, the *difference* between the Hartree term(s) of the WLDA (8.7) and the actual Hartree functional (2.9) belongs to the category of exchange and/or correlation. Following through with this idea, we may introduce the WLDA xc functional as a nonlocal correction to the LDA:

$$E_{\text{xc}}^{\text{WLDA}}[n] = E_{\text{xc}}^{\text{LDA}}[n] + \Delta E_{\text{Hxc}}^{\text{WLDA}}[n] \tag{8.8}$$

where:

$$\Delta E_{\text{Hxc}}^{\text{WLDA}}[n] = -\int d\mathbf{r} \left(\epsilon_{\text{Hxc}}[n](\mathbf{r}) - \epsilon_{\text{Hxc}}[n^*](\mathbf{r})\right)\left(n(\mathbf{r}) - n^*(\mathbf{r})\right). \tag{8.9}$$

Of course, the definitions (8.7) and (8.8) are equivalent, but viewing the WLDA as a correction to the LDA offers a range of advantages. One of them is, that the so-called Hartree correction becomes easy to interpret. Quite simply, it lets the xc functional subtract the Hartree energy of the charge neutral electron density difference $n(\mathbf{r}) - n^*(\mathbf{r})$ from full Hartree energy:

$$\Delta E_{\text{H}}^{\text{WLDA}}[n] = -E_{\text{H}}[n - n^*] = -\frac{1}{2}\iint d\mathbf{r}d\mathbf{r}' \, [n(\mathbf{r}) - n^*(\mathbf{r})] \, v_{\text{c}}(\mathbf{r} - \mathbf{r}') \, [n(\mathbf{r}') - n^*(\mathbf{r}')] . \tag{8.10}$$

In this way, some of the Hartree self-interaction of localized electrons is removed and the delocalization error of the LDA is compensated for.

---

[1]There are a few mathematical details to this argument, which we will not elaborate on in the present thesis for the sake of brevity.

8.1.3   Adiabatic exchange-correlation kernel of the WLDA

Before calculating the kernel, we recall that the role of the weight function is to introduce a finite width to the functional derivative $\delta n^*(\mathbf{r})/\delta n(\mathbf{r}')$ in order to truncate the kernel in reciprocal space. To highlight this procedure, we introduce the γ-function as the difference between $\delta n^*(\mathbf{r})/\delta n(\mathbf{r}')$ and the corresponding δ-function which recovers the LDA,

$$\gamma(\mathbf{r}, \mathbf{r}') = \frac{\delta n^*(\mathbf{r})}{\delta n(\mathbf{r}')} - \delta(\mathbf{r} - \mathbf{r}') = \Phi\big(|\mathbf{r} - \mathbf{r}'|, n(\mathbf{r}')\big) - \delta(\mathbf{r} - \mathbf{r}'), \qquad (8.11)$$

where Equation (8.4) was used to write the γ-function in terms of the so-called linearized weight function,

$$\Phi(r, n) = \frac{\partial \phi(r, n)}{\partial n} n + \phi(r, n). \qquad (8.12)$$

With this, we may recast the Hartree kernel correction, corresponding to the Hartree correction (8.10), in terms of the γ-function:

$$\Delta f_{\mathrm{H}}^{\mathrm{WLDA}}[n](\mathbf{r}, \mathbf{r}') = - \iint d\mathbf{r}_1 d\mathbf{r}_2 \left[\gamma(\mathbf{r}_1, \mathbf{r}) \gamma(\mathbf{r}_2, \mathbf{r}') \right.$$
$$\left. + (n^*(\mathbf{r}_1) - n(\mathbf{r}_1)) \left. \frac{\partial \gamma}{\partial n} \right|_{|\mathbf{r}_2 - \mathbf{r}'|, n(\mathbf{r}')} \delta(\mathbf{r} - \mathbf{r}') \right] v_{\mathrm{c}}(\mathbf{r} - \mathbf{r}'). \quad (8.13)$$

Application of the convolution theorem then reveals, that the Hartree correction of the WLDA results in a *perfect* truncation of the Coulomb kernel for the homogeneous electron gas,

$$f_{\mathrm{H}}^{\mathrm{WLDA}}(n, q) = v_{\mathrm{c}}(q) + \Delta f_{\mathrm{H}}^{\mathrm{WLDA}}(n, q) = \left[1 - \gamma^2(q, n) \right] v_{\mathrm{c}}(q), \qquad (8.14)$$

realizing the natural smooth truncation envisioned in Equation (8.1), with the weight function $\phi(r, n)$ directly determining the shape of the truncation:

$$\Theta(q, n) = 1 - \gamma^2(q, n) = 1 - (\Phi(q, n) - 1)^2 = \Phi(q, n)(2 - \Phi(q, n)). \qquad (8.15)$$

We consider this *the* major result of our work on the WLDA as it in principle allows us to freely truncate the Coulomb kernel in order to approach the correct short wavelength limit of the HEG correlation hole according to the discussion of Section 7.5.

So far, we have not concerned ourselves with the kernel arising from the xc correction of the WLDA. In a similar fashion to the Hartree correction, we may write it in terms

of the γ-function:

$$
\begin{aligned}
\Delta f_{\mathrm{xc}}^{\mathrm{WLDA}}[n](\mathbf{r}, \mathbf{r}') = &-\left(\left.\frac{\partial^2 \epsilon_{\mathrm{xc}}}{\partial n^2}\right|_{n(\mathbf{r})} - \left.\frac{\partial^2 \epsilon_{\mathrm{xc}}}{\partial n^2}\right|_{n^*(\mathbf{r})} \right) \big(n(\mathbf{r}) - n^*(\mathbf{r})\big)\delta(\mathbf{r} - \mathbf{r}') \\
&+\left(\left.\frac{\partial^2 \epsilon_{\mathrm{xc}}}{\partial n^2}\right|_{n^*(\mathbf{r})} \big(n(\mathbf{r}) - n^*(\mathbf{r})\big) \right. \\
&\quad + \left. \left.\frac{\partial \epsilon_{\mathrm{xc}}}{\partial n}\right|_{n(\mathbf{r})} - \left.\frac{\partial \epsilon_{\mathrm{xc}}}{\partial n}\right|_{n^*(\mathbf{r})} \right)\gamma\big(|\mathbf{r} - \mathbf{r}'|, n(\mathbf{r}')\big) \\
&+\left(\left.\frac{\partial^2 \epsilon_{\mathrm{xc}}}{\partial n^2}\right|_{n^*(\mathbf{r}')} \big(n(\mathbf{r}') - n^*(\mathbf{r}')\big) \right. \\
&\quad + \left. \left.\frac{\partial \epsilon_{\mathrm{xc}}}{\partial n}\right|_{n(\mathbf{r}')} - \left.\frac{\partial \epsilon_{\mathrm{xc}}}{\partial n}\right|_{n^*(\mathbf{r}')} \right)\gamma\big(|\mathbf{r} - \mathbf{r}'|, n(\mathbf{r})\big) \\
&-\int d\mathbf{r}'' \left(f_{\mathrm{xc}}^{\mathrm{LDA}}\big(n^*(\mathbf{r}'')\big) - \left.\frac{\partial^2 \epsilon_{\mathrm{xc}}}{\partial n^2}\right|_{n^*(\mathbf{r}'')} n(\mathbf{r}'') \right) \\
&\qquad\qquad\qquad \times \gamma\big(|\mathbf{r}'' - \mathbf{r}|, n(\mathbf{r})\big)\gamma\big(|\mathbf{r}'' - \mathbf{r}'|, n(\mathbf{r}')\big) \\
&+\int d\mathbf{r}'' \left(\left.\frac{\partial \epsilon_{\mathrm{xc}}}{\partial n}\right|_{n^*(\mathbf{r}'')} \big(n(\mathbf{r}'') - n^*(\mathbf{r}'')\big) \right. \\
&\qquad + \left. \epsilon_{\mathrm{xc}}\big(n(\mathbf{r}'')\big) - \epsilon_{\mathrm{xc}}\big(n^*(\mathbf{r}'')\big) \right) \left.\frac{\partial \gamma}{\partial n}\right|_{|\mathbf{r}'' - \mathbf{r}|, n(\mathbf{r})} \delta(\mathbf{r} - \mathbf{r}').
\end{aligned}
$$
(8.16)

On the surface, this looks like an immensely complicated kernel. However, in full analogy with the Hartree correction, there is a simplifying cancellation of terms in the limit of an HEG, where $n^* = n$, such that:

$$
f_{\mathrm{xc}}^{\mathrm{WLDA}}(n, q) = f_{\mathrm{xc}}^{\mathrm{LDA}}(n) + \Delta f_{\mathrm{xc}}^{\mathrm{WLDA}}(n) = f_{\mathrm{xc}}^{\mathrm{LDA}}(n) - \left(f_{\mathrm{xc}}^{\mathrm{LDA}}(n) - \frac{\partial^2 \epsilon_{\mathrm{xc}}}{\partial n^2}n \right)\gamma^2(q, n).
$$
(8.17)

In this way, the WLDA functional (8.7) also realizes a full truncation of the LDA xc kernel up to a factor of $\partial^2\epsilon_{\mathrm{xc}}/\partial n^2\, n$. Given that we are able to find weight functions $\phi(r, n)$, which yield appropriate effective truncation functions $\Theta(q, n)$, the WLDA functional form then more or less achieves the desired truncation of the adiabatic HEG kernel according to Equation (8.1).

8.1.4 Weight functions

At this point, we should address the elephant in the room. How does one choose an appropriate weight function $\phi(r, n)$ and what do we even mean by "appropriate"? This question is best answered with a list of conditions for the weight function. Apart from

mathematical conditions such as being continuous and differentiable in both r and n, we see four key physical conditions for ϕ:

1. **Conservation of charge in the effective density.**

   The central idea of the WLDA functional is to introduce nonlocal contributions based on an effective density where the electrons have been redistributed according to their surroundings. In addition, we have seen that it is necessary to require a weighting procedure, which conserves the electron density of the HEG in order to avoid a divergence in the Hartree kernel correction. Therefore, an appropriate weight function $\phi(r, n)$ should obey charge conservation,

   $$\int d\mathbf{r}\, n^*(\mathbf{r}) = \int d\mathbf{r} \int d\mathbf{r}'\, \phi\big(|\mathbf{r} - \mathbf{r}'|, n(\mathbf{r}')\big) n(\mathbf{r}')$$

   $$= \int d\mathbf{r}'\, n(\mathbf{r}') \int d\mathbf{r}\, \phi\big(|\mathbf{r} - \mathbf{r}'|, n(\mathbf{r}')\big) = \int d\mathbf{r}'\, n(\mathbf{r}'), \qquad (8.18)$$

   which is equivalent to require that:

   $$\phi(q = 0, n) = 4\pi \int_0^\infty r^2 dr\, \phi(r, n) = 1,\ \forall\, n > 0. \qquad (8.19)$$

   When charge is conserved in this sense, $n^* = n$ in the HEG limit, and the WLDA functional (8.7) trivially coincides with that of the LDA, making it exact in this limit.

2. **Conservation of electrons in the effective density**

   By conserving the charge in the effective density, we do not necessarily conserve the number of electrons. To guarantee that the effective density comprises a simple redistribution of the true electron density, as discussed above, $n^*(\mathbf{r})$ also needs to be positive definite. To this end, we require that:

   $$\phi(r, n) \geq 0,\ \forall\, r \geq 0 \vee n > 0. \qquad (8.20)$$

3. **Exact match to the ALDA HEG kernel in the long wavelength limit**

   In the long wavelength limit ($q \to 0$), the ALDA kernel, or more specifically the Coulomb kernel, yields an exact representation of the HEG correlation hole, see Figure 7.1. To retain this behaviour in the WLDA, we must therefore require that the truncation function $\Theta(q, n) \to 1$ for $q \to 0$. Consulting Equation (8.15), this is equivalent to requiring that

   $$\gamma^2(q = 0, n) = 0,\ \forall\, n > 0, \qquad (8.21)$$

   or more specifically, that also the linearized weight function is normalized according to Equation (8.19):

   $$\Phi\big(q = 0, n\big) = 1,\ \forall\, n > 0. \qquad (8.22)$$

   In practice, all the weight functions $\phi(r, n)$, that we considered in this project, fulfilled this condition automatically given the first two conditions. It is however an open question whether the first two conditions are also *sufficient* to guarantee this third condition (8.22).

4. **Truncation of the ALDA HEG kernel in the short wavelength limit**

The last condition is maybe the most obvious one. In order to actually obtain a full truncation of the HEG kernel, we need to require that the truncation function vanishes in the short wavelength limit, $\Theta(q, n) \to 0$ for $q \to \infty$. To achieve this (see Equation (8.15)), we simply require that:

$$\lim_{q \to \infty} \Phi(q, n) = 0, \, \forall \, n > 0. \tag{8.23}$$

This condition is not just obvious, in practice it should also be automatically fulfilled for weight functions $\phi(r, n)$ of finite width according to conditions 1, 2 and 3.

In addition to the listed conditions, we have found it logical only to consider weight functions $\phi(r, n)$ that decrease monotonically with r. This does not seem to be a fundamental requirement of the formalism, but might be related to the automatic fulfillment of condition three given the first two for the considered functional forms.

8.1.4.1 Examples of appropriate weight functions

In this thesis, we consider two of the simplest weight functions fulfilling the conditions 1-4 from above, namely an exponential and a gaussian weight function:

$$\phi_1(r, n) = \frac{(c_1 k_{\mathrm{F}})^3}{8\pi} e^{-c_1 k_{\mathrm{F}} r}, \tag{8.24a}$$

$$\phi_2(r, n) = \frac{(c_1 k_{\mathrm{F}})^3}{\pi^{3/2}} e^{-(c_1 k_{\mathrm{F}} r)^2}. \tag{8.24b}$$

where k_{F} is the Fermi wave number of an homogeneous electron gas of density n, see Equation (7.54). The prefactors have been chosen such as to normalize the weight functions according to Equation (8.19) and $c_1 > 0$ is a dimensionless free parameter, which governs the width of the weight function. The corresponding linearized weight functions are given by

$$\Phi_1(r, n) = \left(2 - \frac{c_1 k_{\mathrm{F}} r}{3}\right) \frac{(c_1 k_{\mathrm{F}})^3}{8\pi} e^{-c_1 k_{\mathrm{F}} r}, \tag{8.25a}$$

$$\Phi_2(r, n) = \left(2 - \frac{2 (c_1 k_{\mathrm{F}} r)^2}{3}\right) \frac{(c_1 k_{\mathrm{F}})^3}{\pi^{3/2}} e^{-(c_1 k_{\mathrm{F}} r)^2}, \tag{8.25b}$$

with reciprocal space representations

$$\Phi_1(q, n) = \Phi_1(q/k_{\mathrm{F}}) = \left(2 - \frac{1 - \frac{1}{3}\tilde{q}^2}{1 + \tilde{q}^2}\right) \frac{1}{(1 + \tilde{q}^2)^2}, \tag{8.26a}$$

$$\Phi_2(q, n) = \Phi_2(q/k_{\mathrm{F}}) = \left(1 + \frac{\tilde{q}^2}{6}\right) e^{-\tilde{q}^2/4}, \tag{8.26b}$$

where $\tilde{q} = q/(c_1 k_{\mathrm{F}})$. By comparing the linearized weight functions (8.26) to the conditions (8.22) and (8.23), it is clear that both the exponential and the gaussian weight function realize an appropriate truncation of the ALDA kernel for the HEG correlation hole.

Left is now only to determine the width parameter c_1. In principle, it could be chosen as a fitting parameter to best match a number of exact limits or to optimize performance for a given dataset, but for the purpose of the present thesis, we fix it to yield truncation functions $\Theta_1(q/k_{\mathrm{F}})$ and $\Theta_2(q/k_{\mathrm{F}})$ with HWHM at $q = 2k_{\mathrm{F}}$. In this way, we achieve a smooth truncation, that qualitatively realizes the phenomenological step function truncation envisioned in Equation (8.1). In Figure 8.1, we present the resulting truncation functions. Both of the weight functions yield a flat plateau in the long wavelength limit, such that the WLDA should retain the exact properties of the Coulomb kernel, for small $q \ll k_{\mathrm{F}}$. The shape of the actual truncation is however different between the two weight functions. Whereas the gaussian weight functions realizes a more or less symmetrical short-range truncation, the exponential weight function yields an asymmetric long-range truncation as a function of wave number q.

Throughout the remainder of the thesis, we will report results for both weight functions in order to illustrate the tuning capabilities of the formalism. However, fine tuning of the weight function shape and width is generally left for future work.

8.2 HEG correlation hole in the WLDA

Finally, we are in a position, where we can compute the coupling-constant averaged correlation hole of the HEG using the WLDA kernel. Inserting Hartree and xc kernels (8.14) and (8.17) into Equation (7.52), we compute the HEG correlation hole as a function of the wave number q, which is presented in Figure 8.2. In comparison to the ALDA, the WLDA clearly improves on the HEG correlation hole for values of $q > 2k_{\mathrm{F}}$.
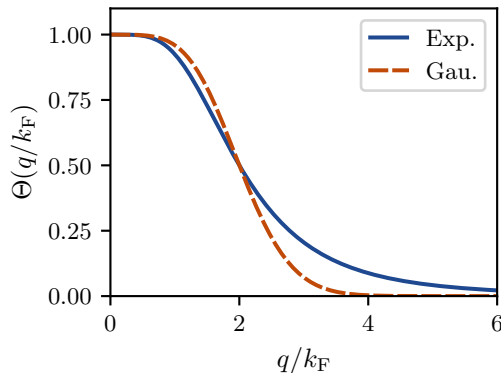

Figure 8.1: Truncation functions (8.15) for the exponential and gaussian weight functions (8.24) with width parameters c_1 chosen such that $\Theta(q = 2k_{\mathrm{F}}) = 1/2$.

Figure 8.2: Reciprocal space coupling-constant averaged correlation hole of the homogeneous electron gas, with insets highlighting the short wavelength limit. An accurate analytical representation of the exact correlation hole [91] is compared to holes calculated within the RPA, ALDA and WLDA approximations, using Equation (7.52) and weight functions (8.24). Each respective panel shows the correlation hole calculated with a given electron density $n = 3/(4\pi r_s^3)$.

However, the extra factor of $\partial^2 \epsilon_{xc}/\partial n^2 \, n$ in the HEG xc kernel (8.17) seems to entail that the ALDA kernel is over-corrected and that the bare Coulomb kernel (RPA) still yields the best description of the short wavelength correlations of the HEG. From Figure 8.2, one may also note that the exponential weight function seems to reproduce a more accurate correlation hole than the gaussian one independent of the electron density. Most likely, this is directly connected to the over-correction of the xc kernel, as the exponential weight function would "turn on" the over-correction more slowly for intermediate values of $q \in [2k_F, 4k_F]$ compared to the gaussian weight function.

8.2.1 Renormalized WLDA

We investigate the over-correction of WLDA in more detail by taking a look at the actual functional form for the LDA exchange kernel. The exchange energy per electron of the HEG is given by

$$\epsilon_x(n) = -C_x n^{1/3}, \tag{8.27}$$

where C_x is independent of the density n, but may be taken as a function of the relative spin-polarization $C_x = C_x(\zeta)$, where $\zeta = (n_\uparrow - n_\downarrow)/n$. The LDA exchange kernel is then given by

$$f_x^{LDA}(n) = \frac{\partial^2 \epsilon_x}{\partial n^2} n + 2\frac{\partial \epsilon_x}{\partial n} = \frac{2C_x}{9}n^{-2/3} - \frac{2C_x}{3}n^{-2/3} = -\frac{4C_x}{9}n^{-2/3}, \tag{8.28}$$

so that

$$f_{\mathrm{x}}^{\mathrm{LDA}}(n) - \frac{\partial^2 \epsilon_{\mathrm{x}}}{\partial n^2} n = 2\frac{\partial \epsilon_{\mathrm{x}}}{\partial n} = -\frac{2C_{\mathrm{x}}}{3} n^{-2/3} = \frac{3}{2} f_{\mathrm{x}}^{\mathrm{LDA}}(n). \qquad (8.29)$$

This means that the WLDA exchange kernel in Equation (8.17) over-corrects the LDA kernel by a factor of $3/2$, independently of the density n:

$$\Delta f_{\mathrm{x}}^{\mathrm{WLDA}}(n) = 2\frac{\partial \epsilon_{\mathrm{x}}}{\partial n} \gamma^2(q,n) = \frac{3}{2} f_{\mathrm{x}}^{\mathrm{LDA}}(n)\gamma^2(q,n). \qquad (8.30)$$

Thus, we may circumvent this over-correction by including only $2/3$ of the WLDA exchange correction. Unfortunately, also the correlation kernel is over-corrected in the WLDA, as is illustrated in Figure 8.3, but not by a constant factor. In order to get a perfect truncation of the LDA correlation kernel, a fraction between $1/2$ to $5/8$ (depending on the density) of the WLDA correlation correction should be included.

Instead of devising a scheme to achieve a perfect truncation of the correlation kernel, we take a more pragmatic approach: We simply include both the exchange and correlation corrections in factors of $2/3$, in what we will denote as the renormalized WLDA (rWLDA):

$$E_{\mathrm{xc}}^{\mathrm{rWLDA}}[n] = E_{\mathrm{xc}}^{\mathrm{LDA}}[n] + \Delta E_{\mathrm{H}}^{\mathrm{WLDA}}[n] + \frac{2}{3}\Delta E_{\mathrm{xc}}^{\mathrm{WLDA}}[n]. \qquad (8.31)$$

This approximation then achieves a perfect truncation of the Coulomb and exchange kernels for the HEG, but is still associated with a slight over-correction of the correlation kernel, although much reduced in comparison to the WLDA functional. In Figure 8.4, we plot the HEG correlation hole computed with the rWLDA kernel. On the contrary to the WLDA case, we now obtain a more or less perfect truncation of
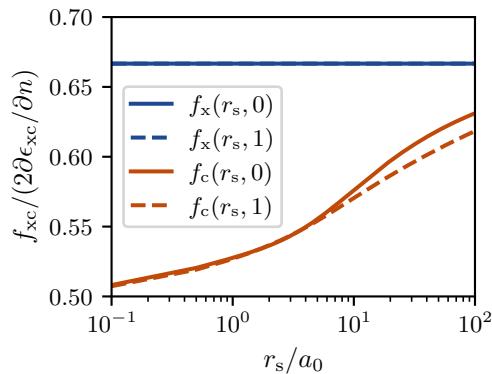
Figure 8.3: Fraction in which to include the exchange/correlation correction (8.9) in order to achieve a perfect truncation of the LDA kernel in the short wavelength limit, see Equation (8.17). The LDA exchange and correlation kernels, $f_{\mathrm{xc}}(r_{\mathrm{s}}, \zeta)$, are plotted independently as a function of the Wigner radius (7.55) for a spin-paired and a fully spin-polarized HEG. For the HEG correlation energy per electron, we use the analytical expression in [99].
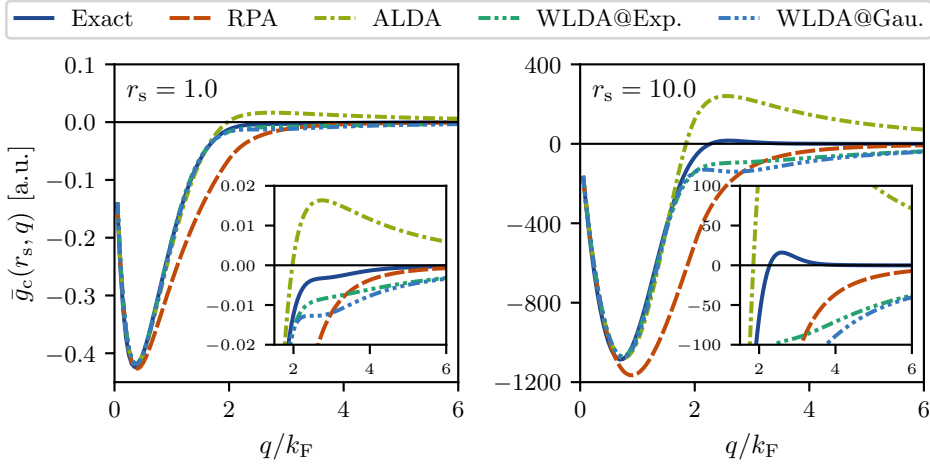
Figure 8.4: Reciprocal space coupling-constant averaged correlation hole of the homogeneous electron gas, with insets highlighting the short wavelength limit. An accurate analytical representation of the exact correlation hole [91] is compared to holes calculated within the RPA, ALDA and rWLDA approximations, using Equation (7.52) and weight functions (8.24). Each respective panel shows the correlation hole calculated with a given electron density $n = 3/(4\pi r_s^3)$.

the HEG correlation hole in the short wavelength limit! The only significant imperfection left, is that the correlation hole is overestimated for an intermediate range of $q \in [2k_F, 4k_F]$. The reason behind is, that the exchange and Coulomb HEG kernels are truncated evenly, as was originally envisioned in Equation (8.1):

$$f_{Hx}^{rWLDA}(n, q) = \left[1 - \gamma^2(q, n)\right] \left[v_c(q) + f_x^{LDA}(n)\right].\tag{8.32}$$

The ALDAx kernel (second term on the right) has a root exactly at $q = 2k_F$ which is directly carried over to the ALDAx HEG correlation hole, see Equation (7.52) and Figure 7.1. As the correlation kernel in small in comparison, this property is qualitatively preserved both by the ALDA and the rWLDA, such that the corresponding correlation holes in Figure 8.4 have roots at $q \simeq 2k_F$. However, this is not a property of the exact HEG correlation hole, which is rootless for dense electron densities ($r_s = 1.0\,a_0$), meaning that the rWLDA as well as the ALDA kernel will overestimate the HEG correlation hole in a region around $2k_F$. As the gaussian weight function achieves a more abrupt truncation than the exponential weight function, see Figure 8.1, it seems to be the better match for the rWLDA kernel because the swift truncation limits the overestimation of the HEG correlation hole in the intermediate range of $q \in [2k_F, 4k_F]$.

8.2.2 Fractionalized WLDA

Finally, we may actually also overcome the overestimation of the rWLDA HEG correlation hole in the intermediate q-range by including only a fraction of 2/3 of the WLDA

Hartree correction, in what we will denote as the fractionalized WLDA (fWLDA):

$$E_{\text{xc}}^{\text{fWLDA}}[n] = E_{\text{xc}}^{\text{LDA}}[n] + \frac{2}{3}\Delta E_{\text{Hxc}}^{\text{WLDA}}[n]. \tag{8.33}$$

This will leave 1/3 of the Coulomb kernel untruncated, and we obtain an astonishingly close match to the exact HEG correlation hole, more or less independently of the wave number q, as illustrated in Figure 8.5. Of course, the remaining Coulomb kernel results in a HEG correlation hole that is slightly underestimated in the short wavelength limit when compared to the rWLDA kernel, but especially for dense electron densities ($r_{\text{s}} = 1.0\,a_0$), the overall accuracy in the fWLDA functional form speaks for itself. Whereas it is the gaussian weight function that achieves this accurate match for $r_{\text{s}} = 1.0\,a_0$, the exponential weight function seems like a better compromise across electron densities, yielding an HEG correlation hole which is terminated around $q \sim 2.5 k_{\text{F}}$ independent of the density n.

At the end of the day, we are not only interested in the homogeneous electron gas properties, but also the performance of the functionals for real materials. As the performance in the uniform and atomic limits might not be transferable, we do not discard any of the developed functionals at this stage. Henceforward, we will refer to the WLDA, rWLDA and fWLDA functionals as "flavors" of the WLDA.
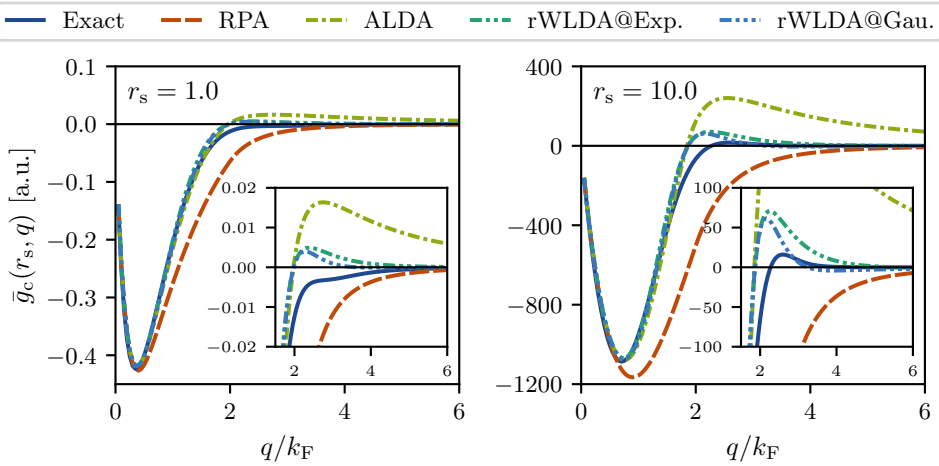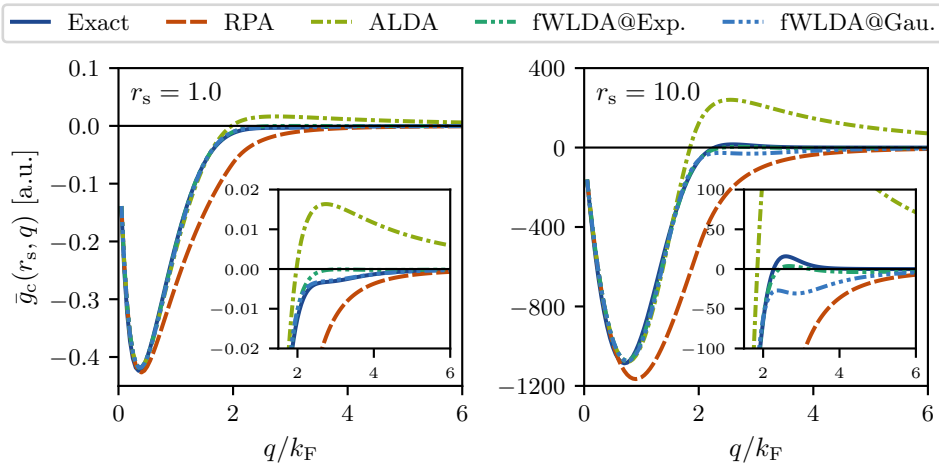

Figure 8.5: Reciprocal space coupling-constant averaged correlation hole of the homogeneous electron gas, with insets highlighting the short wavelength limit. An accurate analytical representation of the exact correlation hole [91] is compared to holes calculated within the RPA, ALDA and fWLDA approximations, using Equation (7.52) and weight functions (8.24). Each respective panel shows the correlation hole calculated with a given electron density $n = 3/(4\pi r_{\text{s}}^3)$.

8.3   Properties of the WLDA

Before assessing the performance of the WLDA, we will take a deeper look at its properties and characteristics.

8.3.1   Interpretation

In order to make a physical interpretation of the effective density scheme, it is illuminating to take a look at a simple concrete example, namely the hydrogen atom. Due to the spherical symmetry of the 1s orbital, it is straight-forward to the compute the effective density for a given weight function $\phi(r, n)$, see Section A.3 of Appendix A, and in Figure 8.6, we show the effective density calculated using the exponential weight function (8.24a). Generally speaking, the density weighting procedure results in a delocalization of the electron density, pushing away the electron from the nucleus. Whereas the true electron density decays exponentially away from the nucleus, the effective density decays sub-exponentially into the vacuum (this is also the case using the gaussian weight function). For this reason, it is not impossible that the WLDA is able to capture long-range correlation effects such as van der Waals forces. However, it also implies that $n^*(r)/n(r)$ diverges as $r \to \infty$ (in vacuum), which turns out to be problematic for the WLDA xc potential correction, as will be shown in the following section.

With a concrete example in hand, we may now give an interpretation to the WLDA correction (8.9). In regions of space where electrons localize, $n(\mathbf{r}) > n^*(\mathbf{r})$, and the "excess localization charge" $n(\mathbf{r}) - n^*(\mathbf{r})$ is distributed to the near surroundings with a "localization charge deficit" $n^*(\mathbf{r}) - n(\mathbf{r}) > 0$, see Figure 8.6(b). The energy per
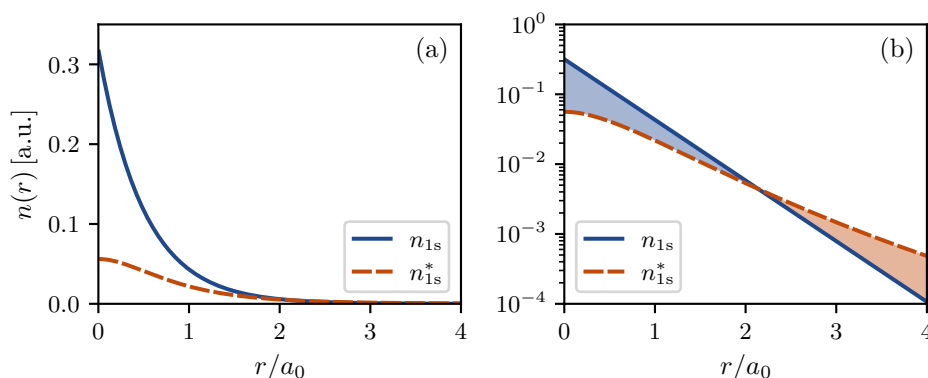
Figure 8.6: True and effective electron densities of the hydrogen atom as a function of the radius r, plotted on a linear and an exponential scale in the two panels respectively. The effective density was calculated with the exponential weight function (8.24a) and in panel (b), the "excess localization charge" and the "localization charge deficit" (definitions in the main body of the text) are shown as the blue and red colored regions between the density curves.

electron is then corrected with two terms. The energy per electron of the "excess localization charge" is replaced with that of the effective (locally more dilute) electron gas: $\Delta\epsilon_{\mathrm{Hxc}}(\mathbf{r}) = \epsilon_{\mathrm{Hxc}}[n^*](\mathbf{r}) - \epsilon_{\mathrm{Hxc}}[n](\mathbf{r})$. Furthermore, the "localization charge deficit" is corrected by a value of $\Delta\epsilon_{\mathrm{Hxc}}(\mathbf{r}) = \epsilon_{\mathrm{Hxc}}[n](\mathbf{r}) - \epsilon_{\mathrm{Hxc}}[n^*](\mathbf{r})$, that is, yet another correctional term in which the energy per electron is replaced with that of a locally more dilute electron gas. In this way, both of the contributions add a compensation from the added electron-electron repulsion associated with the localization of electrons around atomic nuclei. In the best case scenario, this will eliminate the delocalization error of the LDA.

8.3.2 Exchange-correlation potential

In order to solve the ground state problem within the Kohn-Sham scheme, we calculate the WLDA correction to the xc potential:

$$
\begin{aligned}
\Delta V_{\mathrm{Hxc}}^{\mathrm{WLDA}}[n](\mathbf{r}) = \int d\mathbf{r}' \Bigg(& \left[\left. \frac{\partial \epsilon_{\mathrm{xc}}}{\partial n} \right|_{n=n^*(\mathbf{r}')} \big(n(\mathbf{r}') - n^*(\mathbf{r}') \big) \right. \\
& \left. + \epsilon_{\mathrm{xc}}\big(n(\mathbf{r}') \big) - \epsilon_{\mathrm{xc}}\big(n^*(\mathbf{r}') \big) \right] \frac{\delta n^*(\mathbf{r}')}{\delta n(\mathbf{r})} \\
& - \left[\left. \frac{\partial \epsilon_{\mathrm{xc}}}{\partial n} \right|_{n=n(\mathbf{r}')} \big(n(\mathbf{r}') - n^*(\mathbf{r}') \big) \right. \\
& \left. + \epsilon_{\mathrm{xc}}\big(n(\mathbf{r}') \big) - \epsilon_{\mathrm{xc}}\big(n^*(\mathbf{r}') \big) \right] \delta(\mathbf{r} - \mathbf{r}') \Bigg) \\
+ \iint d\mathbf{r}' d\mathbf{r}'' & \left(\frac{\delta n^*(\mathbf{r}')}{\delta n(\mathbf{r})} - \delta(\mathbf{r} - \mathbf{r}') \right) v_{\mathrm{c}}(\mathbf{r}' - \mathbf{r}'') \big(n(\mathbf{r}'') - n^*(\mathbf{r}'') \big).
\end{aligned}
$$
(8.34)

Clearly, also the WLDA correction for the xc potential can be written as a number of correctional terms weighted by the γ-function (8.11). The notable exception is the combination of terms

$$
\int d\mathbf{r}' \left(\left. \frac{\partial \epsilon_{\mathrm{xc}}}{\partial n} \right|_{n=n^*(\mathbf{r}')} \big(n(\mathbf{r}') - n^*(\mathbf{r}') \big) \frac{\delta n^*(\mathbf{r}')}{\delta n(\mathbf{r})} \right.
$$
$$
\left. - \left. \frac{\partial \epsilon_{\mathrm{xc}}}{\partial n} \right|_{n=n(\mathbf{r}')} \big(n(\mathbf{r}') - n^*(\mathbf{r}') \big) \delta(\mathbf{r} - \mathbf{r}') \right).
$$

The partial derivative $\partial \epsilon_{\mathrm{xc}} / \partial n$ gives rise to terms that scale with negative powers of the density (a power of $-2/3$ for exchange). This means, that the term

$$
\left. \frac{\partial \epsilon_{\mathrm{xc}}}{\partial n} \right|_{n=n(\mathbf{r})} n^*(\mathbf{r})
$$

will diverge in vacuum due to the different asymptotic behaviour of the true and effective densities illustrated in Figure 8.6(b). As $\partial \epsilon_{\mathrm{xc}} / \partial n$ is a negative quantity, the

effective Kohn-Sham potential (2.11) becomes leaky as a result. This illustrates that one cannot completely turn the blind eye towards the atomic limit and expect to develop a universally valid functional. The problematic term arises from the $WLDA_1$ part of the WLDA correction, see Equation (8.5a), and in order to obtain a truly universal functional, it seems necessary to define a GWLDA xc correction without it. For the performance assessment made in this thesis however, we simply regularize the divergent term, removing it manually from the potential for densities below a set threshold. For density thresholds chosen sufficiently small, the resulting total energies do not depend on the threshold itself. One can actually run the calculations without a density threshold at all, but using a finite value speeds up the convergence significantly.

Taking a second glance at the WLDA xc potential correction (8.34), one may also notice that the Hartree part of the correction can be written in terms of the Hartree potential of the electron density difference $n(\mathbf{r}) - n^*(\mathbf{r})$. The Hartree contribution to the xc potential is then the difference between this new Hartree potential weighted locally by the linearized weight function, see Equation (8.11), and the corresponding bare Hartree potential. Similarly, the full potential correction may be written:

$$
\Delta V_{\mathrm{Hxc}}^{\mathrm{WLDA}}[n](\mathbf{r}) = \int d\mathbf{r}' \left[\left. \frac{\partial \epsilon_{\mathrm{xc}}}{\partial n} \right|_{n=n^*(\mathbf{r}')} \left(n(\mathbf{r}') - n^*(\mathbf{r}') \right) \right.
$$
$$
\left. + \epsilon_{\mathrm{xc}}\left(n(\mathbf{r}') \right) - \epsilon_{\mathrm{xc}}\left(n^*(\mathbf{r}') \right) \right] \Phi\left(|\mathbf{r} - \mathbf{r}'|, n(\mathbf{r}) \right)
$$
$$
- \left[\left. \frac{\partial \epsilon_{\mathrm{xc}}}{\partial n} \right|_{n=n(\mathbf{r})} \left(n(\mathbf{r}) - n^*(\mathbf{r}) \right) + \epsilon_{\mathrm{xc}}\left(n(\mathbf{r}) \right) - \epsilon_{\mathrm{xc}}\left(n^*(\mathbf{r}) \right) \right]
$$
$$
+ \int d\mathbf{r}' \, \Phi\left(|\mathbf{r} - \mathbf{r}'|, n(\mathbf{r}) \right) V_{\mathrm{H}}[n - n^*](\mathbf{r}') - V_{\mathrm{H}}[n - n^*](\mathbf{r}). \qquad (8.35)
$$

Thus, to compute the xc potential, one has to compute the weighted density $n^*(\mathbf{r})$ and the Hartree potential from electron density difference $n(\mathbf{r}) - n^*(\mathbf{r})$. Then, the WLDA xc potential correction can be calculated as a Φ-weighted integral, where the integrand is straight-forward to evaluate, given $n^*(\mathbf{r})$. Although both the effective density (8.4) and the xc potential (8.35) are calculated by the means of a weighted integral, the xc potential integral is simpler to compute, because the width of the weight function depends on the position $\mathbf{r}$ in which the xc potential is evaluated and not the integrated variable $\mathbf{r}'$.

8.3.3 Exchange-correlation hole

Because of the simple functional form of the WLDA, one can easily derive the exchange-correlation hole density of the approximation, see e.g. Equations (7.26) and (7.29).

Using the HEG xc hole density to rewrite the WLDA xc functional (8.8),

$$\begin{aligned}
E_{\mathrm{xc}}^{\mathrm{WLDA}}[n] = \frac{1}{2} \iint d\mathbf{r} d\mathbf{r}'\, v_{\mathrm{c}}(\mathbf{r}-\mathbf{r}') \Bigg[&n(\mathbf{r})\bar{n}_{\mathrm{xc}}^{\mathrm{HEG}}\big(|\mathbf{r}-\mathbf{r}'|, n^*(\mathbf{r})\big) \\
&+ \int d\mathbf{r}''\phi\big(|\mathbf{r}-\mathbf{r}''|, n(\mathbf{r}'')\big)n(\mathbf{r}'') \\
&\times \Big[\bar{n}_{\mathrm{xc}}^{\mathrm{HEG}}\big(|\mathbf{r}-\mathbf{r}'|, n(\mathbf{r})\big) - \bar{n}_{\mathrm{xc}}^{\mathrm{HEG}}\big(|\mathbf{r}-\mathbf{r}'|, n^*(\mathbf{r})\big)\Big] \\
&- n(\mathbf{r})\big[n(\mathbf{r}') - n^*(\mathbf{r}')\big] \\
&+ \int d\mathbf{r}''\phi\big(|\mathbf{r}-\mathbf{r}''|, n(\mathbf{r}'')\big)n(\mathbf{r}'')\big[n(\mathbf{r}') - n^*(\mathbf{r}')\big]\Bigg].
\end{aligned}$$

Now, interchanging the $\mathbf{r}$ and $\mathbf{r}''$ integration variables in the terms where a weight function $\phi(r, n)$ appears, we obtain the WLDA xc hole density:

$$\begin{aligned}
\bar{n}_{\mathrm{xc}}^{\mathrm{WLDA}}[n](\mathbf{r},\mathbf{r}') =& \bar{n}_{\mathrm{xc}}^{\mathrm{HEG}}\big(|\mathbf{r}-\mathbf{r}'|, n^*(\mathbf{r})\big) - \big(n(\mathbf{r}') - n^*(\mathbf{r}')\big) \\
&+ |\mathbf{r}-\mathbf{r}'| \int d\mathbf{r}''\phi\big(|\mathbf{r}-\mathbf{r}''|, n(\mathbf{r})\big) \Bigg[\frac{n(\mathbf{r}') - n^*(\mathbf{r}')}{|\mathbf{r}'-\mathbf{r}''|} \\
&+ \frac{\bar{n}_{\mathrm{xc}}^{\mathrm{HEG}}\big(|\mathbf{r}'-\mathbf{r}''|, n(\mathbf{r}'')\big) - \bar{n}_{\mathrm{xc}}^{\mathrm{HEG}}\big(|\mathbf{r}'-\mathbf{r}''|, n^*(\mathbf{r}'')\big)}{|\mathbf{r}'-\mathbf{r}''|}\Bigg]. \quad (8.36a)
\end{aligned}$$

The first term is simply the LDA xc hole, see Equation (7.28), but evaluated at the effective density $n^*(\mathbf{r})$. As the LDA xc hole is already normalized and the electron density difference $n(\mathbf{r}) - n^*(\mathbf{r})$ integrates to zero, thanks to charge conservation, the WLDA xc hole is therefore normalized according to (7.9), given that

$$\begin{aligned}
\iint d\mathbf{r}' d\mathbf{r}''\, |\mathbf{r}-\mathbf{r}'|\phi\big(|\mathbf{r}-\mathbf{r}''|, n(\mathbf{r})\big) \Bigg[&\frac{n(\mathbf{r}') - n^*(\mathbf{r}')}{|\mathbf{r}'-\mathbf{r}''|} \\
&+ \frac{\bar{n}_{\mathrm{xc}}^{\mathrm{HEG}}\big(|\mathbf{r}'-\mathbf{r}''|, n(\mathbf{r}'')\big) - \bar{n}_{\mathrm{xc}}^{\mathrm{HEG}}\big(|\mathbf{r}'-\mathbf{r}''|, n^*(\mathbf{r}'')\big)}{|\mathbf{r}'-\mathbf{r}''|}\Bigg] = 0. \quad (8.37)
\end{aligned}$$

In principle, the weight function $\phi(r, n)$ should be chosen, such that (8.37) is fulfilled for any electron density $n(\mathbf{r})$. This seems to be a nontrivial task, and as the WLDA was not developed with its own xc hole density in mind, it may not even be possible. Further investigations into the WLDA xc hole is left for future work.

8.4 WLDA for spin-polarized systems

Before we address the performance of the WLDA for atomic systems (which may have unpaired spins) or magnetic solids, we need to define how the functional accounts for any spin-polarization in the system. As a natural extension of the WLDA functional development, one could in this regard consider the correlation hole of the spin-polarized HEG, but in order to limit the project scope, we will instead make some conservative

choices for the functional form and leave further development of the spin-polarized functional to future studies.

8.4.1 Spin-polarized exchange correction

The exchange energy functional, see e.g. Equation (7.32), depends on the spin degrees of freedom separately, and may be written identically in terms of the spin-paired exchange functional [66]:

$$E_{\mathrm{x}}[n_\uparrow, n_\downarrow] = \frac{E_{\mathrm{x}}[2n_\uparrow] + E_{\mathrm{x}}[2n_\downarrow]}{2}. \tag{8.38}$$

Assuming that the WLDA exchange correction belongs to the category of exchange, we may thus evaluate it directly using the spin-paired functionality:

$$\Delta E_{\mathrm{x}}^{\mathrm{WLDA}}[n_\uparrow, n_\downarrow] = \frac{\Delta E_{\mathrm{x}}^{\mathrm{WLDA}}[2n_\uparrow] + \Delta E_{\mathrm{x}}^{\mathrm{WLDA}}[2n_\uparrow]}{2}. \tag{8.39}$$

In turn, this entails that the WLDA exchange correction to the spin-dependent xc potential only depends on the spin-density of that given spin,

$$\Delta V_{\mathrm{x}}^{\mathrm{WLDA},s}[n_\uparrow, n_\downarrow](\mathbf{r}) = \frac{\delta \Delta E_{\mathrm{x}}^{\mathrm{WLDA}}[n_\uparrow, n_\downarrow]}{\delta n_s(\mathbf{r})} = \Delta V_{\mathrm{x}}^{\mathrm{WLDA}}[2n_s](\mathbf{r}), \tag{8.40}$$

making it possible simply to reuse the spin-paired functionality.

8.4.2 Spin-polarized Hartree correction

Per definition, the WLDA Hartree correction formally constitutes a contribution to the exchange-correlation energy. Even though the Hartree energy (2.9) is strictly independent of the spin-polarization, there is no apparent reason why the WLDA Hartree correction could not be a functional of the spin-polarization as well as the density. In the context of the present thesis, we will therefore explore the following two options:

1. **Spin-neutral Hartree correction.**

   The simplest option is of course to take the WLDA Hartree correction to be independent of the spin-polarization, such that

   $$\Delta E_{\mathrm{H}}^{\mathrm{WLDA}}[n_\uparrow, n_\downarrow] = \Delta E_{\mathrm{H}}^{\mathrm{WLDA}}[n_\uparrow + n_\downarrow], \tag{8.41}$$

   yielding also a spin-neutral Hartree correction to the xc potential:

   $$\Delta V_{\mathrm{H}}^{\mathrm{WLDA},s}[n_\uparrow, n_\downarrow](\mathbf{r}) = \Delta V_{\mathrm{H}}^{\mathrm{WLDA}}[n_\uparrow + n_\downarrow](\mathbf{r}). \tag{8.42}$$

2. **Hartree correction as exchange.**

   As the Hartree correction (8.10) removes the classical Coulomb self-repulsion of the "excess localization charge" as well as the "localization charge deficit",

replacing it with the repulsion between the two, one may induce that it primarily belongs to the category of self-exchange. If this is the case, one may take the WLDA Hartree correction solely as an exchange contribution and use Equation (8.38) to write:

$$E_x^{\text{WLDA}}[n_\uparrow, n_\downarrow] = E_x^{\text{LDA}}[n_\uparrow, n_\downarrow] + \frac{\Delta E_{\text{Hx}}^{\text{WLDA}}[2n_\uparrow] + \Delta E_{\text{Hx}}^{\text{WLDA}}[2n_\uparrow]}{2}. \quad (8.43)$$

With this definition, the Hartree correction to the spin-dependent exchange potential is evaluated analogously to Equation (8.40).

8.4.3   Spin-polarized correlation correction

For the WLDA correlation correction, we cannot write the spin-polarized functional in terms of the spin-paired analogue. Instead, we replace

$$\epsilon_c\big(n(\mathbf{r})\big) \to \epsilon_c\big(n_\uparrow(\mathbf{r}), n_\downarrow(\mathbf{r})\big) \quad \text{and} \quad \epsilon_c\big(n^*(\mathbf{r})\big) \to \epsilon_c\big(n_\uparrow^*(\mathbf{r}), n_\downarrow^*(\mathbf{r})\big) \quad (8.44)$$

in the correlation correction defined by Equations (8.3) and (8.9), such that

$$\Delta E_c^{\text{WLDA}}[n_\uparrow, n_\downarrow] = -\int d\mathbf{r} \left[\epsilon_c\big(n_\uparrow(\mathbf{r}), n_\downarrow(\mathbf{r})\big) - \epsilon_c\big(n_\uparrow^*(\mathbf{r}), n_\downarrow^*(\mathbf{r})\big)\right]\left[n(\mathbf{r}) - n^*(\mathbf{r})\right]. \quad (8.45)$$

To this end, we need to define the effective spin-densities $n_\uparrow^*(\mathbf{r})$ and $n_\downarrow^*(\mathbf{r})$. In order to be consistent with the spin-paired WLDA correction, we need to make sure that $n_\uparrow^*(\mathbf{r}) + n_\downarrow^*(\mathbf{r}) \to n^*(\mathbf{r})$ in the spin-paired limit $n_\uparrow(\mathbf{r}) = n_\downarrow(\mathbf{r})$, where $n^*(\mathbf{r})$ is the spin-paired effective density (8.4). Consistency in the spin-paired limit could be achieved in many ways, but in the present context we will restrict ourselves to the case, where the total effective density, $n_\uparrow^*(\mathbf{r}) + n_\downarrow^*(\mathbf{r})$, matches the spin-paired definition (8.4) independently of the spin-polarization of the system:

$$n_\uparrow^*(\mathbf{r}) + n_\downarrow^*(\mathbf{r}) = n^*(\mathbf{r}) = \int d\mathbf{r}' \,\phi\big(\left|\mathbf{r} - \mathbf{r}'\right|, n(\mathbf{r}')\big)n(\mathbf{r}'). \quad (8.46)$$

Furthermore, we will force the unit-cell averaged effective spin-polarization to equal that of the true electron spin-density (analogously to the fact that n^* preserves the total number of electrons in n):

$$\int_{\Omega_{\text{cell}}} d\mathbf{r} \,\big(n_\uparrow^*(\mathbf{r}) - n_\downarrow^*(\mathbf{r})\big) = \int_{\Omega_{\text{cell}}} d\mathbf{r} \,\big(n_\uparrow(\mathbf{r}) - n_\downarrow(\mathbf{r})\big). \quad (8.47)$$

The simplest way of fulfilling these two conditions is simply to let the individual spin-densities be redistributed according to the total density,

$$n_{\uparrow/\downarrow}^*(\mathbf{r}) = \int d\mathbf{r}' \,\phi\big(\left|\mathbf{r} - \mathbf{r}'\right|, n(\mathbf{r}')\big)n_{\uparrow/\downarrow}(\mathbf{r}'), \quad (8.48)$$

such that the total spin-polarization is conserved, given that the weight function $\phi(r, n)$ is normalized to preserve the total number of electrons.

For the sake of brevity, we leave the derivation of the spin-polarized correlation potential correction to the reader and simply note that it can be carried in a similar fashion to the spin-paired case, see Section 8.3.2.

8.5   Performance of the WLDA

To test the performance of the WLDA functional flavors beyond the HEG correlation hole, we have implemented the WLDA Hartree, exchange and correlation corrections in the GPAW electronic structure methods code [37, 38]. In this regard, there are two major novelties in comparison with previously established functionality for the LDA and semi-local functionals: (1) Evaluation of the effective density (8.4). (2) Evaluation of corrections to the xc potential (8.35). All other ingredients can essentially be evaluated using existing functionality, such as the LDA exchange-correlation energy of the effective density (8.5c) and the Hartree potential of the electron density difference $V_{\mathrm{H}}[n-n^*](\mathbf{r})$. Now, the nonlocal contribution to the xc potential corrections (8.35) can be written as a convolution and may therefore be evaluated efficiently using the convolution theorem and the fast-fourier-transform algorithm. The bottleneck is instead evaluation of the effective density $n^*(\mathbf{r})$. Here we use the indicator function technique, which was developed for the purpose of computing nonlocal van der Waals corrections [100]. As a result, usage of the WLDA functional flavors will at the fundamental level resemble a van der Waals functional in computational complexity. For additional details on the indicator function technique and its implementation, the reader is referred to Asbjørn's thesis [98].

At the current stage, we have not yet developed PAW functionality to support the WLDA functional flavors. Instead, we use a simple basis representations of the all-electron density $n(\mathbf{r})$ and the corresponding effective density $n^*(\mathbf{r})$. Essentially, this corresponds to doing DFT by brute force and is not scalable to calculations of more than a few simple systems. For now, we have implemented the WLDA corrections into the radial GPAW code for atoms, exact for spherically symmetric systems, as well as the generally applicable plane wave code, in which the true and effective densities are represented on a regular real-space grid. In the following, we use the radial code to compute the total energies of a range of bare atoms, as well as the plane wave code to compute atomization energies of a few simple molecules.

8.5.1   Atomic energies

Because the angular degrees of freedom are averaged out in the radial GPAW code for atoms, it is straight-forward to converge the atomic total energies using a dense radial grid on contemporary computational hardware. In Figure 8.7, we present the calculated atomic total energies relative to accurate references using the LDA and PBE functionals as well as the WLDA, rWLDA and fWLDA functional flavors. Of course, the radial code only yields exact results for the atoms, which actually do possess spherical symmetry in the ground state. However, Figure 8.7 clearly shows that the total energy bias of a given functional is a continuous function of the atomic number and we may use the entire data set to draw qualitative conclusions from.

First of all, we see that the LDA consistently overestimates the atomic total energies. This is due to the self-interaction error, which is not cancelled completely by the LDA exchange for systems with localized electrons. This is also the origin of the so-called delocalization error of LDA, meaning that the LDA tends to favor a too delocalized
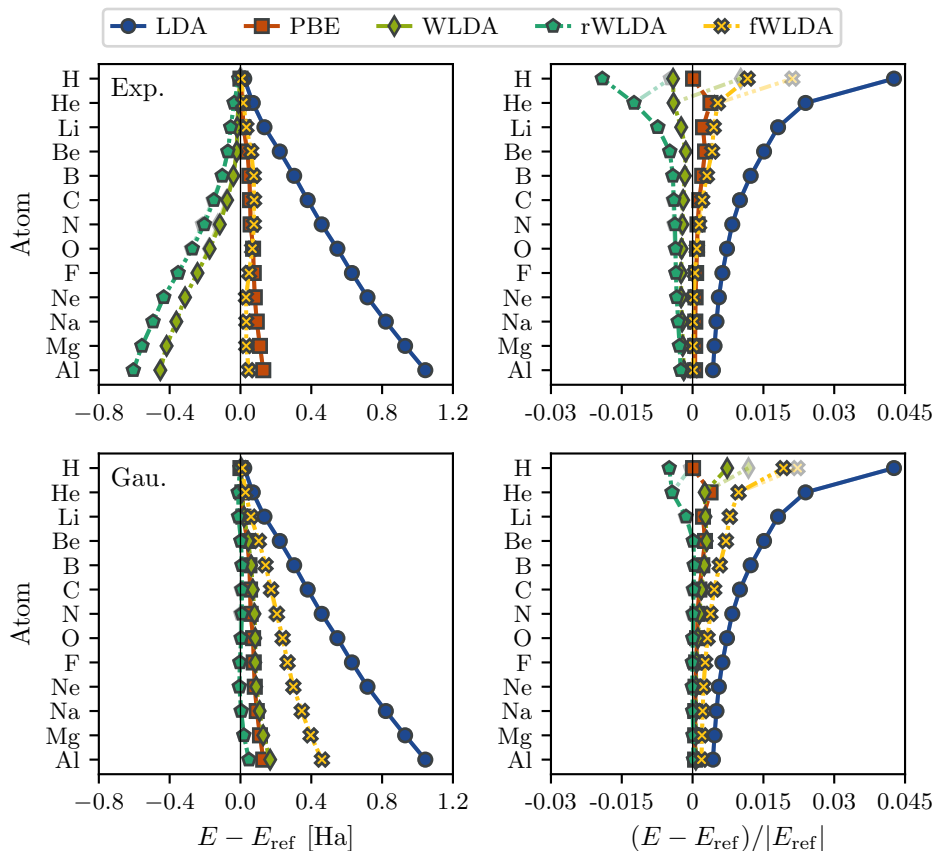
Figure 8.7: Atomic total energy differences and relative differences (left/right panels) relative to accurate references [101–103] of DFT values computed using a range of different xc functionals. The top/bottom panels show results of the WLDA flavors evaluated using the exponential and gaussian weight functions respectively, see Equation (8.24). Opaque and translucent markers indicate results using the *Hartree correction as exchange* and *Spin-neutral Hartree correction* options respectively.

electron density. For the PBE as well as all the WLDA flavors, the atomic total energies are reduced in comparison with LDA, resulting also in a decreased absolute error. Comparing the different WLDA flavors, the fWLDA always yields the smallest correction to the LDA, followed by the WLDA, whereas the largest correction is realized by the rWLDA. Using the picture of "excess localization charges" and "localization charge deficits", it is easy to understand why. As the effective density scheme replaces the Hxc energy with that of a locally more dilute electron gas for the "excess localization charges" and "localization charge deficits" alike, the Hartree correction will decrease the effective electron-electron repulsion, whereas the exchange and correlation corrections will increase it. In comparison to the full WLDA correction, the rWLDA

decreases the energy as a result, because some of the repulsive xc correction is removed. Similarly, the fWLDA increases the total energy in comparison with rWLDA because some of the attractive Hartree correction is removed. Because the entire WLDA Hxc correction consistently decreases the total energy of individual atoms, we may therefore conclude that the attractive Hartree correction dominates the repulsive xc correction, resulting in a functional that yields a consistent compensation to electron localization in comparison with the LDA!

In Figure 8.7, we also observe that the exponential weight function consistently yields a larger energy correction to the LDA than it is the case using the gaussian weight function. This means that the overall bias with respect to the accurate reference is highly weight function dependent. However, for all the functional flavors, at least one of the weight functions investigated yields an overall bias that is comparable to or better than that of the PBE. In principle, we could optimize the weight functional form and width to minimize the atomic energy bias, but that we are able to match the performance of PBE without any fine tuning, is itself a remarkable result.

As a final note on the atomic energy benchmark, it seems that the choice of spin-polarizational dependence of the WLDA Hartree correction is significant only for the hydrogen atom. As a result, it does not seem appropriate to draw any conclusions in this regard based on atomic total energies.

8.5.2 Atomization energies

Converging the atomization energies of molecules using a grid based representation of the true and effective densities is quite a considerable computational challenge due to the memory constraints of the hardware. For the purpose of this thesis, we make an effort to converge the atomization energies to within 1 kcal/mol. In order to achieve as densely a sampled grid as possible, we choose as small a cell as possible (7.5 Å) while staying comfortably within the precision target. The small cell allows us to increase the plane wave cutoff of the calculations up to 4000 eV.

To investigate the convergence with plane wave cutoff (which determines the grid density), we have computed the WLDA atomization energies up to a cutoff of 4000 eV for the seven simple molecules that we will later benchmark. Generally speaking, the molecules fall into three categories, which are illustrated in Figure 8.8, represented by the H_2, H_2O and HF molecules respectively. The three categories are the following: (1) The H_2 molecule is easy to converge and plane wave cutoffs as small as 500 eV seem to work just fine. (2) The H_2O, CO, O_2 and N_2 molecules are challenging to converge, but a 1 kcal/mol precision is achievable with considerable effort, that is, using cutoffs in the range of 1600-2400 eV depending on the system. (3) For the HF and F_2 molecules, we are not able to fully quantify the WLDA atomization energy, as they are only approaching convergence (but not reaching convergence) at 4000 eV. Instead, a reduced precision of 1-3 kcal/mol may be assumed for these molecules. The plane wave convergence data not illustrated in Figure 8.8 can be found in Appendix B, Section B.1.

Using a 4000 eV plane wave cutoff for the remainder of the WLDA correction calcula-
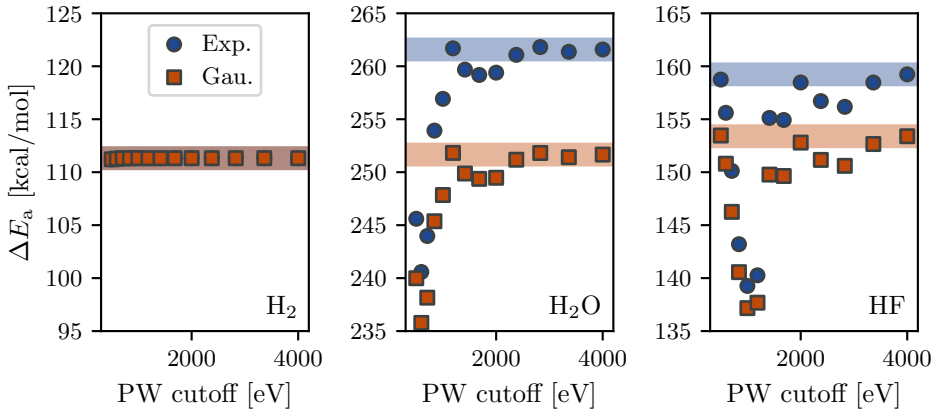
Figure 8.8: WLDA atomization energies of the H$_2$, H$_2$O and HF molecules as a function of the plane wave cutoff, calculated with the exponential and gaussian weight functions, taking the *Hartree correction as exchange*. For reference, a ±1 kcal/mol precision range is shown, centered at the 4000 eV value.

tions, we now present an atomization energy benchmark of the different WLDA flavors. We list the atomization energies calculated for the seven simple molecules in Tables 8.1 and 8.2, where they are compared to the corresponding LDA and PBE values as well as experimental references. LDA is well-known for overestimating binding energies, which is also the case for all the molecules reported here. PBE then achieves a consistent decrease of the atomization energies, yielding an overall improved performance.

	LDA	PBE	WLDA@Exp.	rWLDA@Exp.	fWLDA@Exp.	Expt.
CO	301	281	272 (266)	268 (262)	281 (277)	259
F$_2$	78.3	66	37.2 (35.8)	38.8 (37.4)	50.8 (49.9)	38.4
H$_2$	113	104	111 (120)	113 (122)	112 (118)	110
H$_2$O	268	243	262 (268)	256 (262)	264 (268)	233
HF	162	148	159 (163)	156 (160)	160 (163)	141
N$_2$	267	243	242 (228)	237 (224)	250 (241)	228
O$_2$	179	161	136 (129)	134 (127)	150 (145)	120
ME	34	17	13 (11)	10 (9.2)	20 (19)	
MAE	34	18	13 (12)	10 (11)	20 (19)	
MARE	0.31	0.19	0.076 (0.081)	0.062 (0.07)	0.15 (0.14)	

Table 8.1: Atomization energies in kcal/mol calculated with a range of different xc functionals and compared to experimental references taken from a previous benchmark study [57] of the G2/97 data set. The WLDA corrections are calculated using the exponential weight function. Numbers in parentheses relies on the *Spin-neutral Hartree correction*, otherwise the *Hartree correction as exchange* option is used.

	LDA	PBE	WLDA@Gau.	rWLDA@Gau.	fWLDA@Gau.	Expt.
CO	301	281	271 (267)	267 (264)	281 (278)	259
F$_2$	78.3	66	46 (45.6)	47.3 (46.9)	56.7 (56.5)	38.4
H$_2$	113	104	111 (114)	113 (116)	112 (114)	110
H$_2$O	268	243	252 (253)	247 (249)	257 (258)	233
HF	162	148	153 (155)	151 (152)	156 (157)	141
N$_2$	267	243	241 (231)	237 (227)	249 (243)	228
O$_2$	179	161	142 (138)	140 (136)	154 (151)	120
ME	34	17	12 (11)	10 (8.7)	20 (18)	
MAE	34	18	12 (11)	10 (9)	20 (18)	
MARE	0.31	0.19	0.094 (0.086)	0.089 (0.082)	0.17 (0.16)	

Table 8.2: Atomization energies in kcal/mol calculated with a range of different xc functionals and compared to experimental references taken from a previous benchmark study [57] of the G2/97 data set. The WLDA corrections are calculated using the gaussian weight function. Numbers in parentheses relies on the *Spin-neutral Hartree correction*, otherwise the *Hartree correction as exchange* option is used.

Likewise, we also achieve a consistent decrease of the atomization energies using the WLDA functional flavors with the *Hartree correction as exchange*. However, in a few cases the atomization energy increases in comparison with the LDA using the *Spin-neutral Hartree correction*. This only happens for molecules containing hydrogen, e.g. H$_2$, and is likely due to an overestimation of the hydrogen atomic energy, see Figure 8.7. Still, we achieve a consistent increase in performance among all the WLDA flavors, although there remains a tendency to overbind the molecules, as it is the case with PBE. Similar to the atomic total energies, the largest correction to the LDA atomization energies is generally realized by the rWLDA flavor, followed by the WLDA and fWLDA. On the contrary to the atomic total energies however, the choice of weight functional form seems less important on this data set. Of course, the performance on a data set of seven molecules is not enough to draw any definite conclusions, but the fact that the WLDA flavors are able to compete and in some cases outperform the PBE, before any considerable fine tuning of the weight functions, is incredibly encouraging for the GWLDA framework.

In order to get an impression of the performance of WLDA flavors on a larger data set, we have computed the atomization energies on most of the G2/97 data set using the PAW pseudo density, which is smoother than the all-electron density and therefore much easier to converge. The data is reported in Appendix B, Section B.2. Generally speaking, the trends reported for the seven simple molecules persist in the larger data set, however the relative performance of the *Hartree correction as exchange* and *Spin-neutral Hartree correction* options seems to depend significantly on the choice of weight function. Because many of the G2/97 molecules include hydrogen, there is a risk that conclusions in this regard may be biased and generalize only to organic chemistry, and not inorganic chemistry. Using the pseudo density, the rWLDA flavor seems to match well the performance of PBE, both for the seven simple molecules and in the larger data set of 141 molecules. When comparing the pseudo and all-electron density results

of individual molecules, we see that the atomization energy is always overestimated when using the pseudo density. This is of course natural, as the pseudo density is smooth already before applying the weighting procedure to obtain the effective density. All in all, we therefore expect the rWLDA, or one of the other flavors, to consistently outperform the PBE with regards to atomization energies, not only for the seven simple molecules, but also on the entire G2/97 data set. However, to test this hypothesis, we need a scalable all-electron implementation of the WLDA correction.

8.6   Conclusions and outlook

In this work, we have shown that there does indeed exist ways of improving the accuracy of the LDA functional based on the homogeneous electron gas, before moving on to include density gradient corrections and kinetic energy density corrections. In this sense, we propose the existence of an alternative Jacob's ladder of DFT, where the rungs following the LDA do not belong to the GGA and meta-GGA semi-local functionals, but rather a new class of nonlocal functionals that seek to improve on the ALDA kernel for the HEG, before moving on to consider the atomic limit.

Using a weighted density scheme, we have developed the GWLDA class of functionals specifically to truncate the HEG Hxc kernel in reciprocal space in order to improve the description of the HEG coupling-constant averaged correlation hole. Not only do the developed kernels approach an accurate description of the HEG correlation hole, we have also shown that the corresponding xc energy functionals consistently improve the LDA performance in the atomic limit, in some cases even outperforming the PBE.

However, to appropriately validate the performance of the WLDA for a wider variety of systems, further method development is needed. We need to go beyond a brute force evaluation of the true and effective densities on a regular real-space grid, and instead implement a more tractable density representation, possibly relying on the PAW method. This could pave the way for benchmarks of e.g. lattice constants, cohesive energies, band gaps, noncovalent interactions and exchange splittings. One may also test the GWLDA functionals and kernels for the purpose of evaluating total energies using the ACFD framework, performing real-time propagation TDDFT or to compute quasi-particle dispersion relations for plasmons and magnons.

One of the great advantages of the GWLDA framework is, that the functional forms are simple and easy to interpret, yielding also an accessible way of fine tuning the functionals in terms of the weight function $\phi(r, n)$. In this regard, we see two possible routes for the framework: (1) That of a universal WLDA functional, fulfilling as many exact constraints as possible. (2) That of an optimized WLDA functional, minimizing the error on a set of scientifically relevant material properties. In terms of the first route, one could e.g. make an effort to normalize the WLDA exchange-correlation hole, find a functional form without a leaky xc potential and consider the correlation hole of the spin-polarized homogeneous electron gas in addition to the spin-paired. With a universal WLDA functional in hand one may also try to add density gradient corrections and kinetic energy density corrections to the functional in order to further climb the ladder towards chemical accuracy.

CHAPTER 9

Atomic simulation recipes

The final contribution to the present thesis relates to the continuous effort of the CAMD section to develop community open-source Python software providing accurate, modular and scalable computer implementations of electronic structure methods and workflows. As a part of this effort, we have developed the "Atomic Simulation Recipes" (ASR) library, which is documented in Publication [D]. The ASR framework aims at providing the user with a range of flexible easy-to-implement tools that can help integrate individual computational steps seamlessly into a larger computational workflow, while automatically providing a long range of useful functionality such as caching and data provenance without any noteworthy developmental overhead.

Once more, we will rely on the publication itself to present the details of the work and in the main text only highlight some of the major benefits of the ASR framework with respect to the present project scope. In particular, the computational workflow behind a magnon spectrum calculation is outlined, and it is illustrated how the magnon workflow can be integrated into the ASR framework, simply by decorating separate Python functional calls to the GPAW electronic structure code with a Python function wrapper. This automatically provides the magnon workflow with a caching mechanism, logging of metadata for data provenance, a command-line interface (CLI) as well as automatic packaging of the data in form of an interactive database that can be shared and reused according to the FAIR Data Principles [104].

9.1 Publication D: Atomic Simulation Recipes – A Python framework and library for automated workflows

The ASR framework has been designed and developed with two major objectives in mind: (1) To provide the necessary computational infrastructure to streamline high-throughput screening studies (in particular the computational 2D materials database project [105, 106]). (2) To provide an attractive framework in which the property specific expertise of individual researchers can be collected into a library of easy-to-use material simulation recipes.

By providing a common framework for computational material property recipes, individual researchers can bundle their expert-level insights regarding the computation of a specific material property into a recipe, such that other researchers without much domain specific experience can compute the same property in an effective, accurate and

robust way. With such a library of recipes, high-throughput studies as well as in-depth material research can leverage the build-up cohort experience of many individual researchers to perform the electronic structure calculations in a reliable and reproducible way. Furthermore, the conduction of a high-throughput study then simplifies to the design of a combined Python workflow script for the evaluation of a number of material property recipes, running the workflow at one or several super-computing facilities, before collecting the generated material data into an ASR database. It should be mentioned, that the ASR does not in itself perform workflow management at the scheduler level of a super-computing cluster. Instead, ASR is designed to integrate with the MyQueue scheduler front-end and task based workflow manager [107].

9.1.1   Structure of a recipe

In the ASR framework, a Recipe is simply a Python script that includes a number of Python functions, one of which composes the `main` function which is executed when running the script. For any modular Python code, all tasks can essentially be formulated in terms of such a script. In particular, this is the case for all material simulation tasks, which can be performed by using an Atomic Simulation Environment (ASE) [108] `Calculator` object with a given electronic structure code. Over the years, plenty of such first principles calculation scripts have been developed, and with ASR it should be as simple as possible to convert a polished Python script into an ASR Recipe, which then wraps the script in a common ASR interface as well as caching functionality, logging of metadata and so forth. In order to do so, we ask the developer to conform to a set of simple design rules and principles, hopefully without imposing any fundamental constraints in terms of scripting flexibility.

We ask the developer to think about a Recipe as a list of Instructions that needs to be followed in order to produce a specific material property. Each simulation task which takes a well-defined set of inputs and produces a result with stand-alone value, should be written as its own separate Python function. By decorating the function with a Python function wrapper supplied by the ASR library, the function becomes an ASR Instruction. Once an ASR Instruction, the function can be evaluated through the CLI and is wrapped in a caching layer, meaning that if the same Instruction is called multiple times with the same inputs, only the first call triggers an actual evaluation of the function. The result produced by the first call to the Instruction is stored in the cache as an ASR `Record` (including a long list of metadata), which is then read and returned at all subsequent calls of the Instruction with exactly the same inputs. The `main` Instruction of a Recipe will then typically call a list of other Instructions (its dependencies) to provide the necessary ingredients that it needs in order to calculate a certain material property. At the most basic level of ASR, this is all the development needed in order to produce a Recipe: Divide separate tasks into separate Python functions, wrap them in an ASR decorator and combine their results in a `main` function, producing the desired material property. At this point, the reader will likely benefit from consulting Figure 2 of Publication [D], which can be found on page 147 of the thesis.

9.1.2   Constructing a magnons recipe

To give a concrete example of the ASR Recipe structure, we present here the computational steps needed in order to compute the transverse magnetic susceptibility in the GPAW code. It should be mentioned that an actual `asr.magnons` recipe has not yet been added to the ASR Recipe library. Instead, the calculations conducted in the work leading to this thesis have utilized an early prototype of the ASR code. This is mostly due to the fact that the first stable version of the ASR software package has yet to be released.

For the `magnons` Recipe, it is assumed that an ASE `Atoms` object characterizing the material in question has been prepared and written as a structure file in a specific directory. The written `Atoms` object should also contain a list of initial magnetic moments for each atom corresponding to the magnetic ground state of the system. Computing the magnon spectrum then consists of the following Recipe Instructions:

1. `gs` (ground state). Compute the self-consistent ground state density and magnetization of the material. Important input parameters: k-point grid and xc functional (LSDA or LSDA+U with a specific value for U).

2. `es` (excited states). Converge additional unoccupied Kohn-Sham orbitals. Important input parameters: Number of empty-shell bands. Dependencies: `gs`.

3. `qpoints`. Generate a list of all wave vectors **q** that are commensurate with the ground state k-point grid along a specific high-symmetry path. Important input parameters: High-symmetry path. Dependencies: `gs`.

4. `tms`. Compute the transverse magnetic susceptibility at a given wave vector **q**. Important input parameters: Plane wave cutoff, broadening parameter η, frequency grid, q-id on the high-symmetry path and xc kernel (ALDA or λALDA+U). Dependencies: `es` and `qpoints`.

Here, the `tms` Instruction represents the main function of the Recipe, which is directly executed when the Recipe is called from the CLI. In addition to the dedicated `tms` input parameters, it also takes as input the parameters of all its dependencies (and the dependencies of its dependencies and so on...). When the `tms` Instruction is called to compute the transverse magnetic susceptibility, it calls first the `es` Instruction to provide the LR-TDDFT calculation with the necessary ground state DFT ingredients. The `es` then calls the `gs` recipe to compute the ground state density and magnetization, before the `es` Python function itself converges the extra unoccupied bands and returns the full set of Kohn-Sham single-particle eigenstates to the `tms` Instruction. When the `qpoints` Instruction is called next, the `gs` Instruction has already been called once and the existing `gs` result is simply returned from the cache so that the `qpoints` Instruction can find wave vectors that are commensurate with the `gs` k-point grid. Lastly, the `tms` functionality computes the transverse magnetic susceptibility at the given wave vector **q**. When running the `tms` Recipe at a later time using a different wave vector **q** or a different frequency sampling, the `gs`, `es` and `qpoints` Instructions will be called once more, but as the results already exist in the cache, no further computations are needed.

In the `tms` Recipe outlined above, one may wonder why the `gs` and `es` instructions are separated. This is done in order to make the library of Instructions as flexible as possible. As an example, a band structure Recipe or a projected density of states Recipe might not benefit from the calculation of any additional unoccupied Kohn-Sham orbitals, meaning that they will want to call only the `gs` Instruction. Furthermore, if one needs to conduct a convergence analysis for the number of empty shell bands included in the `tms` calculation, but at a fixed k-point density, only the `gs` result can be directly reused from the cache in all calculations. For this reason, the `gs` computational step is said to have stand-alone value and should be its own Instruction in the ASR framework.

Atomic Simulation Recipes – A Python framework and library for automated workflows

Morten Gjerding [*], Thorbjørn Skovhus, Asbjørn Rasmussen, Fabian Bertoldo, Ask Hjorth Larsen, Jens Jørgen Mortensen, Kristian Sommer Thygesen

Computational Atomic-scale Materials Design (CAMD), Department of Physics, Technical University of Denmark, 2800 Kgs. Lyngby, Denmark

ABSTRACT

The Atomic Simulation Recipes (ASR) is an open source Python framework for working with atomistic materials simulations in an efficient and sustainable way that is ideally suited for high-throughput projects. Central to ASR is the concept of a Recipe: a high-level Python script that performs a well defined simulation task robustly and accurately while keeping track of the data provenance. The ASR leverages the functionality of the Atomic Simulation Environment (ASE) to interface with external simulation codes and attain a high abstraction level. We provide a library of Recipes for common simulation tasks employing density functional theory and many-body perturbation schemes. These Recipes utilize the GPAW electronic structure code, but may be adapted to other simulation codes with an ASE interface. Being independent objects with automatic data provenance control, Recipes can be freely combined through Python scripting giving maximal freedom for users to build advanced workflows. ASR also implements a command line interface that can be used to run Recipes and inspect results. The ASR Migration module helps users maintain their data while the Database and App modules makes it possible to create local databases and present them as customized web pages.

1. Introduction

As computing power continues to increase and the era of exascale approaches, the development of software solutions capable of exploiting the immense computational resources becomes a key challenge for the scientific community. In the field of materials science, ab initio electronic structure (aiES) calculations are increasingly being conducted in a high-throughput fashion to screen thousands of materials for various applications [1–16] and to generate large reference data sets for training machine learning algorithms to predict fundamental materials properties [17–22] or design interatomic potentials [23–26]. The results from such aiES high-throughput calculations are often stored in open databases allowing the data to be efficiently shared and deployed beyond the original purpose [27–37].

While a few thousands of calculations can be managed manually, a paradigm in which data drives scientific discovery calls for dedicated workflow solutions that automatically submit and retrieve the calculations, store the results in organized data structures, and keep track of the origin, history and dependencies of all data, i.e. the data provenance. Ideally, the workflow should also attach explanatory descriptions to the data that allows them to be easily accessed, understood, and deployed – also by users with limited domain knowledge.

Materials scientists from the aiES community are employing a large and heterogeneous set of simulation codes based mainly on density functional theory (DFT) [38]. These codes differ substantially in the way they implement and solve the fundamental physical equations. This is due to the fact that different types of problems require different numerical approaches, e.g. high accuracy vs. large system sizes, periodic vs. finite vs. open boundary conditions, or ground state vs. excited state properties. In principle, the large pool of available aiES codes provides users with a great deal of flexibility and freedom to pick the code that best suits the problem at hand. In practice, however, the varying numerical implementations and the diverse and often rudimentary user interfaces make it challenging for users to switch between the different aiES codes leading to a significant "code barrier".

To some extent, a similar situation exists with respect to materials properties. Although aiES codes provide access to a rich variety of physical and chemical properties, individual researchers often focus on properties within a specific scientific domain. While this may be sufficient in many cases, several important contemporary problems

addressed by the aiES community are multi-physical in nature and require properties and insights from several domains. For example, evaluating the potential of a material as a photocatalyst involves an assessment of solar light absorption, charge transport, and chemical reactions at a solid–liquid interface. Calculating new types of properties for the first time is often a time-consuming process involving trial and error and the acquisition of technical, implementation-specific knowledge of no direct benefit for the user or the overall project aim. This situation may result in a "property barrier" that hampers researchers' exploitation of the full capacity of aiES codes.

In this paper, we introduce The Atomic Simulation Recipes (ASR) – a highly flexible Python framework for developing and working with computational materials workflows. The ASR reduces code and property barriers and makes it easy to perform high-throughput computations with advanced workflows while adhering to the FAIR Data Principles [39]. There are already some workflow solutions available in the field, some of the most prominent being AFlow [30], Fireworks [40], AiiDA [41], and Atomate [42]. However, these are either designed for one specific simulation code and/or constitute rather colossal integrated entities, the complexity of which could represent an entry barrier to some users. The ASR differs from the existing solutions in several important ways, and we expect it to appeal to a large crowd of computational researchers, e.g. those with Python experience who like to develop their own personalized (workflow) scripts and databases, less experienced users who prefer plug-and-play solutions, and those who wish to apply non-standard methodologies, e.g. compute GW band structures or Raman spectra, but feel they lack the expertise required for using standard low-level codes.

The basic philosophy of ASR is to prioritize usability and simplicity over system perfection. More specifically, ASR is characterized by the following qualities:

- **Flexibility:** The Python scripting interface and high degree of modularity provide users with almost unlimited freedom for developing and deploying workflows.
- **Modularity:** The key components of ASR, namely the workflow development framework (ASR core), the Database and App modules, the task scheduler (MyQueue), and the simulation codes, are separate independent entities. Moreover, the Recipe library concept supports modular workflow designs and reuse of code.
- **Data locality:** Generated data is stored in a special folder named `.asr` where it can be accessed transparently via command line tools (similar to Git).
- **Compatibility:** For compatibility with external simulation codes, the ASR core is fully simulation code-independent while specific Recipe implementations communicate with simulation codes via the abstract ASE Calculator interface.
- **Minimalism and pragmatism:** ASR is based on simple solutions that work efficiently in practice. This makes ASR fast to learn, easy to use, and relatively uncomplicated to adapt to future demands.

At the core of ASR is the concept of a *Recipe*. In essence, a Recipe is a piece of code that can perform a certain simulation task (e.g. relax an atomic structure, calculate a Raman spectrum, or identify covalently bonded components of a material) while recording all relevant results and metadata. The use of Recipes makes it simple to run simulations from either Python or the command line. For example,

```
$ asr run "asr.bandstructure –atoms structure.json"
```

will calculate the electronic band structure of the material `structure.json`. Subsequently, the command

```
$ asr results asr.bandstructure
```

will produce a plot of the band structure. With two additional commands, the ASR results can be inspected in a web browser, see example in Fig. 6.

In practice, Recipes are implemented as Python modules building on the Atomic Simulation Environment (ASE) [43]. Recipes conform to certain naming and structured programming conventions, making them largely self-documenting and easy to read. To keep track of data provenance, Recipes utilize a caching mechanism that automatically logs all exchange of data with the user and other Recipes in a uniquely identifiable `Record` object. Not only does this guarantee the documentation and reproducibility of the results, it also allows ASR to determine whether a given Recipe task has already been performed (such that its result can be directly loaded and returned) and to detect if a Recipe task needs to be rerun because another piece of data in its dependency chain has changed. In addition, Recipes implement presentation and explanatory descriptions of their outputs and may also define a web panel for online presentation.

The Recipes of the current ASR library cover a variety of computational tasks and properties (see Table 1). Most of the 40+ available Recipes utilize DFT. However, some Recipes do not involve calls to a simulation code (e.g. symmetry analysis or construction of phase diagrams) while others employ beyond-DFT methodology (e.g. the GW method or the Bethe–Salpeter equation). These library Recipes can be used "out of the box" or modified to fit the user's need. New Recipes may be developed straightforwardly following the documentation and large body of available examples. Recipes can be combined into complex workflows using Python scripting for maximal flexibility and compatibility with ASE and other relevant Python libraries like PymatGen [44], Spglib [45] and Phonopy [46]. The Python workflows may be executed on supercomputers using the MyQueue [47] task scheduler front-end or other similar systems.

The ASR contains a number of tools for working with the ASE database module, which makes it easy to generate and maintain local materials databases. Relying on the Recipes' web panel implementations, these databases may be straightforwardly presented in a browser allowing for easy inspection, querying, and sharing of results on a local or public network. As an example of an ASR-driven database project we refer to the Computational 2D Materials Database (C2DB) [32,48].[1]

While the core of ASR, i.e. the Recipe concept and caching system, is fully simulation code-independent, most Recipe implementations of the current library contain calls to the specific aiES code GPAW [49]. At the moment, among the Recipes calling an external simulation code, only the asr.relax and asr.stiffness Recipes generalize to all ASE calculators, which support the calculation of stresses and atomic forces. We are currently working on a generalization of the ASE Calculator interface which will decouple Recipe implementations from simulation codes. In the future, many Recipes will therefore work with multiple simulation codes.

Another on-going effort is to generalize the organization of calculated results. For example results are currently presented mainly by material. This is practical for a database which primarily associates a number of properties with each material, but not for presenting sets of results parametrized over other variables than the material. These limitations will be removed over the next releases.

The rest of this paper is organised as follows: In Section 2 we provide a general overview of the main components of ASR. Section 3 zooms in on the central Recipe concept and its caching system while Section 4 gives an overview of the currently available Recipes. In Section 5, the Database and App modules are described. Section 6 gives a brief presentation of the Computational 2D Materials Database as an example of an ASR-driven high-throughput database project and provides a few concrete examples of Recipe implementations. Section 7 describes the different user interfaces supported by ASR while Sections 8 and 9 explain how ASR manages data migration and provenance, respectively. Sections 10 and 11 cover documentation and technical specifications.

---

[1] http://c2db.fysik.dtu.dk.

Table 1

List of Recipes currently implemented in the ASR library. Most of the Recipes depend explicitly on the GPAW electronic structure code. The Recipes are grouped under thematic headings and listed in alphabetic order.

Recipe name	Description
Atomic structure	
asr.database.duplicates	Remove duplicate structures from a database
asr.database.rmsd	Root mean square distance between structures
asr.dimensionality	Dimensionality of covalently bonded substructures of a material
asr.push	Push atoms along specific phonon mode
asr.relax	Relax atomic structure
asr.setup.defects	Generate native point defects
asr.setup.displacements	Generate structures with a single displaced atom
asr.setup.magnetize	Initialize atomic magnetic moments
asr.setup.reduce	Reduce supercell to primitive cell
asr.setup.symmetrize	Symmetrize an atomic structure
asr.structureinfo	Extract structural information
Thermodynamic properties	
asr.chc	Constrained convex hull stability analysis
asr.convex_hull	Convex hull stability analysis
asr.defectformation	Formation energy of neutral point defect
asr.fere	Fitted elemental reference energies
Mechanical properties	
asr.phonopy	Phonon band structure and dynamical stability
asr.piezoelectrictensor	Piezoelectric tensor
asr.stiffness	Stiffness tensor
Electronic properties	
asr.bader	Bader charge analysis
asr.bandstructure	Kohn–Sham band structure
asr.berry	Various band topology invariants
asr.borncharges	Born effective charge tensor
asr.deformationpotentials	Deformation potentials (only for 2D)
asr.dos	Density of states
asr.emasses	Effective masses
asr.fermisurface	Fermi surface
asr.formalpolarization	Formal polarization phase
asr.gs	Electronic ground state
asr.gw	G_0W_0 quasiparticle band structure
asr.hse	HSE06 band structure
asr.pdos	Orbital projected density of states
asr.proj_bandstructure	Orbital projected Kohn–Sham band structure
Magnetic properties	
asr.exchange	Magnetic exchange coupling
asr.magnetic_anisotropy	Magnetic anisotropy
asr.magstate	Determine magnetic state
Optical properties	
asr.bse	Optical absorption from Bethe–Salpeter Equation (BSE)
asr.infraredpolarizability	Infrared polarizability (caused by vibrations)
asr.plasmafrequency	Plasma frequency (from intraband transitions)
asr.polarizability	Optical polarizability (caused by electrons)
asr.raman	Raman spectrum (first-order)
asr.shg	Second harmonics generation
asr.shift	Shift current

Finally, Section 12 summarises the paper and presents our future perspectives for ASR.

2. Overview of ASR

Fig. 1 shows a schematic overview of the main components of the ASR and their mutual dependencies. An arrow from X to Y indicates a direct dependence of Y on X, e.g. via function calls (Y calls X). The ASR modules have been divided into the ASR core modules (Cache and Recipe) and the ASR user interfaces (command-line interface, Python, Task scheduler front-end, and Apps). In addition, the ASR Database and Data migration modules contain tools for working with databases and maintaining data, respectively.

Recipes implement specific, well defined materials simulation tasks as Python modules building on the ASE [43] and other Python libraries. A Recipe integrates with a Cache module that keeps track of performed tasks and manages all relevant metadata. The Cache also allows the user

to inspect the data generated by a Recipe via the ASR command line interface (CLI) or using Python. Likewise, the Recipes may be executed directly from the CLI or called via Python scripts, the latter giving maximal flexibility and compatibility with existing Python libraries. For the purpose of high-throughput computations, advanced Python workflows combining several Recipes may be constructed and executed remotely using task scheduling systems like MyQueue [47].

The ASR Cache and Recipe modules work on a folder/file basis. This locality of data makes the ASR highly transparent for the user. The ASR Database module contains functions for converting the ASR data stored in a tree of folders into an ASE database and vice versa. The ASR App module generates web pages for online presentation, browsing and searching of the databases generated by the ASR Database module. Finally, the Data migration module provides tools for transforming data (results or metadata) to ensure backward compatibility when Recipes are updated.
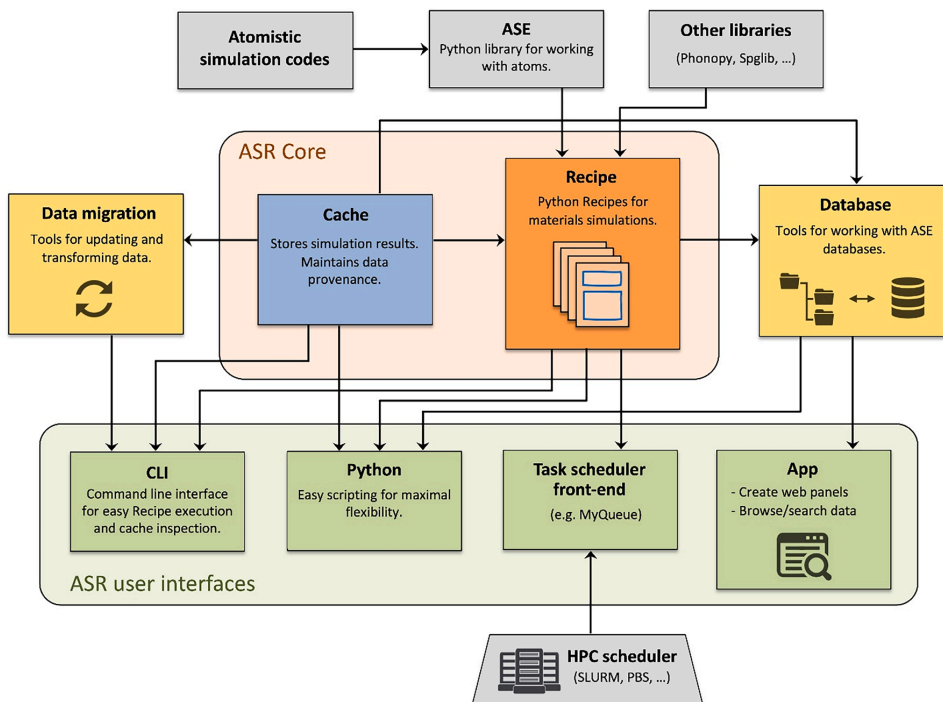
Fig. 1. Schematic overview of the main modules of the ASR and their interrelations. ASR consists of a Python library of Recipes for materials simulations and a caching system for recording of results and metadata. Recipes are envisioned to communicate with simulation codes via ASE interfaces, although most current Recipe implementations contain parts that are specific to the GPAW code. An arrow from X to Y means that Y calls X. The blue frames on the Instructions of the Recipe box symbolise a caching layer that records all data flow to/from the Recipes.

3. What is a Recipe?

A Recipe is a Python module implementing the Instructions needed to obtain a particular result, for example to relax an atomic structure, calculate an electronic band structure or a piezoelectric tensor. This section describes the structure and main components of a Recipe. A schematic overview of the Recipe concept is shown in Fig. 2.
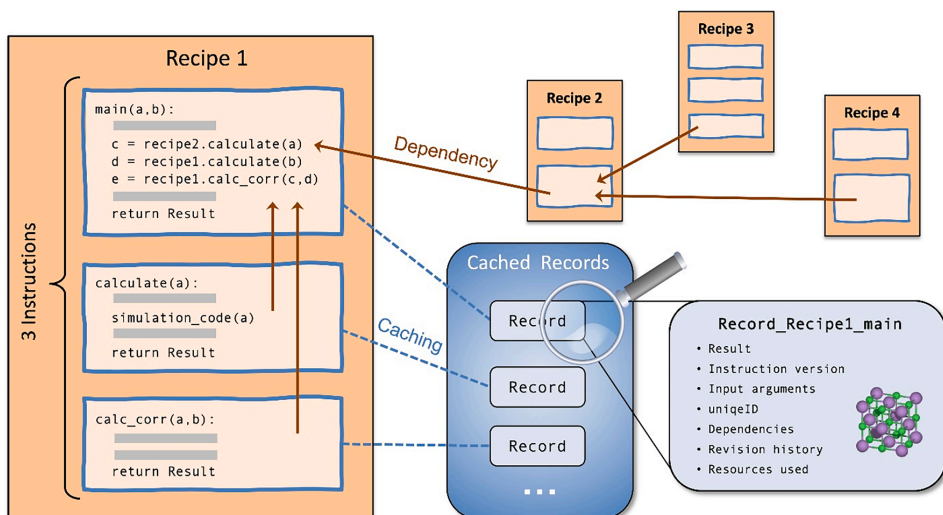
Fig. 2. A Recipe consists of a set of Instructions (see Fig. 3) implementing the computational steps needed to obtain a desired result. An Instruction may call other Instructions of the same, or separate, Recipes. An Instruction always returns a `Record` holding its result, normally represented as a `Result` data structure, together with the dependencies on other Instructions and all additional metadata required to trace back and reproduce the result.

3.1. Instruction

An Instruction is to be understood as a Python function wrapped in a caching layer provided by ASR, see Fig. 3. Whenever an Instruction is called, the caching layer intercepts the input arguments and asks the cache whether the result of the particular Instruction call already exists (cache hit) or whether there are no matching results (cache miss). If a matching result exists (because it was calculated previously), the caching layer skips the actual evaluation of the Instruction and simply reads and returns the previously calculated result. In the case of a cache miss, the Instruction is evaluated, after which the result is intercepted by the caching layer and stored together with the relevant metadata in a `Record` object. The precise content of the `Record` object and the conditions for a cache hit/miss are described in Section 3.3.

One of the great benefits of this design is its simplicity. Because the Instruction/caching layer is implemented as a simple wrapper around a Python function, usage of the caching functionality requires minimal additional knowledge. In practice, this means that working with ASR and implementing new ASR Recipes becomes really simple.

The caching system works on a per-folder basis (similar to Git): a cache is initialized by the user in a folder and any instruction evaluated within this folder or sub-folders will utilize this cache. This mimics the behaviour of the MyQueue task scheduler so as to maximize the synergy between these tools. In practice, the "one-cache-per-folder" system works well together with a "one-material-per-folder" structure. The latter is currently still a requirement for utilizing the Database functionalities described in Section 5. However, the caching system can work with several atomic structures in the same folder as the cache can distinguish ASR tasks performed on different atomic structures. Data written by ASR is encoded as `JSON`.

Any Instruction can be called directly by the user (from Python or the CLI), but special importance is given to the "main Instruction". The main Instruction usually provides the primary interface for the user to the Recipe and returns the final result of the Recipe. Other Instructions are called by the main Instruction and evaluated as needed. These may be Instructions implemented in the Recipe itself but may also be Instructions of separate Recipes. The main Instruction takes all input arguments required by the Recipe and uses them to call other Instructions.

Having multiple Instructions in a Recipe is usually motivated by code reusability or reduction of resources. The former is relevant when another Recipe needs to perform an identical Instruction (see Section on *Dependencies*). The latter is relevant when the task can be divided into Instructions with different resource requirements, in which case the separation may save computational time or resources. In particular, this is useful if a recalculation of a subset of the generated data is required.

The *input arguments* of an Instruction comprise all the information required to specify its task. When calls to an external simulation code are involved, the input arguments include a code specification, the computational parameters like *k*-point density, basis set specification, or exchange–correlation (xc) functional, as well the atomic structure.

An Instruction carries a *version number* to facilitate data migrations, i. e. transformations of the values or organisation of data produced by the Instruction. This may be required for backward compatibility when Instructions are updated, see Section 8.

3.2. Dependencies

It often happens that an Instruction can benefit from the functionality implemented by other Instructions. An example is the main Instruction of the "band structure" Recipe which calls an Instruction of the "ground state" Recipe to compute the electron density that the band structure should be based on. The caching layer logs whenever an Instruction requests data from another Instruction and uses that information to build a list of data dependencies. The data dependency list is stored in the `Record` object making it possible to trace what other pieces of data were used in the construction of the current result.

Implementation of data-dependencies in Recipes requires no extra coding. Whenever an Instruction calls another Instruction, the caching layer will *automatically* intercept the call and (1) determine if there exists a matching Record (cache hit/miss); (2) log the data dependency by registering the unique IDs and revision UIDS (see Section 8) of any dependent Records.

3.3. The `Record` object

The `Record` object is the basic data unit of ASR. It stores the results of Instructions together with metadata documenting how the results were obtained, and is used by the cache system to identify already performed Instruction calls. The `Record` object contains the following information:

- `Result` object (see Section 3.4)
- Input arguments, if relevant including
  – Atomic structure
  – Simulation code specification
  – Computational parameters
- Instruction version (see Section 8)
- External codes versions
- Randomly generated unique ID
- Dependencies (see Section 3.2)
- Revision History (see Section 8)
- Execution time and resources (number of cores)

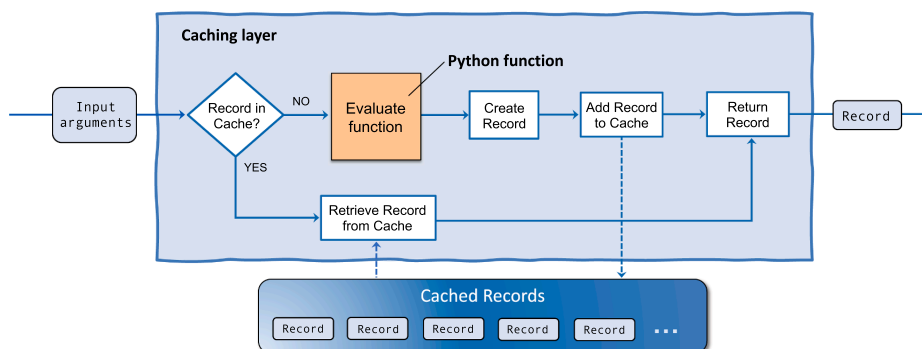**Fig. 3.** An Instruction is a Python function (orange) wrapped in a caching layer (light blue). When the function is called with a set of input arguments, the caching layer consults the cache to check if a `Record` for that exact function call already exists. In case of a cache hit, the `Record` is read and returned. In case of a cache miss, the function is evaluated and the `Record` is stored before it is returned.

To identify a cache hit/miss when evaluating an Instruction, the caching layer searches the cache for `Records` with matching Instruction name, version, and input arguments. A cache hit is then defined as the existence of a matching `Record`. A recursive comparison is used to compare input arguments with those from existing `Records` within a small numerical tolerance for floating point numbers. Any later evaluations of the Instruction with identical arguments will result in a cache hit.

3.4. The `Result` object

To store and document the result produced by a Recipe, ASR offers a `Result` object that wraps the actual result data (stored as a Python dictionary) in a simple data structure that also contains specification of the result data types along with short explanatory descriptions of the data. In addition, the `Result` object may implement methods to present itself in different formats, see below. Using the `Result` object is optional, but in practice all Instructions that return more than a simple object or value utilizes a `Result` object for improved data documentation.

3.5. Presentation of results

The `Result` object may implement presentation options of the result data in various formats, for example text to terminal, figures, and web panels. The ASR Database and App modules draw on the Recipes' web panel implementation to create web pages for presenting, browsing, and distributing databases containing collected `Result` objects, see Sections 5 and 6. This provides an efficient way of inspecting and sharing data as it is generated, which is highly practical for projects involving multiple collaborators.

3.6. General principles for Recipe development

To maintain and exploit the modular structure of ASR, the development of new Recipes should follow a few general design principles. First, the task performed by a Recipe should be well defined and clearly bounded to make it easy to use in different contexts. It should always be considered whether the Recipe could be split into smaller independent Recipes that could be useful individually. Additionally, it is encouraged that Recipes are designed/programmed so as to be as broadly applicable as possible, e.g. with respect to the type of material (structure dimensionality, chemical composition, magnetic/non-magnetic, metallic/ insulating, etc.). Any information required to define the simulation task should be included in the input argument of the Recipe, i.e. hard coding of parameters should be avoided. This should be done to ensure a flexible use and enhance the data provenance (input arguments are stored in the `Records`). Recipes should employ conservative parameter settings as default to ensure that the results are numerically well converged independent of the application, e.g. material type. Finally, in order to keep ASR Recipes simple and easy-to-read, and in order to enhance the modularity, code-extensive functionalities should be separated out into ASE functions and called from ASR whenever it is possible and sensible, i.e. when the ASE function is useful in other contexts than the specific Recipe.

4. The Recipe library

The ASR currently provides more than 40 complete Recipes allowing users to perform a broad range of materials simulation tasks ranging from construction and analysis of crystal structures over DFT calculations of thermodynamic, mechanical, electronic, magnetic, and optical properties to many-body methods for evaluating response functions, quasiparticle band structures, and collective excitations. A nonexhaustive list of available Recipes is provided in Table 1. It should be stressed that the list constitutes a snapshot of the current state of the Recipe library, which is continuously expanding. For example, we are currently developing Recipes for creating and modeling layered van der Waals structures and point defects in semiconductors.

Most of the currently implemented Recipes rely specifically on the GPAW [49] electronic structure code. As previously mentioned, we are currently working on a generalisation of the ASE Calculator interface to make the Recipes – or a large portion of them – simulation code-independent. Until then, usage of ASR with other simulation codes than GPAW is possible by porting of existing Recipes or development of new ones. The amount of work involved will depend on the type of Recipe and the state of the ASE interface for the specific simulation code.

A few specific examples of Recipe implementations are given in Section 6 where we outline the main computational steps and the final output of the `asr.bandstructure` and `asr.emasses` Recipes, respectively.

5. The ASR Database and App modules

The ASR Database and web App modules make it possible to package, inspect, share, and present ASR-driven projects easily and efficiently. The main tools and opportunities provided by these modules are described in more detail below.

5.1. Database

The ASR Database module can be used to collect `Record` objects from a directory tree into an ASE database. This is achieved by the command `asr database fromtree`. The procedure assumes a "one-material-per-folder" structure, relying on the existence of an atomic structure file in each folder to select `Records` pertaining to that atomic structure. This assumption, which is not fundamental, was chosen as a practical solution given the data layout of the computational 2D materials database. Alternative, more general solutions are being explored. The Database module proceeds to collect atomic structure-`Record` data sets and assign them to a particular row of an ASE database. We shall refer to such a database as an ASR database. Once an ASR database has been collected, it is possible to define key–value-pairs and relate property data to specific atomic structures.

The Database module also enables the reverse operation, that is, unpacking an existing ASR database to a directory tree containing `Record` objects. This is achieved by the command `asr database totree`. The function is useful when continuing a project, e.g. because existing data must be updated or new data must be added, for which the database is available but not the original directory tree. Moreover, the Database module provides tools for merging and splitting databases.

It is possible to collect a database for any number of materials/`Record` objects – even for a single material – and thereby take advantage of the App tools for presenting and inspecting results in a browser with no extra efforts. However, collecting databases is obviously most powerful in cases involving many materials/properties where the database makes it possible to search and filter the data via the defined key–value-pairs.

The easy installation of ASE through the standard PyPI Python package manager makes the ASE database format highly accessible. Furthermore, the portability of an ASE database (via several backends, e. g. SQLite, PostgreSQL, MariaDB and MySQL) enables easy packaging and distribution of data among different parties.

5.2. Web App

The ASE provides a flexible and easily extensible database web application making it possible to present and inspect the content of an ASE database in a browser. ASR leverages this ASE functionality to customize the web application layout and provide more sophisticated features such as the automatic generation of web panels, generation of figures, and documentation of the presented data by utilizing the web

panel data structures encoded in the `Result` objects. Normally a Recipe generates one web panel. However, panels gathering data from several Recipes may be created. One example of the latter is the "Summary" panel of the C2DB web pages discussed in the next section. In this case, a number of Recipes write data to a web panel data structure named "Summary" in their `Result` object. This information is stored in the database when collected. When generating the C2DB web pages from the C2DB database, the App constructs all web panels that are defined in the data pertaining to a particular material. If several Recipes have written to the same web panel, the data will be combined in an order controlled by a priority keyword written together with the web panel data.

5.2.1. Adding information fields

To enhance the accessibility of the data, it is possible to add an explanatory description to specific data entries, i.e, key–value pairs and data files, of an ASR database. These descriptions will appear as text boxes when clicking a "?"-icon placed next to the data on the web panels, see Fig. 5. General information boxes for web panels are always generated by ASR. They contain a customised field that can be manually edited, e.g. providing a short explanation of the data presented in the panel and/or links to relevant literature, and an automatically generated field listing the ASR Recipes that have produced data for the web panel and the key input parameters for the calculations. An example of such an information box is shown in Fig. 5.

5.2.2. Linking rows of databases

ASR provides functionality to create links between rows of the same, or different, ASR databases. This allows the developer to connect relevant materials when designing web panels such that the end user can move swiftly between them when browsing databases. For example, the `asr.convex_hull` Recipe creates the convex hull phase diagram of a material using an ASR reference database of stable materials (originally from the OQMD [28]), and creates a table with links to all the materials on the phase diagram. Other examples, could be to link different defective versions of the same crystalline material or different isomers of the same material/molecule.

The links are defined in `links.json` files in the folders of the relevant materials. These files may be generated manually or automatically using the Recipe `asr.database.treelinks`. When collecting the database, ASR reads the `links.json` file for each folder and stores the information in the `Data` dictionary of the corresponding row. The Recipe `asr.database.crosslinks` then creates links between rows of the collected database and rows of other databases that are given as input to the Recipe. When generating the web panels, ASR uses this information to generate hyperlinks in `HTML` format and present them in the web application for each material.

6. High-throughput example: The C2DB

In this section we present an example of what can be accomplished by the ASR in the realm of data intensive high-throughput applications, showcase some examples of ASR-generated web panels, and discuss two specific Recipe implementations.

Historically, the ASR evolved in a symbiotic relationship with the Computational 2D Materials Database (C2DB) — an extensive database project organising various properties of more than 4000 two-dimensional (2D) materials [32,48].

The C2DB distinguishes itself from existing computational databases of bulk [28–30] and low-dimensional [50,15,51] materials by the large number of physical properties available. These include convex hull diagrams, stiffness tensors, phonons (at high-symmetry points), projected density of states, electronic band structures with spin–orbit effects, effective masses, band topology indices, work functions, Fermi surfaces, plasma frequencies, magnetic anisotropies, magnetic exchange couplings, Bader charges, Born charges, infrared polarisabilities, optical

absorption spectra, Raman spectra, and second harmonics generation spectra. The use of beyond-DFT theories for excited state properties (GW band structures and BSE absorption for selected materials) and Berry-phase techniques for band topology and polarization quantities (spontaneous polarization, Born charges, piezoelectric tensors), are other unique features of the C2DB.

Building the first version of C2DB without a fully functioning workflow framework was a long and painstaking endeavour, but absolutely critical for the successful development of the ASR. Today, the entire C2DB project can be generated by a single (MyQueue) Python workflow script comprising a sequence of ASR Recipe calls and simple Python code for controlling and directing the workflow via statements like "if band_gap > 0:". Relying on the MyQueue task scheduler (see Section 7.3), generation of the C2DB is accomplished by the single command "mq workflow c2db_workflow.py tree/*/*/*/", which will submit the C2DB workflow in folders matching the pattern tree/ */*/*/. With the current C2DB workflow, this statement will launch up to 23 unique Instructions for each of the 4047 materials amounting to a total of 59822 individual aiES calculations (some Recipes like phonon and stiffness calculations launch multiple aiES calculations). When the current workflow is run with the GPAW code, about 258 calculations are unsuccessful (most often due to convergence errors in the self-consistency DFT cycle) corresponding to a success rate of 99.5%.

Apart from the data provenance control that ensures the documentation and reproducibility of the data, there are two aspects of the ASR that are particularly crucial for making high-throughput computations work efficiently in practice. First, the caching functionality ensures that Recipes which have already been performed are automatically skipped by ASR (unless something in the input for a Recipe has changed since it was last executed). This means that only a single workflow script needs to be maintained and submitted every time something has been changed, e.g., new materials have been added, the workflow script has been updated, it has been decided to rerun certain tasks with new parameters, or a Recipe has been modified. Such functionality is essential because running and maintaining high-throughput projects inevitably requires that subsets of calculations are repeated at different points in time. Secondly, the carefully designed and well tested Recipes minimise the number of unsuccessful calculations and the risk of human errors.

6.1. Recipe and web page examples

Below we present a few examples of output generated by the ASR-C2DB workflow (for a full impression we refer the reader to the C2DB website).

6.1.1. Search page

Fig. 4 shows the C2DB search page, which consists of a search/filtering section followed by a list of the database rows presented by a selected number of key–value pairs. Clicking one of the highlighted key names once (twice) will sort the rows in increasing (decreasing) order of that key. Which keys should be shown by default can be customized, but the user can always add extra keys via the "Add column" button. By default, the search page generated by the ASR App module will contain only the search field in the upper section, but additional fields or buttons may be added for easy filtering according to the most relevant parameters.

6.1.2. "Summary" panel

Fig. 5 shows the C2DB web page for monolayer MoS_2. All the web panels produced by the various Recipes of the workflow are seen, but only the "Summary" panel is unfolded. This panel is designed to provide an overview of the most basic properties of the material, and gathers data from the `Result` objects generated by the following Recipes: `asr.gs`, `asr.gw`, `asr.hse`, `asr.phonons`, `asr.magstate`, `asr.stiffness`, `asr.convex_hull` and `asr.structureinfo`.

Fig. 5 also shows the information box of the "Effective masses" web

Fig. 4. The search page of C2DB with the first few rows of the database shown below. The default web page generated by ASR includes only the top most search field, but the panel can be customized by additional fields and buttons for more convenient data filtering.

panel. It contains a short explanation of the effective mass tensor and how it is evaluated by the Recipe as well as a link to a relevant paper. The automatically generated part shows that the panel contains data generated by the `asr.emasses` Recipe. The two fields at the top of the page "Download raw data" and "Browse raw data" provide access to the entire data set comprised by all `Result` objects of the specific material entry of the database.

6.1.3. *"Band structure" Recipe*

As another example, Fig. 6 shows the "Electronic band structure" panel for monolayer CrW_3S_8 as calculated and presented by the Recipe `asr.bandstructure`. The band structure is calculated with the PBE xc-functional including spin–orbit interactions. The out-of-plane spin projections of the states is shown by the color code. The main computational steps carried out by this Recipe are:

- Perform a self-consistent ground state calculation (by calling the `calculate` Instruction of the ground state Recipe `asr.gs`) to obtain a converged electron density.
- Determine crystal symmetries and corresponding band path (uses ASE functionalities).
- Calculate the Kohn–Sham eigenvalues along the band path. For magnetic materials, this step calls the Recipe `asr.magnetic_anisotropy` to obtain the magnetic easy axis for evaluating spin projections.
- Call the main Instruction of the ground state Recipe to get the Fermi level (in 3D) or the vacuum level (in $< 3D$) for use as zero-point energy for the band structure.

In addition to these computational steps, the main Instruction of the Recipe formats two figures to present the band structure itself and the Brillouin zone with the band path and the positions of the valence band maximum (VBM) and conduction band minimum (CBM). Note that the

position of the VBM and CBM, as well as a number of other properties like the band gap and band edge energies (not shown), are determined by the Recipe `asr.gs`, which is called by `asr.bandstructure`.

6.1.4. *"Effective masses" Recipe*

Fig. 7 shows a screenshot of the "Effective masses" panel for monolayer CrW_3S_8 generated by the Recipe `asr.emasses`. The effective mass tensor is calculated with the PBE xc-functional including spin–orbit interactions. The color code represents the spin projections along the z-axis. In addition to the effective masses themselves, the Recipe evaluates a "band parabolicity" parameter defined as the mean absolute relative error (MARE) between the parabolic fit and the true bands in an energy range of 25 meV. The main computational steps carried out by this Recipe involve three subsequent k-point grid refinements; specifically:

- Perform a self-consistent ground state calculation on a uniform k-point grid (by calling the `calculate` Instruction of the Recipe `asr.gs`) to obtain a converged electron density as well as Kohn–Sham band energies.
- Locate the preliminary positions of the VBM and CBM and calculate band energies on a higher-density k-point grid around the VBM and CBM to locate the VBM and CBM positions with higher accuracy.
- Define final high-density k-point grids in the vicinity of the VBM and CBM points, and calculate band energies.
- Locate VBM and CBM and fit bands by second-order polynomial using band energies in an energy range of 1 meV from the band extremum.
- Calculate band structures for the web panel and evaluate the "parabolicity parameter".

It should be noted that even though effective mass calculations appear to be a simple task, it is surprisingly tricky to design a scheme that performs efficiently, robustly, and accurately across all types of
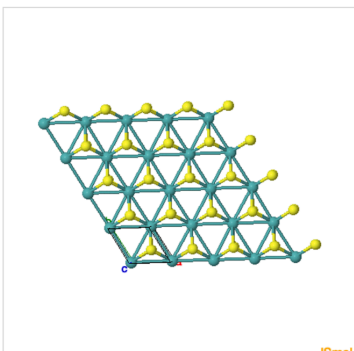
MoS₂

Download raw data ⬇   Browse raw data ▢

C2DB
The Computational 2D Materials Database

Summary

Structure info	Value
Crystal type ⓘ	AB2-187-bi
Material class ⓘ	TMDC-H
Space group ⓘ	P-6m2
Space group number ⓘ	187
Point group ⓘ	-6m2
Related ICSD id ⓘ	38401
Related COD id ⓘ	9007661
Reported DOI ⓘ	10.1103/PhysRevLett.105.136805

Stability

Thermodynamic ⓘ	HIGH
Dynamical (phonons) ⓘ	HIGH
Dynamical (stiffness) ⓘ	HIGH

Electronic properties

Magnetic ⓘ	False
Band gap (PBE) ⓘ	1.58 eV
Band gap (HSE) ⓘ	2.09 eV
Band gap (G0W0) ⓘ	2.53 eV

JSmol

Download ▾   Unit cell ▾

Axis	x (Å)	y (Å)	z (Å)	Periodic
1	3.184	0.000	0.000	True
2	-1.592	2.757	0.000	True
3	0.000	0.000	18.127	False

Lengths (Å):	3.184	3.184	18.127
Angles (°):	90.000	90.000	120.000

ⓘ Thermodynamic stability
ⓘ Stiffness tensor
ⓘ Phonons
ⓘ Basic electronic properties (PBE)
ⓘ Electronic band structure (PBE)
ⓘ Projected band structure and DOS (PBE)
ⓘ Effective masses (PBE)
ⓘ Electronic band structure (HSE)
ⓘ Electronic band structure (G0W0)
ⓘ Born charges
ⓘ Optical polarizability (RPA)
ⓘ Infrared polarizability (RPA)
ⓘ Raman spectrum
ⓘ Optical absorption (BSE and RPA)
ⓘ Bader charges
ⓘ Piezoelectric tensor

General panel information

The effective mass tensor represents the second derivative of the band energy w.r.t. wave vector at a band extremum. The effective masses of the valence bands (VB) and conduction bands (CB) are obtained as the eigenvalues of the mass tensor. The latter is determined by fitting a 2nd order polynomium to the band energies on a fine k-point mesh around the band extrema. Spin-orbit interactions are included. The "parabolicity" of the band is quantified by the mean absolute relative error (MARE) of the fit to the band energy in an energy range of 25 meV.

Relevant article(s):

- S. Haastrup et al. The Computational 2D Materials Database: high-throughput modeling and discovery of atomically thin crystals, 2D Mater. 5 042002 (2018).

Relevant recipes
This panel contains information calculated with the following ASR Recipes:

- asr.emasses

Fig. 5. Screenshot of the web page for monolayer MoS₂ from the C2DB project (only the "Summary" panel is unfolded). The panel presents data from the `Result` objects generated by the following Recipes: `asr.gs`, `asr.gw`, `asr.hse`, `asr.phonons`, `asr.magstate`, `asr.stiffness`, `asr.convex_hull`, `asr.structureinfo`.
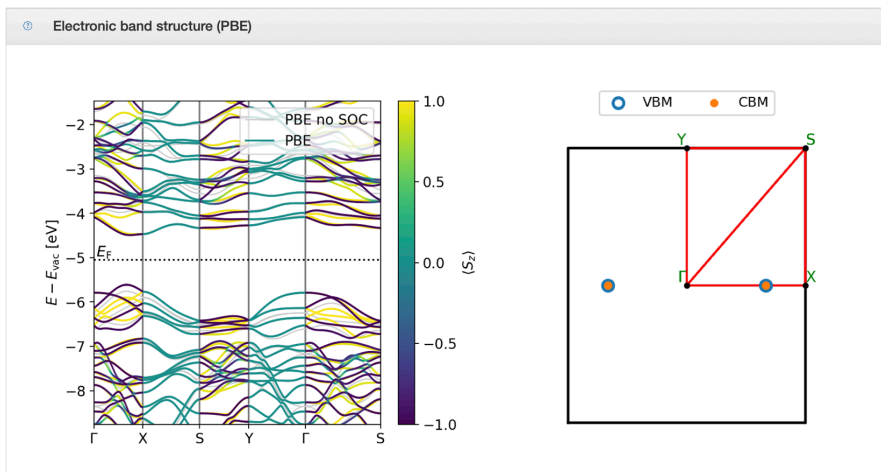
Fig. 6. Screenshot of the "Band structure" panel for monolayer CrW_3S_8 from the C2DB project. The web panel contains data computed by the `asr.band-structure` Recipe.
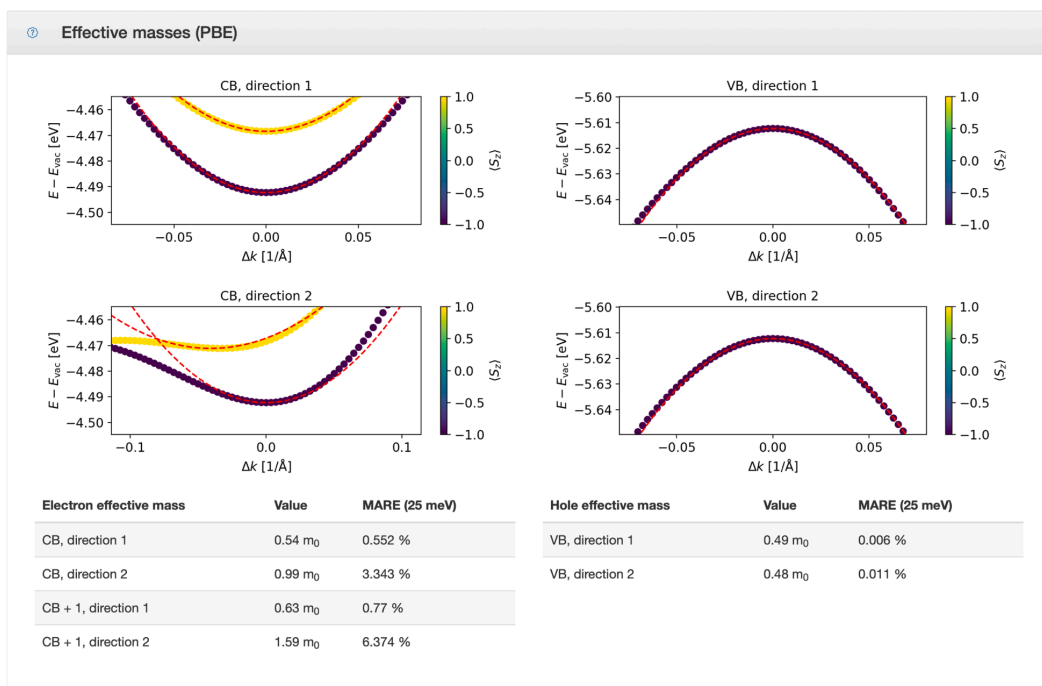

Electron effective mass	Value	MARE (25 meV)
CB, direction 1	0.54 m_0	0.552 %
CB, direction 2	0.99 m_0	3.343 %
CB + 1, direction 1	0.63 m_0	0.77 %
CB + 1, direction 2	1.59 m_0	6.374 %

Hole effective mass	Value	MARE (25 meV)
VB, direction 1	0.49 m_0	0.006 %
VB, direction 2	0.48 m_0	0.011 %

Fig. 7. Screenshot of the "Effective masses" panel for monolayer CrW_3S_8 from the C2DB project. The panel contains data computed by the `asr.emasses` Recipe.

band structures including flat bands, highly dispersive bands, highly anisotropic bands, and bands exhibiting complex spin–orbit effects like Rashba splittings.

6.1.5. General comments

In contrast to the "Summary" panel, which has been customized for the C2DB project (that is, the web panel sections of the relevant Recipes have been appropriately adjusted), the "Electronic band structure" and "Effective masses" panels are the default web panels produced by the

`asr.bandstructure` and `asr.emasses` Recipes, respectively.

The examples given here concern two-dimensional (2D) materials. However, the Recipes `asr.bandstructure` and `asr.emasses` (like all other Recipes of the current ASR library) apply also to 1D and 3D materials, as well as 0D where it is meaningful. As mentioned in Section 3.6, this kind of generality should always be strived for when designing Recipes. Achieving this may be straightforward or more involved depending on the Recipe. The Recipe for the stiffness tensor represents an easy case, where the dimensionality merely dictates the number of

axes along which the material must be strained. The Recipe for the band structure is more involved in this regard, as the determination of the band path requires separate treatments in 2D and 3D as does the determination of the spin projection axis (in 2D the out-of-plane direction is a natural choice while in 3D the magnetic easy axis is more appropriate).

7. User interfaces

The ASR can be used via four different interfaces, c.f. Fig. 1: A command line interface (CLI), a Python interface, a task scheduling front-end, and an app-based interface. Below we describe each interface in more detail.

7.1. The CLI

The CLI provides convenient commands for easy interaction with ASR via the `cache` and `run` subcommands. The `cache` subcommand allows inspection of the `Records` stored in the cache, in particular their `Result` data. For example, $ `asr cache ls name=asr.gs` will list all `Records` produced by the "ground state" Recipe. The `run` subcommand can be used to execute Recipes directly from the command line. For example, $ `asr run asr.gs` will run the *ground state* Recipe.

7.2. Python interface

The Python scripting interface allows inspection of `Records` and execution of Recipes directly from Python. This makes it possible to implement more complex logic and integrate directly with ASE and any other tools in the user's Python toolkit.

7.3. MyQueue interface

For high-throughput computations, ASR can be used in combination with a workflow manager that can handle the interaction with the scheduler of the supercomputer, such as Fireworks [40] or MyQueue [47]. The latter is a personal, decentralized, and lightweight front-end for schedulers (currently supporting SLURM, PBS, and LSF), which has been co-designed with ASR. MyQueue has a command line interface, which allows for submission of thousands of jobs in one command and provides easy-to-use tools for generating an overview of the status of jobs ('done', 'queued', 'failed' etc.). It also has a Python interface that can be used to define workflows. A Python script defines a dependency tree of *tasks* that MyQueue will submit without user involvement. The dependencies take the form: "if task X is done then submit task Y". MyQueue works directly with folders and files, which makes it transparent and easy to use. Together ASR and MyQueue provide a powerful and extremely flexible toolkit for high-throughput materials computations.

Individual Instructions of the Recipes may be defined as separate MyQueue tasks, such that computational resources can be specifically dedicated each Instruction ensuring a flexible and efficient execution of any workflow. It is, however, not a requirement to specify resources on a per Instruction basis, in which case the resources specified for the main Instruction will apply to all Instructions of the Recipe.

7.4. App interface

The App interface is a web-based read-only interface that allows the user to present and inspect the data stored in an ASE database on a local or public network. Distributing the data on a local network is convenient for larger projects and/or projects involving several users, as it allows for easy sharing and monitoring of the data as the project evolves. Once a project is finalized, the App may be used as a platform to present the data to the world via web pages. The data presentation used by the App is defined in the `Result` object of the Recipes.

8. Data maintenance

It sometimes happens that a Recipe, or one of its Instructions, has to be updated, e.g. because a bug has been detected or it has been found appropriate to store additional metadata. Such updates may imply that previously generated `Records` are no longer consistent with the current implementation of the Recipe. Depending on the nature of the change
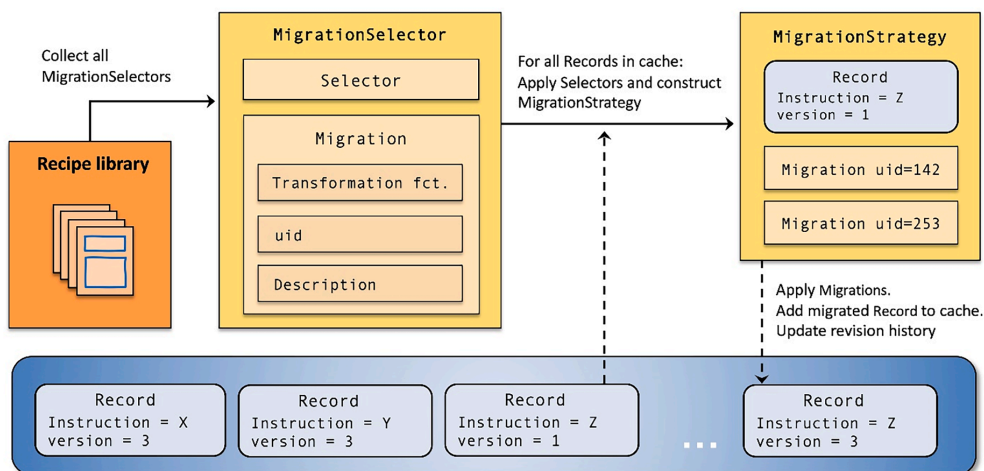
Fig. 8. To support data maintenance, ASR provides migration tools for bringing `Records` up-to-date with the latest version of the Instructions that produced them thereby avoiding recalculations whenever possible. The ASR migration procedure consists of the main steps: (1) Collect all `MigrationSelectors` from all available `Instructions`. (2) Select the migratable `Records` of the cache. (3) Determine a migration strategy (an ordered list of `Migrations`) for each migratable `Record`. (4) Apply transformation functions to migrate the `Records` and add them to the cache. (5) Update the revision history by a `Revision` object that documents the effect of the migration.

made to the Recipe, it may be possible to update the Record objects without rerunning the Recipe (data migration) or it may be necessary to rerun the entire Recipe or some of its Instructions (data regeneration).

To support the migration of data, ASR implements a simple versioning system for Instructions. An Instruction is associated with a integer version number which is stored in the Record and identifies the version of the Instruction at the time of creation. When an Instruction is changed, its version number may be increased by the developer. Since the caching layer matches the current Instruction version number against Records in the cache (see Section 3.3), older Records would no longer yield cache hits and are then said to be invalidated.

To facilitate the migration of invalidated Records, it is possible to specify Migrations that can be associated with an Instruction and thereby provide a way to bring old Records up to date. In practice, a Migration bundles a Record transformation function, a unique migration ID and a human readable description of the effect of the migration, see Fig. 8. In general, a Record transformation function induces a change to a Record. For example, this could be to convert a Record of version n to a later version $n+1$ without rerunning the Instruction, but in general the effect of the transformation could be anything. Use of transformation functions is typically possible when the update involves changes to metadata and/or data restructuring while the actual result of the Instruction is unchanged.

When a Migration is applied to a Record, a Revision object is produced. A Revision contains a randomly generated UID, the UID of the applied Migration, an explanatory description of the changes made to the Record, and an automatically generated list of the Record entries that were changed, added or deleted. The auto-generated list of changes is constructed by comparing the Record returned by the transformation function to the input Record.

Upon migration of a Record, a revision history is updated by the latest Revision and stored in the migrated Record. The revision history can be inspected by users to learn which revisions, if any, have previously been applied to a given Record.

A Selector is used to identify the Records to be migrated, e.g. based on the Instruction name and version number. The Selector is bundled together with a Migration into a MigrationSelector, which can determine whether a particular Record matches the selection criteria of the Selector. To migrate a Record, ASR searches through all Recipes to collect their MigrationSelectors (if they have any) and apply them to the Record to find a "migration strategy", i.e., which Migrations to be applied and in which order. The migration strategy is then encoded in a MigrationStrategy, which couples a particular Record to an ordered list of Migrations. The particular MigrationStrategy can then be applied to the Cache to execute the migration of the associated Record.

ASR provides a simple CLI, via asr cache migrate, to analyse existing Records in the cache, and identify migratable Records.

Whenever the asr version used in a given project is upgraded, a project participant should identify migratable Records, migrate them and then rerun the project workflow. Up-to-date Records will then be taken directly from the cache, whereas the Instructions with invalidated Records and no associated Migration, i.e. Records that the developer cannot migrate directly to the newest version, will be rerun.

In order to minimize the computational cost of bringing data up-to-date with ASR, developers are strongly advised to supply Migrations with their Recipe updates whenever possible.

To provide the best conditions for the long term deployment of ASR-generated data, the asr version of important projects should be upgraded regularly and the project workflow rerun. Obviously, this action may induce changes in the data. Whether this is acceptable or not is ultimately a strategic decision. However, for dynamic data projects, a regular version upgrade not only ensures that the data is of the highest quality, it also makes it easier for other parties to deploy the data because existing results (Records) can be reused directly with the newest version of ASR without having to rerun Recipes to bring the data

Table 2
Technical specifications.

Source code	https://gitlab.com/asr-dev/asr
Releases	https://pypi.org/project/asr/
License	GNU GPLv3 or newer (free software)
Documentation	https://asr.readthedocs.io/en/latest/

up-to-date.

9. Data provenance

Simply stated, data provenance is the documentation of the circumstances under which a piece of data came into existence. This includes how the data originally was constructed, how the data has changed over time (also known as data-lineage) and a documentation of relevant system specifications such as architecture, operating system, important system packages, executables etc. If data provenance is handled perfectly, then data will in principle be reproducible, i.e. given access to exactly the same systems and software, any piece of data can be reproduced. In a scientific context, where reproducibility is key, data provenance is naturally very important.

In ASR, the basic unit of data is the Record object, which connects the result of an Instruction with various pieces of contextual metadata, see Section 3.3. Taken together, the metadata tell the story of how the original Record came into existence (Instruction name/version and input arguments), which other Records were implicitly used for the construction of this Record (Dependencies), what external package versions were used, and how the Record has transformed over time (Revision history). For simplicity, since it would be outside the scope of ASR, system information is not stored with the Record, which, in our experience, is not practically relevant for the purposes of ASR. As such, we characterize ASR as practically, but not perfectly, data provenant.

10. Documentation

ASR itself is documented on Read the Docs. The data is documented through the Record and Result objects, see previous Section on data provenance.

11. Technical specifications

Some technical specifications are listed in Table 2. ASR can be installed via pip using the command pip install asr.

ASR requires or is normally used with the following software:

- Python libraries: ASE, numpy, matplotlib, plotly, flask, click
- Computational and workflow software: GPAW or other ASE codes, MyQueue (SLURM/PBS/LSF)
- Optional extras: spglib, phonopy, and pymatgen (for Recipes); jinja, mysql or other ASE database backends

For community support see https://asr.readthedocs.io/en/latest/src/contact.html.

12. Summary and outlook

This article has introduced The Atomic Simulation Recipes (ASR) as an open source Python framework for developing materials simulation workflows and managing the data they produce.

To facilitate the transition to a paradigm of data-intensive science, ASR was designed to support the development of materials simulation workflows that operate in accordance with the FAIR data principles, by providing tools and concepts that are general enough that they do not restrict the user whilst being concrete enough to make a real difference. The ASR achieves this through the notion of a Recipe: a general Python

script that performs a well defined simulation task and is wrapped in a caching layer that logs all relevant metadata without involving the user. This construction places essentially no restrictions on the developer's freedom to design and control the workflow, but resolves the critical and complex issue of keeping track of the data provenance. We stress that the core of ASR, i.e. the Recipe concept and the caching system, is fully simulation code independent. In particular, it is not tied to materials simulations and could potentially be useful in other areas of computational science.

Beyond the built-in data documentation, there are many benefits of using standardized, well tested, and well documented Recipes. For example, it saves time and promotes a more sustainable scripting culture by reducing the need for individual researchers to write and maintain their own personal scripts (which can be hard for other to read and are often lost when the developer leaves the group). Furthermore, it reduces the risk of human errors and lowers the barrier for researchers to undertake simulation tasks with which they have little prior experience.

The fact that Recipes are independent units with own data provenance control implies that they can be freely combined to create advanced workflows using Python scripting for maximal flexibility. Such workflows can be executed on supercomputers using a workflow management software that supports a Python interface. To this end, we have developed the MyQueue [47] task manager that works as a front-end to the most common schedulers (currently SLURM, PBS, and LSF). While MyQueue will resubmit jobs that have timed out or crashed due to lack of memory, code-related failures must be handled manually. In the future, ASR should integrate more closely with MyQueue to permit that errors from the simulation codes are automatically analysed and reacted upon. Along the same lines, an automated estimation of the HPC resources (time/memory/nodes) required by individual tasks could limit the number of failed jobs and improve the utilization of resources.

The current Recipe library already covers a wide range of materials simulation tasks and more are continuously being added. Of special importance are Recipes for advanced beyond-DFT calculations where the benefits in terms of a lowered user barrier, improved data quality, and increased utilization of computing resources, are particularly large. The Recipe concept should also be advantageous for implementation of machine learning methods that could integrate with ASR databases and "standard" Recipes to make for more intelligent and computationally efficient workflows.

The ASR makes extensive use of the Atomic Simulation Environment (ASE) as a toolkit to process atomistic calculations. In particular, ASE is used as a front-end for ASR to communicate with external simulation codes. This has the clear advantage that ASR can become decoupled from the simulation codes. This decoupling is currently not in place, and the majority of the existing Recipe implementations contain code parts that are specific to the GPAW electronic structure code. To make ASR fully simulation code-independent, the ASE Calculator interfaces must be further generalized. This includes extensions of the interfaces to access outputs of calculations as well as a systematic mechanism to control multi-step tasks. The adaptation of this interface to multiple codes will eventually require a community effort that we hope many code developers will take part in. Until then, Recipes must to some extent be code specific.

CRediT authorship contribution statement

Morten Gjerding: Conceptualization, Methodology, Software, Validation, Writing - original draft, Writing - review & editing, Visualization. **Thorbjørn Skovhus:** Conceptualization, Software, Validation, Writing - review & editing, Visualization. **Asbjørn Rasmussen:** Conceptualization, Software, Validation, Writing - review & editing. **Fabian Bertoldo:** Conceptualization, Software, Validation, Writing - review & editing. **Ask Hjorth Larsen:** Conceptualization, Software, Validation, Writing - review & editing. **Jens Jørgen Mortensen:** Conceptualization, Software, Validation, Writing - review & editing.

Kristian Sommer Thygesen: Conceptualization, Validation, Writing - original draft, Writing - review & editing, Visualization, Funding acquisition, Project administration.

Declaration of Competing Interest

The authors declare that they have no known competing financial interests or personal relationships that could have appeared to influence the work reported in this paper.

Acknowledgments

References

[1] J. Greeley, T.F. Jaramillo, J. Bonde, I. Chorkendorff, J.K. Nørskov, Nat. Mater. 5 (2006) 909–913.
[2] G.K. Madsen, J. Am. Chem. Soc. 128 (2006) 12140–12146.
[3] S. Curtarolo, et al., Nat. Mater. 12 (2013) 191–201.
[4] S. Kirklin, B. Meredig, C. Wolverton, Adv. Energy Mater. 3 (2013) 252–262.
[5] K.B. Ørnsø, J.M. Garcia-Lastra, K.S. Thygesen, Phys. Chem. Chem. Phys. 15 (2013) 19478–19486.
[6] Z. Zhang, et al., ACS Omega 4 (2019) 7822–7828.
[7] W. Chen, et al., J. Mater. Chem. C 4 (2016) 4414–4426.
[8] J. Hachmann, R. Olivares-Amaya, S. Atahan-Evrenk, C. Amador-Bedolla, R. S. Sánchez-Carrera, A. Gold-Parker, L. Vogt, A.M. Brockway, A. Aspuru-Guzik, J. Phys. Chem. Lett. 2 (2011) 2241–2251.
[9] S. Bhattacharya, G.K. Madsen, Phys. Rev. B Condens. Matter 92 (2015), 085205.
[10] I.E. Castelli, et al., Energy Environ. Sci. 5 (2012) 5814–5819.
[11] G. Hautier, A. Miglio, G. Ceder, G.M. Rignanese, X. Gonze, Nat. Commun. 4 (2013) 1–7.
[12] L. Yu, A. Zunger, Phys. Rev. Lett. 108 (2012), 068701.
[13] K. Kuhar, M. Pandey, K.S. Thygesen, K.W. Jacobsen, ACS Energy Lett. 3 (2018) 436–446.
[14] M. Aykol, S. Kim, V.I. Hegde, D. Snydacker, Z. Lu, S. Hao, S. Kirklin, D. Morgan, C. Wolverton, Nat. Commun. 7 (2016) 1–12.
[15] N. Mounet, M. Gibertini, P. Schwaller, D. Campi, A. Merkys, A. Marrazzo, T. Sohier, I.E. Castelli, A. Cepellotti, G. Pizzi, et al., Nat. Nanotechnol. 13 (2018) 246–252.
[16] L.Q. Chen, L.D. Chen, S.V. Kalinin, G. Klimeck, S.K. Kumar, J. Neugebauer, I. Terasaki, NPJ Comput. Mater. 1 (2015) 1–2.
[17] M. Rupp, A. Tkatchenko, K.R. Müller, O.A. Von Lilienfeld, Phys. Rev. Lett. 108 (2012), 058301.
[18] J. Lee, A. Seko, K. Shitara, K. Nakayama, I. Tanaka, Phys. Rev. B 93 (2016), 115104.
[19] T. Xie, J.C. Grossman, Phys. Rev. Lett. 120 (2018), 145301.
[20] L.M. Ghiringhelli, J. Vybiral, S.V. Levchenko, C. Draxl, M. Scheffler, Phys. Rev. Lett. 114 (2015) 105503.
[21] P.B. Jørgensen, E.G. del Río, M.N. Schmidt, K.W. Jacobsen, Phys. Rev. B 100 (2019) 104114.
[22] K. Ghosh, A. Stuke, M. Todorović, P.B. Jørgensen, M.N. Schmidt, A. Vehtari, P. Rinke, Adv. Sci. 6 (2019) 1801367.
[23] V.L. Deringer, G. Csányi, Phys. Rev. B 95 (2017), 094203.
[24] S. Lorenz, A. Groß, M. Scheffler, Chem. Phys. Lett. 395 (2004) 210–215.
[25] J. Behler, M. Parrinello, Phys. Rev. Lett. 98 (2007), 146401.
[26] N. Artrith, A. Urban, Comput. Mater. Sci. 114 (2016) 135–150.
[27] K.S. Thygesen, K.W. Jacobsen, Science 354 (2016) 180–181.
[28] J.E. Saal, S. Kirklin, M. Aykol, B. Meredig, C. Wolverton, JOM 65 (2013) 1501–1509.
[29] A. Jain, et al., APL Mater. 1 (2013), 011002.
[30] S. Curtarolo, W. Setyawan, G.L. Hart, M. Jahnatek, R.V. Chepulskii, R.H. Taylor, S. Wang, J. Xue, K. Yang, O. Levy, et al., Comput. Mater. Sci. 58 (2012) 218–226.
[31] C. Draxl, M. Scheffler, J. Phys.: Mater. 2 (2019), 036001.
[32] S. Haastrup, M. Strange, M. Pandey, T. Deilmann, P.S. Schmidt, N.F. Hinsche, M.N. Gjerding, D. Torelli, P.M. Larsen, A.C. Riis-Jensen, et al., 2D Mater 5 (2018) 042002.
[33] S.S. Borysov, R.M. Geilhufe, A.V. Balatsky, PloS One 12 (2017), e0171501.
[34] K.T. Winther, M.J. Hoffmann, J.R. Boes, O. Mamun, M. Bajdich, T. Bligaard, Sci. Data 6 (2019) 1–10.
[35] L. Talirz, S. Kumbhar, E. Passaro, A.V. Yakutovich, V. Granata, F. Gargiulo, M. Borelli, M. Uhrin, S.P. Huber, S. Zoupanos, et al., Sci. Data 7 (2020) 1–12.
[36] R. Armiento, Mach. Learn. Meets Quant. Phys. (2020) 377–395.
[37] L. Himanen, A. Geurts, A.S. Foster, P. Rinke, Adv. Sci. 6 (2019) 1900808.
[38] W. Kohn, L.J. Sham, Phys. Rev. 140 (1965) A1133.
[39] M.D. Wilkinson, M. Dumontier, I.J. Aalbersberg, G. Appleton, M. Axton, A. Baak, N. Blomberg, J.W. Boiten, Santos L.B. da Silva, P.E. Bourne, et al., Sci. Data 3 (2016) 1–9.

[40] A. Jain, et al., Concurr. Comput. 27 (2015) 5037–5059.
[41] G. Pizzi, A. Cepellotti, R. Sabatini, N. Marzari, B. Kozinsky, Comput. Mater. Sci. 111 (2016) 218–230.
[42] K. Mathew, J.H. Montoya, A. Faghaninia, S. Dwarakanath, M. Aykol, H. Tang, I.h. Chu, T. Smidt, B. Bocklund, M. Horton, et al., Comput. Mater. Sci. 139 (2017) 140–152.
[43] A.H. Larsen, J.J. Mortensen, J. Blomqvist, I.E. Castelli, R. Christensen, M. Dułak, J. Friis, M.N. Groves, B. Hammer, C. Hargus, et al., J. Phys.: Condens. Mat. 29 (2017), 273002.
[44] S.P. Ong, W.D. Richards, A. Jain, G. Hautier, M. Kocher, S. Cholia, D. Gunter, V. L. Chevrier, K.A. Persson, G. Ceder, Comput. Mater. Sci. 68 (2013) 314–319.

[45] A. Togo, I. Tanaka, 2018 arXiv preprint arXiv:1808.01590.
[46] A. Togo, L. Chaput, I. Tanaka, Phys. Rev. B 91 (2015), 094306.
[47] J. Mortensen, M. Gjerding, K. Thygesen, J. Open Sour. Softw. 5 (2020) 1844.
[48] M. Gjerding, et al., 2D Mater 8 (2021), 044002.
[49] J. Enkovaara, C. Rostgaard, J.J. Mortensen, J. Chen, M. Dułak, L. Ferrighi, J. Gavnholt, C. Glinsvad, V. Haikola, H. Hansen, et al., J. Phys.: Condens. Mat. 22 (2010), 253202.
[50] M. Ashton, J. Paul, S.B. Sinnott, R.G. Hennig, Phys. Rev. Lett. 118 (2017), 106101.
[51] J. Zhou, L. Shen, M.D. Costa, K.A. Persson, S.P. Ong, P. Huck, Y. Lu, X. Ma, Y. Chen, H. Tang, et al., Sci. Data 6 (2019) 1–10.

Summary

Starting from the basic Kubo theory for the generalized susceptibility, it has been shown how one-body excitations to the ground state electronic structure of real materials are accessible within the framework of linear response time-dependent density functional theory. In terms of the electronic structure, both the fundamental fluctuations of the system and the system's response to weak external perturbations can be characterized in terms of a single quantity, the four-component susceptibility tensor. Taking the spin-density functional theory as a starting point, it is shown how the susceptibility tensor can be computed in a simple procedure involving the calculation of the single-particle Kohn-Sham susceptibility and the exchange-correlation kernel, from which the many-body susceptibility is obtained through the inversion of a Dyson equation.

In particular, we have developed a computer implementation to calculate the transverse magnetic susceptibility for collinear systems in the nonrelativistic limit using the adiabatic local density approximation for the exchange-correlation kernel. The implementation makes use of a plane wave basis, which in combination with the projector augmented-wave method in principle allows us to compute the susceptibility in a given approximation without loss of generality. Through a meticulous numerical investigation of the Kohn-Sham Stoner continuum, we manage to show that the magnon dispersion in itinerant ferromagnets can be converged in terms of all relevant computational parameters, once the gap error has been appropriately corrected for. This allows us to make an accurate benchmark of the adiabatic local density approximation to the magnon dispersion in the itinerant ferromagnets Fe, Ni, Co and MnBi as well as the insulating antiferromagnet Cr_2O_3.

We show that a good correspondence with experiment is obtained for the dispersion in Fe and Co, whereas the magnon dispersivity (at least along certain directions) is overestimated by roughly a factor of two in both Ni, MnBi and Cr_2O_3. There are various reasons for this shortcoming, but they all relate to the local approximation for the exchange and correlation. In the case of MnBi, we manage to improve the description by including a Hubbard correction, but for Ni and Cr_2O_3 such a correction does not consistently improve the magnon dispersion.

Despite the shortcomings at the current level of theory, we are able to study itinerant electron effects in ferromagnets and antiferromagnets as well as investigate the potential for materials engineering via doping and strain. In particular, the developed methods have allowed us to study the magnon dispersion jumps induced by stripe-like Stoner pair features in the Kohn-Sham spectrum, the Landau damping and disappearance of magnons inside the Stoner continuum, the intense Stoner pair scattering of antiferromagnetic Cr and the appearance of a novel collective mode of excitation in

Cr which seems to elude the effect of Landau damping. In addition, we have rendered it probable that the inherent magnetic frustration of MnBi places the material on the interface of a magnetic phase transition to helical order and proposed how such a phase transition may be realized using a Cr alloy, possibly in combination with uni-axial compressive strain. We consider the latter conclusion an important achievement of theoretical magnon spectroscopy as it required a unified treatment of both strongly correlated short-range magnetic interactions as well as the long-range interactions from the itinerant electrons in the system. Furthermore, it showcases the potential for the theory to compliment experiments in terms of engineering the magnetic phases of complex quantum materials.

Concurrent with our theoretical magnon spectroscopy studies, we have also developed a new class of nonlocal functionals that rely on an effective weighted electron density to improve the description of short wavelength correlation effects in the local density approximation. We have shown that the so-called generalized weighted local density approximation facilitates functionals with a nearly accurate description of the coupling-constant averaged correlation hole of the homogeneous electron gas. Furthermore, the same approximations seem to yield consistent improvements over the local density approximation, also in the atomic limit. In particular, it seems that the functionals may outperform the generalized gradient expansion for the atomization energies of molecules.

Finally, we have presented a new Python framework, in which computational recipes for the calculation of various material properties can be easily compiled into a powerful library for high-throughput computations in particular, but also for material science in general.

Outlook

Generally speaking, theoretical magnon spectroscopy is a young field of research with a grand potential, but a high barrier of entry. By documenting the theoretical background in detail, we hope to have lowered this barrier, but even so, our computational implementation leaves plenty of potential for improvement. As proposed in the thesis, this may include an implementation of the linear tetrahedron interpolation method to facilitate a faster convergence of the single-particle Stoner continuum. Similarly, it is quite likely that plane waves provide a suboptimal basis representation for the transverse magnetic susceptibility. In the future, one may want to look towards more local basis sets, especially to enable the study of nano-structured materials such as the emerging platform of magnetic two-dimensional materials. Such a development would not just allow the treatment of larger systems, it could also bring the methodology closer to a feasible use in a high-throughput setting, maybe relying on the Atomic Simulation Recipes for the integration with a larger materials simulation workflow?

Improving the numerical efficiency of the computer implementation is one thing, another is to increase the scope of the implementation. The underlying theoretical framework does in principle generalize to noncollinear magnetic ground states, including also relativistic effects such as the spin-orbit coupling. In such an extension of the implementation, one could as an example study the coupling between magnon and plasmon quasi-particles. However, already at the current stage there are plenty of exciting possibilities for exploring new frontiers, both in terms of itinerant electronic effects, such as the optical collective mode in antiferromagnetic Cr, but also in terms of new materials. This could include a continued study of the magnetic frustration in the transition metal pnictides, and may eventually lead to a study of the fundamental magnetic fluctuations in antiferromagnetic phases of matter that appear at the interface of superconducting phase transitions.

For the weighted local density approximation, many similar considerations apply. First of all, the focus should be to develop a feasible implementation of the functional that can provide an accurate benchmark of its performance for a representative range of materials and properties. Once such an implementation is realized, one can explore a range of different functional flavors, both in the direction of universality and optimized functional performance. However, already at the current stage, one could try to investigate additional material properties which only require a minimal unit cell and therefore a fewer number of plane waves in the basis representation. One such example could be the lattice constants of elemental solids. Finally, it will be interesting to see, if the weighted local density approximation can provide a new level of accuracy for methods that currently rely on (semi-)local approximations to the kernel, such as the adiabatic connection fluctuation-dissipation framework or theoretical magnon spectroscopy.

Spherically symmetric systems and the homogeneous electron gas

In this appendix, a number of helpful identities are given for spherically symmetric and uniform systems, including definitions of the Fourier transform. This is mostly to aid the discussion of the homogeneous electron gas and the weighted local density approximation. Along with the presented identities follows also some simple derivations of key results.

A.1   Spatial Fourier transforms under spherical symmetry

Adopting the Fourier transform definitions in [A], the Fourier transform of a spherically symmetric function $f(\mathbf{r}) = f(r)$ is without loss of generality calculated by assuming $\mathbf{q} = q\,\mathbf{e}_z$:

$$
\begin{aligned}
f(q) &= \int d\mathbf{r}\, f(\mathbf{r}) e^{-iq\,\mathbf{e}_z \cdot \mathbf{r}} = 2\pi \int_0^\pi \sin\theta\, d\theta \int_0^\infty r^2 dr\, f(r) e^{-i\cos\theta\, qr} \\
&= 4\pi \int_0^\infty r^2 dr\, f(r) \frac{\sin(qr)}{qr},
\end{aligned} \tag{A.1}
$$

with the inverse transform (assuming $\mathbf{r} = r\,\mathbf{e}_z$):

$$
\begin{aligned}
f(r) &= \int \frac{d\mathbf{q}}{(2\pi)^3} f(\mathbf{q}) e^{i\mathbf{q}\cdot\mathbf{e}_z r} = \frac{1}{(2\pi)^2} \int_0^\pi \sin\theta\, d\theta \int_0^\infty q^2 dq\, f(q) e^{i\cos\theta\, qr} \\
&= \frac{1}{2\pi^2} \int_0^\infty q^2 dq\, f(q) \frac{\sin(qr)}{qr}.
\end{aligned} \tag{A.2}
$$

Furthermore, the associated integral form for the Dirac δ-function is given by [109]:

$$
\delta(q - q') = \frac{2}{\pi} \int_0^\infty dr\, \sin(qr)\sin(q'r). \tag{A.3}
$$

A.2   Correlation energy and hole for the homogeneous electron gas

In the homogeneous electron gas, all one-point functions of position are constants and two-point functions depend only on the distance between the points, for instance $\chi(\mathbf{r}, \mathbf{r}', \omega) = \chi(\mathbf{r} - \mathbf{r}', \omega) = \chi(\Delta r, \omega)$. The correlation energy per electron, $\epsilon_c(n)$, may be calculated from Equation (7.40) by carrying out the frequency integration along the imaginary frequency axis [40]:

$$E_c(n) = \int d\mathbf{r}\, \epsilon_c(n) n$$
$$= -\frac{\hbar}{2\pi} \int d\mathbf{r} \left(\int d\mathbf{r}'\, v_c(\mathbf{r} - \mathbf{r}') \int_0^1 d\lambda \int_0^\infty du\, [\chi_\lambda(\mathbf{r} - \mathbf{r}', iu) - \chi_0(\mathbf{r} - \mathbf{r}', iu)] \right). \tag{A.4}$$

By inserting the inverse Fourier transform (A.2) for $v_c(r)$, $\chi_0(r, iu)$ and $\chi_\lambda(r, iu)$ respectively, the Dirac δ-function (A.3) is identified, yielding a diagonal expression for $\epsilon_c(n)$, also in reciprocal space:

$$\epsilon_c(n) = -\frac{2\hbar}{n} \int_0^\infty r^2 dr\, v_c(r) \int_0^1 d\lambda \int_0^\infty du\, [\chi_\lambda(r, iu) - \chi_0(r, iu)]$$
$$= -\frac{\hbar}{\pi^2 n} \int_0^\infty \frac{q^2}{4\pi} dq\, v_c(q) \int_0^1 d\lambda \int_0^\infty du\, [\chi_\lambda(q, iu) - \chi_0(q, iu)]. \tag{A.5}$$

Taking similar steps, one may start from Equation (7.47) and write the correlation energy per electron in terms of the reciprocal space representation of the coupling-constant averaged correlation hole:

$$\epsilon_c(n) = 2\pi n \int_0^\infty r^2 dr\, v_c(r) \bar{g}_c(r) = \frac{n}{\pi} \int_0^\infty \frac{q^2}{4\pi} dq\, v_c(q) \bar{g}_c(q). \tag{A.6}$$

Comparison with Equation (A.5) then yields a simple expression for the coupling-constant averaged correlation hole of the homogeneous electron gas:

$$\bar{g}_c(q) = -\frac{\hbar}{\pi n^2} \int_0^1 d\lambda \int_0^\infty du\, [\chi_\lambda(q, iu) - \chi_0(q, iu)]. \tag{A.7}$$

A.3   Effective density of the hydrogen atom

In the hydrogen atom, the true electron density is spherically symmetric,

$$n_{1s}(r) = \frac{1}{\pi a_0^3} e^{-2r/a_0}, \tag{A.8}$$

meaning that we may evaluate the effective density (8.4) without loss of generality, by assuming that $\mathbf{r} = r\mathbf{e}_z$. The distance $|\mathbf{r} - \mathbf{r}'|$ is then expressed in terms of the spherical

coordinates for $\mathbf{r}'$:

$$|\mathbf{r} - \mathbf{r}'|^2 = \sin^2\theta\,\cos^2\phi\,r'^2 + \sin^2\theta\,\sin^2\phi\,r'^2 + (r - \cos\theta\,r')^2$$
$$= r^2 - 2\cos\theta\,rr' + r'^2. \tag{A.9}$$

With this, we rewrite the effective density (8.4):

$$n_{1s}^*(r\mathbf{e}_z) = \int_0^{2\pi} d\phi \int_0^{\pi} \sin\theta\,d\theta \int_0^{\infty} r'^2 dr'\,\phi\big(r^2 - 2\cos\theta\,rr' + r'^2, n_{1s}(r')\big)n_{1s}(r'). \tag{A.10}$$

The angular part of the integral can be carried out analytically (at least for the exponential and gaussian weight functions), yielding the corresponding radial-component weight functions,

$$\phi(r, r', n) = \int_0^{2\pi} d\phi \int_0^{\pi} \sin\theta\,d\theta\,\phi\big(r^2 - 2\cos\theta\,rr' + r'^2, n\big)$$
$$= 2\pi \int_{-1}^{1} d(\cos\theta)\phi\big(r^2 - 2\cos\theta\,rr' + r'^2, n\big), \tag{A.11}$$

such that the calculation of the effective density reduces to a single integral,

$$n_{1s}^*(r) = \int_0^{\infty} r'^2 dr'\,\phi\big(r, r', n_{1s}(r')\big)n_{1s}(r'), \tag{A.12}$$

which then can be carried out numerically.

Supplementary WLDA data

In this appendix, we supplement the WLDA data already presented in the main body of the text.

B.1 Plane wave convergence of all-electron atomization energies

In the main body of the text, the WLDA atomization energy convergence with plane wave cutoff was presented for the H_2, H_2O and HF molecules calculated using the *Hartree correction as exchange* option. In this section, we present data of the remaining molecules as well as the *Spin-neutral Hartree correction* option.

B.1.1 Remaining molecules

Figure B.1: WLDA atomization energies of the CO and O_2 molecules as a function of the plane wave cutoff, calculated with the exponential and gaussian weight functions, taking the *Hartree correction as exchange*. For reference, a ± 1 kcal/mol precision range is shown, centered at the 4000 eV value.

Figure B.2: WLDA atomization energies of the N_2 and F_2 molecules as a function of the plane wave cutoff, calculated with the exponential and gaussian weight functions, taking the *Hartree correction as exchange*. For reference, a ± 1 kcal/mol precision range is shown, centered at the 4000 eV value.

As shown in Figures B.1 and B.2, the CO, O_2 and N_2 molecules can all be converged to within a precision of 1 kcal/mol using plane wave cutoffs in the range of 1600-2400 eV. On the contrary, the F_2 molecule is merely approaching convergence at 4000 eV.

B.1.2 Spin-neutral Hartree correction
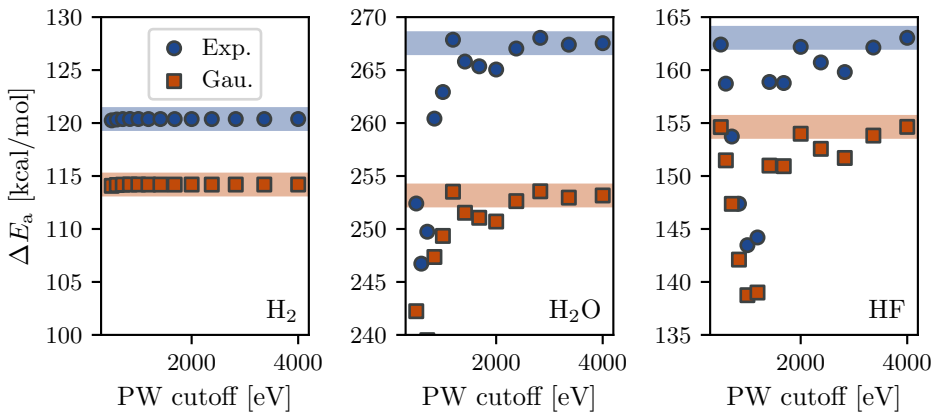
Figure B.3: WLDA atomization energies of the H_2, H_2O and HF molecules as a function of the plane wave cutoff, calculated with the exponential and gaussian weight functions, using the *Spin-neutral Hartree correction*. For reference, a ± 1 kcal/mol precision range is shown, centered at the 4000 eV value.
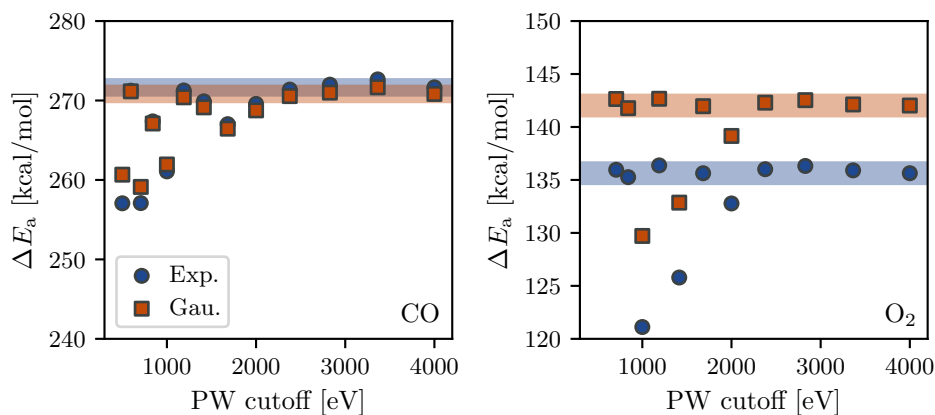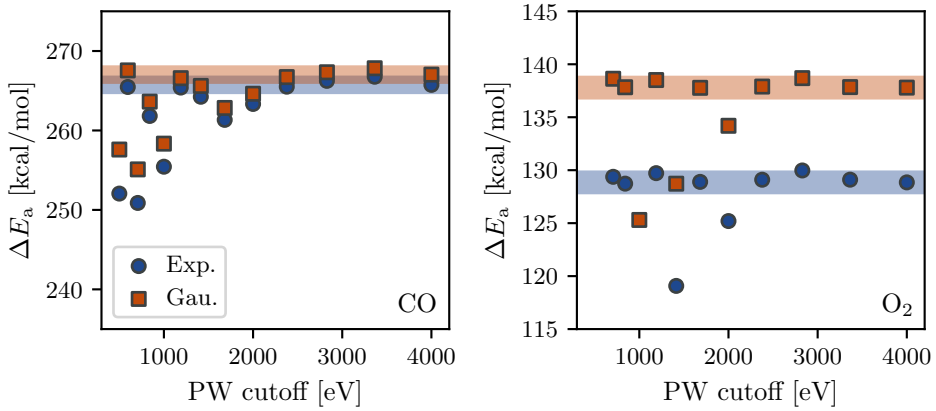
Figure B.4: WLDA atomization energies of the CO and O_2 molecules as a function of the plane wave cutoff, calculated with the exponential and gaussian weight functions, using the *Spin-neutral Hartree correction*. For reference, a ± 1 kcal/mol precision range is shown, centered at the 4000 eV value.
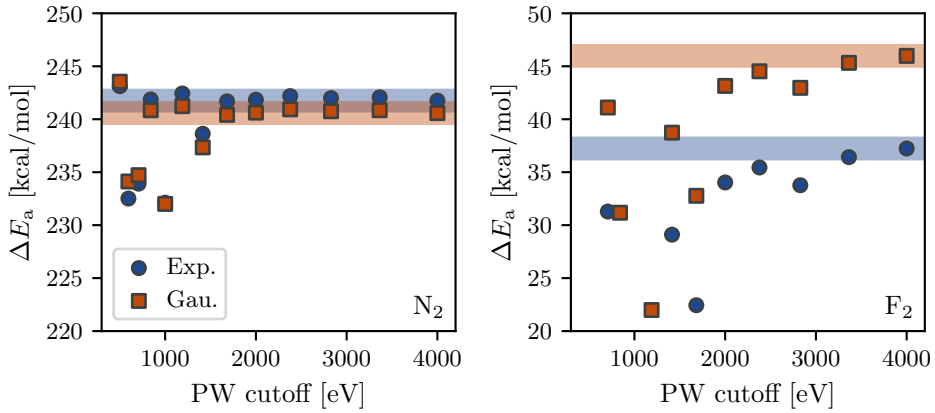

Figure B.5: WLDA atomization energies of the N_2 and F_2 molecules as a function of the plane wave cutoff, calculated with the exponential and gaussian weight functions, using the *Spin-neutral Hartree correction*. For reference, a ± 1 kcal/mol precision range is shown, centered at the 4000 eV value.

As shown in Figures B.3, B.4 and B.5, the plane wave convergence trends are not only independent of the weight function, but also the choice of spin-polarization option for the Hartree correction.

B.2   Atomization energies with the pseudo density

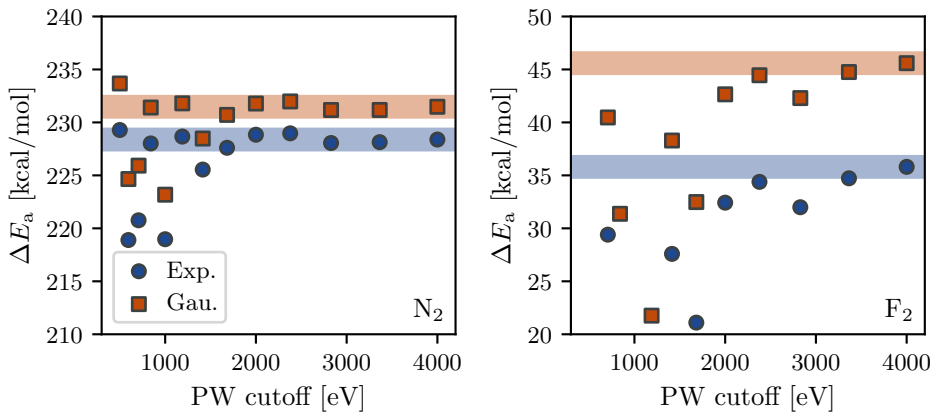In this section, we present the WLDA atomization energy performance on the G2/97 data set, calculated using the PAW pseudo density. In Tables B.1 and B.2, we give the concrete atomization energies for the seven simple molecules also reported in the main body of the text, while the overall performance metrics are listed in Table B.3.

	LDA	PBE	WLDA@Exp.	rWLDA@Exp.	fWLDA@Exp.	Expt.
CO	301	280	289 (285)	284 (280)	293 (290)	259
F_2	78.4	66.1	46.3 (46.1)	45 (44.8)	57 (56.9)	38.4
H_2	113	104	111 (120)	113 (122)	112 (118)	110
H_2O	268	243	269 (276)	263 (270)	269 (273)	233
HF	162	148	163 (168)	160 (164)	163 (166)	141
N_2	266	243	255 (244)	250 (239)	259 (251)	228
O_2	179	161	148 (144)	145 (140)	158 (155)	120
ME	34	17	22 (22)	18 (19)	26 (26)	
MAE	34	18	22 (22)	18 (19)	26 (26)	
MARE	0.31	0.19	0.14 (0.15)	0.12 (0.13)	0.2 (0.2)	

Table B.1: Atomization energies in kcal/mol calculated with a range of different xc functionals and compared to experimental references taken from a previous benchmark study [57] of the G2/97 data set. The WLDA corrections are calculated using the exponential weight function and the pseudo density. Numbers in parentheses relies on the *Spin-neutral Hartree correction*, otherwise the *Hartree correction as exchange* option is used.

	LDA	PBE	WLDA@Gau.	rWLDA@Gau.	fWLDA@Gau.	Expt.
CO	301	280	286 (282)	282 (277)	291 (288)	259
F_2	78.4	66.1	51.7 (51.6)	50.7 (50.6)	60.6 (60.5)	38.4
H_2	113	104	111 (114)	113 (116)	112 (114)	110
H_2O	268	243	260 (261)	255 (256)	263 (263)	233
HF	162	148	158 (159)	155 (156)	159 (160)	141
N_2	266	243	255 (244)	250 (239)	259 (251)	228
O_2	179	161	152 (148)	149 (145)	161 (158)	120
ME	34	17	20 (18)	18 (16)	25 (24)	
MAE	34	18	20 (18)	18 (16)	25 (24)	
MARE	0.31	0.19	0.15 (0.14)	0.14 (0.13)	0.21 (0.2)	

Table B.2: Atomization energies in kcal/mol calculated with a range of different xc functionals and compared to experimental references taken from a previous benchmark study [57] of the G2/97 data set. The WLDA corrections are calculated using the gaussian weight function and the pseudo density. Numbers in parentheses relies on the *Spin-neutral Hartree correction*, otherwise the *Hartree correction as exchange* option is used.

	ME	MAE	MARE
LDA	84.47	84.48	0.1987
PBE	26.3	26.94	0.08254
WLDA@Exp.	33.92 (41.33)	36.86 (44.37)	0.08873 (0.1001)
rWLDA@Exp.	22.92 (30.36)	27.32 (34.94)	0.07147 (0.08317)
fWLDA@Exp.	51.05 (55.91)	51.42 (56.31)	0.1203 (0.1275)
WLDA@Gau.	34.47 (32.64)	35.32 (33.62)	0.087 (0.08131)
rWLDA@Gau.	25.49 (23.67)	27.05 (25.39)	0.07129 (0.06566)
fWLDA@Gau.	51.32 (50.05)	51.32 (50.05)	0.1227 (0.1185)

Table B.3: Subset of the G2/97 atomization energy performance (141 molecules) listed in kcal/mol. WLDA corrections are calculated using the pseudo density. Numbers in parentheses uses the *Spin-neutral Hartree correction*. Otherwise the *Hartree correction as exchange* option is used. Performance metrics are given with respect to the experimental references listed in a previous benchmark study [57].

Bibliography

[1] A. L. Wysocki, A. Kutepov, and V. P. Antropov, "Strength and scales of itinerant spin fluctuations in 3d paramagnetic metals," Physical Review B **94**, 140405(R) (2016).

[2] A. L. Wysocki, V. N. Valmispild, A. Kutepov, S. Sharma, J. K. Dewhurst, E. K. Gross, A. I. Lichtenstein, and V. P. Antropov, "Spin-density fluctuations and the fluctuation-dissipation theorem in 3d ferromagnetic metals," Physical Review B **96**, 1 (2017).

[3] T. Moriya, *Spin fluctuations in itinerant electron magnetism*, Vol. 56, Springer Series in Solid-State Sciences (Springer-Verlag Berlin Heidelberg, 1985).

[4] S. Neusser and D. Grundler, "Magnonics: Spin waves on the nanoscale," Advanced Materials **21**, 2927 (2009).

[5] P. Monthoux, D. Pines, and G. G. Lonzarich, "Superconductivity without phonons," Nature **450**, 1177 (2007).

[6] D. J. Scalapino, "A common thread: The pairing interaction for unconventional superconductors," Reviews of Modern Physics **84**, 1383 (2012).

[7] W. Wu, J. Cheng, K. Matsubayashi, P. Kong, F. Lin, C. Jin, N. Wang, Y. Uwatoko, and J. Luo, "Superconductivity in the vicinity of antiferromagnetic order in CrAs," Nature Communications **5**, 5508 (2014).

[8] J.-G. Cheng, K. Matsubayashi, W. Wu, J. P. Sun, F. K. Lin, J. L. Luo, and Y. Uwatoko, "Pressure Induced Superconductivity on the border of Magnetic Order in MnP," Physical Review Letters **114**, 117001 (2015).

[9] Y. Wang, Y. Feng, J.-G. Cheng, W. Wu, J. L. Luo, and T. F. Rosenbaum, "Spiral magnetic order and pressure-induced superconductivity in transition metal compounds," Nature Communications **7**, 13037 (2016).

[10] K. Yosida, *Theory of magnetism* (Springer Berlin, 1996).

[11] A. T. Boothroyd, *Principles of Neutron Scattering from Condensed Matter* (Oxford University Press, 2020).

[12] H. Xiang, C. Lee, H.-J. Koo, X. Gong, and M.-H. Whangbo, "Magnetic properties and energy-mapping analysis," Dalton Trans. **42**, 823 (2013).

[13] T. Olsen, "Assessing the performance of the random phase approximation for exchange and superexchange coupling constants in magnetic crystalline solids," Physical Review B **96**, 125143 (2017).

[14] D. Torelli, K. S. Thygesen, and T. Olsen, "High throughput computational screening for 2D ferromagnetic materials: the critical role of anisotropy and local correlations," 2D Materials **6**, 045018 (2019).

[15] A. Liechtenstein, M. Katsnelson, V. Antropov, and V. Gubanov, "Local spin density functional approach to the theory of exchange interactions in ferromagnetic metals and alloys," Journal of Magnetism and Magnetic Materials **67**, 65 (1987).

[16] P. Bruno, "Exchange Interaction Parameters and Adiabatic Spin-Wave Spectra of Ferromagnets: A " Renormalized Magnetic Force Theorem"," Physical Review Letters **90**, 087205 (2003).

[17] M. I. Katsnelson and A. I. Lichtenstein, "Magnetic susceptibility, exchange interactions and spin-wave spectra in the local spin density approximation," Journal of Physics: Condensed Matter **16**, 7439 (2004).

[18] P. Buczek, A. Ernst, and L. M. Sandratskii, "Different dimensionality trends in the Landau damping of magnons in iron, cobalt, and nickel: Time-dependent density functional study," Physical Review B **84**, 174418 (2011).

[19] C. Friedrich, M. C. T. D. Müller, and S. Blügel, "Many-Body Spin Excitations in Ferromagnets from First Principles," in *Handbook of materials modeling: methods: theory and modeling*, edited by W. Andreoni and S. Yip (Springer International Publishing, Cham, 2020), pages 919–956.

[20] L. Van Hove, "Time-Dependent Correlations between Spins and Neutron Scattering in Ferromagnetic Crystals," Physical Review **95**, 1374 (1954).

[21] K. Zakeri, "Elementary spin excitations in ultrathin itinerant magnets," Physics Reports **545**, 47 (2014).

[22] H. J. Qin, K. Zakeri, A. Ernst, L. M. Sandratskii, P. Buczek, A. Marmodoro, T. H. Chuang, Y. Zhang, and J. Kirschner, "Long-living terahertz magnons in ultrathin metallic ferromagnets," Nature Communications **6**, 6126 (2015).

[23] F. Aryasetiawan and K. Karlsson, "Green's function formalism for calculating spin-wave spectra," Physical Review B **60**, 7419 (1999).

[24] K. Karlsson and F. Aryasetiawan, "Spin-wave excitation spectra of nickel and iron," Physical Review B **62**, 3006 (2000).

[25] E. Şaşıoğlu, A. Schindlmayr, C. Friedrich, F. Freimuth, and S. Blügel, "Wannier-function approach to spin excitations in solids," Phys. Rev. B **81**, 054434 (2010).

[26] C. Friedrich, E. Şaşıoğlu, M. Müller, A. Schindlmayr, and S. Blügel, "Spin Excitations in Solids from Many-Body Perturbation Theory," in *First principles approaches to spectroscopic properties of complex materials*, edited by C. Di Valentin, S. Botti, and M. Cococcioni (Springer Berlin Heidelberg, 2014), pages 259–301.

[27] M. C. T. D. Müller, C. Friedrich, and S. Blügel, "Acoustic magnons in the long-wavelength limit: Investigating the Goldstone violation in many-body perturbation theory," Physical Review B **94**, 064433 (2016).

[28]   S. Lounis, A. T. Costa, R. B. Muniz, and D. L. Mills, "Theory of local dynamical magnetic susceptibilities from the Korringa-Kohn-Rostoker Green function method," Physical Review B **83**, 035109 (2011).

[29]   M. Niesert, "Ab initio calculations of spin-wave spectra from time-dependent density-functional theory," PhD thesis (RWTH Aachen University, 2011).

[30]   B. Rousseau, A. Eiguren, and A. Bergara, "Efficient computation of magnon dispersions within time-dependent density functional theory using maximally localized Wannier functions," Physical Review B **85**, 054305 (2012).

[31]   N. Singh, P. Elliott, T. Nautiyal, J. K. Dewhurst, and S. Sharma, "Adiabatic generalized gradient approximation kernel in time-dependent density functional theory," Physical Review B **99**, 035151 (2019).

[32]   S. Y. Savrasov, "Linear response calculations of spin fluctuations," Physical Review Letters **81**, 2570 (1998).

[33]   K. Cao, H. Lambert, P. G. Radaelli, and F. Giustino, "Ab initio calculation of spin fluctuation spectra using time-dependent density functional perturbation theory, plane waves, and pseudopotentials," Physical Review B **97**, 024420 (2018).

[34]   N. Tancogne-Dejean, F. G. Eich, and A. Rubio, "Time-Dependent Magnons from First Principles," Journal of Chemical Theory and Computation **16**, 1007 (2020).

[35]   E. Runge and E. K. U. Gross, "Density-Functional Theory for Time-Dependent Systems," Physical Review Letters **52**, 997 (1984).

[36]   E. K. U. Gross and W. Kohn, "Local density-functional theory of frequency-dependent linear response," Physical Review Letters **55**, 2850 (1985).

[37]   J. J. Mortensen, L. B. Hansen, and K. W. Jacobsen, "Real-space grid implementation of the projector augmented wave method," Physical Review B **71**, 035109 (2005).

[38]   J. Enkovaara, C. Rostgaard, J. J. Mortensen, J. Chen, M. Dułak, L. Ferrighi, J. Gavnholt, C. Glinsvad, V. Haikola, H. a. Hansen, H. H. Kristoffersen, M. Kuisma, a. H. Larsen, L. Lehtovaara, M. Ljungberg, O. Lopez-Acevedo, P. G. Moses, J. Ojanen, T. Olsen, V. Petzold, N. a. Romero, J. Stausholm-Møller, M. Strange, G. a. Tritsaris, M. Vanin, M. Walter, B. Hammer, H. Häkkinen, G. K. H. Madsen, R. M. Nieminen, J. K. Nørskov, M. Puska, T. T. Rantala, J. Schiøtz, K. S. Thygesen, and K. W. Jacobsen, "Electronic structure calculations with GPAW: a real-space implementation of the projector augmented-wave method," Journal of Physics: Condensed Matter **22**, 253202 (2010).

[39]   P. E. Blöchl, "Projector augmented-wave method," Physical Review B **50**, 17953 (1994).

[40]   M. Lein, E. K. U. Gross, and J. P. Perdew, "Electron correlation energies from scaled exchange-correlation kernels: Importance of spatial versus temporal non-locality," Physical Review B **61**, 13431 (2000).

[41]   R. Kubo, "Statistical-Mechanical Theory of Irreversible Processes. I. General Theory and Simple Applications to Magnetic and Conduction Problems," Journal of the Physical Society of Japan **12**, 570 (1957).

[42]   J. Jensen and A. R. Mackintosh, *Rare earth magnetism: structures and excitations*, The International Series of Monographs on Physics (Clarendon Press, Oxford, 1991).

[43]   H. Nyquist, "Thermal Agitation of Electric Charge in Conductors," Physical Review **32**, 110 (1928).

[44]   H. B. Callen and T. A. Welton, "Irreversibility and Generalized Noise," Physical Review **83**, 34 (1951).

[45]   R. Kubo, "The fluctuation-dissipation theorem," Rep. Prog. Phys. **29**, 255 (1966).

[46]   L. Onsager, "Reciprocal Relations in Irreversible Processes. I.," Physical Review **37**, 405 (1931).

[47]   L. Onsager, "Reciprocal Relations in Irreversible Processes. II.," Physical Review **38**, 2265 (1931).

[48]   H. B. G. Casimir, "On Onsager's Principle of Microscopic Reversibility," Reviews of Modern Physics **17**, 343 (1945).

[49]   L. D. Landau and E. M. Lifshitz, *Statistical physics*, Course of Theoretical Physics (Pergamon Press, Oxford, 1969).

[50]   N. Nagaosa, J. Sinova, S. Onoda, A. H. MacDonald, and N. P. Ong, "Anomalous Hall effect," Reviews of Modern Physics **82**, 1539 (2010).

[51]   P. Hohenberg and W. Kohn, "Inhomogeneous Electron Gas," Physical Review **136**, B864 (1964).

[52]   W. Kohn and L. J. Sham, "Self-Consistent Equations Including Exchange and Correlation Effects," Physical Review **140**, A1133 (1965).

[53]   U. von Barth and L. Hedin, "A local exchange-correlation potential for the spin polarized case. i," Journal of Physics C: Solid State Physics **5**, 1629 (1972).

[54]   K. Capelle and G. Vignale, "Nonuniqueness of the Potentials of Spin-Density-Functional Theory," Physical Review Letters **86**, 5546 (2001).

[55]   H. Eschrig and W. Pickett, "Density functional theory of magnetic systems revisited," Solid State Communications **118**, 123 (2001).

[56]   A. K. Rajagopal and J. Callaway, "Inhomogeneous Electron Gas," Physical Review B **7**, 1912 (1973).

[57]   J. Wellendorff, K. T. Lundgaard, A. Møgelhøj, V. Petzold, D. D. Landis, J. K. Nørskov, T. Bligaard, and K. W. Jacobsen, "Density functionals for surface science: Exchange-correlation model development with Bayesian error estimation," Physical Review B **85**, 235149 (2012).

[58]   B. Himmetoglu, A. Floris, S. de Gironcoli, and M. Cococcioni, "Hubbard-corrected DFT energy functionals: The LDA+U description of correlated systems," International Journal of Quantum Chemistry **114**, 14 (2014).

[59]   V. I. Anisimov, J. Zaanen, and O. K. Andersen, "Band theory and Mott insu-
       lators: Hubbard U instead of Stoner I," Physical Review B **44**, 943 (1991).

[60]   A. I. Liechtenstein, V. I. Anisimov, and J. Zaanen, "Density-functional theory
       and strong interactions: Orbital ordering in Mott-Hubbard insulators," Physical
       Review B **52**, R5467 (1995).

[61]   S. L. Dudarev, G. A. Botton, S. Y. Savrasov, C. J. Humphreys, and A. P. Sutton,
       "Electron-energy-loss spectra and the structural stability of nickel oxide: An
       LSDA+U study," Physical Review B **57**, 1505 (1998).

[62]   M. A. Marques, C. A. Ullrich, F. Nogueira, A. Rubio, K. Burke, and E. K. U.
       Gross, editors, *Time-dependent density functional theory*, Lecture Notes in Physics
       (Springer Berlin Heidelberg, Berlin, Heidelberg, 2006).

[63]   S. L. Adler, "Quantum Theory of the Dielectric Constant in Real Solids," Phys-
       ical Review **126**, 413 (1962).

[64]   N. Wiser, "Dielectric Constant with Local Field Effects Included," Physical
       Review **129**, 62 (1963).

[65]   E. Gross and K. Burke, "Basics," in *Time-dependent density functional theory*,
       edited by M. A. Marques, C. A. Ullrich, F. Nogueira, A. Rubio, K. Burke, and
       E. K. U. Gross (Springer Berlin Heidelberg, Berlin, Heidelberg, 2006), pages 1–
       13.

[66]   T. Olsen, C. E. Patrick, J. E. Bates, A. Ruzsinszky, and K. S. Thygesen, "Beyond
       the RPA and GW methods with adiabatic xc-kernels for accurate ground state
       and quasiparticle energies," npj Computational Materials **5**, 106 (2019).

[67]   J. Yan, J. J. Mortensen, K. W. Jacobsen, and K. S. Thygesen, "Linear density
       response function in the projector augmented wave method: Applications to
       solids, surfaces, and interfaces," Physical Review B **83**, 245122 (2011).

[68]   F. G. Eich, S. Pittalis, and G. Vignale, "A shortcut to gradient-corrected magnon
       dispersion: exchange-only case," The European Physical Journal B **91**, 173
       (2018).

[69]   T. J. Williams, A. E. Taylor, A. D. Christianson, S. E. Hahn, R. S. Fishman,
       D. S. Parker, M. A. McGuire, B. C. Sales, and M. D. Lumsden, "Extended
       magnetic exchange interactions in the high-temperature ferromagnet MnBi,"
       Applied Physics Letters **108**, 192403 (2016).

[70]   M. A. McGuire, H. Cao, B. C. Chakoumakos, and B. C. Sales, "Symmetry-
       lowering lattice distortion at the spin reorientation in MnBi single crystals,"
       Physical Review B **90**, 174425 (2014).

[71]   V. P. Antropov, V. N. Antonov, L. V. Bekenov, A. Kutepov, and G. Kotliar,
       "Magnetic anisotropic effects and electronic correlations in MnBi ferromagnet,"
       Physical Review B **90**, 054404 (2014).

[72]   K. V. Shanavas, D. Parker, and D. J. Singh, "Theoretical study on the role of
       dynamics on the unusual magnetic properties in MnBi," Scientific Reports **4**,
       7222 (2015).

[73] E. Samuelsen, M. Hutchings, and G. Shirane, "Inelastic neutron scattering in- vestigation of spin waves and magnetic interactions in Cr2O3," Physica **48**, 13 (1970).

[74] J. Kohanoff, *Electronic structure calculations for solids and molecules* (Cam- bridge University Press, Cambridge, 2006).

[75] J. F. Dobson and B. P. Dinte, "Constraint Satisfaction in Local and Gradient Susceptibility Approximations: Application to a van der Waals Density Func- tional," Physical Review Letters **76**, 1780 (1996).

[76] O. Gunnarsson and B. I. Lundqvist, "Exchange and correlation in atoms, molecules, and solids by the spin-density-functional formalism," Physical Review B **13**, 4274 (1976).

[77] J. Harris and R. Jones, "On the surface energy of a bounded electron gas," Physics Letters A **46**, 407 (1974).

[78] D. Langreth and J. Perdew, "The exchange-correlation energy of a metallic surface," Solid State Communications **17**, 1425 (1975).

[79] R. O. Jones and O. Gunnarsson, "The density functional formalism, its appli- cations and prospects," Reviews of Modern Physics **61**, 689 (1989).

[80] D. J. Singh, "Weighted-density-approximation ground-state studies of solids," Physical Review B **48**, 14099 (1993).

[81] L. E. Ballentine, *Quantum Mechanics - A Modern Development* (World Scien- tific Publishing Co. Pte. Ltd., Singapore, 2015).

[82] L. Hedin and S. Lundqvist, "Effects of Electron-Electron and Electron-Phonon Interactions on the One-Electron States of Solids," in *Solid state physics - ad- vances in research and applications*, Vol. 23, C (1970), pages 1–181.

[83] J. P. Perdew and A. Zunger, "Self-interaction correction to density-functional approximations for many-electron systems," Physical Review B **23**, 5048 (1981).

[84] A. D. Becke, "Density-functional thermochemistry. III. The role of exact ex- change," The Journal of Chemical Physics **98**, 5648 (1993).

[85] C. Adamo and V. Barone, "Exchange functionals with improved long-range be- havior and adiabatic connection methods without adjustable parameters: The mPW and mPW1PW models," The Journal of Chemical Physics **108**, 664 (1998).

[86] J. P. Perdew, A. Ruzsinszky, G. I. Csonka, O. A. Vydrov, G. E. Scuseria, V. N. Staroverov, and J. Tao, "Exchange and correlation in open systems of fluctuat- ing electron number," Physical Review A **76**, 040501 (2007).

[87] J. Harl, L. Schimka, and G. Kresse, "Assessing the quality of the random phase approximation for lattice constants and atomization energies of solids," Physical Review B **81**, 115126 (2010).

[88] P. Hessler, J. Park, and K. Burke, "Several Theorems in Time-Dependent Den- sity Functional Theory," Physical Review Letters **82**, 378 (1999).

[89]   P. Hessler, J. Park, and K. Burke, "Erratum: Several Theorems in Time-Dependent Density Functional Theory [Phys. Rev. Lett. 82, 378 (1999)]," Physical Review Letters **83**, 5184 (1999).

[90]   J. Lindhard, "On the properites of a gas of charged particles," Dan. Mat. Phys. Medd. **28**, 1 (1954).

[91]   J. P. Perdew and Y. Wang, "Pair-distribution function and its coupling-constant average for the spin-polarized electron gas," Physical Review B **46**, 12947 (1992).

[92]   J. P. Perdew, K. Burke, and M. Ernzerhof, "Generalized Gradient Approximation Made Simple," Physical Review Letters **77**, 3865 (1996).

[93]   T. Olsen and K. S. Thygesen, "Extending the random-phase approximation for electronic correlation energies: The renormalized adiabatic local density approximation," Physical Review B **86**, 081103 (2012).

[94]   T. Olsen and K. S. Thygesen, "Beyond the random phase approximation: Improved description of short-range correlation by a renormalized adiabatic local density approximation," Physical Review B **88**, 115131 (2013).

[95]   C. E. Patrick and K. S. Thygesen, "Adiabatic-connection fluctuation-dissipation DFT for the structural properties of solids—The renormalized ALDA and electron gas kernels," The Journal of Chemical Physics **143**, 102802 (2015).

[96]   J. Tao, J. P. Perdew, V. N. Staroverov, and G. E. Scuseria, "Climbing the Density Functional Ladder: Nonempirical Meta–Generalized Gradient Approximation Designed for Molecules and Solids," Physical Review Letters **91**, 146401 (2003).

[97]   J. Sun, A. Ruzsinszky, and J. Perdew, "Strongly Constrained and Appropriately Normed Semilocal Density Functional," Physical Review Letters **115**, 1 (2015).

[98]   A. Rasmussen, "New Non-local XC Functionals and High-throughput Studies of 2D Materials," PhD thesis (Department of Physics, Technical University of Denmark, 2021).

[99]   J. P. Perdew and Y. Wang, "Accurate and simple analytic representation of the electron-gas correlation energy," Physical Review B **45**, 13244 (1992).

[100] G. Román-Pérez and J. M. Soler, "Efficient Implementation of a van der Waals Density Functional: Application to Double-Wall Carbon Nanotubes," Physical Review Letters **103**, 096102 (2009).

[101] J. S. Lee and S. Y. Park, "Basis set convergence of correlated calculations on He, H2, and He2," The Journal of Chemical Physics **112**, 10746 (2000).

[102] S. J. Chakravorty, S. R. Gwaltney, E. R. Davidson, F. A. Parpia, and C. F. p Fischer, "Ground-state correlation energies for atomic ions with 3 to 18 electrons," Physical Review A **47**, 3649 (1993).

[103] E. R. Davidson, S. A. Hagstrom, S. J. Chakravorty, V. M. Umar, and C. F. Fischer, "Ground-state correlation energies for two- to ten-electron atomic ions," Physical Review A **44**, 7071 (1991).

[104] M. D. Wilkinson, M. Dumontier, I. J. Aalbersberg, G. Appleton, M. Axton, A. Baak, N. Blomberg, J.-W. Boiten, L. B. da Silva Santos, P. E. Bourne, J. Bouwman, A. J. Brookes, T. Clark, M. Crosas, I. Dillo, O. Dumon, S. Edmunds, C. T. Evelo, R. Finkers, A. Gonzalez-Beltran, A. J. Gray, P. Groth, C. Goble, J. S. Grethe, J. Heringa, P. A. 't Hoen, R. Hooft, T. Kuhn, R. Kok, J. Kok, S. J. Lusher, M. E. Martone, A. Mons, A. L. Packer, B. Persson, P. Rocca-Serra, M. Roos, R. van Schaik, S.-A. Sansone, E. Schultes, T. Sengstag, T. Slater, G. Strawn, M. A. Swertz, M. Thompson, J. van der Lei, E. van Mulligen, J. Velterop, A. Waagmeester, P. Wittenburg, K. Wolstencroft, J. Zhao, and B. Mons, "The FAIR Guiding Principles for scientific data management and stewardship," Scientific Data **3**, 160018 (2016).

[105] S. Haastrup, M. Strange, M. Pandey, T. Deilmann, P. S. Schmidt, N. F. Hinsche, M. N. Gjerding, D. Torelli, P. M. Larsen, A. C. Riis-Jensen, J. Gath, K. W. Jacobsen, J. Jørgen Mortensen, T. Olsen, and K. S. Thygesen, "The Computational 2D Materials Database: high-throughput modeling and discovery of atomically thin crystals," 2D Materials **5**, 042002 (2018).

[106] M. N. Gjerding, A. Taghizadeh, A. Rasmussen, S. Ali, F. Bertoldo, T. Deilmann, N. R. Knøsgaard, M. Kruse, A. H. Larsen, S. Manti, T. G. Pedersen, U. Petralanda, T. Skovhus, M. K. Svendsen, J. J. Mortensen, T. Olsen, and K. S. Thygesen, "Recent progress of the computational 2D materials database (C2DB)," 2D Materials **8**, 044002 (2021).

[107] J. Mortensen, M. Gjerding, and K. Thygesen, "MyQueue: Task and workflow scheduling system," Journal of Open Source Software **5**, 1844 (2020).

[108] A. Hjorth Larsen, J. Jørgen Mortensen, J. Blomqvist, I. E. Castelli, R. Christensen, M. Dułak, J. Friis, M. N. Groves, B. Hammer, C. Hargus, E. D. Hermes, P. C. Jennings, P. Bjerre Jensen, J. Kermode, J. R. Kitchin, E. Leonhard Kolsbjerg, J. Kubal, K. Kaasbjerg, S. Lysgaard, J. Bergmann Maronsson, T. Maxson, T. Olsen, L. Pastewka, A. Peterson, C. Rostgaard, J. Schiøtz, O. Schütt, M. Strange, K. S. Thygesen, T. Vegge, L. Vilhelmsen, M. Walter, Z. Zeng, and K. W. Jacobsen, "The atomic simulation environment—a Python library for working with atoms," Journal of Physics: Condensed Matter **29**, 273002 (2017).

[109] G. B. Arfken and A. H. J. Weber, *Mathematical methods for physicists* (Elsevier Academic Press, Burlington, 2005).

In modern human life, we depend on a wide range of electronic technologies to perform vital tasks such as to illuminate, refrigerate and communicate. Typically, we also have some intuition for the physics behind: In a computer, for example, information is processed using currents of electrons, a process governed by Ohm's law. However, on the topic of magnetic materials and technologies, many will instead blank. It is not that magnetic materials are not common in our daily lives. Most people have seen how a piece of iron may be magnetized using a permanent magnet, but one thing is to see, another to understand, and classroom experiments in magnetism typically raise more questions than they answer: How do magnetic materials work? What can we use them for? Why aren't magnetic devices as common as electric ones?

It can be both frustrating and captivating to discover that a fundamental understanding of magnetic properties requires quantum mechanics. In particular, an electron is not only characterized by a position and velocity, but also a spin. That is, a direction in which it points. An atom is magnetic, if it tends to have an excess amount of electrons pointing in a given direction, and a material is magnetic, if it prefers the electrons of neighbouring magnetic atoms to align according to a specific pattern. In ferromagnets, like iron, electrons of neighbouring magnetic atoms tend to point in the same direction, but many more complicated patterns also exist in nature.

Now, similar to the fact that the water molecules of an ice crystal vibrate at finite temperatures, only to form a perfect crystal in the temperature limit of absolute zero, the local orientation of the electronic spins also fluctuates in a magnet at finite temperatures. These fluctuations are characterized by the fundamental magnetic excitations of the magnet, that is, excitations that form wave-like patterns in the spin texture of the material.

In this thesis, it is shown how one may compute spin wave properties of arbitrary materials, starting from the fundamentals of quantum mechanics. To this end, the theories of linear response and time-dependent density functional theory are presented and combined into a computer implementation in the open-source GPAW code. Beyond the fundamental theory, the thesis presents a thorough benchmark of the code as well as state-of-the-art calculations of the spin wave spectra in Fe, Ni, Co, MnBi, Cr and Cr_2O_3. Lastly, an effort to improve the core approximations of the theory, namely approximations to the exchange-correlation functional, is presented.

Technical University of Denmark
DTU Physics
Department of Physics

Fysikvej 311
2800 Kongens Lyngby, Denmark
Phone: +45 4525 3344
info@fysik.dtu.dk

www.fysik.dtu.dk

DTU